ROCK STRENGTH UNDER TRUE TRIAXIAL LOADING, SEISMOTECTONICS OF NORTHERN SOUTH AMERICA AND GEOMECHANICS AND COAL BED METHANE PRODUCTION IN THE POWDER RIVER BASIN

A DISSERTATION
SUBMITTED TO THE DEPARTMENT OF GEOPHYSICS
AND THE COMMITTEE ON GRADUATE STUDIES
OF STANFORD UNIVERSITY
IN PARTIAL FULFILLMENT OF THE REQUIREMENTS
FOR THE DEGREE OF
DOCTOR OF PHILOSOPHY

Lourdes Belén Colmenares

December, 2004

I certify that I have read this dissertation and that, in my opinion, it is fully adequate in scope and quality as a dissertation for the degree of Doctor of Philosophy.

Mark D. Zoback (Principal Adviser)

I certify that I have read this dissertation and that, in my opinion, it is fully adequate in scope and quality as a dissertation for the degree of Doctor of Philosophy.

Jerry Harris

I certify that I have read this dissertation and that, in my opinion, it is fully adequate in scope and quality as a dissertation for the degree of Doctor of Philosophy.

Anthony Kovscek

I certify that I have read this dissertation and that, in my opinion, it is fully adequate in scope and quality as a dissertation for the degree of Doctor of Philosophy.

Norman Sleep

Approved for the University Committee on Graduate Studies.

Abstract

In this Ph.D. thesis, I present three research projects in the areas of rock mechanics, seismotectonics and geomechanics. In the rock mechanics study, I examined seven different failure criteria by comparing them to published polyaxial test data ($\sigma_1>\sigma_2>\sigma_3$) for five different rock types at a variety of stress states. I employed a grid search algorithm to find the best set of parameters that describe failure for each criterion and the associated misfits. Overall, I found that the polyaxial criteria Modified Wiebols and Cook and Modified Lade achieved a good fit to most of the test data. This is especially true for rocks with a highly σ_2-dependent failure behavior (e.g. Dunham dolomite, Solenhofen limestone). However, for some rock types (e.g. Shirahama Sandstone, Yuubari shale), the intermediate stress hardly affects failure and the Mohr-Coulomb and Hoek and Brown criteria fit these test data equally well, or even better, than the more complicated polyaxial criteria. The values of Co yielded by the Inscribed and the Circumscribed Drucker-Prager criteria bounded the Co value obtained using the Mohr Coulomb criterion as expected. In general, the Drucker-Prager failure criterion did not accurately indicate the value of σ_1 at failure. The value of the misfits achieved with the empirical 1967 and 1971 Mogi criteria were generally in between those obtained using the triaxial and the polyaxial criteria. The disadvantage of these failure criteria is that they cannot be related to strength parameters such as Co. I also found that if only data from triaxial tests are available, it is possible to incorporate the influence of σ_2 on failure by using a polyaxial failure criterion. The results for two out of three rocks that could be analyzed in this way were encouraging.

In a second study, the combination of the in situ stress, neotectonic, and GPS data was used to generate an integrated stress map of northern South America, which shows that the stress field in the region varies systematically in both orientation and relative magnitude. It is most compressive in the Ecuadorian Andes province where the direction of maximum compression is approximately E-W, less compressive in the North Andes province with maximum compression approximately NW-SE, and least compressive in the San Sebastian–El Pilar province that shows a NE-SW direction of extension. This systematic change in the stress field appears to reflect both relative plate motions and the negative buoyancy of the subducted Caribbean slab.

The third project I worked on is about the geomechanics and wellbore completion methods of Coalbed Methane (CBM) wells in the Powder River basin, Wyoming. After drilling and under-reaming the coal section of a CBM well, a common completion

technique used by many operators in the Powder River basin is to pump water into the wellbore to "enhance" production. Through analyzing the data during these operations, it is clear that the "water-enhancement" activities in the Powder River Basin result in hydraulic fracturing of the coal (and in some cases the adjacent strata) thereby perhaps resulting in both excess CBM water production and inefficient depressurization of coals. I have obtained water-enhancement tests data in coals from about ~550 wells to obtain the magnitude of the least principal stress in the coal seams. These data indicate that vertical fracture growth occurs in many places in the basin whereas the hydrofracs appear to be horizontal in other areas. I also investigated the relationship between hydraulic fracture orientation and water and gas production. I found that water production from wells with vertical hydraulic fractures tends to exceed water production from wells with horizontal fractures for the same coal in the same general area. In one specific region of the PRB, 71% of the CBM water from the Big George coal is produced by only 32% of the wells, all of which are characterized by vertically propagating hydraulic fractures. In these same wells with exceptionally high water production, the time at which gas production starts is significantly delayed relative to wells with vertical fractures and low water production, that is, water production comparable to that of the wells with horizontal fractures. Wells with vertical fractures tend to be excellent gas producers, which implies that the face cleats in the coals must be efficiently connected by the induced vertical fracture. In general, I have found that in areas where a coal seam has a thickness greater than 60 feet, S_3 is equivalent to the minimum horizontal stress, therefore fractures propagate in the vertical direction. In areas of known vertical fracture propagation it is necessary to limit the injection during the water enhancement tests in order to prevent propagation of induced fractures into the overlying water-bearing formations. In areas where S_3 is unknown, a minifrac (~2 bpm for ~2 min) should be done to determine the magnitude of S_3 and thus whether fracture propagation would be vertical or horizontal. If S_3 corresponds to the overburden, horizontal fracture propagation will occur and the water enhancement activities can proceed as usual. As wells with horizontal fractures tend to be poor gas producers, it is also suggested that such wells are hydraulically fractured (and propped) to enhance gas production. If the shut-in pressure is significantly less than the overburden, vertical hydraulic fracture growth is implied and significantly reduced pumping is advised. This would be beneficial from the perspective of minimizing produced waters and decreasing the time for initial gas production.

Acknowledgements

Almost six years since I arrived at Stanford and it still seems as if it was yesterday when I stood right next to Prof. Mark Zoback in B59 where he was introducing me to Dave and Wendy. I felt very small, for obvious reasons since I am not tall and Mark is, but I also felt so excited about the new chapter of my life that was just starting at that very moment. After many sleepless nights and lots and lots of work with a sprinkle of fun here and there, I have finally finished my PhD. As it is expected, for the completion of my projects I had to ask for many favors and now is a good time to acknowledge all those who willingly gave me their support either through advice, data, finances or words of affirmation. First and foremost, thank you Mark for accepting me in your group, and most especially for introducing me to the Swiss guy who eventually became my husband. I will be forever grateful for that. I thank you not only for the way you have been towards me but for how I have seen you caring for my fellow group-mates. It is comforting to realize that I had a knowledgeable and caring mentor, qualities that should be praised and almost required if a professor wants to become an advisor. You are an example of hard work, constancy, tenacity, perseverance but also a great example of a very busy guy who absolutely adores his family. This is what made me the happiest about being your student, the fact that your priorities are straight: work is important but family comes first. Thank you to my committee: Mark Zoback, Tony Kovscek, Jerry Harris and Norm Sleep for their availability, insights and support. Thank you to Simon Klemperer and George Thompson for their input with respect to the second project in which I was involved. Thank you especially to Simon for welcoming me in his research group as one of his own, I learned immensely in the seminars and had great fun in the field trips and parties. Kevin Arrigo was great to work with while I was the TA liaison for the department and when I TA'd one of his classes but I will always be thankful for his cheery personality and for inheriting most of my plants.

Thank you Prof. Jerry Harris for being a great Chair of the Department of Geophysics. I enjoyed working with you when I was in GSAC and I also enjoyed our many conversations throughout the years. I admire your desire and resolution of making this department a better one, not only academically but also in terms of friendliness.

Thank you to PDVSA-CIED, the Stanford Rock Physics and Borehole Geophysics Project, the Western Resources Project and the Global Climate Energy Project for funding different phases of my PhD career.

Things could be tougher around the department if it was not for the wonderful staff that works in it. They all show that they care and I am deeply thankful for that. Thanks especially to Jeannette, who has been like a second mother to me, for better or for worse; then again, I have been like a daughter to her, for better or for worse, so it is a tie. Thanks also to Susan, for the delightful matzo sweets, for all the very interesting conversations we have had and for always being so nice to me.

During a time, the library became my second home and it was great to realize that we truly count on knowledgeable people in it who were always willing to help me find all the resources needed for my research.

I have been fortunate to spend some quality time with my research group, the Stress and Crustal Mechanics Group. We all have different backgrounds and nationalities and yet we all have this geeky hallo and this stubborn attitude that can only mean one thing, we were all meant to come to Stanford. It has been great to be in a friendly atmosphere in which every person is him/herself and everybody has a delightful sense of humor. You guys are awesome! With respect to my officemates, I have been very lucky with them. The only times I had to play my own music was when I did not have them. Thank you for the interesting chats, the music and the laughs.

I have made so many friends throughout the years that I hope we will always find ways to reunite in the future. I do not want to say names because it is too dangerous; I am terrified of leaving somebody out. Thank you for the smiles and for the willingness to be my friends. Thank you for the dinners, long and short conversations, game nights, craft nights, movie nights, concerts, BBQ's, runs, hikes, phone calls and e-mails. Thank you for the walks to the dish, the bookstore, the post-office or the bank. All the activities that we shared gave me the boost to go back to the office and work non-stop for a thousand hours more. I will always be deeply thankful to all my prayer buddies for your solidarity, love, support, and constant reminder of the power of prayer. It has been wonderful to count on God-fearing and God-seeking people like you.

Balz, my husband, my friend and an outstanding scientist. I am so grateful to be your wife. You have had so much patience; you have truly made me become a better person. You have always been there to motivate me, to tell me how great you think my research is and you were always available to listen to my ideas, even when it was too early or too late for you. Thank you for the love, I hope I am as great as a partner for you as you are for me.

Thanks to my parents, for believing that I can achieve great things, but most of all for your love and for having the immense courage and maturity of letting me go away from the nest so I can find my own path and my own purpose and role in this world.

In my undergrad thesis I acknowledged God for giving me strength when I thought I could not keep on going and I find myself again needing to acknowledge Him for all the wonderful things He has done for me. He has not only given me the strength to keep on going and to finish this work but He has also shown me, when I was needing Him the most, that He was certainly there for me, to cheer me up and to pick me up if necessary. He showed me that indeed, I can do all things through Christ who strengthens me (Philippians 4:13). Thank you Lord for never forsaking me. This PhD is not mine, it is His.

Table of Contents

List of Tables

List of Illustrations

CHAPTER 1.

Strength Under True Triaxial Loading, Seismotectonics of Northern South America and Geomechanics and Coal Bed Methane Production in the Powder River Basin:

Introduction

1.1 INTRODUCTION

Knowledge of stress magnitudes and direction are crucial in understanding global tectonics and have a tremendous impact on the mining, and oil and gas industries. In my thesis, I have investigated a number of ways in which earth stresses impact observations made on a large variety of scales, ranging from the tectonic activity in northern South America, to the water and gas production from coalseams in the Powder River Basin (PRB) in Wyoming, to the conditions under which rocks fail on a small scale. More specifically, this work looks into the following processes: In Chapter 2, I aim to understand the impact of the magnitude of stresses to determine conditions under which rocks fail. A large number of publications have put forward different failure criteria to better describe rock failure. In this work, I systematically investigate which published failure criteria are adequately representing rock failure observations obtained from polyaxial laboratory testing. In Chapter 3, I evaluate the magnitude and orientation of earth stresses with the goal of understanding the seismotectonic processes taking place specifically in northern South America. And finally, in Chapter 4 I have investigated the magnitude of the least principal stress in coal seams. The findings from Chapter 4, have a number of applications, such as prediction of the direction of propagation of hydraulic fractures in coal seems, and the consequences of such propagation for the coalbed methane and water production in the PRB.

To evaluate the stress magnitudes and direction I used a variety of data. For the first project (Chapter 2), stress data from laboratory testing were used. For the second project (Chapter 3) earthquake focal mechanism data, as well as in situ stress measurements such as image logs and geologic indicators were used to obtain the direction of the maximum horizontal stress. For the third project (Chapter 4) I was able to determine the magnitude of the least principal stress from water enhancement tests in CBM wells. Interestingly, these tests were not intended to generate any information on the in situ state of stress. However, as the work presented in Chapter 4 shows, it was evident that the abundant water enhancement tests in the Powder River Basin serve the purpose of measuring the magnitude of S_3 and therefore of identifying the propagation direction of hydraulic fractures that are created by these tests. With the obtained stress data I was able to tackle small scale problems (first project, Chapter 2), middle scale projects (third project, Chapter 4), as well as regional settings (second project, Chapter 3).

My PhD thesis is a reminder and an affirmation of the applicability and the value of stress data, which can be useful on different issues and the scope of its application is wide enough to go from small scale to regional scales.

1.2 STRUCTURE AND CONTENTS OF THIS THESIS

Since my thesis is the compendium of three well defined projects, I have written one chapter for each project. In the following sections I will briefly introduce each of them.

1.2.1 Evaluation of rock failure criteria (Chapter 2)

In attempt to describe stress conditions under which rocks fail, a number of different failure criteria have been proposed to describe brittle rock failure. In this study, I aim to find which failure criterion, and which parameters, best describes the behavior of each rock type by minimizing the misfit between the predicted failure stress and the experimental data. With this approach, the different criteria can be benchmarked against a variety of rock strength data for a variety of lithologies. This work also allowed me to investigate the influence of the intermediate stress on rock failure. I tested two conventional "triaxial" criteria (the Mohr-Coulomb and the Hoek and Brown criteria), which ignore the influence of the intermediate principal stress and are thus applicable to conventional triaxial test data ($\sigma_1>\sigma_2=\sigma_3$), three true triaxial, or polyaxial criteria (Modified Wiebols and Cook, Modified Lade, and Drucker-Prager), which consider the influence of the intermediate principal stress in polyaxial strength tests ($\sigma_1>\sigma_2>\sigma_3$) and two empirical criteria (Mogi 1967 and Mogi 1971). It is very important to mention that the behavior of the conventional "triaxial" criteria in their 3D versions (taking into account σ_2) was not investigated, as they have been widely used in their standard 2D version, especially when studying wellbore stability. The five rock types investigated were: amphibolite from the "Kontinentalen Tiefbohrung" (KTB) site, Dunham dolomite, Solenhofen limestone, Shirahama sandstone and Yuubari shale.

In the different sections of Chapter 2, I first define the various failure criteria I am evaluating and the rock types tested. I then define the statistical procedure I developed for evaluating the various strength criteria for each rock type. After presenting the results of our statistical analysis and evaluating the fit of each criterion for each rock type, I briefly examine the question of whether rock strength parameters obtained with triaxial tests (Co, μ_i) can be utilized in polyaxial failure criteria.

1.2.2 Stress field and seismotectonics of northern South America (Chapter 3)

The present-day tectonics of northern South America is complex as four plates interact in the region—the South American, Caribbean, and Nazca plates and the Costa Rica–Panama microplate. The area of study corresponds to the southern part of the Caribbean plate whose origin, as well as its boundaries remain a topic of debate. As early as 1970, Nagle expressed frustration: "*The number of attempts to synthesize the tectonic framework of the Caribbean are infinite, as are the number of different frameworks which have been suggested…In terms of the plate tectonic 'revolution' in earth sciences, it would be very much preferable if the Caribbean area and the Bahamas did not exist."* In this work, I am compiling a comprehensive data set, which should help in shedding at least some light on the tectonic processes in the area.

In the sections of Chapter 3 I first describe the major tectonic features of the study area. I then summarize several key seismotectonics models proposed previously by other authors and show the findings of different GPS studies and establish relationships with the tectonics of the region. After, I explain the kind of data collected in order to construct the integrated stress map of northern South America and I later define the stress provinces of the region. I finish the chapter with a thorough discussion and conclusions.

1.2.3 Geomechanics and the effectiveness of wellbore completion methods of CBM wells (Chapter 4)

The Powder River Basin (PRB) of Wyoming and Montana is the site of the fastest growing domestic natural gas play – the development of the coalbed methane (CBM) from the Wyodak and Big George coal beds. Within the next 10 years, as much as 75% of the growth in coalbed methane production in the U.S. is expected to occur in this region. However, along with the growth in CBM production has been the growth in produced water, as part of dewatering the coal formations in order to depressurize and thus enable the coals to release their adsorbed methane. Even after gas production is initiated, large volumes of water are still produced. Water produced during the dewatering of coalbed wells is disposed in several ways: discharged into surface drainage and streams, containment in surface ponds where it infiltrates, evaporates or is used for ranch and stock watering needs, atomization and when the water quality is not good enough for any of the above activities, the water is injected back into the ground. The

water is generally of potable quality in the center of the basin, becoming more saline to the north and south, where it becomes hard to handle. Consequently, the disposal of water produced by coalbed methane wells is a major environmental issue at many well locations, especially in areas where the water produced has high sodium content. Our goal in this study is to evaluate wellbore completion practices to determine if there are ways to produce less CBM water and still achieve adequate depressurization for CBM production. After a relatively short period of production (several months), it appears that an appreciable amount of the water produced may come not only from the producer coal but also from the formations adjacent to the coal layers. Therefore, minimizing water production from other formations would have appreciable beneficial consequences.

I start this chapter by briefly explaining the origin of coal bed methane and the geology of the PRB. Then I present an overview of the drilling and completion methods used in the basin. Later I explain how I obtain the magnitude of the least principal stress (S_3) and I show the variation of S_3 across the basin and give possible explanations to such variation. Since the comparison between the magnitudes of S_3 and S_v indicates the direction of propagation of a hydraulic fracture I am able to establish a relationship between hydraulic fracture orientation and water and gas production. This allows me to investigate the question of what is responsible for a large water production or a low water production in areas of vertical hydraulic fracturing. I also obtained some pore pressure data, which enabled me to evaluate the relationship between pore pressure and gas production. To finalize, I present the recommendations to achieve best well completion practices, a summary and conclusions.

CHAPTER 2.

A Statistical Evaluation of Intact Rock Failure Criteria Constrained by Polyaxial Test Data for Five Different Rocks

Colmenares, L. and M. D. Zoback, 2002, A statistical evaluation of rock failure criteria constrained by polyaxial test data for five different rocks, International Journal of Rock Mechanics and Mining Sciences, v. 39, pp. 695-729.

2.1 ABSTRACT

In this study I examine seven different failure criteria by comparing them to published polyaxial test data ($\sigma_1>\sigma_2>\sigma_3$) for five different rock types at a variety of stress states. I employed a grid search algorithm to find the best set of parameters that describe failure for each criterion and the associated misfits. Overall, I found that the polyaxial criteria Modified Wiebols and Cook and Modified Lade achieved a good fit to most of the test data. This is especially true for rocks with a highly σ_2-dependent failure behavior (e.g. Dunham dolomite, Solenhofen limestone). However, for some rock types (e.g. Shirahama Sandstone, Yuubari shale), the intermediate stress hardly affects failure and the Mohr-Coulomb and Hoek and Brown criteria fit these test data equally well, or even better, than the more complicated polyaxial criteria. The values of Co yielded by the Inscribed and the Circumscribed Drucker-Prager criteria bounded the Co value obtained using the Mohr Coulomb criterion as expected. In general, the Drucker-Prager failure criterion did not accurately indicate the value of σ_1 at failure. The value of the misfits achieved with the empirical 1967 and 1971 Mogi criteria were generally in between those obtained using the triaxial and the polyaxial criteria. The disadvantage of these failure criteria is that they cannot be related to strength parameters such as Co. I also found that if only data from triaxial tests are available, it is possible to incorporate the influence of σ_2 on failure by using a polyaxial failure criterion. The results for two out of three rocks that could be analyzed in this way were encouraging.

2.2 INTRODUCTION

A number of different criteria have been proposed to describe brittle rock failure. In this study I aim to find which failure criterion, and which parameters, best describes the behavior of each rock type by minimizing the misfit between the predicted failure stress and the experimental data. With this approach the different criteria can be benchmarked against a variety of rock strength data for a variety of lithologies. This work also allowed me to investigate the influence of the intermediate stress on rock failure. The following failure criteria were tested: two conventional “triaxial” criteria (the Mohr-

Coulomb and the Hoek and Brown criteria), which ignore the influence of the intermediate principal stress and are thus applicable to conventional triaxial test data ($\sigma_1>\sigma_2=\sigma_3$), three true triaxial or polyaxial criteria (Modified Wiebols and Cook, Modified Lade, and Drucker-Prager), which consider the influence of the intermediate principal stress in polyaxial strength tests ($\sigma_1>\sigma_2>\sigma_3$) and two empirical criteria (Mogi 1967 and Mogi 1971). It is very important to mention that the behavior of the conventional "triaxial" criteria in their 3D versions (taking into account σ_2) were not investigated, as they have been widely used in their standard 2D version, especially when studying wellbore stability. The five rock types investigated were: amphibolite from the "Kontinentalen Tiefbohrung" (KTB) site, Dunham dolomite, Solenhofen limestone, Shirahama sandstone and Yuubari shale.

In this paper σ_{ij} is defined as the effective stress and is given by

$$\sigma_{ij} = S_{ij} - P_o \tag{1}$$

where S_{ij} is total stress and P_o is pore pressure.

2.2.1 Mohr-Coulomb Criterion

Mohr proposed that when shear failure takes place across a plane, the normal stress σ_n and the shear stress τ across this plane are related by a functional relation characteristic of the material

$$|\tau| = S_o + \mu_i \sigma_n \tag{2}$$

where S_o is the shear strength or cohesion of the material and μ_i is the coefficient of internal friction of the material.

Since the sign of τ only affects the sliding direction, only the magnitude of τ matters. The linearized form of the Mohr failure criterion may also be written as

$$\sigma_1 = C_0 + q\sigma_3 \tag{3}$$

where

$$q = [(\mu_i^2 + 1)^{1/2} + \mu_i]^2 = \tan^2(\pi/4+\phi/2) \quad (4)$$

where σ_1 is the major principal effective stress at failure, σ_3 is the least principal effective stress at failure, *Co* is the uniaxial compressive strength and ϕ is the angle of internal friction equivalent to atan(μ_i). This failure criterion assumes that the intermediate principal stress has no influence on failure.

The yield surface of this criterion is a right hexagonal pyramid equally inclined to the principal-stress axes. The intersection of this yield surface with the π–plane is a hexagon. The π–plane (or deviatoric plane) is the plane which is perpendicular to the straight-line $\sigma_1=\sigma_2=\sigma_3$. Figure 2.1 shows the yield surface of the Mohr-Coulomb criterion and Figure 2.2a shows the representation of this criterion in $\sigma_1 - \sigma_2$ space for a Co = 60 MPa and $\mu_i = 0.6$.

2.2.2 Hoek and Brown Criterion

This empirical criterion uses the uniaxial compressive strength of the intact rock material as a scaling parameter, and introduces two dimensionless strength parameters, *m* and *s*. After studying a wide range of experimental data, Hoek and Brown (1980) stated that the relationship between the maximum and minimum stress is given by

$$\sigma_1 = \sigma_3 + C_o\sqrt{m\frac{\sigma_3}{C_o} + s} \quad (5)$$

where *m* and *s* are constants that depend on the properties of the rock and on the extent to which it had been broken before being subjected to the failure stresses σ_1 and σ_3.

The Hoek and Brown failure criterion was originally developed for estimating the strength of rock masses for application to excavation design.

According to Hoek and Brown (1980, 1997), *m* depends on rock type and *s* depends on the characteristics of the rock mass. Below, a list of ranges for *m*-values is given for some characteristic rock types:

$5 < m < 8$ Carbonate rocks with well developed crystal cleavage (dolomite, limestone, marble).

$4 < m < 10$ Lithified argillaceous rocks (mudstone, siltstone, shale, slate).

$15 < m < 24$ Arenaceous rocks with strong crystals and poorly developed crystal cleavage (sandstone, quartzite).

$16 < m < 19$ Fine-grained polyminerallic igneous crystalline rocks (andesite, dolerite, diabase, rhyolite).

$22 < m < 33$ Coarse-grained polyminerallic igneous and metamorphic rocks (amphibolite, gabbro, gneiss, granite, norite, quartz-diorite).

While these values of *m* obtained from lab tests on intact rock are intended to represent a good estimate when laboratory tests are not available, they will be compared to the values obtained for the five rocks studied here. For intact rock materials, *s* is equal to one. For a completely granulated specimen or a rock aggregate, *s* is equal to zero.

Figure 2.1 shows that the intersection of the Hoek and Brown yield surface with the π–plane is a hexagon, as was the case for the Mohr-Coulomb criterion. In Figure 2.2b is possible to see the behavior of this criterion in $\sigma_1 - \sigma_2$ space for Co = 60 MPa, *m* = 16 and s = 1. Hoek and Brown is represented by straight lines like Mohr Coulomb.

2.2.3 Modified Lade Criterion

The Lade criterion is a three-dimensional failure criterion for frictional materials without effective cohesion. It was developed for soils with curved failure envelopes (1977). This criterion is given by

$$((I_1^3 / I_3) - 27)(I_1 / p_a)^{m'} = \eta_1 \tag{6}$$

where

$$I_1 = S_1 + S_2 + S_3 \tag{7}$$

$$I_3 = S_1 \cdot S_2 \cdot S_3 \tag{8}$$

p_a is atmospheric pressure expressed in the same units as the stresses, and m' and η_1 are material constants.

In the modified Lade criterion developed by Ewy (1999), m' was set equal to zero in order to obtain a criterion, which is able to predict a linear shear strength increase with increasing I_1. In this way the criterion is similar to that proposed by Lade and Duncan (1975) in which $(I_1^3/I_3)=\kappa_1$ where κ_1 is a constant whose value depends on the density of the soil. For considering materials with cohesion, Ewy (1999) introduced the parameter S and also included the pore pressure as a necessary parameter.

Doing all the modifications and defining appropriate stress invariants the following failure criterion was obtained by Ewy (1999)

$$(I'_1)^3 / I'_3 = 27 + \eta \tag{9}$$

where

$$I'_1 = (\sigma_1 + S) + (\sigma_2 + S) + (\sigma_3 + S) \tag{10}$$

and

$$I'_3 = (\sigma_1 + S)(\sigma_2 + S)(\sigma_3 + S) \tag{11}$$

where S and η are material constants. The parameter S is related to the cohesion of the rock, while the parameter η represents the internal friction.

These parameters can be derived directly from the Mohr-Coulomb cohesion S_o and internal friction angle ϕ by

$$S = S_o / \tan\phi \tag{12}$$

$$\eta = 4 (\tan\phi)^2 (9 - 7\sin\phi) / (1 - \sin\phi) \tag{13}$$

where $\tan\phi = \mu_i$ and $S_o = C_o / (2\, q^{1/2})$ with q as defined in Eqn. 4.

The modified Lade criterion first predicts a strengthening effect with increasing intermediate principal stress σ_2 followed by a slight reduction in strength once σ_2 becomes "too high" (Ewy, 1999). This typical behavior of the Modified Lade criterion can be observed in Figure 2.2c where it has been plotted in $\sigma_1 - \sigma_2$ space for Co = 60 MPa and $\mu_i = 0.6$.

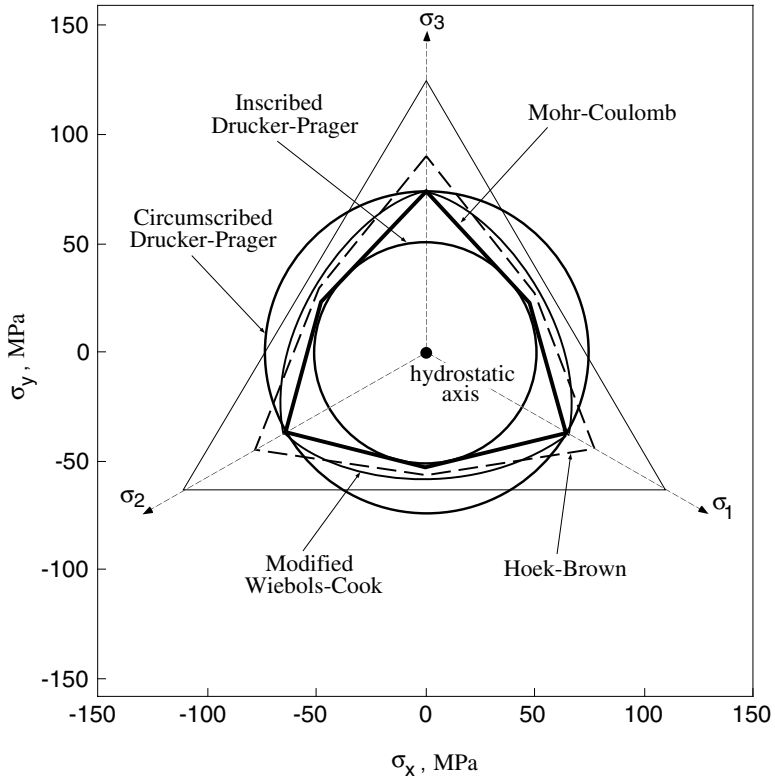

Figure 2.1: Yield envelopes projected in the π-plane for the Mohr-Coulomb criterion, the Hoek and Brown criterion, the Modified Wiebols and Cook criterion and the Circumscribed and Inscribed Drucker-Prager criterion.

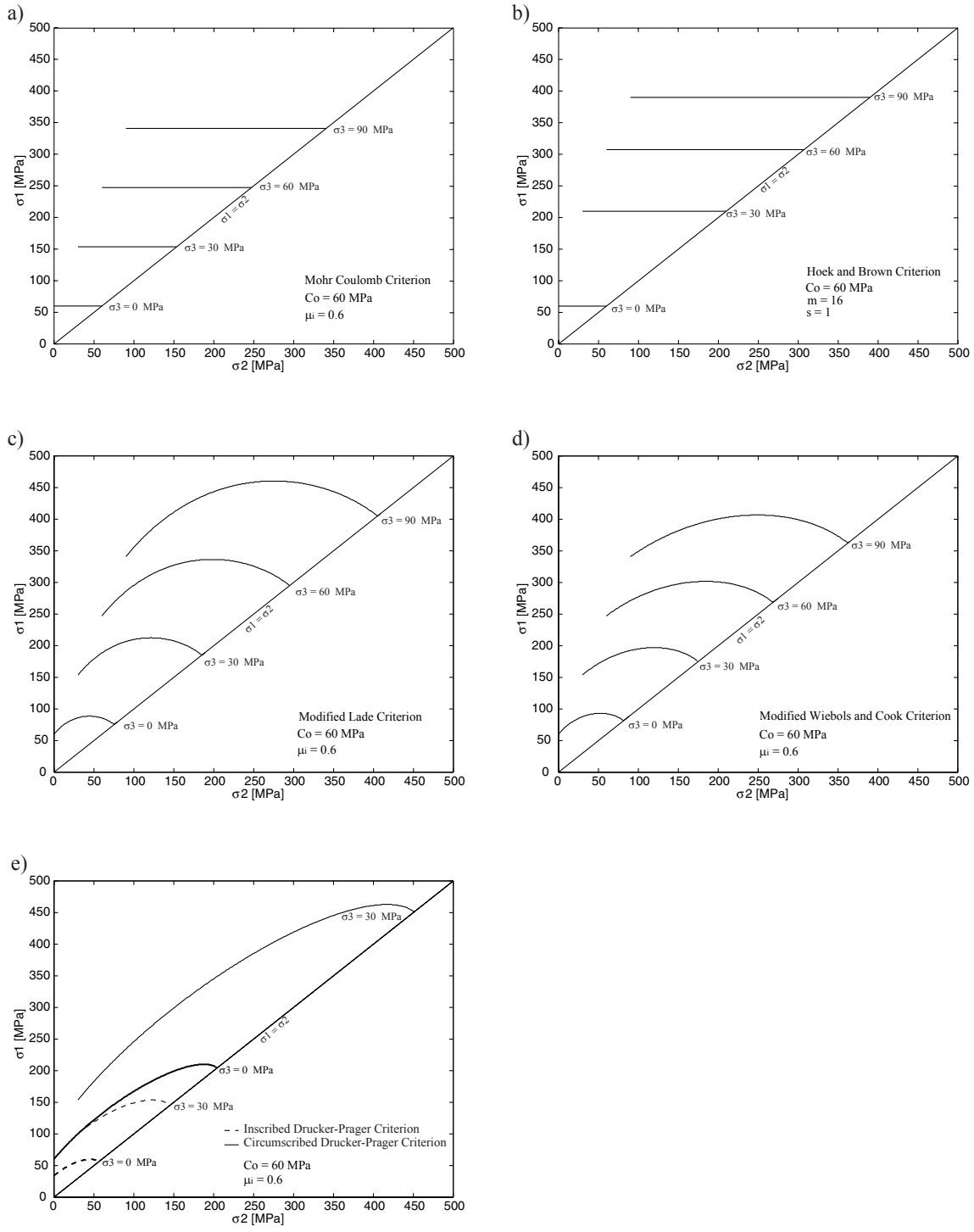

Figure 2.2: In order to observe how some of the failure criteria analyzed in this study behave in the σ_1-σ_2 space, the curves corresponding to σ_3 = 0, 30, 60 and 90 MPa were plotted using Co = 60 MPa and μ_i = 0.6. For the Hoek and Brown criterion a Co = 60 MPa, m = 16 and s=1 were used. a) Mohr-Coulomb criterion. b) Hoek and Brown criterion. c) Modified Lade criterion. d) Modified Wiebols and Cook criterion. e) Inscribed and Circumscribed Drucker-Prager criterion only for σ_3 = 0 and 30 MPa.

2.2.4 Modified Wiebols and Cook Criterion

Zhou (1994) presented a failure criterion, which is an extension of the Circumscribed Drucker-Prager criterion (described later) with features similar to the effective strain energy criterion of Wiebols and Cook (1968).

The failure criterion described by Zhou predicts that a rock fails if

$$J_2^{1/2} = A + BJ_1 + CJ_1^2 \tag{14}$$

where

$$J_1 = (1/3) * (\sigma_1 + \sigma_2 + \sigma_3) \tag{15}$$

and

$$J_2^{1/2} = \sqrt{\frac{1}{6}((\sigma_1 - \sigma_2)^2 + (\sigma_1 - \sigma_3)^2 + (\sigma_2 - \sigma_3)^2)} \tag{16}$$

J_1 is the mean effective confining stress and $J_2^{1/2}$ is equal to $(3/2)^{1/2}\tau_{oct}$, where τ_{oct} is the octahedral shear stress

$$\tau_{oct} = \frac{1}{3}\sqrt{(\sigma_1 - \sigma_2)^2 + (\sigma_2 - \sigma_3)^2 + (\sigma_2 - \sigma_1)^2} \tag{17}$$

The parameters A, B, and C are determined such that Eqn. 14 is constrained by rock strengths under triaxial ($\sigma_2 = \sigma_3$) and biaxial ($\sigma_1 = \sigma_2$) conditions. By substituting the given conditions plus the uniaxial rock strength ($\sigma_1 = C_o$, $\sigma_2 = \sigma_3 = 0$) into Eqn. 14, it is determined that

$$C = \frac{\sqrt{27}}{2C_1 + (q-1)\sigma_3 - C_o}\left(\frac{C_1 + (q-1)\sigma_3 - C_o}{2C_1 + (2q+1)\sigma_3 - C_o} - \frac{q-1}{q+2}\right) \tag{18}$$

with $C_1 = (1 + 0.6\ \mu_i)C_o$.

$$B = \frac{\sqrt{3}(q-1)}{q+2} - \frac{C}{3}(2C_o + (q+2)\sigma_3) \tag{19}$$

and

$$A = \frac{C_o}{\sqrt{3}} - \frac{C_o}{3}B - \frac{C_o^{\,2}}{9}C \tag{20}$$

The rock strength predictions produced using Eqn. 14 are similar to that of Wiebols and Cook (1968) and thus the model described by Eqn. 14 represents a modified strain energy criterion, which is called the Modified Wiebols and Cook criterion. For polyaxial states of stress, the predictions made by this criterion are greater than that of the Mohr Coulomb criterion. This can be seen in Figure 2.1 because the failure envelope of the Modified Wiebols and Cook criterion just coincides with the outer apices of the Mohr-Coulomb hexagon. This criterion is also plotted in σ_1–σ_2 space in Figure 2.2d.

2.2.5 Mogi 1967 Empirical Criterion

Mogi studied the influence of the intermediate stress on failure by performing confined compression tests ($\sigma_1>\sigma_2=\sigma_3$), confined extension tests ($\sigma_1=\sigma_2>\sigma_3$) and biaxial tests ($\sigma_1>\sigma_2>\sigma_3=0$) on different rocks. He recognized that the influence of the intermediate principal stress on failure is non-zero, but considerably smaller than the effect of the minimum principal stress (Mogi, 1967). When he plotted the maximum shear stress $(\sigma_1-\sigma_3)/2$ as a function of $(\sigma_1+\sigma_3)/2$ for failure of Westerly Granite, he observed that the extension curve lay slightly above the compression curve and the opposite happened when he plotted the octahedral shear stress τ_{oct} as a function of the mean normal stress $(\sigma_1+\sigma_2+\sigma_3)/3$ for failure of the same rock. Therefore, if $(\sigma_1+\beta\sigma_2+\sigma_3)$ is taken as the abscissa (instead of $(\sigma_1+\sigma_3)$ or $(\sigma_1+\sigma_2+\sigma_3)$), the compression and the extension curves become coincidental at a suitable value of β. Mogi argued that this β value is nearly the same for all brittle rocks, but this assertion will be tested.

The empirical criterion has the following formula

$$(\sigma_1 - \sigma_3)/2 = f_1 [(\sigma_1+\beta\sigma_2+\sigma_3)/2] \quad (21)$$

where β is a constant smaller than 1. The form of the function f_1 in Eqn. 21 is dependent on rock type and it should be a monotonically increasing function. This criterion postulates that failure takes place when the distortional energy increases to a limiting value, which increases monotonically with the mean normal pressure on the fault plane. The term ($\beta\sigma_2$) may correspond to the contribution of σ_2 to the normal stress on the fault plane because the fault surface, being irregular, is not exactly parallel to σ_2 and it would be deviated approximately by arcsin(β).

2.2.6 Mogi 1971 Empirical Criterion

This empirical fracture criterion was obtained by generalization of the von Mises's theory. It is formulated by

$$\tau_{oct} = f_1(\sigma_1 + \sigma_3) \quad (22)$$

where f_1 is a monotonically increasing function. According to Mogi (1971) the data points tend to align in a single curve for each rock, although they slightly scatter in some silicate rocks. The octahedral stress is not always constant but increases monotonically with ($\sigma_1+\sigma_3$). Failure will occur when the distortional strain energy reaches a critical value that increases monotonically with the effective mean pressure on the slip planes parallel to the σ_2 direction. The effective mean pressure on faulting is ($\sigma_1 + \sigma_3$)/2 or $\sigma_{m,2}$; therefore, τ_{oct} at fracture is plotted against $\sigma_{m,2}$. Mogi applied this failure criterion to different kinds of rocks and it always gave satisfactory results.

For both Mogi criteria, as f_1 has to be a monotonically increasing function, the data was fitted using three kinds of functions: power law, linear and 2nd order polynomial, in order to find the best fitting curve, that is, the one with the least mean misfit.

2.2.7 Drucker-Prager Criterion

The von Mises criterion may be written in the following way

$$J_2 = k^2 \tag{23}$$

where k is an empirical constant. The extended von Mises yield criterion or Drucker-Prager criterion was originally developed for soil mechanics (Drucker and Prager, 1952).

The yield surface of the modified von Mises criterion in principal stress space is a right circular cone equally inclined to the principal-stress axes. The intersection of the π–plane with this yield surface is a circle. The yield function used by Drucker and Prager to describe the cone in applying the limit theorems to perfectly plastic soils has the form:

$$J_2^{1/2} = k + \alpha J_1 \tag{24}$$

where α and k are material constants. The material parameters α and k can be determined from the slope and the intercept of the failure envelope plotted in the J_1 and $(J_2)^{1/2}$ space. α is related to the internal friction of the material and k is related to the cohesion of the material, in this way, the Drucker-Prager criterion can be compared to the Mohr-Coulomb criterion. When α is equal to zero Eqn. 24 reduces to the Von Mises criterion.

The Drucker-Prager criterion can be divided into an outer bound criterion (or Circumscribed Drucker-Prager) and an inner bound criterion (or Inscribed Drucker-Prager). These two versions of the Drucker-Prager criterion come from comparing the Drucker-Prager criterion with the Mohr-Coulomb criterion. In Figure 2.1 the two Drucker-Prager options are plotted together with the Mohr-Coulomb criterion in the π–plane. The inner Drucker-Prager circle only touches the inside of the Mohr-Coulomb criterion and the outer Drucker-Prager circle coincides with the outer apices of the Mohr-Coulomb hexagon.

The Inscribed Drucker-Prager criterion is obtained when (McLean and Addis, 1990; Veeken et al., 1989)

$$\alpha = \frac{3\sin\phi}{\sqrt{9+3\sin^2\phi}} \tag{25}$$

and

$$k = \frac{3C_o\cos\phi}{2\sqrt{q}\sqrt{9+3\sin^2\phi}} \tag{26}$$

where ϕ is the angle of internal friction, that is, $\phi = \tan^{-1}\mu_i$.

The Circumscribed Drucker-Prager criterion is obtained when (McLean and Addis, 1990; Zhou, 1994)

$$\alpha = \frac{6\sin\phi}{\sqrt{3}(3-\sin\phi)} \tag{27}$$

and

$$k = \frac{\sqrt{3}C_o\cos\phi}{\sqrt{q}(3-\sin\phi)} \tag{28}$$

As Eqns. 25 and 27 show, α only depends on ϕ, which means that α has an upper bound for both cases. When $\phi = 90^o$, $\mu_i = \infty$ as $\tan(90)=\infty$, so the value of α converges to 0.866 in the Inscribed Drucker-Prager case and to 1.732 in the Circumscribed Drucker-Prager case. Figure 2.3 shows the behavior of α with respect to μ_i. The asymptotic values are represented by a thick dashed line for each case. As α is obtained from the slope of the failure envelope in J_1 - $(J_2)^{1/2}$ space, according to its value I am able to discern whether the Inscribed or the Circumscribed Drucker-Prager criteria can be applied to the data. If the value of α for a specific rock is greater than the upper bound (asymptotic

value), the values of Co and μ_i cannot be obtained, which means that the Drucker-Prager criteria cannot be compared to Mohr Coulomb. If it is not necessary to find the values of Co and μ_i then the Drucker-Prager failure criterion can always be applied.

Figure 2.2e presents the behavior of both Drucker-Prager criteria for Co = 60 MPa and μ_i = 0.6 in comparison with other failure criteria studied here. As it is shown in Figure 2.2e, for the same values of Co and μ_i, the Inscribed Drucker-Prager criterion predicts failure at lower stresses than the Circumscribed Drucker-Prager criterion.

2.3 STRENGTH DATA

The five rock types investigated were amphibolite from the KTB site, Dunham dolomite, Solenhofen limestone, Shirahama sandstone and Yuubari shale. The polyaxial data of these rocks were obtained from published works as follows: Dunham dolomite and Solenhofen limestone from Mogi (1971), Shirahama sandstone and Yuubari Shale from Takahashi & Koide (1989) and the data of the amphibolite from the KTB site was kindly provided by Chang and Haimson. Tables 2.A.1 to 2.A.5 in Appendix 2.A show the polyaxial test data for each rock. It is important to mention that I am not assessing the quality of the data in this study. Instead, the goal is to statistically find the best fitting parameters with different failure criteria by utilizing the experimental data in a statistically comprehensive manner.

In order to quantify the influence of σ_2 on failure, the correlation coefficient between σ_1 and σ_2 for each σ_3 for every rock was calculated.

The correlation coefficient is the correlation of two variables, defined by (Riley et al., 1998)

$$Corr[X,Y] = \frac{Cov[X,Y]}{s_X s_Y} \tag{29}$$

where s_X and s_Y are the standard deviations of X and Y respectively. The correlation function lies between –1 and +1. If the value assumed is negative, X and Y are said to be negatively correlated, if it is positive they are said to be positively correlated and if it is

zero they are said to be uncorrelated. If σ_1 increases with σ_2, the correlation coefficient also increases. If σ_1 does not change with σ_2, then the correlation coefficient would be near zero.

Figure 2.4 shows the correlation coefficient of σ_1 to σ_2 to illustrate the influence of σ_2 on strength for the different rocks as a function of σ_3. The rocks with the highest influence of σ_2 on failure are Dunham dolomite, Solenhofen limestone and the amphibolite from the KTB site. The Yuubari shale shows an intermediate influence of σ_2 on failure and the Shirahama sandstone presents an unusual behavior as the influence of σ_2 on failure markedly varies with σ_3. The strong σ_2 dependence of strength of most of the rocks tested suggest that, in general, polyaxial strength criteria would be expected to work best. Although the behavior of Shirahama sandstone is so variable that it is difficult to assess which kind of failure criterion would work best.

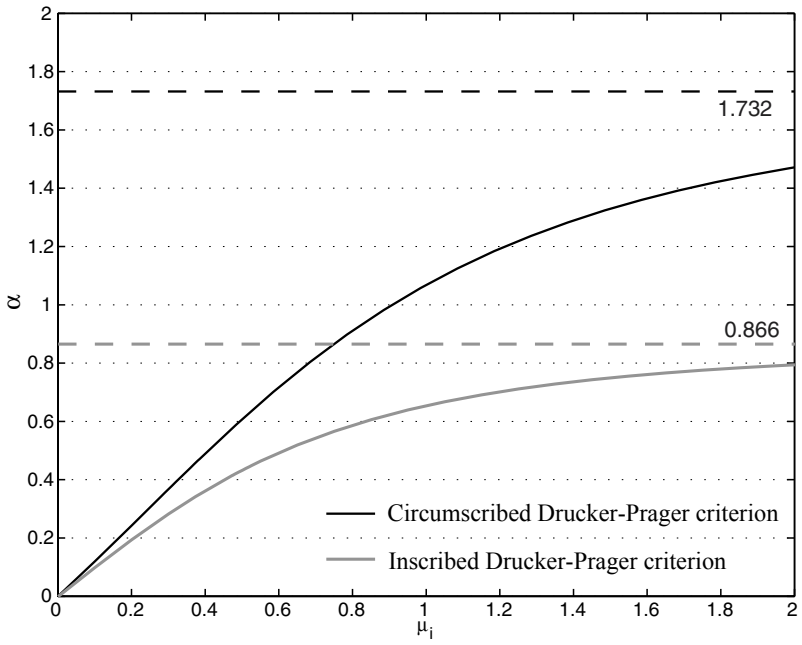

Figure 2.3: Parameter α from the Drucker-Prager criterion versus μ_i. The asymptotic value of α is represented by a thick dashed line. For the Inscribed Drucker-Prager (Eqn. 25) the asymptotic value of α is 0.866 and for the Circumscribed Drucker-Prager (Eqn. 27) the asymptotic value of α is 1.732.

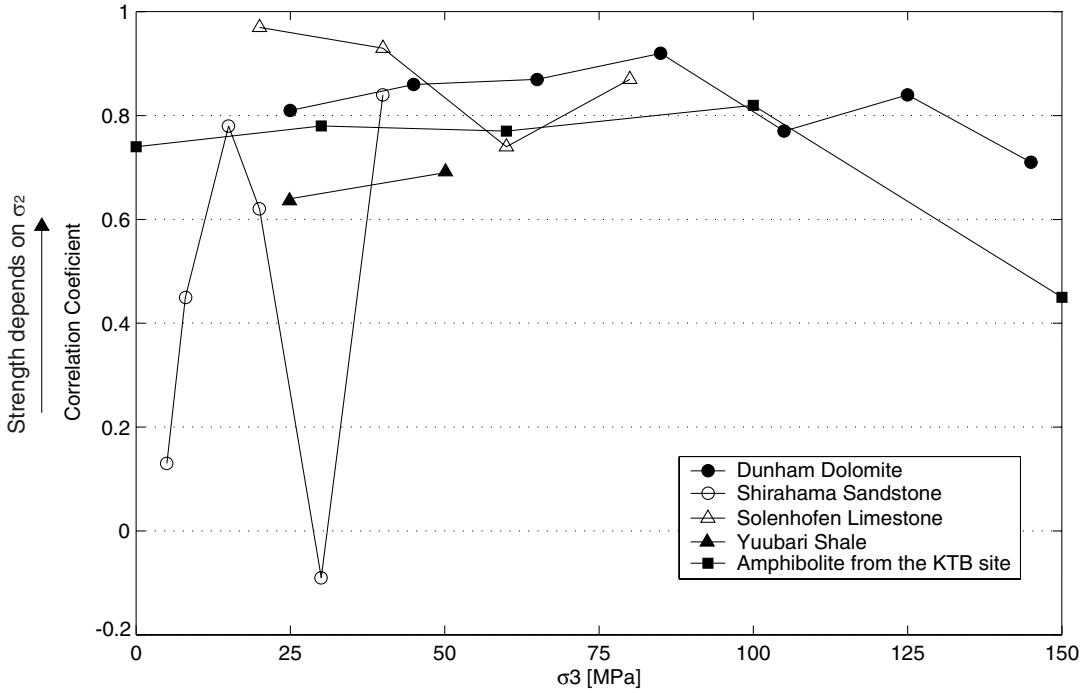

Figure 2.4: Correlation coefficient versus σ_3 for all the rocks studied in this work. When the correlation coefficient approximates to 1, that means that σ_1 increases with σ_2, which also means that failure occur at higher stresses than if σ_1 does not depend of σ_2.

2.4 RESULTS

To consider the applicability of four of the failure criteria to the experimental data, a grid search was performed allowing Co and μ_i to vary over a specific range. For a specific rock, the best-fitting combination of Co and μ_i was chosen by minimizing the mean standard deviation misfit to the test data. The failure criteria analyzed using this approach were the Mohr Coulomb criterion, the Hoek and Brown criterion, the Modified Lade criterion and the Modified Wiebols and Cook criterion. As the Hoek and Brown criterion does not depend on μ_i, but on *m* and *s*, the grid search was made varying Co, *m* and *s*. Figure 2.5a shows the misfit contours for the Modified Wiebols and Cook criterion to the Shirahama sandstone data. A minimum is very well defined allowing me to accurately determine the Co and μ_i that describe the failure of this rock in terms of this criterion. In Figure 2.5b, the fit of this criterion with the best fitting parameters is shown. By doing a grid search, in addition to obtaining the best-fitting parameters Co and μ_i, it

enables me to observe the sensitivity of the failure criterion when the parameters are changed – this can be observed in Appendix 2.B. That is, a grid search allows me to look at the whole solution space at once.

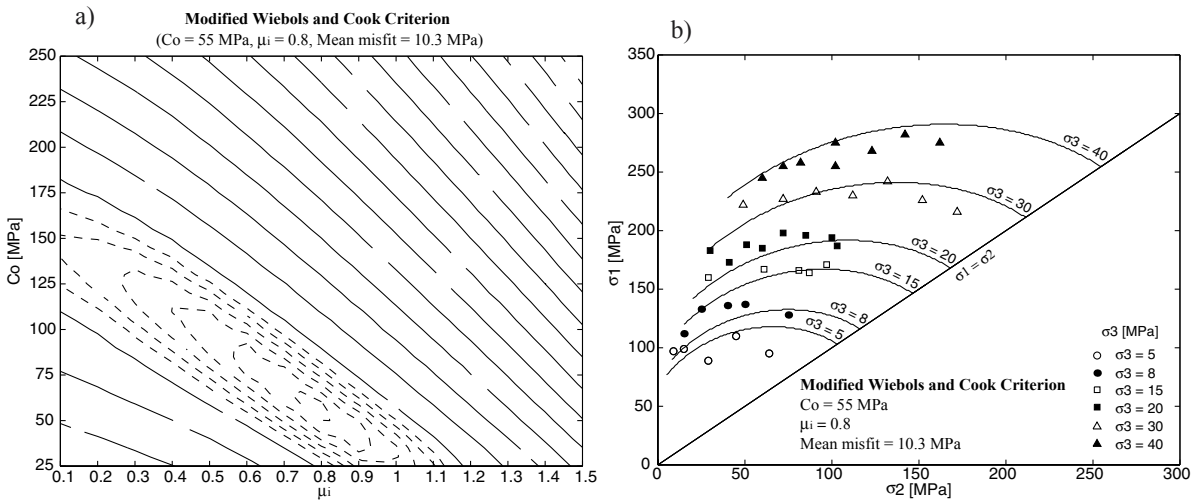

Figure 2.5: Modified Wiebols and Cook criterion for the Shirahama sandstone. a) Best-fitting solution compared to the actual data. b) Contour plot of the misfit to the experimental data for various combinations of Co and μ_i.

Figure 2.6 presents all the results for the Mohr-Coulomb criterion with the best fitting parameters for each rock type. As the Mohr-Coulomb does not take into account the influence of σ_2, the fit is a horizontal straight line. Therefore, the best fit would be one that goes through the middle of the data set for each σ_3. The smallest misfits associated with utilizing the Mohr Coulomb criterion were obtained for the Shirahama sandstone and the Yuubari shale. The largest misfits were for Dunham dolomite, Solenhofen limestone and KTB amphibolite, which are rocks presenting the greatest influence of the intermediate principal stress on failure (Figure 2.4). The mean misfit obtained using the Mohr Coulomb criterion is consistently larger than that obtained using the polyaxial failure criteria for rocks presenting a large influence of σ_2 on failure like Dunham dolomite and Solenhofen limestone. It is important to realize that the Mohr Coulomb criterion tends to overestimate the value of Co when applied to polyaxial data. The misfit data shown in Figure 2.B.1 indicates that the Mohr Coulomb criterion is always very well constrained with respect to Co and μ_i.

As can be seen in Figure 2.7, the Hoek and Brown criterion fit the experimental data well, especially for the Yuubari shale and the Shirahama sandstone. The values of *m* found in this study coincide with those reported by Hoek and Brown, for the same kinds of rocks except for the Solenhofen limestone, for which a value of $m = 4.6$ was obtained and the values of *m* reported are in the range of 5 to 8. However, Figure 2.B.2b shows that for $m = 5$, the misfit is essentially the same ($\pm$ 3 MPa) as for $m = 4.6$. The value of *s* was 1 for every rock studied, as expected for intact rocks. The compressive strength (Co) found using the Hoek and Brown criterion was consistently lower than that found using the Mohr-Coulomb criterion but (as shown below) was greater than those found using the polyaxial criteria. The only exception is the KTB amphibolite for which the Hoek and Brown criterion, the Modified Lade criterion and the Modified Wiebols and Cook criterion yield the same values for Co. As can be seen in Figure 2.B.2, the contour misfits for the Hoek and Brown failure criterion allows me to constrain Co but not *m*; i.e., for the same misfit, there is a wide range of values of *m* capable of reproducing approximately that same misfit.

The Modified Lade criterion (Figure 2.8) works very well for the rocks with a high σ_2-dependance on failure, that is, Dunham dolomite and Solenhofen limestone. For the KTB amphibolite, this criterion reasonably reproduces the trend of the experimental data but not as well as for the Dunham dolomite. A similar result was obtained for the Yuubari shale, which was expected, as this rock presents an intermediate σ_2-dependance on failure. The fit to the Shirahama sandstone data do not reproduce the trends very well. This is due to the varying σ_2-dependance for different σ_3, which makes the approximations more difficult. Figure 2.B.3 shows that the Modified Lade criterion yields well constrained rock strength parameters.

Similar to the Modified Lade criterion, the Modified Wiebols and Cook criterion also works best for rocks with a strong influence of σ_2 on failure. The results obtained for this criterion are shown in Figure 2.9. The Modified Wiebols and Cook criterion and the Modified Lade criterion, both achieve very good fits. For rocks with a high σ_2-dependance, the Modified Wiebols and Cook criterion works very well, as was the case for the Dunham dolomite, KTB amphibolite and Solenhofen limestone. For the Yuubari shale, with an intermediate σ_2-dependance, the criterion reproduces the trend of the data

equally well. For rocks presenting a variable σ_2-dependance, the fitting can be more complicated. Some sets of σ_3 are very well matched while others in the same rock present a poor fit. This is the case for the Shirahama Sandstone, where the Modified Wiebols and Cook criterion does not reproduce the trend of the data very well due to the varying σ_2-dependance of failure for different σ_3. As shown in Figure 2.B.4, both Co and μ_i are very well constrained for this failure criterion.

Figure 2.10 shows the results obtained for each rock using the Mogi 1967 empirical criterion. The maximum shear stress $(\sigma_1-\sigma_3)/2$ was plotted against the appropriate normal stress $(\sigma_1+\beta\sigma_2+\sigma_3)/2$. The different symbols show different σ_3 values and they form a single relation for each rock. The values of β are reported in Table 2.1. As Figure 10 shows, the strength data points can be fit by a power law approximation for every rock. While the Mogi 1967 criterion works well and gives insight into the influence of σ_2 on failure, it does not provide directly the strength parameter Co.

Table 2.1: Best fitting parameters and mean misfits for the Mogi 1967 failure criterion in $(\sigma_1-\sigma_3)/2$ - $(\sigma_1+\beta\sigma_2+\sigma_3)/2$ space.

Type of Rock	**Failure Criterion**	**Mean misfit [MPa]**
Dunham dolomite	$\frac{\sigma_1-\sigma_3}{2} = 5.09 * \left[\frac{\sigma_1+0.5*\sigma_2+\sigma_3}{2}\right]^{0.68}$	8.1
Solenhofen limestone	$\frac{\sigma_1-\sigma_3}{2} = 7.61 * \left[\frac{\sigma_1+0.45*\sigma_2+\sigma_3}{2}\right]^{0.59}$	5.7
Shirahama sandstone	$\frac{\sigma_1-\sigma_3}{2} = 1.95 * \left[\frac{\sigma_1+0.06*\sigma_2+\sigma_3}{2}\right]^{0.81}$	1.7
Yuubari shale	$\frac{\sigma_1-\sigma_3}{2} = 2.74 * \left[\frac{\sigma_1+0.25*\sigma_2+\sigma_3}{2}\right]^{0.71}$	2.6
KTB amphibolite	$\frac{\sigma_1-\sigma_3}{2} = 1.77 * \left[\frac{\sigma_1+0.15*\sigma_2+\sigma_3}{2}\right]^{0.87}$	11.7

The value of β for Dunham dolomite was 0.5, which is markedly different than the value of 0.1 reported by Mogi (1967), which means that the fracture plane is deviated by 30^o from the σ_2-direction and not by 5.7^o. In addition, the value of β for Solenhofen limestone was not nearly zero as reported by Mogi (1971) but 0.45 which is equivalent to

a deviation angle of ~27 ^{o}. The differences between the results found in this study and the ones carried out by Mogi for this failure criterion, are due to the difference in data taken into account, that is, Mogi worked with triaxial (compression and extension) test data and biaxial test data and I worked with polyaxial test data.

Chang and Haimson (2000) reported that the amphibolite from the KTB site failed in brittle fashion along a fracture plane striking sub parallel to the direction of σ_2. According to our findings, the fracture plane should be deviated approximately ~8^{o} from the σ_2-direction, which agrees with the observations of Chang and Haimson who made an extensive study of the polyaxial mechanical behavior of the KTB amphibolite. The Shirahama sandstone presented the lowest value of β equal to 0.06, which means that the fracture plane is almost parallel (~3^{o}) to the σ_2-direction. The value of β for the Yuubari shale was 0.25 equivalent to ~14^{o}.

Figure 2.11 shows the results obtained for the Mogi 1967 empirical criterion in σ_1 - σ_2 space. It can be seen that this failure criterion is represented by a quasi-rectilinear function. In Tables 2.7 to 2.11 the mean misfits in σ_1 - σ_2 space are reported. It can be seen that for the Dunham dolomite and the Solenhofen limestone (i.e., the rocks with higher σ_2-dependence), the mean misfit achieved by this criterion is between the values of the misfit achieved by the triaxial failure criteria and the other two polyaxial failure criteria (Modified Lade and Modified Wiebols and Cook). For the KTB amphibolite and the Shirahama sandstone, the mean misfit is greater than those obtained by the same triaxial and polyaxial criteria mentioned before. For the Yuubari shale, the Mogi 1967 failure criterion achieved the least mean misfit; however, the mean misfit yielded by the Modified Wiebols and Cook criterion was only 20% larger than the one obtained using the Mogi 1967 criterion. As the latter does not provide information about Co, it might be better, in general, to use the Modified Wiebols and Cook criterion, which does provide information about Co and μ_i.

Figure 2.12 shows the results obtained for the Mogi 1971 empirical criterion. τ_{oct} at fracture is plotted against $(\sigma_1+\sigma_3)/2$ or $\sigma_{m,2}$. The different symbols show different σ_3 values and they form a single curve for each rock. The data were fitted using three kinds of functions: power law, linear and 2nd order polynomial, in order to find the best fitting

curve, that is, the one with the least mean misfit. Tables 2.2 to 2.6 show the mean misfits associated to each function for each rock. In Figure 2.12, only the best fitting functions are shown. For the amphibolite of the KTB site, the power law failure criterion reported by Chang and Haimson (2000) was used. The 2nd order polynomial and linear fittings were also analyzed for the same rock, but these functions did not fit the data as well as the power law function.

In summary, the Mogi 1971 empirical failure criterion is able to reproduce all the failure stresses for the rocks in the τ_{oct} - $\sigma_{m,2}$ space using a monotonically increasing function. In most cases, a power law fit works best. However, in the σ_1 - σ_2 space, as can be seen in Figure 2.13, this failure criterion yields (in some cases), physically unreasonable solutions. It first predicts a strengthening effect with increasing intermediate principal stress σ_2 followed by a considerable 40 - 60% reduction in strength once σ_2 becomes too high. Also, for Shirahama sandstone and KTB amphibolite there are some values of σ_2 having two values of σ_1 at failure, which is physically impossible. This is not an artifact of the graphic representation but of the mathematical definition. The reason why this failure criterion fits the data so well in the τ_{oct} - $\sigma_{m,2}$ space is because it takes advantage of this dual solution to actually fit the data in that space. For the Shirahama sandstone the best fitting failure criterion is the Modified Wiebols and Cook as well as for the KTB amphibolite, the latter contradicting the results of Chang and Haimson (2000), who reported the Mogi 1971 failure criterion as the best fitting failure criterion for the KTB amphibolite. However, this failure criterion does a very good job fitting the data of the Dunham dolomite, the Solenhofen limestone and the Yuubari shale in both spaces. In Tables 2.7 to 2.11, the mean misfits for the σ_1-σ_2 space, associated to each rock, are reported.

Table 2.2: Best fitting parameters and mean misfits for the Mogi 1971 criterion for the Dunham dolomite in τ_{oct} - $\sigma_{m,2}$ space.

Type of function	**Failure Criterion**	**Mean misfit [MPa]**
Power law	$\tau_{oct} = 5.03\ \sigma_{m,2}^{0.67}$	5.5
2nd order polynomial	$\tau_{oct} = -0.0001\ \sigma_{m,2}^2 + 0.58\ \sigma_{m,2} + 66.53$	10.4
Linear	$\tau_{oct} = 0.46\ \sigma_{m,2} + 89.41$	5.7

Table 2.3: Best fitting parameters and mean misfits for the Mogi 1971 criterion for the Solenhofen limestone in τ_{oct} - $\sigma_{m,2}$ space.

Type of function	**Failure Criterion**	**Mean misfit [MPa]**
Power law	$\tau_{oct} = 8.12\ \sigma_{m,2}^{0.57}$	4.8
2nd order polynomial	$\tau_{oct} = 0.0003\ \sigma_{m,2}^2 + 0.2\ \sigma_{m,2} + 111.4$	4.7
Linear	$\tau_{oct} = 0.41\ \sigma_{m,2} + 86.79$	4.66

Table 2.4: Best fitting parameters and mean misfits for the Mogi 1971 criterion for the Shirahama sandstone in τ_{oct} - $\sigma_{m,2}$ space.

Type of function	**Failure Criterion**	**Mean misfit [MPa]**
Power law	$\tau_{oct} = 1.82\ \sigma_{m,2}^{0.79}$	2.015
2nd order polynomial	$\tau_{oct} = -0.0009\ \sigma_{m,2}^2 + 0.7\ \sigma_{m,2} + 5.5$	2.023
Linear	$\tau_{oct} = 0.54\ \sigma_{m,2} + 14.48$	2.2

Table 2.5: Best fitting parameters and mean misfits for the Mogi 1971 criterion for the Yuubari shale in τ_{oct} - $\sigma_{m,2}$ space.

Type of function	**Failure Criterion**	**Mean misfit [MPa]**
Power law	$\tau_{oct} = 2.75\ \sigma_{m,2}^{0.69}$	2.573
2nd order polynomial	$\tau_{oct} = -0.0003\ \sigma_{m,2}^2 + 0.5\ \sigma_{m,2} + 19.05$	2.571
Linear	$\tau_{oct} = 0.43\ \sigma_{m,2} + 23.93$	2.572

Table 2.6: Best fitting parameters and mean misfits for the Mogi 1971 criterion for the KTB amphibolite in τ_{oct} - $\sigma_{m,2}$ space.

Type of function	**Failure Criterion**	**Mean misfit [MPa]**
Power law (Chang and Haimson,	$\tau_{oct} = 1.77\ \sigma_{m,2}^{0.86}$	12.4
2nd order polynomial	$\tau_{oct} = -0.0001\ \sigma_{m,2}^2 + 0.7\ \sigma_{m,2} + 8.28$	16.3
Linear	$\tau_{oct} = 0.64\ \sigma_{m,2} + 36.37$	13.6

To analyze the rock strength data with the Drucker-Prager criterion, the relationship between J_1 and $(J_2)^{1/2}$ was obtained using minimum least squares and finding the mean misfit directly, without a grid search. I was able to determine which criteria are applicable for which rocks, based on the range of values that α (Eqns. 25 and 27) is allowed to have.

As it was shown in Figure 2.3, the parameter α ranges between 0 and 0.866 for the Inscribed Drucker-Prager criterion and between 0 and 1.732 for the Circumscribed Drucker-Prager criterion. If the value of α obtained using the linear fit falls within these values, it is possible to find the respective Co and μ_i for a given rock. This is the case for Dunham dolomite, Solenhofen limestone, Shirahama sandstone and Yuubari shale. The values of Co obtained for each rock using the Inscribed and the Circumscribed Drucker-Prager criterion give a range within which the value of Co obtained using Mohr-Coulomb is contained, as was expected. However, for the KTB amphibolite, the value of α was within the range for the Circumscribed Drucker-Prager criterion but outside the range for the Inscribed Drucker-Prager criterion, therefore only the parameters for Co and μ_i using the relationships from the Circumscribed Drucker-Prager criterion were found. All best fitting strength parameters are summarized in Tables 2.7 to 2.11.

Figure 2.14 presents the fits of the rock strength data and the respective coefficients in the J_1 and $(J_2)^{1/2}$ space, in which the Drucker-Prager criterion was developed. The parameters Co and μ_i are summarized in the table presented in the same figure. Figure 2.15 shows the data in σ_1 - σ_2 space. At low values of σ_2 ($\sigma_2 < 100$ MPa), the Drucker-Prager criterion is able to reproduce the trend of the data for the Dunham dolomite, the Solenhofen limestone and the Yuubari shale (for $\sigma_3 = 25$ MPa), but for the other rocks, the curves do not even reproduce the trend of the data. That is, the Drucker-Prager failure criterion does not accurately indicate the value of σ_1 at failure.

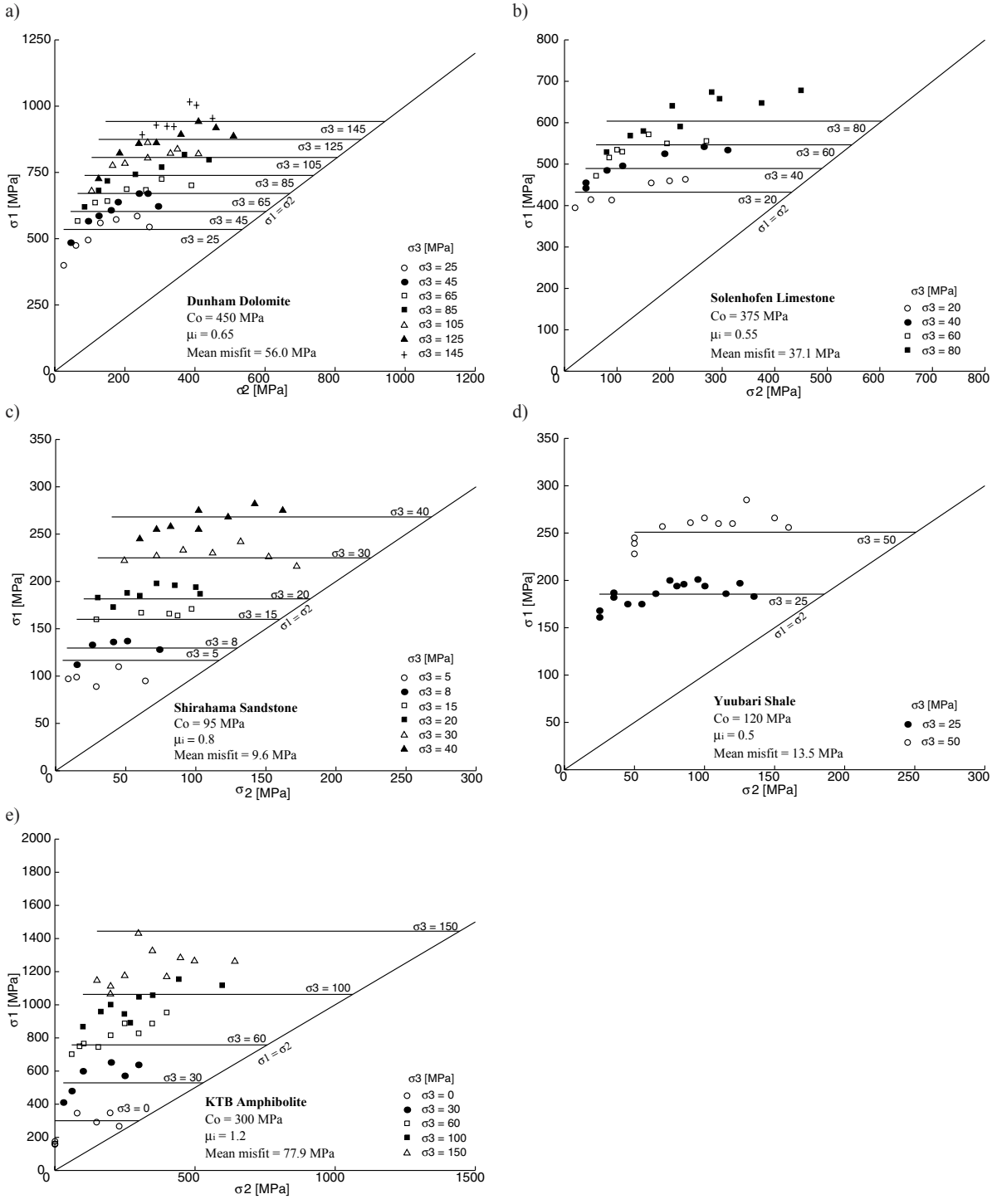

Figure 2.6: Best-fitting solution for all the rocks using the Mohr-Coulomb criterion (Eqn. 3). a) Dunham dolomite. b) Solenhofen limestone. c) Shirahama sandstone. d) Yuubari shale. e) KTB amphibolite.

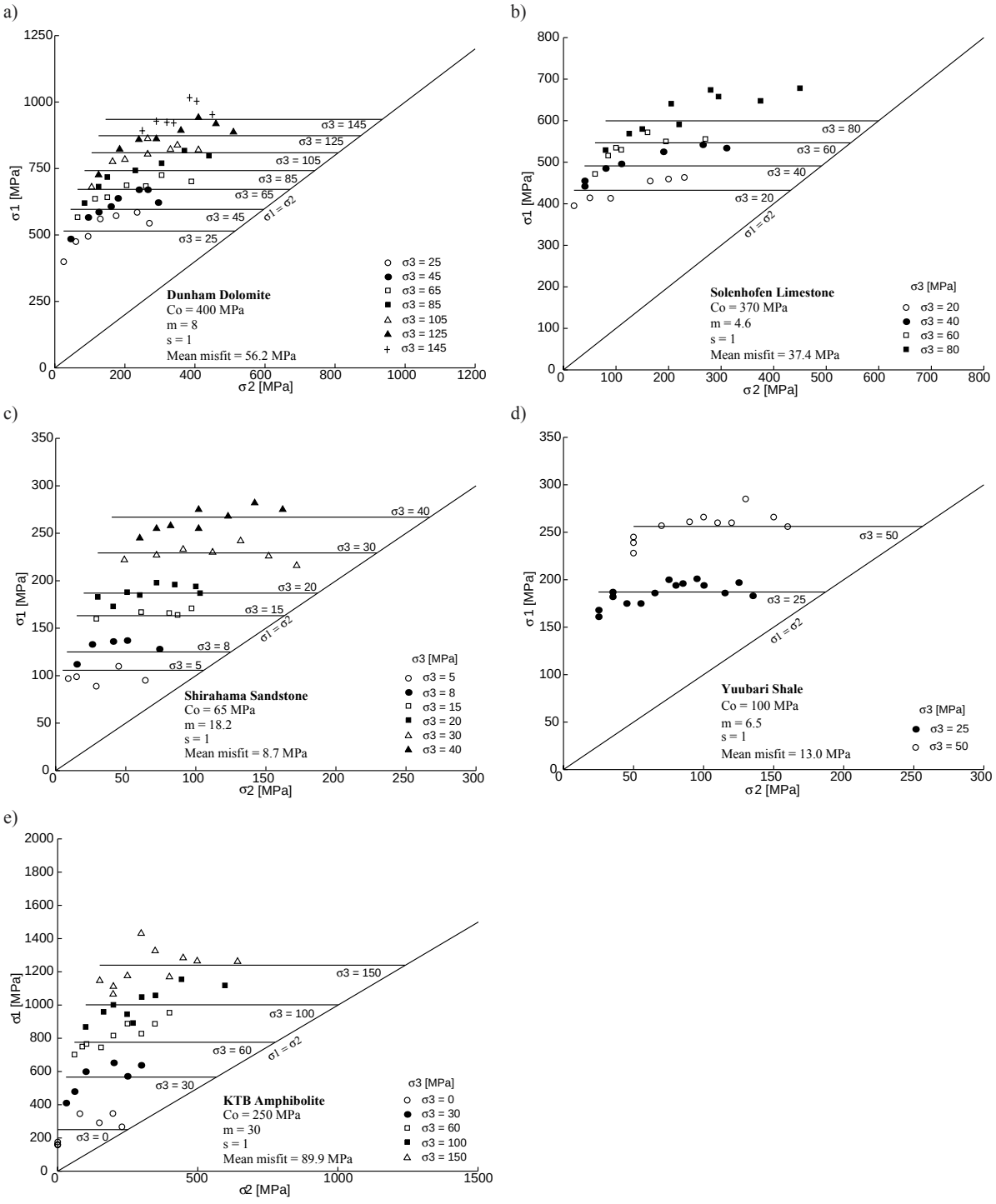

Figure 2.7: Best-fitting solution for all the rocks using the Hoek and Brown criterion (Eqn. 5). a) Dunham dolomite. b) Solenhofen limestone. c) Shirahama sandstone. d) Yuubari shale. e) KTB amphibolite.

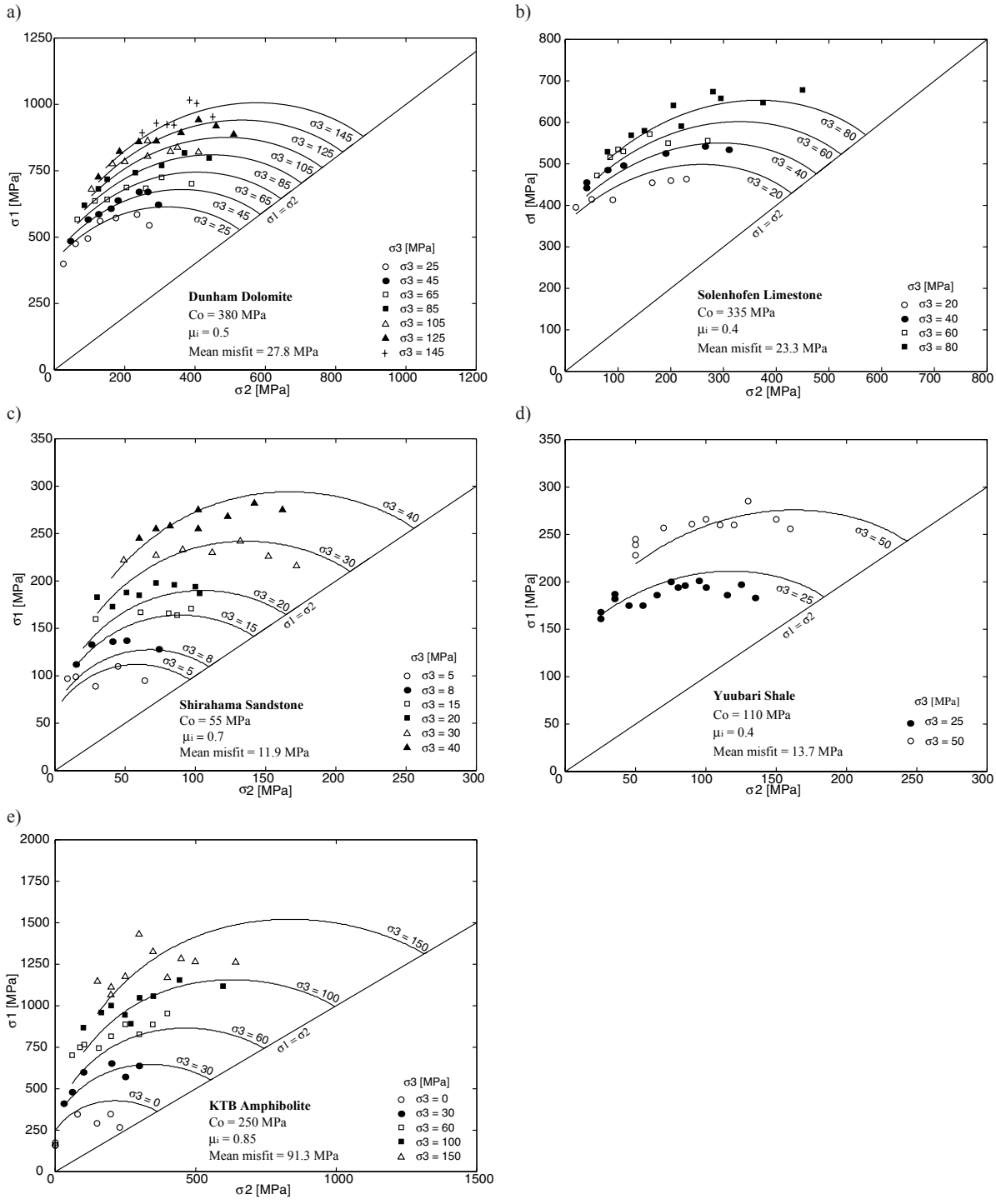

Figure 2.8: Best-fitting solution for all the rocks using the Modified Lade criterion (Eqn. 9). a) Dunham dolomite. b) Solenhofen limestone. c) Shirahama sandstone. d) Yuubari shale. e) KTB amphibolite.

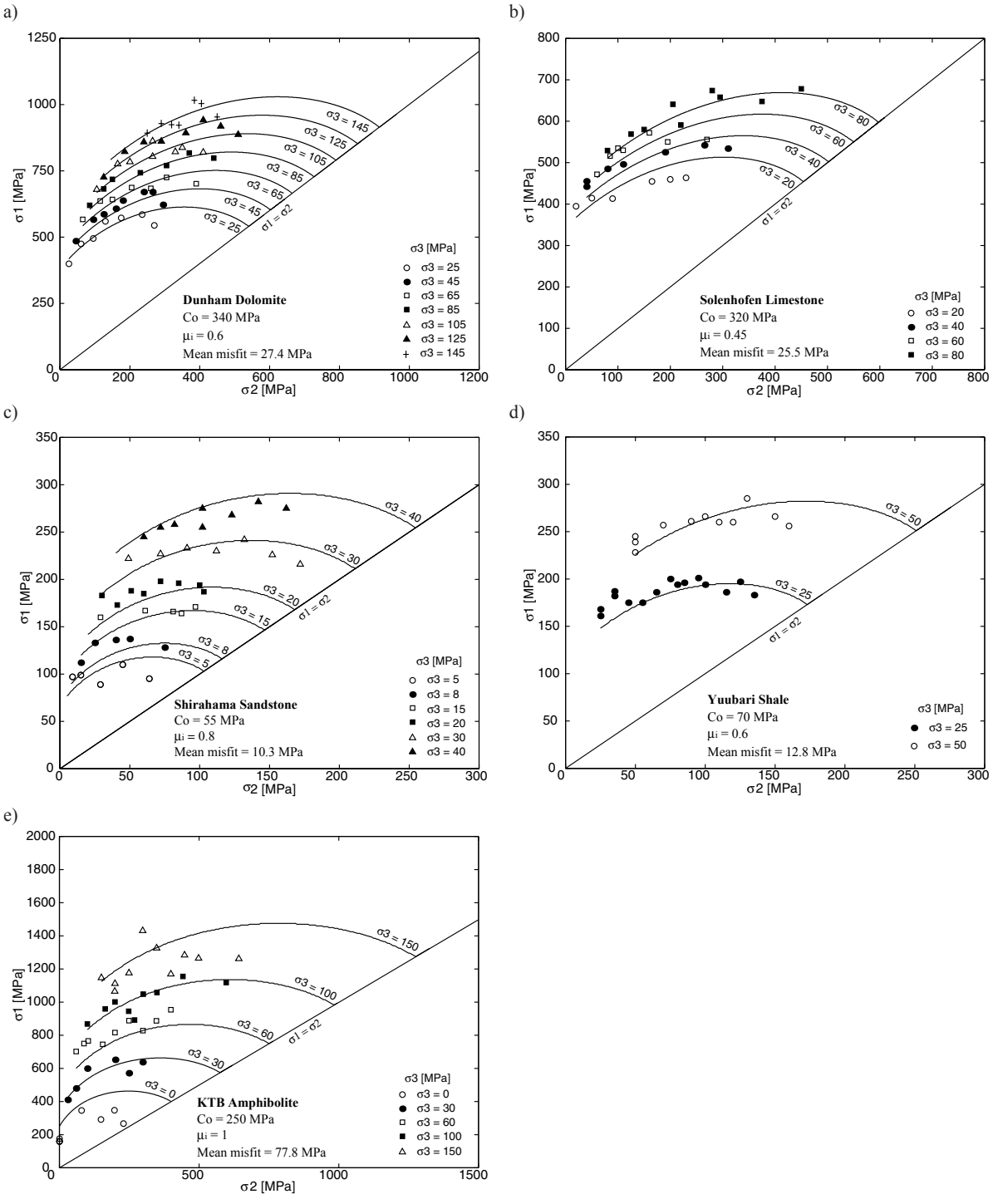

Figure 2.9: Best-fitting solution for all the rocks using the Modified Wiebols and Cook criterion (Eqn. 14). a) Dunham dolomite. b) Solenhofen limestone. c) Shirahama sandstone. d) Yuubari shale. e) KTB amphibolite.

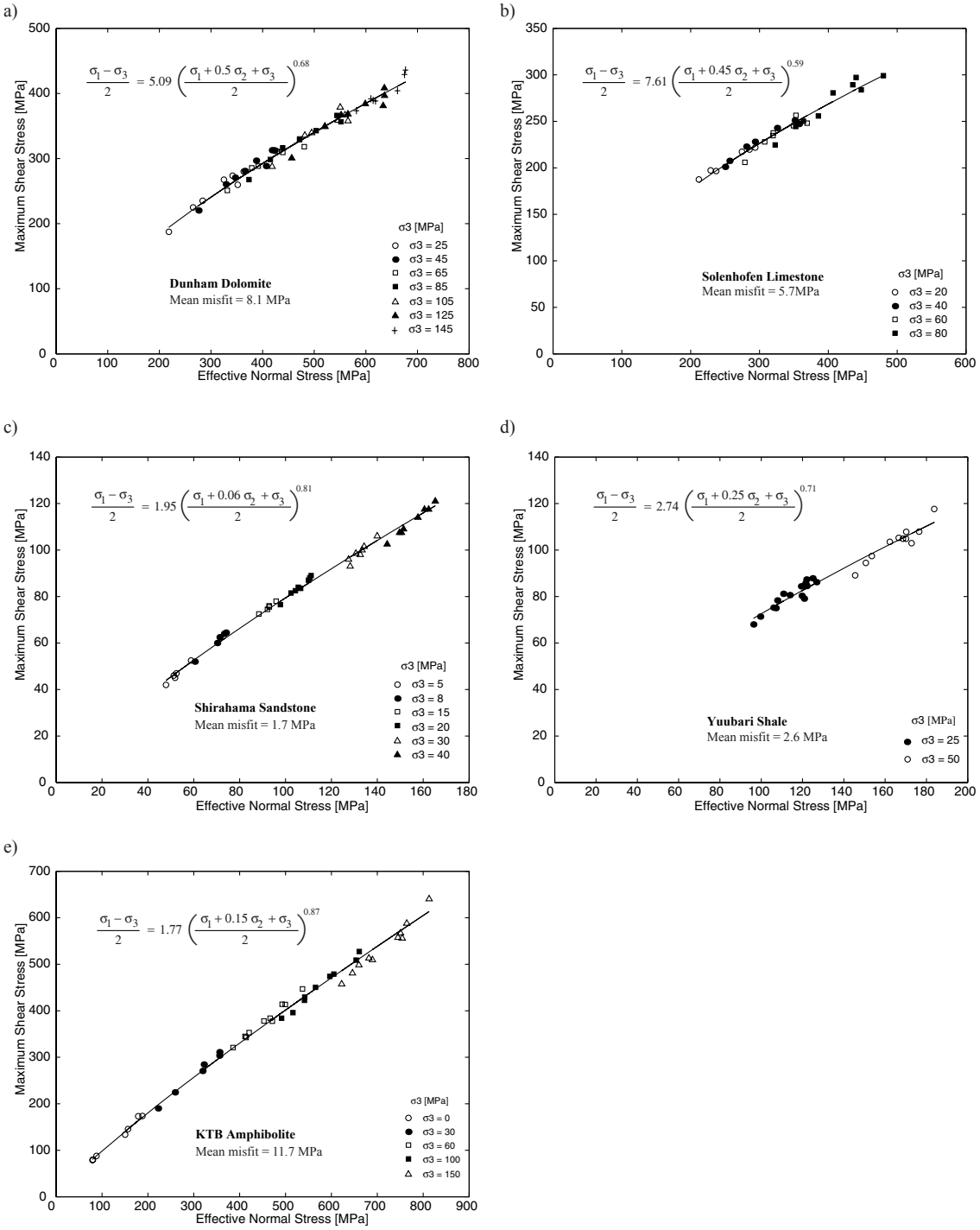

Figure 2.10: Best-fitting solution for all the rocks using the Mogi 1967 criterion plotted in $(\sigma_1-\sigma_3)/2$ - $(\sigma_1+\beta\sigma_2+\sigma_3)/2$ space (Eqn. 21). a) Dunham dolomite. b) Solenhofen limestone. c) Shirahama sandstone. d) Yuubari shale. e) KTB amphibolite.

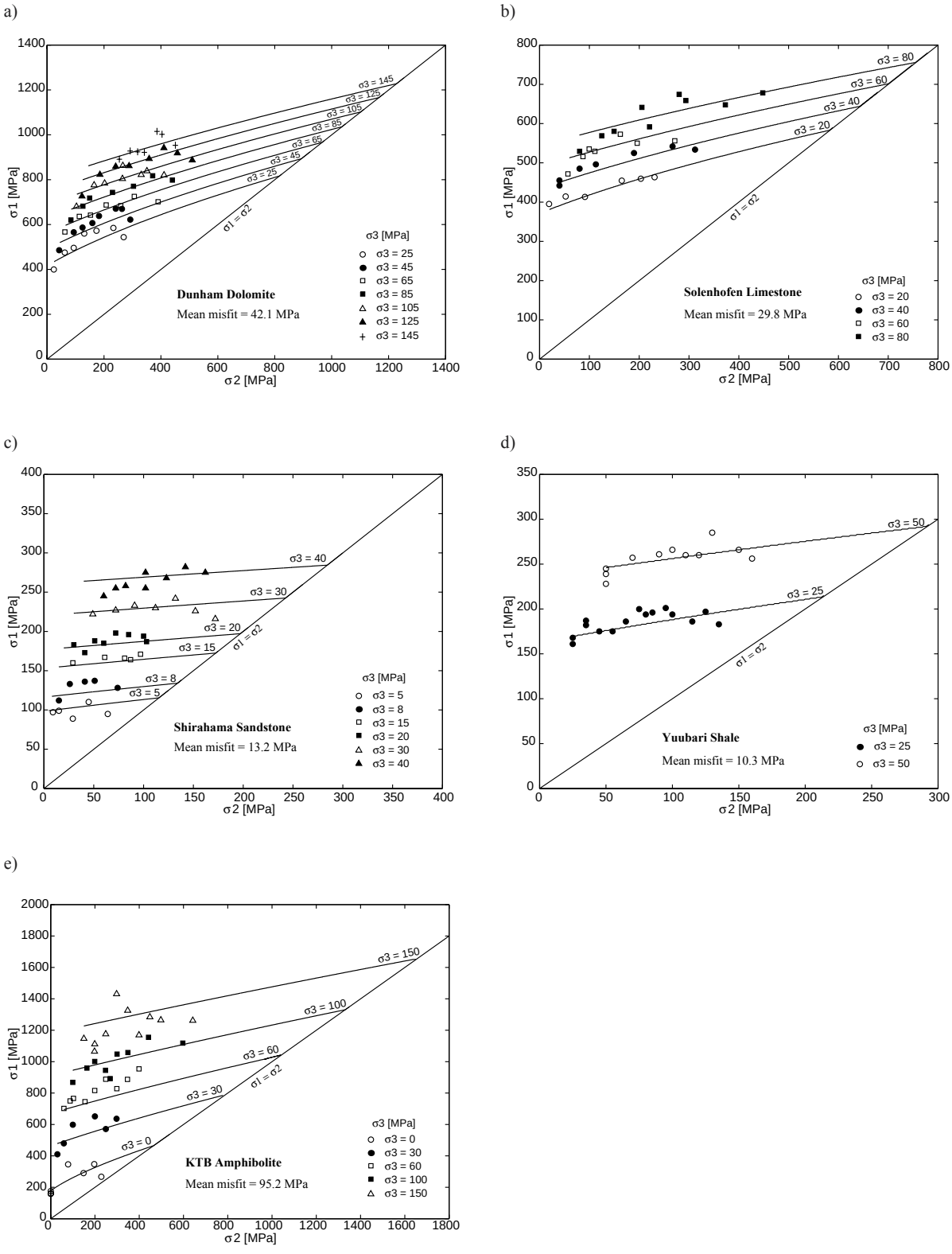

Figure 2.11: Best-fitting solution for all the rocks using the Mogi 1967 criterion plotted in σ_1-σ_2 space. a) Dunham dolomite. b) Solenhofen limestone. c) Shirahama sandstone. d) Yuubari shale. e) KTB amphibolite.

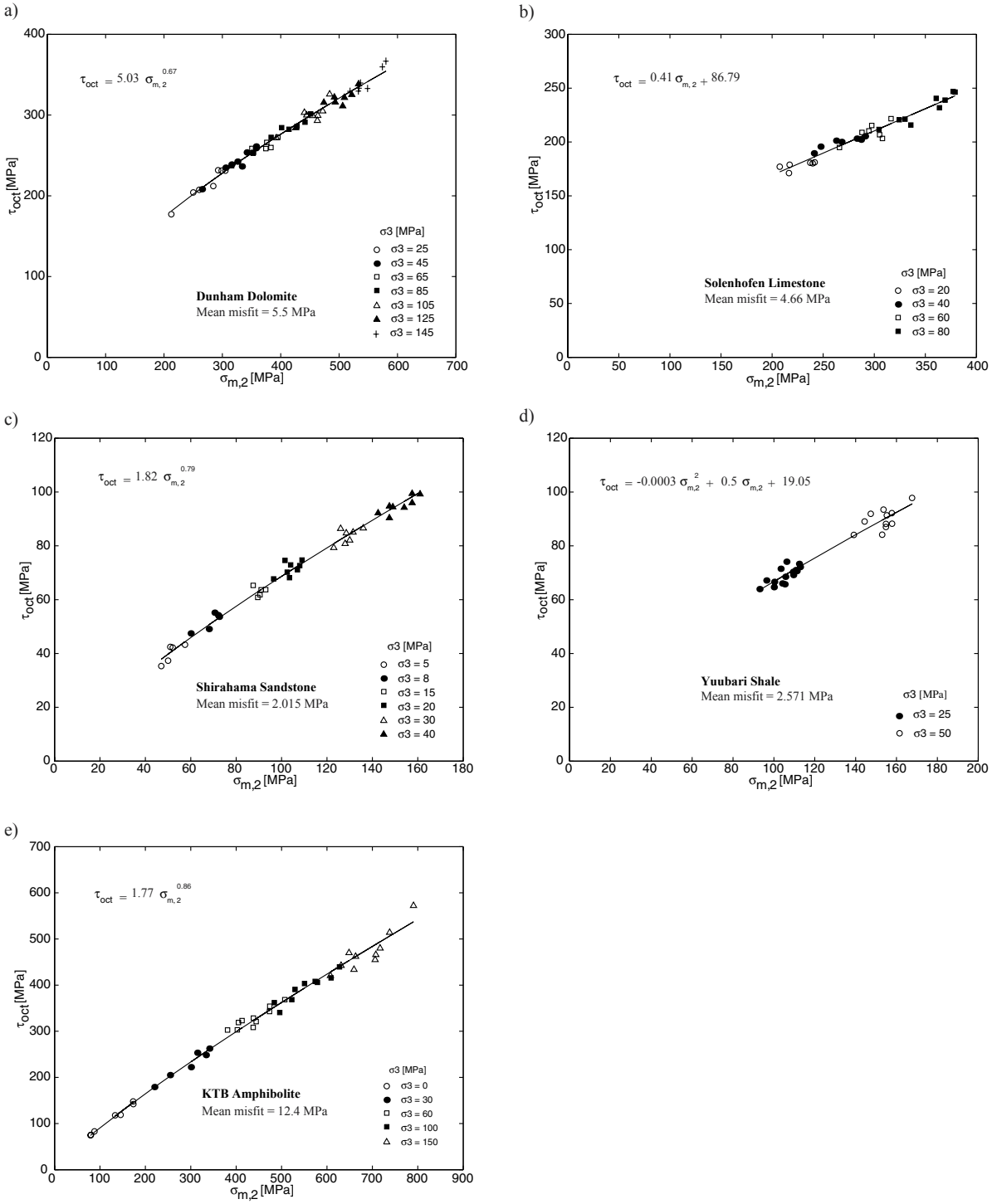

Figure 2.12: Best-fitting solution for all the rocks using the Mogi 1971 criterion plotted in τ_{oct} - $\sigma_{m,2}$ space (Eqn. 22). a) Dunham dolomite. b) Solenhofen limestone. c) Shirahama sandstone. d) Yuubari shale. e) KTB amphibolite.

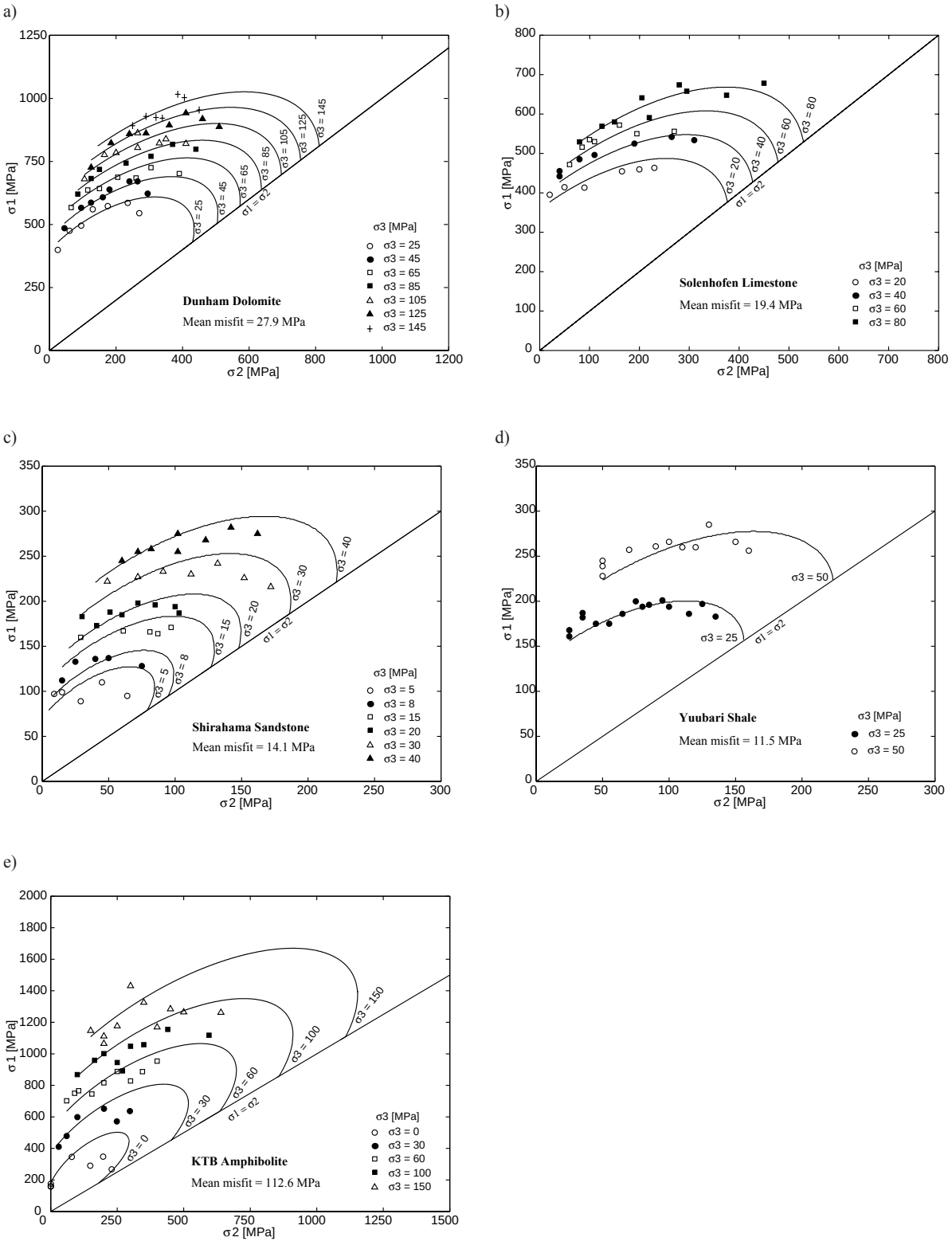

Figure 2.13: Best-fitting solution for all the rocks using the Mogi 1971 criterion plotted in σ_1-σ_2 space. a) Dunham dolomite. b) Solenhofen limestone. c) Shirahama sandstone. d) Yuubari shale. e) KTB amphibolite.

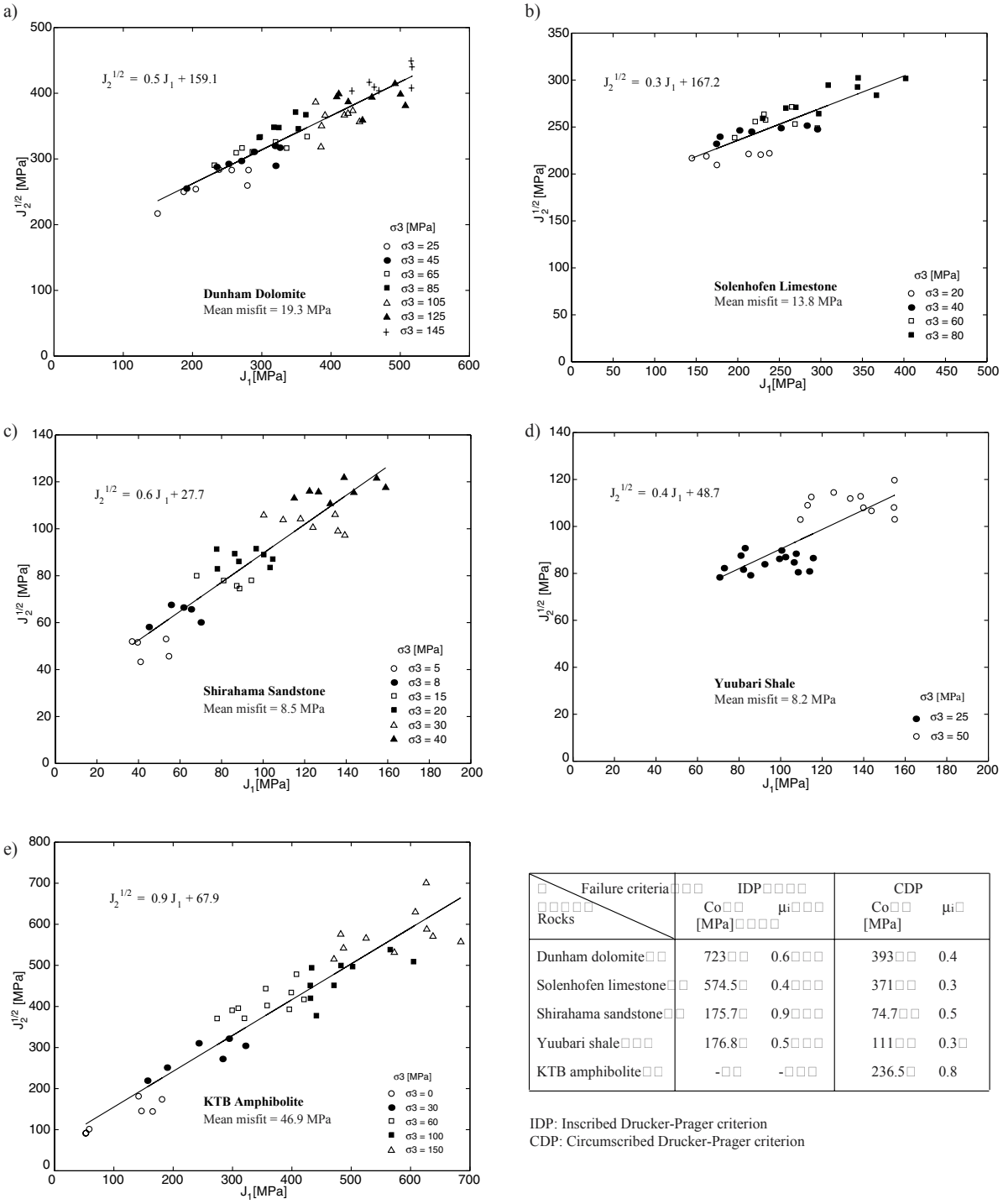

Failure criteria / Rocks	IDP Co [MPa]	IDP μ_i	CDP Co [MPa]	CDP μ_i
Dunham dolomite	723	0.6	393	0.4
Solenhofen limestone	574.5	0.4	371	0.3
Shirahama sandstone	175.7	0.9	74.7	0.5
Yuubari shale	176.8	0.5	111	0.3
KTB amphibolite	-	-	236.5	0.8

IDP: Inscribed Drucker-Prager criterion
CDP: Circumscribed Drucker-Prager criterion

Figure 2.14: Best-fitting solution for all the rocks using the Drucker-Prager criterion plotted in J_1 - $(J_2)^{1/2}$ space (Eqn. 24). a) Dunham dolomite. b) Solenhofen limestone. c) Shirahama sandstone. d) Yuubari shale. e) KTB amphibolite. The parameters Co and μ_i are summarized in the table for each rock for the Inscribed (IDP) and Circumscribed (CDP) Drucker-Prager criterion.

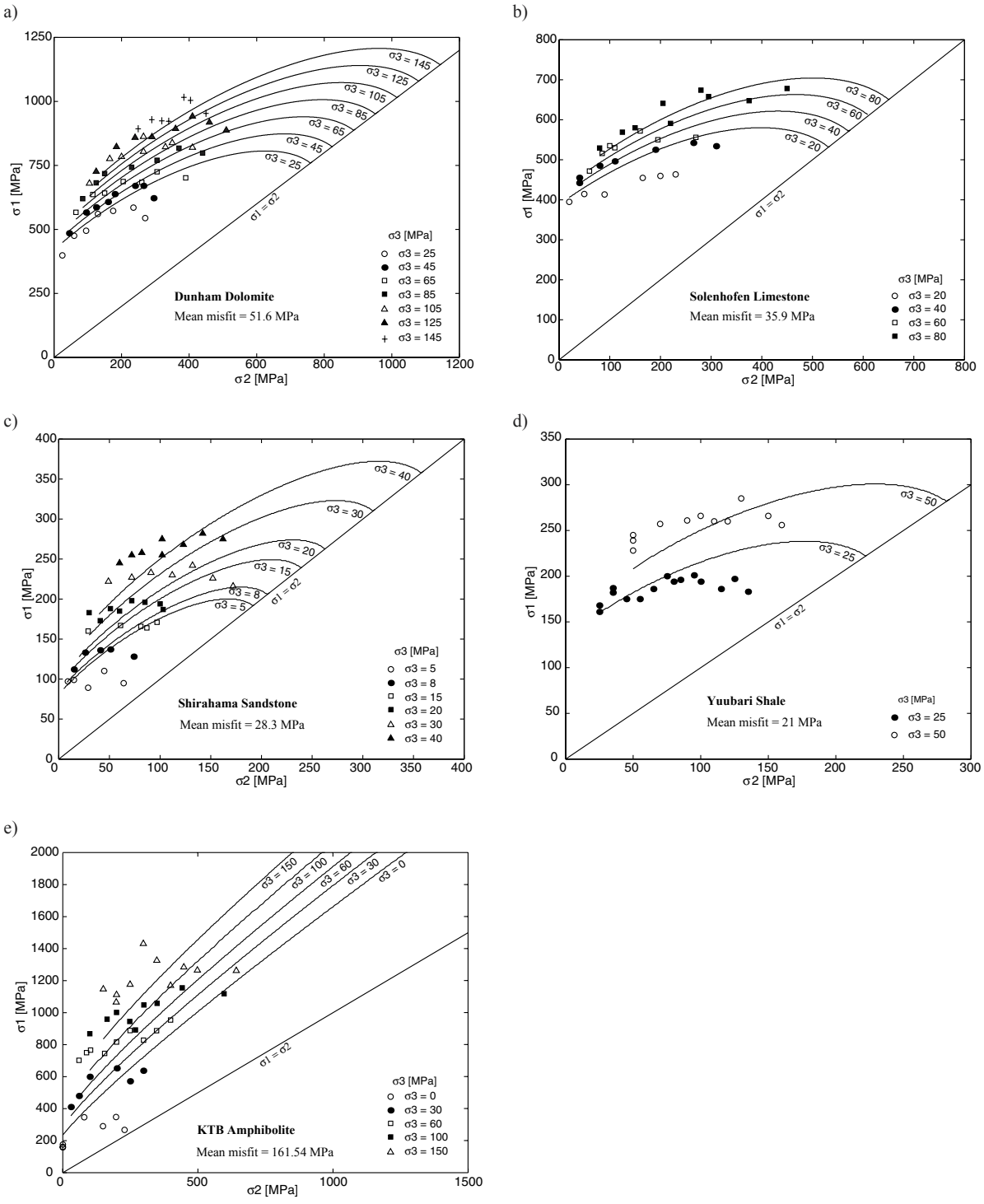

Figure 2.15: Best-fitting solution using the Drucker-Prager criterion plotted in σ_1-σ_2 space. a) Dunham dolomite. b) Solenhofen limestone. c) Shirahama sandstone. d) Yuubari shale. e) KTB amphibolite.

Table 2.7: Best-fitting parameters and mean misfits (in σ_1 - σ_2 space) for Dunham dolomite.

Failure Criterion	**Co [MPa]**	**μ_i**	**m**	**s**	**Mean misfit [MPa]**
Mohr-Coulomb	450	0.65	-	-	56.0
Hoek-Brown	400	-	8	1	56.2
Modified Wiebols-Cook	340	0.6	-	-	27.4
Modified Lade	380	0.5	-	-	27.8
Mogi 1967	$\frac{\sigma_1-\sigma_3}{2}=5.09*\left[\frac{\sigma_1+0.5*\sigma_2+\sigma_3}{2}\right]^{0.68}$				42.1
Mogi 1971	$\tau_{oct}=5.03\ \sigma_{m,2}^{0.67}$				27.9
Drucker-Prager	$J_2^{1/2}=0.5\ J_1+159.1$				51.6
Inscribed Drucker-Prager	723	0.64	-	-	-
Circumscribed Drucker-Prager	393	0.42	-	-	-

Table 2.8: Best-fitting parameters and mean misfits (in σ_1 - σ_2 space) for Solenhofen limestone.

Failure Criterion	**Co [MPa]**	**μ_i**	**m**	**s**	**Mean misfit [MPa]**
Mohr-Coulomb	375	0.55	-	-	37.1
Hoek-Brown	370	-	4.6	1	37.4
Modified Wiebols-Cook	320	0.45	-	-	25.5
Modified Lade	335	0.4	-	-	23.3
Mogi 1967	$\frac{\sigma_1-\sigma_3}{2}=7.61*\left[\frac{\sigma_1+0.45*\sigma_2+\sigma_3}{2}\right]^{0.59}$				29.8
Mogi 1971	$\tau_{oct}=0.41\ \sigma_{m,2}+86.79$				19.4
Drucker-Prager:	$J_2^{1/2}=0.3\ J_1+167.2$				35.9
Inscribed Drucker-Prager	574.5	0.37	-	-	-
Circumscribed Drucker-Prager	371	0.28	-	-	-

Table 2.9: Best-fitting parameters and mean misfits (in σ_1 - σ_2 space) for Shirahama sandstone.

Failure Criterion	**Co [MPa]**	**μ_i**	**m**	**s**	**Mean misfit [MPa]**
Mohr-Coulomb	95	0.8	-	-	9.6
Hoek-Brown	65	-	18.2	1	8.7
Modified Wiebols-Cook	55	0.8	-	-	10.3
Modified Lade	55	0.7	-	-	11.9
Mogi 1967	$\frac{\sigma_1-\sigma_3}{2}=1.95*\left[\frac{\sigma_1+0.06*\sigma_2+\sigma_3}{2}\right]^{0.81}$				13.2
Mogi 1971	$\tau_{oct} = 1.82\ \sigma_{m,2}^{0.79}$				14.1
Drucker-Prager	$J_2^{1/2} = 0.6\ J_1 + 27.7$				28.3
Inscribed Drucker-Prager	175.7	0.88	-	-	-
Circumscribed Drucker-Prager	74.7	0.51	-	-	-

Table 2.10: Best-fitting parameters and mean misfits (in σ_1 - σ_2 space) for Yuubari shale.

Failure Criterion	**Co [MPa]**	**μ_i**	**m**	**s**	**Mean misfit [MPa]**
Mohr-Coulomb	120	0.50	-	-	13.5
Hoek-Brown	100	-	6.5	1	13.0
Modified Wiebols-Cook	70	0.6	-	-	12.8
Modified Lade	110	0.4	-	-	13.7
Mogi 1967	$\frac{\sigma_1-\sigma_3}{2}=2.74*\left[\frac{\sigma_1+0.25*\sigma_2+\sigma_3}{2}\right]^{0.71}$				10.3
Mogi 1971	$\tau_{oct} = -0.0003\ \sigma_{m,2}^2 + 0.5\ \sigma_{m,2} + 19.05$				11.5
Drucker-Prager:	$J_2^{1/2} = 0.4\ J_1 + 48.7$				21.0
Inscribed Drucker-Prager	176.8	0.48	-	-	-
Circumscribed Drucker-Prager	111	0.34	-	-	-

Table 2.11: Best-fitting parameters and mean misfits (in σ_1 - σ_2 space) for the KTB amphibolite.

Failure Criterion	**Co [MPa]**	**μ_i**	**m**	**s**	**Mean misfit [MPa]**
Mohr-Coulomb	300	1.2	-	-	77.9
Hoek-Brown	250	-	30	1	89.9
Modified Wiebols-Cook	250	1	-	-	77.8
Modified Lade	250	0.85	-	-	91.3
Mogi 1967	$\frac{\sigma_1-\sigma_3}{2} = 1.77 * \left[\frac{\sigma_1 + 0.15*\sigma_2 + \sigma_3}{2}\right]^{0.87}$				95.2
Mogi 1971 (Chang and Haimson, 2000)	$\tau_{oct} = 1.77\ \sigma_{m,2}^{0.86}$				112.6
Drucker-Prager:	$J_2^{1/2} = 0.9\ J_1 + 67.9$				161.5
Inscribed Drucker-Prager	-	-	-	-	-
Circumscribed Drucker-Prager	236.5	0.75	-	-	-

2.5 BEHAVIOR OF THE DIFFERENT FAILURE CRITERIA IN RELATION TO EACH ROCK

As summarized in Tables 2.7 to 2.11, the mean misfits obtained using the two triaxial failure criteria are about within ~10% of each other and the mean misfits using the two polyaxial failure criteria are also within ~10% of each other. However, the mean misfits for the polyaxial failure criteria, are ~ 40 to 50% less than for the triaxial failure criteria. The Mogi 1967 empirical criteria yielded the lowest mean misfit for the Yuubari shale but it was only 20% less than the mean misfit yielded by the Modified Wiebols and Cook for the same rock. The Mogi 1971 empirical criterion yielded the lowest mean misfit for the Solenhofen limestone but it was only 17% less than the misfit yielded by the Modified Lade criterion. The mean misfits for the Drucker-Prager failure criterion were within the 10% of the triaxial failure criteria misfits for the Dunham dolomite and the Solenhofen limestone. However, for the other rocks, the misfits using the Drucker-

Prager criterion were 2 to 3 times larger than the misfits using the simpler triaxial failure criteria.

In Figure 2.16 a summary of the best fitting curves is presented for all the rocks in this study, for all the failure criteria at the minimum and maximum values of σ_3 used in the lab tests. It demonstrates that obtaining data under nearly biaxial conditions ($\sigma_2 \sim \sigma_1$) would be helpful in characterizing rock failure.

The parameters giving the best fit for each criterion are summarized in Table 2.7 for the Dunham dolomite. Failure of Dunham dolomite depends strongly on the intermediate principal stress. The triaxial Hoek and Brown and Mohr Coulomb criteria misfits are essentially the same and the Co values determined with the two criteria differ by ~10% (~50MPa). The value of *s* is 1 (for an intact rock) and *m* = 8, which is in the range of values reported by Hoek and Brown (1980, 1997) for carbonate rocks. As shown in Figure 2.B.2a, the *m* values that range between 7 and 8 fit the data almost equally well, as for *m* = 5, the misfits would be twice as large as the misfit for *m* = 8. The Modified Lade criterion is able to fit almost all the data points. Note that the misfit with this polyaxial criterion is less than half of that from the triaxial criteria. The Modified Wiebols and Cook criterion has the same misfit as the Modified Lade criterion. Co only differs by ~12% (~40 MPa) and μ_i by 20% (0.1). The Modified Wiebols and Cook yielded the least mean misfit for this rock. The Mogi empirical failure criteria fit the data very well as it can be seen in Figures 2.11 and 2.13. The misfit associated to the Mogi 1967 criterion is 1.5 times larger than the one associated to the best fitting failure criterion for this rock. The misfit yielded by the Mogi 1971 failure criterion is the same as the Modified Lade and Modified Wiebols and Cook criteria. The values of Co corresponding to the Inscribed and the Circumscribed Drucker-Prager criteria (Figure 2.12) bound the value of Co for the Mohr Coulomb criterion as expected. Figure 2.16a shows that the best fitting failure criteria for this rock are the Modified Lade and the Modified Wiebols and Cook.

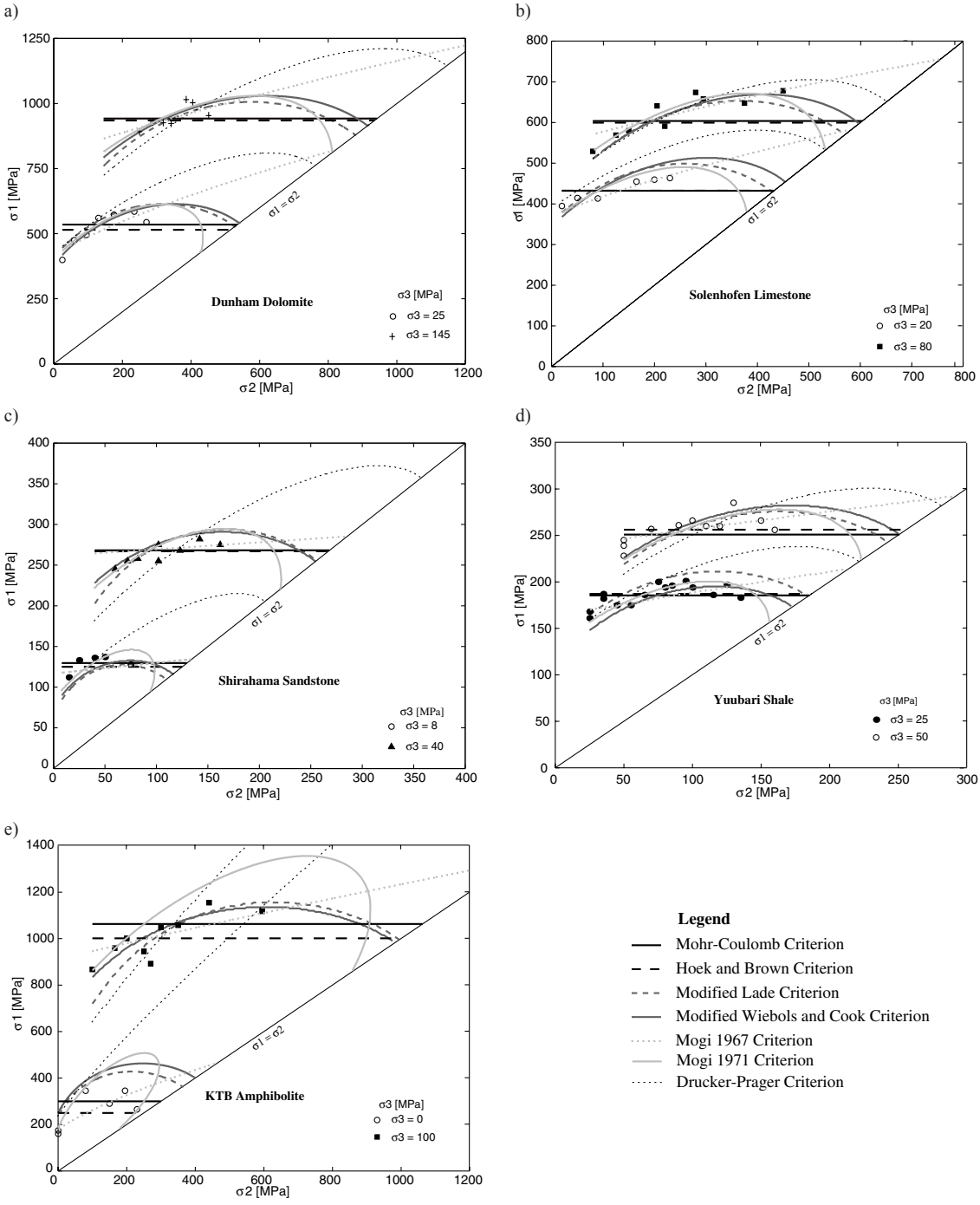

Figure 2.16: Summary of the best-fitting solution compared to the actual data for all the failure criteria. The best-fitting parameters (Co and μ_i) are summarized in Tables 2.7 to 2.11. a) Dunham dolomite. b) Solenhofen limestone. c) Shirahama sandstone. d) Yuubari shale. e) KTB amphibolite.

The results for the Solenhofen limestone were qualitatively similar for the triaxial and the polyaxial (Modified Lade and Modified Wiebols and Cook) failure criteria (Table 2.8). The Mohr Coulomb and the Hoek and Brown criteria fit the data equally well and represent an average fit of the data as it can be seen in Figures 2.6b and 2.7b. The value of *m* was 4.6, which is 10% lower than the lower bound of the range of *m* corresponding to carbonate rocks ($5 < m < 8$). However, Figure 2.B.2b shows that for $m = 5$, the misfit is essentially the same ($\pm$ 3 MPa) than for $m = 4.6$. The Modified Wiebols and Cook and the Modified Lade criterion yielded very similar values of Co and μ_i and their misfits are very similar. Figures 2.8b and 2.9b show that for both criteria, the fitting curves corresponding to all the σ_3 values are very good except for $\sigma_3 = 20$ MPa. The Mogi 1967 empirical failure criterion (Figure 2.11b) reproduces the trend of the data very well, indicating that the value of β indeed corresponds to the contribution of σ_2 on failure. The value of β equal to 0.45 implies that the fracture plane is about 26.7^o deviated from the direction of σ_2. The misfit achieved by this failure criterion was 35% larger than the misfit achieved by the Mogi 1971 criterion, which yielded the least mean misfit for this rock. Figure 2.13b shows that this criterion fits the data very well, however, as it does not provide information about the compressive strength or the coefficient of internal friction then it would be more practical to use the values of these parameters given by the Modified Lade criterion which yielded a mean misfit only 16% larger than the mean misfit obtained using the Mogi 1971 criterion. The Drucker-Prager criterion (Figure 2.15b) only slightly reproduces the trend of the data and its misfit is approximately 1.5 times larger than the one obtained with the Modified Wiebols and Cook criterion. Figure 2.16b shows that the best fitting failure criteria for this rock are the Mogi 1967, the Modified Lade and the Modified Wiebols and Cook criteria. It also shows that the fit of the data by the triaxial failure criteria is equivalent. The Drucker-Prager criterion gives the worst prediction of σ_1 at failure.

According to the misfits given by each criterion for the Shirahama sandstone (Table 2.9), it would be logical to think that both triaxial criteria (Mohr Coulomb and Hoek and Brown), the Modified Lade criterion and the Modified Wiebols and Cook criterion fit the data well, as their respective misfits are nearly the same. However, the

way they approximate the data is different and as the Shirahama sandstone presents an unusual σ_2-dependence, the approximations are not completely satisfactory. The Mohr-Coulomb criterion fits the data very well for some values of σ_3 but not for the entire data set because of the unusual σ_2-dependence. The Hoek and Brown criterion (Figures 2.6c and 2.7c) achieves better fit than the Mohr-Coulomb criterion, probably because it has an additional degree of freedom. It was found that the value of *m* for this rock is 18.2, which is within the range of *m* values for arenaceous rocks. As shown in Figure 2.B.2c the *m* values that range between 16 and 20 fit the data similarly well, as for *m* = 15 (lower limit) and *m* = 24 (upper limit), the misfit would be approximately twice as large as the misfit for *m* = 18.2. The Hoek and Brown criterion yielded the least mean misfit for this rock. Both the Modified Lade criterion and Modified Wiebols and Cook criterion (Figures 2.8c and 2.9c) do not accurately predict the failure stress for this data set. Both give essentially the same Co, and μ_i. It can be seen that as the Modified Lade criterion accounts for a high σ_2-dependence at low σ_2 (Figure 2.8), the slope of the curve at the beginning is steeper than the slope of the Modified Wiebols and Cook curve (Figure 2.9), which is why the latter fits the data better. The Mogi 1967 failure criterion does a good job reproducing the trend of the data. According to the value of β found using the Mogi 1967 criterion, the fracture plane is almost parallel (~3^o) to the σ_2-direction. This criterion approximates the data better than does the Mogi 1971 failure criterion, which yielded the duality of values of σ_1 for the higher values of σ_2 for a specific value of σ_3, as it can be seen in Figure 2.13c. The misfit achieved by the Mogi 1971 criterion was 1.6 times larger than the one achieved by the Hoek and Brown criterion. The Drucker-Prager criterion does not represent the trend of the data set (Figure 2.15c) and therefore, it does not predict σ_1 at failure correctly. The misfit of the Drucker-Prager criterion is approximately 3 times larger than the misfits obtained using the triaxial failure criteria. Figure 2.16c shows that the failure criteria fit the data in the same average manner, except for the Drucker-Prager criterion and the Mogi 1971 criterion as indicated above.

The results for the Yuubari shale are summarized in Table 2.10. The misfits associated to the Mohr Coulomb, the Hoek and Brown, the Modified Lade and the Modified Wiebols and Cook criteria are all approximately the same. Using the Hoek and Brown criterion a value of *m* = 6.5 was obtained, which is within the range of values

reported by Hoek and Brown (1980, 1997) for argillaceous rocks. As shown in Figure 2.B.2d the *m* values that range between 5.5 and 7.5 fit the data almost equally well, as for the lower and upper bounds of *m*, the misfits would be approximately 3 times larger than the misfit for *m* = 6.5. The misfits yielded by the Mogi criteria are also very similar, differing only by 1MPa. The Mogi 1967 failure criterion reproduces the trend of the data very well as it can be seen in Figure 2.11d. The least mean misfit for this rock is achieved using the Mogi 1967 criterion, however, as it does not provide direct information about Co or μ_i, it would be better to use the Modified Wiebols and Cook criterion which only yielded a mean misfit ~1.2 times higher than the one yielded by the former criterion. The Mogi 1971 failure criterion also does a good job fitting the data (Figure 2.13d). Figure 2.15d shows that the fitting curve for the Drucker-Prager criterion for σ_3= 25 MPa reproduces the trend of the data until $\sigma_2 \approx 100$ MPa, but for $\sigma_3 = 50$ MPa, the fitting curve does not even represent the trend of the data. Therefore, the Drucker-Prager criterion does not give reliable values of σ_1 at failure. As it can be seen in Figure 2.16d, the triaxial criteria and two of the polyaxial criteria (Modified Lade and Modified Wiebols and Cook), fit the data in approximately the same manner and predict almost equal values of σ_1 at failure when $\sigma_1 = \sigma_2$.

For the KTB amphibolite, the Mohr Coulomb criterion represents a good general fit to the data except for $\sigma_3 = 150$ MPa as it can be seen in Figure 2.6e. In contrast, the Hoek and Brown criterion represents a good fit to all the experimental data. It was found that *m*=30, which is in the range of values reported by Hoek and Brown (1980, 1997) for coarse-grained polyminerallic igneous rocks. As shown in Figure 2.B.2e, the *m* values that range between 26 and 33 fit the data almost equally well, as for *m* = 22 and, the misfit would be approximately1.5 times larger than the misfit for *m* = 30. Both, Modified Lade and Modified Wiebols and Cook criterion (Figures 2.8e and 2.9e) achieve a similar fit to the data and yield the same value of Co. However, the misfits differ by 20%, which is most likely due to the shape of the failure envelope of each criterion as the slope of the curve for low values of σ_2 is greater for the Modified Lade criterion than for the Modified Wiebols and Cook criterion. The latter yielded the least mean misfit for this rock as it is reported in Table 2.11. As it can be seen in Figures 2.10e and 2.12e, both Mogi empirical failure criteria fit the data very well in the Mogi space. However, in the σ_1-σ_2 space the

fitting is different. As can be seen in Figure 2.11e, the Mogi 1967 criterion somewhat reproduces the trend of the data. For high σ_2 on a given σ_3, the Mogi 1971 failure criterion yield two values of σ_1 at failure which is physically impossible (see Figure 2.13e). The failure criterion that best describes failure on the KTB amphibolite is the Modified Wiebols and Cook criterion and not the Mogi 1971 criterion as proposed by Chang and Haimson (2000). The Drucker-Prager criterion does not reproduce the trend of the data whatsoever as can be seen in Figures 2.15e and 2.16e. It was impossible to find the values of Co and μ_i according to the Inscribed Drucker-Prager criterion because the value of α was greater than the asymptotic value of α for this criterion. This might be due to the fact that the Drucker-Prager criterion was originally derived for soils and perhaps should not be applied to strong rocks such as the KTB amphibolite. In Figure 2.16e it is possible to see that the Modified Lade and the Modified Wiebols and Cook criteria give a better fit of the data for σ_3=100 MPa than for σ_3=0 MPa. However, the Mohr Coulomb and the Hoek and Brown criteria give a good average fit of the data for both values of σ_3.

2.6 APPLICATION: HOW NECESSARY ARE POLYAXIAL TESTS?

Polyaxial tests are very difficult to perform and it would be preferable to do triaxial tests. In this section I briefly explore the possibility of working with triaxial test data to see if it is possible to predict the σ_2-dependence on failure using polyaxial failure criteria.

Triaxial test data were used for Solenhofen limestone (Mogi, 1967), KTB amphibolite (Chang and Haimson, 2000) and Dunham dolomite (Mogi, 1967). It is important to remember that these rocks have a large σ_2-dependence on failure. A grid search was performed to find the best fitting parameters Co and μ_i using the conventional Mohr Coulomb criterion. These parameters were used to fit the data with the Modified Lade criterion and the Modified Wiebols and Cook criterion and they yielded very good fits of the triaxial data (Figures 2.17 to 2.19). The best fitting parameters for each rock are summarized in Tables 2.12 to 2.14. For the Solenhofen limestone and the KTB amphibolite the parameters obtained using the triaxial test data are very similar to those

obtained using the polyaxial failure criteria on the polyaxial test data. As shown in Table 2.12 for the Solenhofen limestone, if only triaxial test data was available, I would have obtained a value of Co $\pm$ 3% those obtained using polyaxial failure criteria on polyaxial test data. The misfit associated with using the triaxial parameters in the polyaxial failure criteria for the Solenhofen limestone was only 10% larger, which is a very reasonable result if I only have to work with triaxial data. For the KTB amphibolite I obtained a Co 13% smaller than that obtained for the polyaxial test data using the polyaxial failure criteria. The misfits for using the triaxial parameters in the polyaxial criteria were larger, especially for the Modified Lade criterion. For the Modified Wiebols and Cook the misfit was only 5% larger which is still considered to be acceptable. However, for the Dunham dolomite, the Co obtained with the triaxial test data was ~1.6 times smaller than those obtained using the polyaxial test data and μ_i is approximately half the value found for the polyaxial test data. As for the misfits, they are approximately 15 to 20 times larger than the original misfit for the polyaxial failure criteria. This result cannot be attributed merely to the fact that Dunham dolomite has a large σ_2-dependence because such results were not obtained for the Solenhofen limestone or the KTB amphibolite, which also have a large σ_2-dependence. The reason why the results for Dunham dolomite are so unsatisfactory might be due to the fact that the triaxial test data reported by Mogi (1967) considered values of σ_3 up to 33 MPa, while the polyaxial test data reported by Mogi (1971) considered values of σ_3 up to 145 MPa. Therefore, the difference between the Co and μ_i obtained using the triaxial test data and the values from the analysis of polyaxial test data might simply be because of the different pressures considered.

Thus, in two of the three rocks studied, the rock strength parameters yielded by the triaxial test data are very similar to those found using polyaxial test data. This is very helpful because it allows one to perform triaxial tests instead of polyaxial tests to obtain the rock strength parameters and then apply those parameters using a polyaxial failure criterion. However, it is necessary to have a good triaxial test data set covering a wide range of pressures, otherwise the results could be inaccurate as it was the case for the Dunham dolomite.

Table 2.12: Best-fitting parameters for the triaxial test data of the Solenhofen limestone.

Failure criterion	**Co [MPa]**	**μ_i**	**Mean misfit [MPa]**	**Mean misfit using triaxial parameters in polyaxial criterion [MPa]**
Triaxial test Mohr Coulomb	325	0.4	9.5	-
Polyaxial test Modified Lade	320	0.45	25.5	27
Polyaxial test Modified Wiebols and Cook	335	0.4	23.2	25

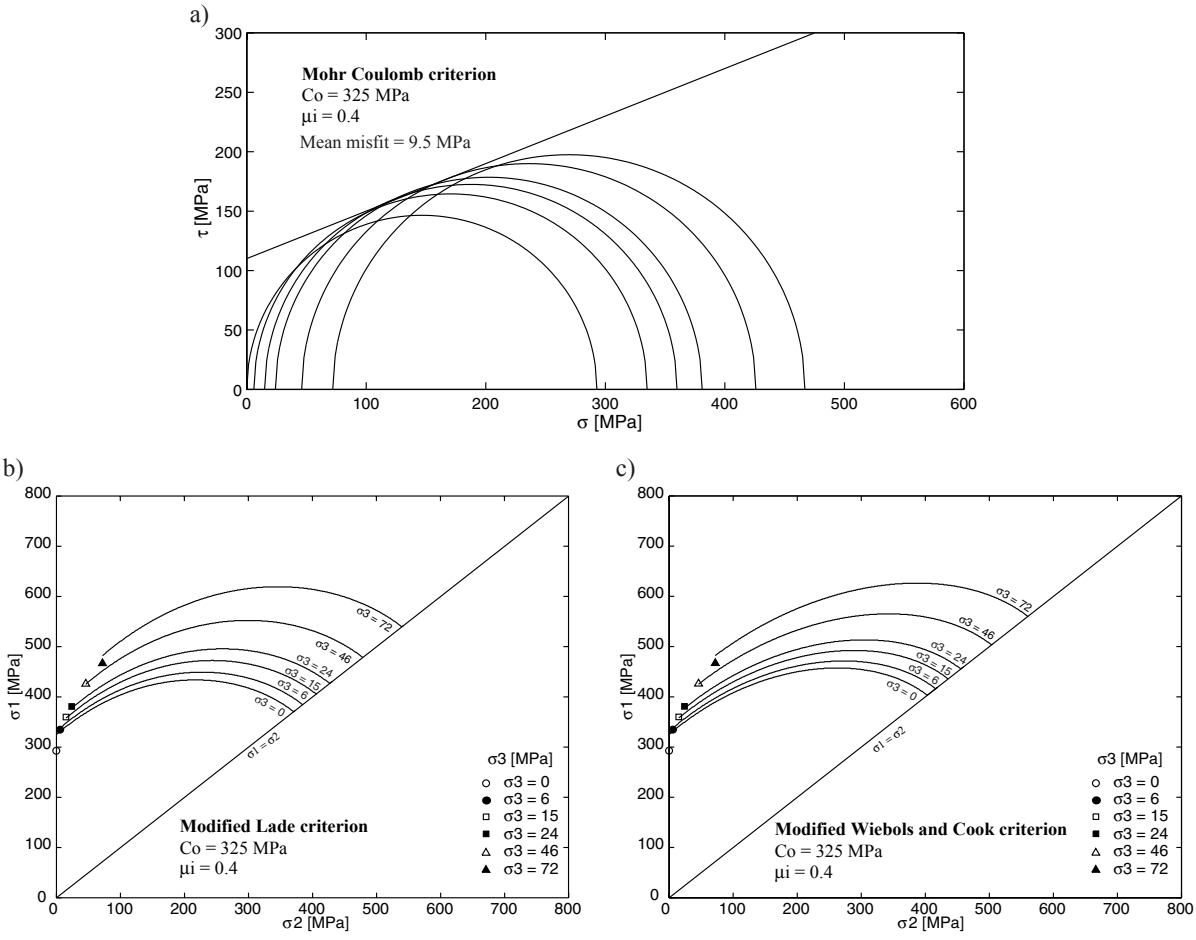

Figure 2.17: Best-fitting solution for the Solenhofen limestone using the triaxial test data. a) Mohr Coulomb criterion. b) Modified Lade criterion. c) Modified Wiebols and Cook criterion. The best fitting parameters obtained using the Mohr-Coulomb criterion are reported in Table 2.12.

Table 2.13: Best-fitting parameters for the triaxial test data of the KTB amphibolite.

Failure criterion	**Co [MPa]**	**μ_i**	**Mean misfit [MPa]**	**Mean misfit using triaxial parameters in polyaxial criterion [MPa]**
Triaxial test Mohr Coulomb	220	1	55.1	-
Polyaxial test Modified Lade	250	0.85	91.3	163
Polyaxial test Modified Wiebols and Cook	250	1	77.8	82

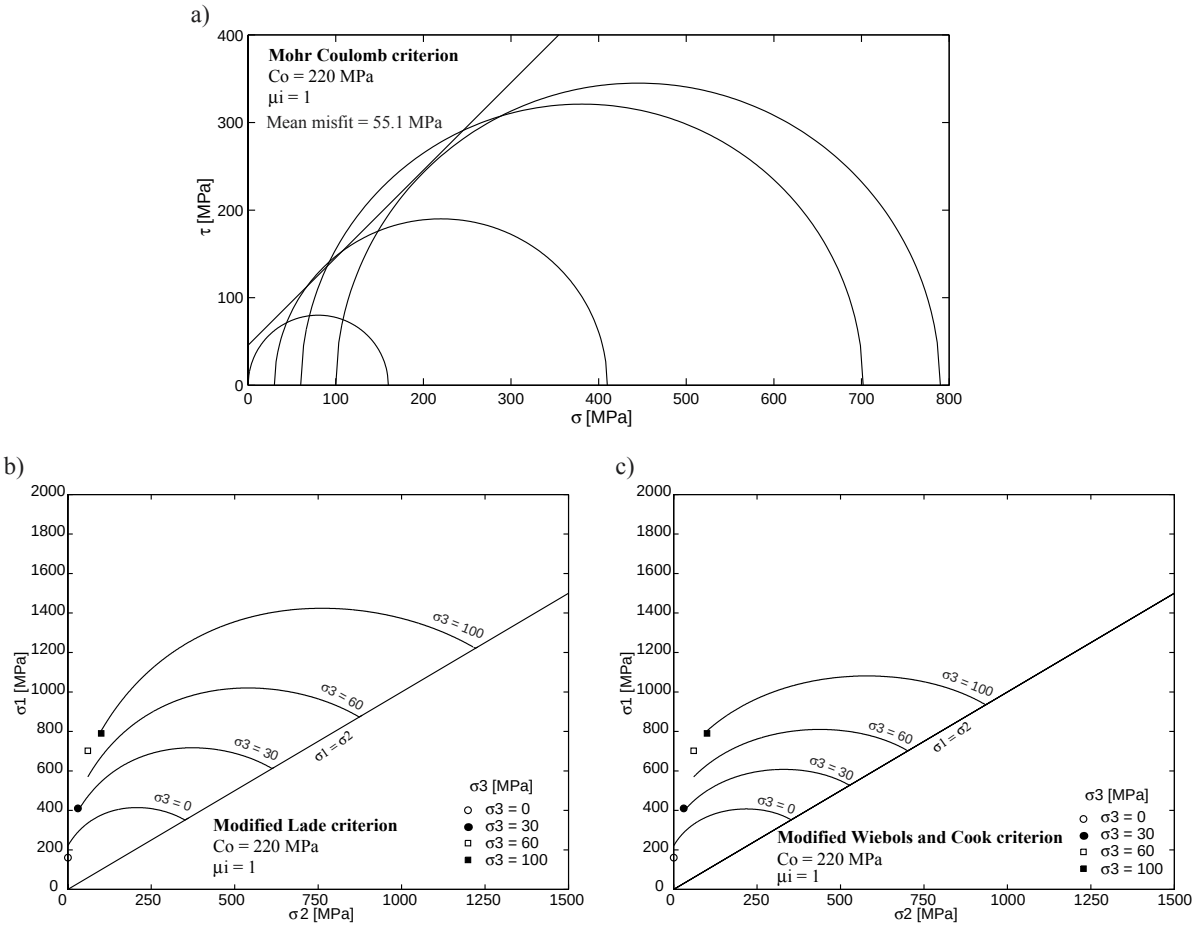

Figure 2.18: Best-fitting solution for the KTB amphibolite using the triaxial test data. a) Mohr Coulomb criterion. b) Modified Lade criterion. c) Modified Wiebols and Cook criterion. The best fitting parameters obtained using the Mohr-Coulomb criterion are reported in Table 2.13.

Table 2.14: Best-fitting parameters for the triaxial test data of the Dunham dolomite.

Failure criterion	**Co [MPa]**	**μ_i**	**Mean misfit [MPa]**	**Mean misfit using triaxial parameters in polyaxial criterion [MPa]**
Triaxial test Mohr Coulomb	235	1.2	11.1	-
Polyaxial test Modified Lade	380	0.5	27.8	550
Polyaxial test Modified Wiebols and Cook	340	0.6	27.4	300

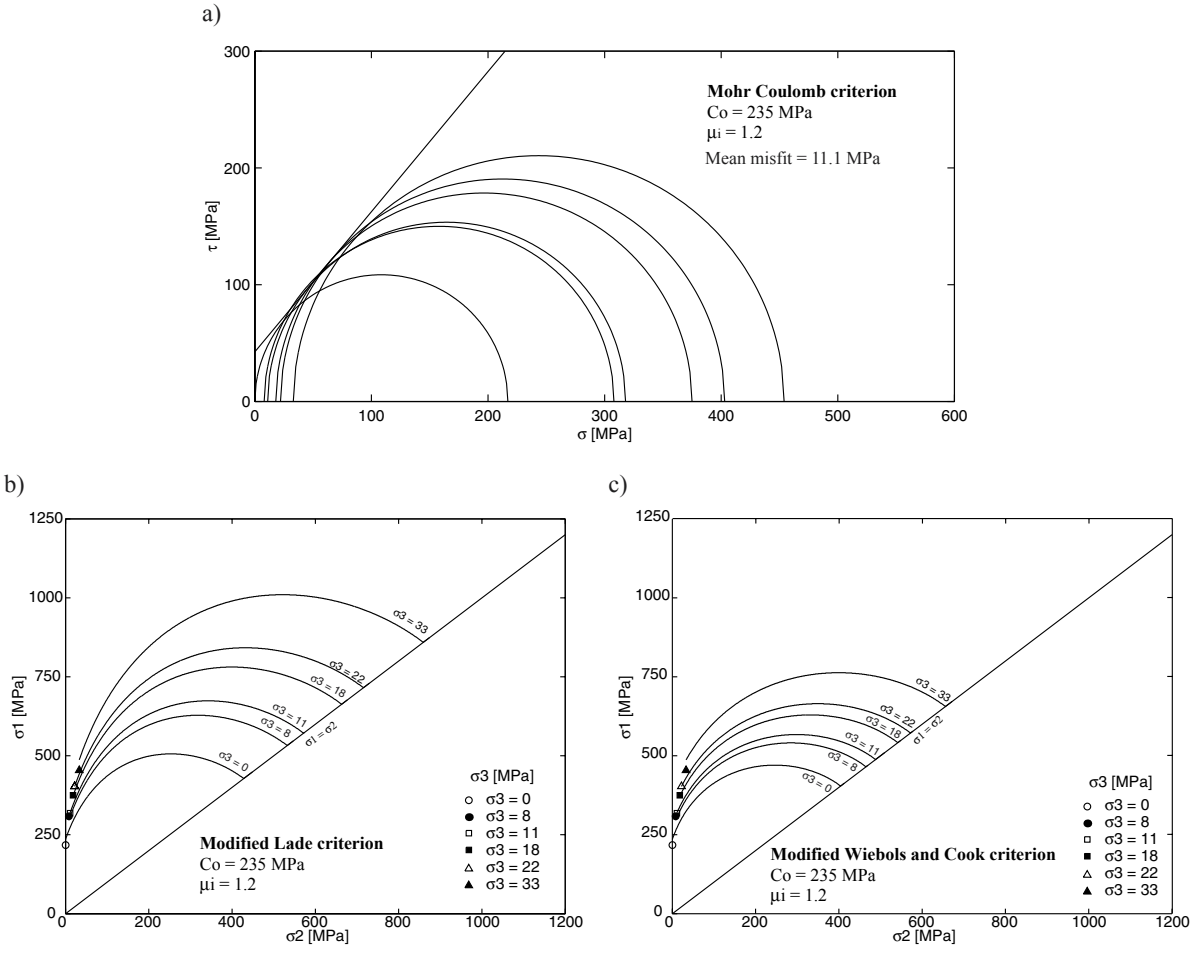

Figure 2.19: Best-fitting solution for the Dunham dolomite using the triaxial test data. a) Mohr Coulomb criterion. b) Modified Lade criterion. c) Modified Wiebols and Cook criterion. The best fitting parameters obtained using the Mohr-Coulomb criterion are reported in Table 2.14.

2.7 CONCLUSIONS

By comparing the different failure criteria to the polyaxial test data I demonstrated that the way a failure criterion fits the data will depend on the type of failure criterion (i.e. triaxial, polyaxial) and on the σ_2-dependence of the rock in question. In general, it was found that the Modified Wiebols and Cook and the Modified Lade criteria achieved good fits to most of the test data. This is especially true for rocks with a highly σ_2-dependent failure behavior (e.g. Dunham dolomite, Solenhofen limestone). The Modified Wiebols and Cook criterion fit the polyaxial data much better than did the Mohr-Coulomb criterion. However, for some rock types (e.g. Shirahama Sandstone, Yuubari shale), the intermediate stress hardly affects failure at some values of σ_3 and the Mohr-Coulomb and Hoek and Brown criteria fit these test data equally well, or even better, than the more complicated polyaxial criteria.

The values of Co corresponding to the Inscribed and the Circumscribed Drucker-Prager criterion bounded the Co value obtained using the Mohr Coulomb criterion as expected. The values of Co obtained using the Modified Wiebols and Cook and the Modified Lade criteria were always smaller than the lower bound of the Drucker-Prager criterion, except for the KTB amphibolite for which it was not possible to find both bounds with the Drucker-Prager criterion.

The Mogi 1967 empirical criterion was always able to reproduce the trend of the experimental data for all the rocks. Even though it yielded the least mean misfit for the Yuubari shale, it would be better to use the Modified Wiebols and Cook criterion to fit the data, as the Mogi failure criteria cannot be related to Co or to other parameters used for characterizing rock strength. The Mogi 1971 failure criterion is mathematically problematic because it yields two values of σ_1 at failure for the same value of σ_2 for the Shirahama sandstone, the KTB amphibolite and for low σ_3 values of Dunham dolomite.

The two triaxial failure criteria analyzed in this study (Mohr Coulomb and Hoek and Brown) always yielded comparable misfits. Furthermore, the Modified Lade and the Modified Wiebols and Cook criteria, both polyaxial criteria, also gave very similar fits of the data. The Drucker-Prager failure criterion did not accurately indicate the value of σ_1 at failure and had the highest misfits.

The σ_2-dependence on failure varies for different rock types but can be very important. I have shown that the use of polyaxial failure criteria can provide meaningful results even in the absence of polyaxial test data when only triaxial test data are available.

The results for two out of three rocks that could be analyzed in this way were encouraging. This finding can be very useful as polyaxial test data is hard to perform and therefore uncommon.

2.8 RECOMMENDATIONS

The use of the Modified Wiebols and Cook criterion is recommended even when polyaxial test data is unavailable, as this criterion did not tend to overestimate the strength of the rock as much as the Mohr-Coulomb criterion (Co was always ~55% – 80% lower than those obtained using the Mohr-Coulomb criterion) and it consistently gave low misfits. The Modified Lade criterion also gave very good results.

If only a bound of the rock strength is needed then the Drucker-Prager criterion might be appropriate, as it is able to give the lower and upper bound of Co with respect to the Mohr Coulomb criterion, however, the lower bound was always greater than the Co given by the Modified Wiebols and Cook criterion, that is, the Drucker-Prager criterion tends to overestimate the rock strength.

2.9 NOMENCLATURE

σ_{ij}	=	effective stress with i and j = 1, 2, 3 (Eqn. 1)
S_{ij}	=	total stress with i and j = 1, 2, 3 (Eqn. 1)
P_o	=	pore pressure (Eqn. 1)
τ	=	shear stress (Eqn. 2)
S_o	=	shear strength or cohesion of the material (Eqn. 2)
μ_i	=	coefficient of internal friction (Eqn. 2)
σ_n	=	normal stress (Eqn. 2)

σ_1 = major principal effective stress at failure (Eqn. 3)

σ_3 = least principal effective stress at failure (Eqn. 3)

Co = uniaxial compressive strength (Eqn. 3)

m = constant that depends on rock type (Eqn. 5)

s = constant that depends on the quality of the rock mass (Eqn. 5)

I_1 = first stress invariant (Eqns. 6 and 7)

I_3 = third stress invariant (Eqns. 6 and 8)

p_a = atmospheric pressure (Eqn. 6)

m', η_1 = material constants (Eqn. 6)

κ_1 = constant that depends on the density of the soil

I_1' = modified first stress invariant (Eqns. 9 and 10)

I_3' = modified third stress invariant (Eqns. 9 and 11)

S = parameter related to the cohesion of the rock (Eqns. 9 and 12)

η = parameter representing the internal friction of the rock (Eqns. 9 and 13)

ϕ = angle of internal friction (Eqn. 4)

J_1 = mean effective confining stress (Eqn. 15)

J_2 = $(3/2)^{1/2}\tau_{oct}$ (Eqn. 16)

τ_{oct} = octahedral shear stress (Eqn. 17)

A = parameter related to Co and μ_i (Eqns. 14 and 20)

B = parameter related to Co and μ_i (Eqns. 14, 19 and 20)

C = parameter related to Co and μ_i (Eqns. 14, 18, 19 and 20)

C_1 = parameter related to Co and μ_i (Eqn. 18)

β = may represent the contribution of σ_2 to the normal stress on the fault plane (Eqn. 21)

$\sigma_{m,2}$ = effective mean pressure on faulting ($(\sigma_1 + \sigma_3)/2$)

k = empirical constant (Eqns. 23 and 24)

α = material constant (Eqn. 24)

X, Y = variables (Eqn. 29)

$Corr[X,Y]$ = correlation of two variables X and Y (Eqn. 29)

$Cov[X,Y]$ = covariance of two variables X and Y (Eqn. 29)

s_X = standard deviation of X (Eqn. 29)

s_Y = standard deviation of Y (Eqn. 29)

ACKNOWLEDGEMENTS

I thank Balz Grollimund, Paul Hagin and Pavel Peska for their valuable advice during this work. This study was supported by the Stanford Rock Physics and Borehole Geophysics Project (SRB).

REFERENCES

Chang, C. & Haimson, B., 2000, True triaxial strength and deformability of the German Continental Deep Drilling Program (KTB) deep hole amphibolite: J. Geophys. Res. **105**, 18,999-19,013.

Drucker, D. & Prager, W., 1952, Soil mechanics and plastic analysis or limit design: Q. Appl. Math. **10**, 157-165.

Ewy, R. 1999. Wellbore-stability predictions by use of a modified Lade criterion: SPE Drill. & Completion **14** (2), 85-91.

Hoek, E. & Brown, E., 1980, Empirical strength criterion for rock masses: Journal of the Geotechnical Engineering Division **106** (GT9), 1013-1035.

Hoek, E. & Brown, E., 1997, Practical estimates of rock mass strength: Int. J. Rock Mech. Min. Sci. **34** (8), 1165-1186.

Lade, P., 1977, Elasto-plastic stress-strain theory for cohesionless soil with curved yield surfaces: International Journal of Solids and Structures **13**, 1019-1035.

Lade, P. & Duncan, J., 1975, Elasto-plastic stress-strain theory for cohesionless soil: J. Geotechnical Eng. Div. ASCE **101**, 1037-1053.

McLean, M. & Addis, M., 1990, Wellbore stability: the effect of strength criteria on mud weight recommendations: 65th Annual Technical Conference and Exhibition of the Society of Petroleum Engineers, New Orleans, 9-17. SPE 20405.

Mogi, K., 1967, Effect of the intermediate principal stress on rock failure: J. Geophys. Res. **72**, 5117-5131.

Mogi, K., 1971, Fracture and flow of rocks under high triaxial compression: J. Geophys. Res. **76**, 1255-1269.

Riley, K.F., Hobson, M.P. and Bence, S.J. Mathematical methods for physics and engineering. Cambridge: Cambridge University Press, 1998.

Takahashi, M. & Koide, H., 1989, Effect of the intermediate principal stress on strength and deformation behavior of sedimentary rocks at the depth shallower than 2000m. In V. Maury & D. Fourmaintraux (eds), Rock at Great Depth, 19-26. Rotterdam: Balkema.

Veeken, C., Walters, J., Kenter, C. & Davies, D., 1989, Use of plasticity models for predicting borehole stability. In V. Maury & D. Fourmaintraux (eds), Rock at Great Depth, 835-844. Rotterdam: Balkema.

Wiebols, G. & Cook, N., 1968, An energy criterion for the strength of rock in polyaxial compression: Int. J. Rock Mech. Min. Sci **5**, 529-549.

Zhou, S., 1994, A program to model the initial shape and extent of borehole breakout: Computers & Geosciences **20** (7/8), 1143-1160.

APPENDIX 2.A. POLYAXIAL TEST DATA

The polyaxial test data of the rocks studied here were obtained from published works as follows: Dunham dolomite and Solenhofen limestone from Mogi (1971), Shirahama sandstone and Yuubari Shale from Takahashi & Koide (1989) and the data of the amphibolite from the KTB site was kindly provided by Chang and Haimson. Tables 2.A.1 to 2.A.5 show the polyaxial test data for each rock.

Table 2.A.1.
Polyaxial test data for the Dunham dolomite (digitize from Mogi, 1971)

σ_1 [MPa]	σ_2 [MPa]	σ_3 [MPa]	σ_1 [MPa]	σ_2 [MPa]	σ_3 [MPa]
399.9	23.5	25	770.6	303.5	85
475.2	61.8	25	817.5	371	85
495.6	93.8	25	798.2	440.3	85
560.4	130.3	25	680.3	103.3	105
572.5	173.1	25	776.1	165.2	105
585.1	232.9	25	784.1	202.1	105
544	268.8	25	804.2	264.9	105
485.6	42.8	45	822.1	330.7	105
566	93.7	45	838.7	350.8	105
586.4	124.3	45	820.4	411	105
606.9	159.3	45	862.5	266.2	105
638.7	182.5	45	726.3	122.7	125
670.5	241.3	45	822.6	185.8	125
670	263.3	45	858.8	241.1	125
622.1	292.5	45	861.6	288.1	125
567	62.5	65	893.3	358.8	125
636.3	113.3	65	941.7	410.5	125
641.9	152.4	65	918.4	457.8	125
687.1	207.6	65	887.1	510.1	125
683.9	258.9	65	892.1	254.2	145
725.2	306.4	65	928.5	292.3	145
701.4	390.1	65	924	318.7	145
620.4	83.9	85	922	341.6	145
682.1	125.9	85	1015.7	386.6	145
718	149.7	85	1003.2	404.4	145
743.3	230	85	952.9	450.9	145

Table 2.A.2.
Polyaxial test data for the Solenhofen limestone (digitize from Mogi, 1971)

σ_1 [MPa]	σ_2 [MPa]	σ_3 [MPa]
395	19.1	20
414.4	52.2	20
413.3	91	20
454.6	165	20
459.4	203.4	20
463.6	230.9	20
442.1	40.1	40
455	39.9	40
485.6	80.4	40
496.1	112.8	40
525.8	189.6	40
542.2	267.2	40
534.3	312.4	40
471.9	57	60
516	87.1	60
535.2	99.5	60
529.4	111.1	60
572.9	162.1	60
550.5	196.1	60
556.1	271.4	60
529.3	80.5	80
568.9	124.9	80
580.3	149.6	80
641.3	205.4	80
591.6	220.9	80
674.4	280.3	80
658.7	293.8	80
647.7	373	80
678.2	448.1	80

Table 2.A.3.
Polyaxial test data for the Shirahama sandstone (digitize from Takahashi and Koide, 1989)

σ_1 [MPa]	σ_2[MPa]	σ_3 [MPa]
97	9	5
99	15	5
89	29	5
110	45	5
95	64	5
112	15	8
133	26	8
136	41	8
137	51	8
128	74	8
160	29	15
167	61	15
166	81	15
164	87	15
171	97	15
183	30	20
173	41	20
188	51	20
185	60	20
198	72	20
196	85	20
194	100	20
187	103	20
222	49	30
227	72	30
233	91	30
230	112	30
242	132	30
226	152	30
216	172	30
245	60	40
255	72	40
258	82	40
255	102	40
275	102	40
268	123	40
282	142	40
275	162	40

Table 2.A.4.
Polyaxial test data for the Yuubari shale (digitize from Takahashi and Koide, 1989)

σ_1 [MPa]	σ_2 [MPa]	σ_3 [MPa]
160.975	25.673	25
167.713	25.558	25
181.677	35.567	25
187.369	35.947	25
175.436	45.417	25
175.05	56.153	25
186.264	65.469	25
199.69	76.48	25
193.765	79.118	25
196.405	85.347	25
200.678	96.286	25
194.04	100.093	25
185.64	114.289	25
197.359	124.28	25
183.191	133.23	25
228.364	50.194	50
238.904	49.941	50
244.782	49.652	50
257.171	69.38	50
260.564	89.876	50
265.544	99.982	50
259.646	110.003	50
259.761	121.581	50
285.345	129.164	50
265.797	148.138	50
255.91	158.967	50

Table 2.A.5.
Polyaxial test data for the KTB amphibolite (kindly provided by Chang and Haimson)

σ_1 [MPa]	σ_2 [MPa]	σ_3 [MPa]	σ_1 [MPa]	σ_2 [MPa]	σ_3 [MPa]
158	0	0	954	399	60
160	0	0	815	449	60
176	0	0	868	100	100
346	79	0	959	164	100
291	149	0	1001	199	100
347	197	0	945	248	100
267	229	0	892	269	100
410	30	30	1048	300	100
479	60	30	1058	349	100
599	100	30	1155	442	100
652	200	30	1118	597	100
571	249	30	1147	150	150
637	298	30	1065	198	150
702	60	60	1112	199	150
750	88	60	1176	249	150
766	103	60	1431	298	150
745	155	60	1326	348	150
816	199	60	1169	399	150
888	249	60	1284	448	150
828	299	60	1265	498	150
887	347	60	1262	642	150

APPENDIX 2.B. MISFIT CONTOURS PLOTS

Figures 2.B.1 to 2.B.4 show the misfit contours plots for all the rocks for the Mohr Coulomb criterion, the Hoek and Brown criterion, the Modified Lade criterion and the Modified Wiebols and Cook criterion. These figures show a well defined minimum, which allowed accurate selection of the Co and μ_i that describe the failure of each rock in terms of the respective criterion.

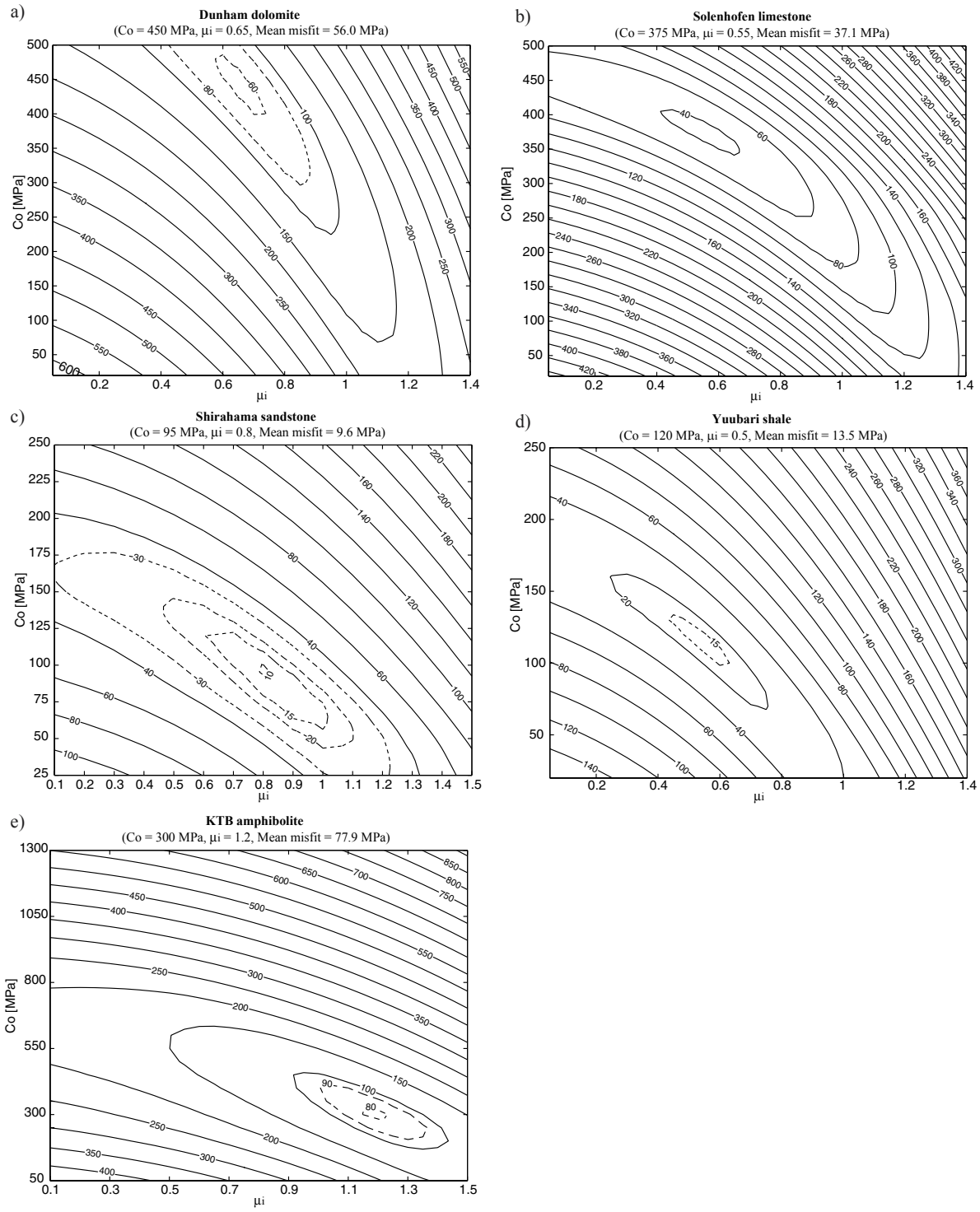

Figure 2.B.1: Misfit contours for the Mohr-Coulomb criterion. a) Dunham dolomite. b) Solenhofen limestone. c) Shirahama sandstone. d) Yuubari shale. e) KTB amphibolite.

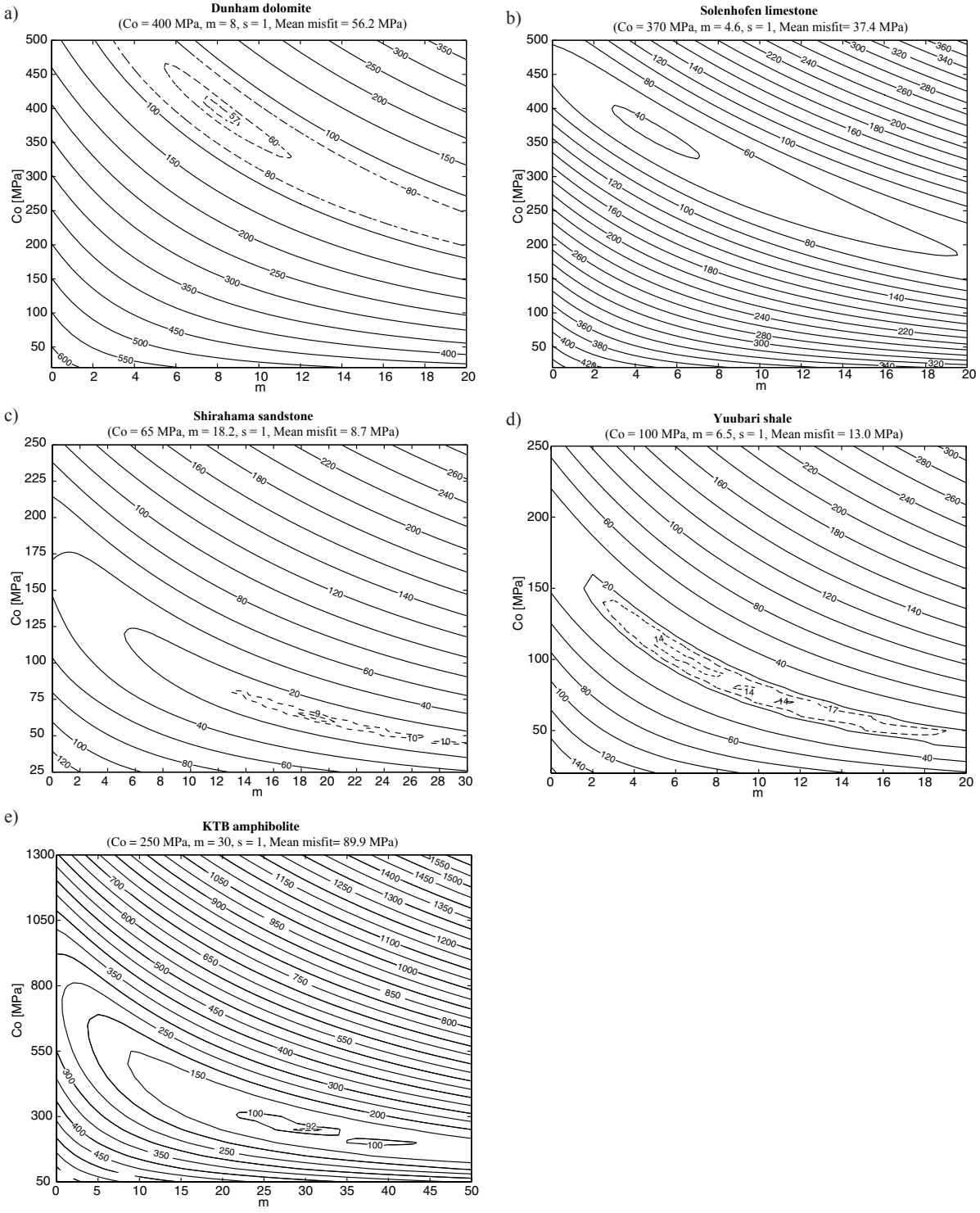

Figure 2.B.2: Misfit contours for the Hoek and Brown criterion. a) Dunham dolomite. b) Solenhofen limestone. c) Shirahama sandstone. d) Yuubari shale. e) KTB amphibolite.

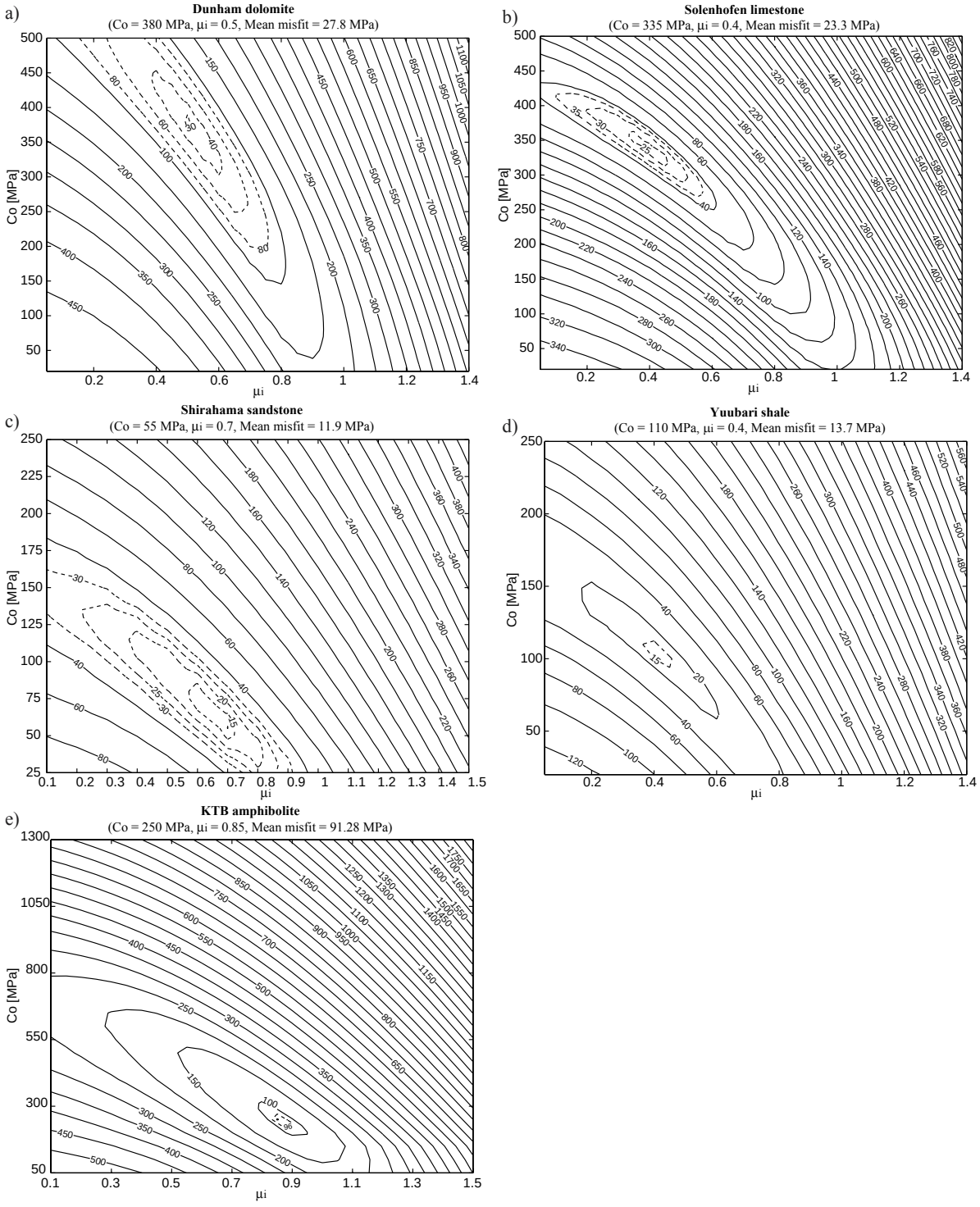

Figure 2.B.3: Misfit contours for the Modified Lade criterion. a) Dunham dolomite. b) Solenhofen limestone. c) Shirahama sandstone. d) Yuubari shale. e) KTB amphibolite.

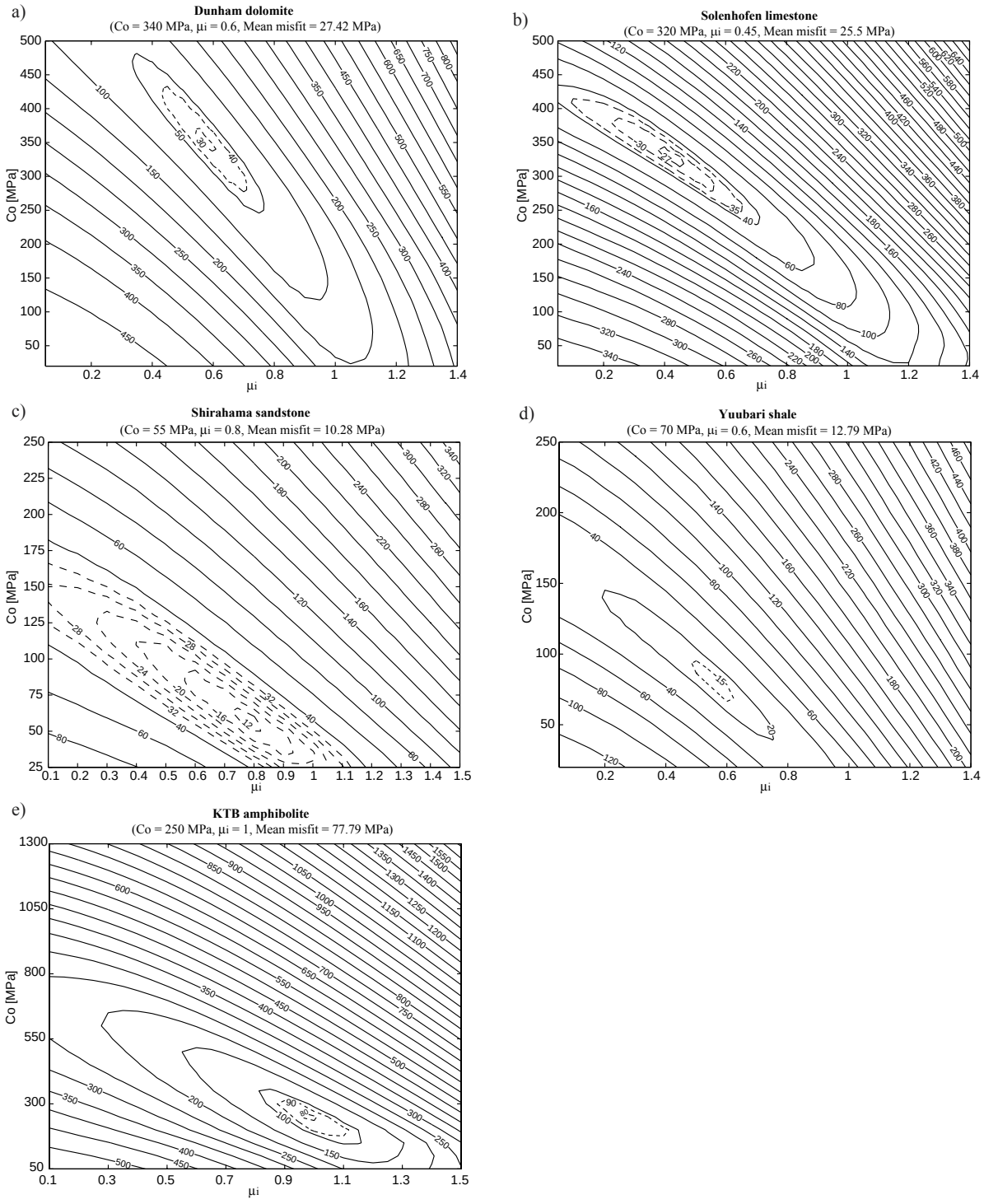

Figure 2.B.4: Misfit contours for the Modified Wiebols and Cook criterion. a) Dunham dolomite. b) Solenhofen limestone. c) Shirahama sandstone. d) Yuubari shale. e) KTB amphibolite.

Chapter 3.

Stress field and seismotectonics of northern South America

Colmenares, L. and M. D. Zoback, 2003, Stress field and seismotectonics of northern South America, Geology, v. 31, pp. 721-724.

3.1 ABSTRACT

I have integrated in situ stress, neotectonic, and Global Positioning System (GPS) data to investigate the complex interactions among the South American, Caribbean, and Nazca plates and the Costa Rica–Panama microplate and to examine different seismotectonic models that have been proposed for the region. The resulting data set was used to generate an integrated stress map of the region which shows that the stress field in northern South America varies systematically in both orientation and relative magnitude. In the southwestern part of the study area, the Ecuadorian Andes stress province exhibits strong E-W compression resulting from the subduction of the Nazca plate beneath the South American plate. In the North Andes stress province, the observed NW-SE compression may result from the convergence between the Caribbean and the South American plates and/or the negative buoyancy of the already-subducted Caribbean plate beneath northwestern South America. Possible convergence between the Costa Rica–Panama microplate with respect to northwestern South America may also be a source of compression in this region. In north and northeastern Venezuela, normal and strike-slip faulting with a NE-SW direction of extension characterizes the San Sebastian–El Pilar stress province.

3.2 INTRODUCTION

The present-day tectonics of northern South America is complex because four plates interact in the region—the South American, Caribbean, and Nazca plates and the Costa Rica–Panama microplate. The major tectonic features of the area are shown in Figure 3.1, which is a synthesis of the work by Taboada et al. (2000), Gonzalez de Juana et al. (1980), Pennington (1981), Robertson and Burke (1989), Dashwood and Abbotts (1990), Mann et al. (1990), Beltrán (1993), Perez et al. (1997a), ECOPETROL (1998), Gutscher et al. (1999) and Mann (1999). The most important fault systems, basins and cordilleras are also shown. Two of the most prominent tectonic features of the area are the North Andean block and the Maracaibo block. The N. Andean block corresponds to the block where the Andean ranges of Ecuador, Colombia, and Venezuela are located. It

is supposed to be moving toward the NE relative to the South American plate along a transpressive system of faults along the front of the Eastern Cordillera of Colombia (Pennington, 1981; Trenkamp et al., 2002). The Maracaibo block is a triangular-shaped block of continental crust bounded to the east by the Bocono fault and to the west by the Santa Marta–Bucaramanga fault (Mann et al., 1990). The goal of this study is to obtain a comprehensive understanding of the regional stress field and seismotectonics of northern South America.

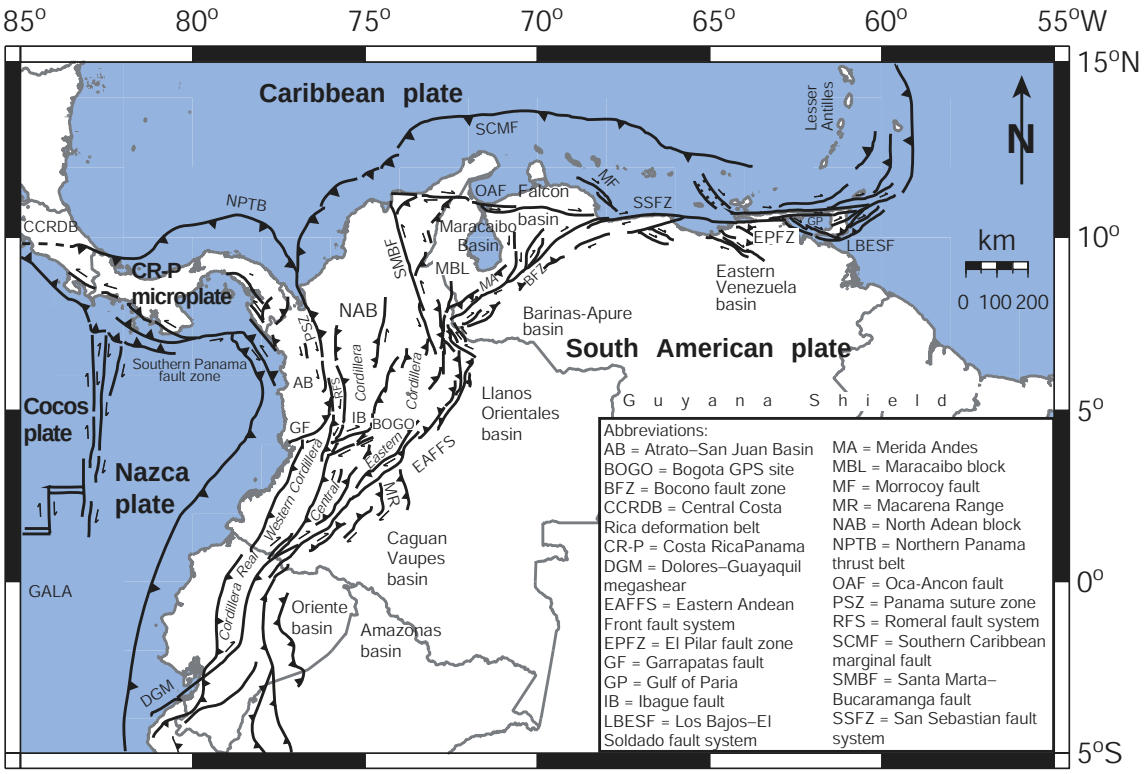

Figure 3.1: Major Tectonic features of northern South America.

3.3 SEISMOTECTONIC MODELS

In this section, five models that try to explain the tectonic setting in northern South America are summarized. Three models concentrate on northwestern South America and the other two models focus on northeastern Venezuela. Figures 3.2 and 3.3 show the models for comparison.

Pennington (1981) studied the intermediate-depth seismicity of northwestern South America and realized that the seismicity is clustered into three distinct zones, interpreted as representing segments of subducted lithosphere. Two of those segments – the Bucaramanga and the Cauca segments– will be described here. The Bucaramanga segment dips at 20° – 25° toward N109°E and is apparently continuous with the oceanic crust of the Caribbean seafloor northwest of Colombia and the zone of deformation in and near the Panamanian isthmus. This segment of oceanic lithosphere contains the Bucaramanga cluster of intermediate-depth earthquakes. Pennington considered the northern Andes to constitute a separate crustal block, or microplate, which is being compressed and underthrust from the east by the South American plate and from the west by the Nazca plate and is 'pinching out' to the NNE. Even though Pennington was able to identify the subduction of part of the Caribbean plate under the South American plate, the boundaries near the northern edge of the Andean block and the southern Caribbean were not resolved (Figure 3.2a). The Cauca segment is a piece of subducted lithosphere south of 5.2°N. This piece is apparently continuous with the oceanic crust underthrusting South America at the trench from the Panama-Colombia border (7°N) to 1.5°N. The segment is dipping at 35° toward N120°E, as seen in Figure 3.2a.

Perez et al. (1997a) presented seismological evidence for the existence of a slab dipping to the southeast beneath northwestern Venezuela. In their model, the subduction of the Caribbean seafloor beneath northwestern Venezuela terminates in the vicinity of a series of NW-trending faults, collectively termed the Morrocoy fault zone (MF in Figure 3.1). The southern end of the Morrocoy fault zone coincides with the northeastern end of the Bocono fault system and the western end of the E-W oriented, San Sebastian fault system along the Venezuelan coast. The authors did not specify where the Caribbean plate subducts beneath the South American plate, but they emphasized the major role of

the Bocono fault in the multibranched plate boundary between Caribbean and South American plates (Figure 3.2b).

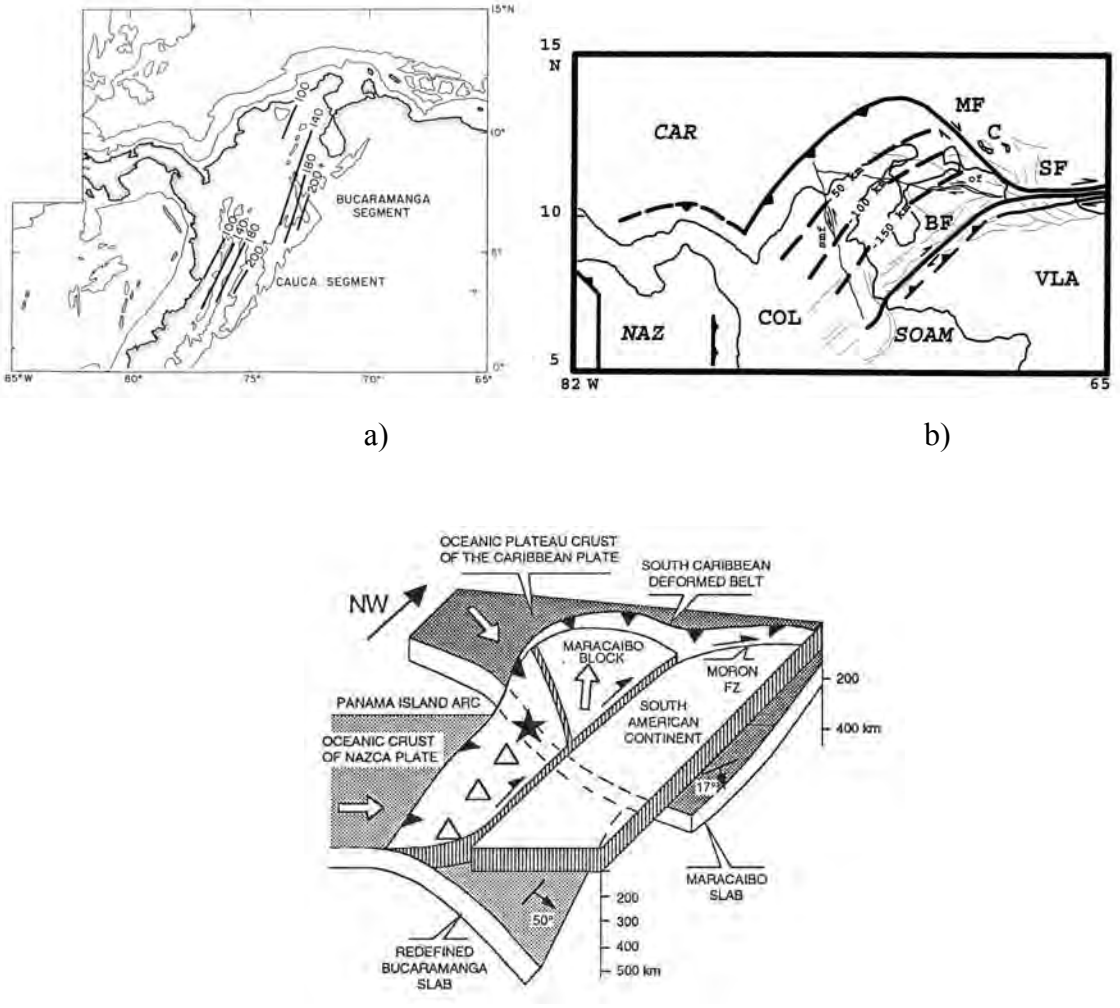

a) b)

c)

Figure 3.2: Three models of the subduction beneath northwestern South America. a) Pennington (1981), b) Perez et al. (1997a), and c) van der Hilst and Mann (1994). Contour lines represent contours to Benioff zones beneath South America in kilometers. See text for details.

Seismic tomography enabled van der Hilst and Mann (1994) to improve the mapping of the upper mantle's seismic structure southwest of the Caribbean plate and, in particular, to obtain additional information about Pennington's (1981) Bucaramanga slab. Two slabs were identified: a steep slab or what the authors called the "redefined

Bucaramanga slab" and a shallow-dipping slablike zone that they referred to as the Maracaibo slab. The tomographic images supported evidence that the South Caribbean deformed belt was the major boundary between the Caribbean and South American plates (Figure 3.2c).

The southeastern boundary of the Caribbean plate is as poorly identified as the southwestern one. Figure 3.3 shows two models for comparison.

Based on microseismicity and teleseismic data, Perez and Aggarwal (1981) interpreted underthrusting of the Atlantic seafloor to continue along the Lesser Antilles to the southeast of Trinidad. This subduction appears to terminate abruptly in the vicinity of the Los Bajos – El Soldado fault zone, which trends WNW – NW and is located in the Gulf of Paria west of Trinidad, joining up with the E-W right-lateral strike-slip El Pilar – Casanay fault system in northeastern Venezuela. It appears that the total slip in the Los Bajos – El Soldado fault zone is at least 22 km. This model predicts that hinge faulting should occur in the southeastern part of this fault zone as a result of vertical motion between the southwestern edge of the subducted slab and the South American continent, that is, between the subducted oceanic part and the unsubducted continental part of the South American plate. This model does not require strike slip motion along the presumed extension of the El Pilar fault into the Gulf of Paria and northern Trinidad (see Figure 3.3a).

Field work in the El Pilar fault zone of Trinidad and interpretation of offshore seismic data lead Robertson and Burke (1989) to conclude that the dominant tectonic process in the region was strike-slip motion on five or more major fault systems within a 250 km wide east-west-trending plate-boundary zone extending north to south from Grenada to the Urica fault zone. Westward, they extended the plate-boundary zone along the El Pilar and Coche fault zones into the Cariaco basin and then farther west along the San Sebastian fault and other offshore equivalents. East of Trinidad and Tobago, the east-trending strike-slip faults turn to the northeast. The arc terrane of Tobago and Margarita also swings to the northeast and terminates against the active Lesser Antilles arc complex. The major strike-slip faults near Trinidad swing northeast into a poorly understood area (Figure 3.3b).

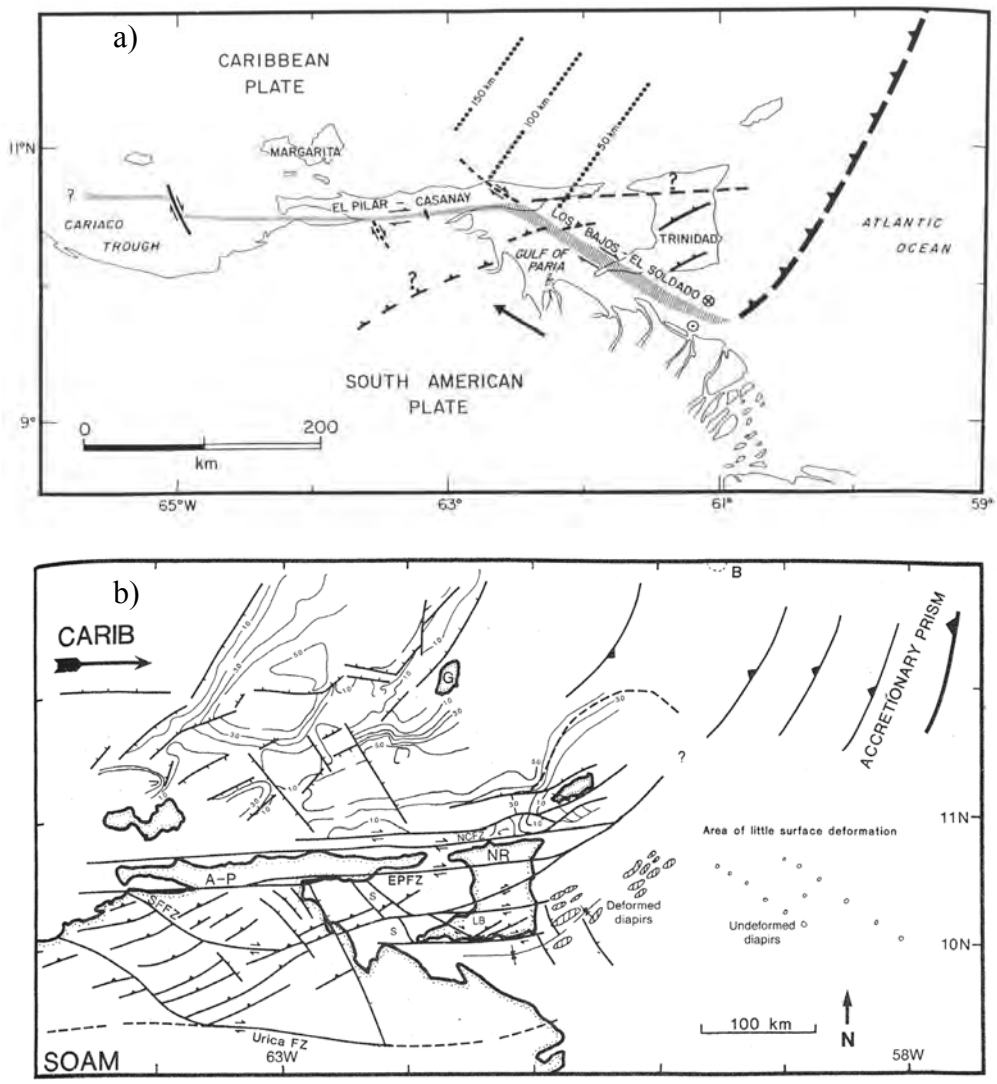

Figure 3.3: Two models of subduction beneath northeastern South America. a) Perez and Aggarwal (1981), b) Robertson and Burke (1989). See section text for details.

3.4 GPS FINDINGS AND TECTONICS

As expressed by DeMets et al. (2000), due to the complexity of the plate boundaries between the Caribbean plate and its surrounding plates, the Caribbean region was an early target of GPS geodesy. A very peculiar aspect of the Caribbean plate is that areas of positive relief, and consequently the GPS sites, are located at or very near plate boundaries, causing some of the sites to be influenced by local deformation.

The GPS geodetic studies of the Caribbean and northern South America have been carried on by different authors and therefore in different times and campaigns. Different GPS geodetic studies have indicated that the Caribbean plate is moving eastward at a rate of ~20mm/year. The studies have been made in specific sub-regions of the Caribbean and northern South America in order to investigate the interaction of the Caribbean plate with its neighboring plates. For example, Freymueller et al. (1993) and Kellog and Vega (1995), studied the southwestern part of the Caribbean plate and its interaction with Cocos, Nazca and the North Andes block; Dixon and Mao (1997) studied the interaction between the North America plate and the South American plate; Dixon et al (1998) studied the relative motion between the Caribbean plate and the North America plate as well as DeMets et al. (2000); Norabuena et al. (1999) published a paper about the decrease of the rate between the Nazca and South American plates and also between the Nazca and Pacific plates; Weber et al. (2001) and Perez et al. (2001) estimated the relative motion between the Caribbean and South American plates using almost the same GPS sites for their study, with the difference that Perez et al. studied more sites in Venezuelan territory. Kaniuth et al. (1998) published the results corresponding to the Venezuelan part of the CASA (Central America – South America) project. It is important to mention that this paper is the only publication presenting GPS results along the Bocono fault in Venezuela, however, their overall results differ in azimuth from previous studies and the methodology applied on analyzing the GPS data was different from that of previous researchers and the authors do not offer an explanation to account for this difference. Therefore, their results may not be reliable.

The main findings of the most recent GPS studies can be summarized as follows:

Kellog and Vega (1995). The GPS geodetic data from the CASA (Central America – South America) project, suggested the existence of a rigid Panama-Costa Rica microplate that is moving northward relative to the stable Caribbean plate and continuing to collide eastward with the northern Andes. The northern Andes are moving northeast relative to stable South America. Preliminary GPS results also suggest a Caribbean-North Andean convergence, with most of the deformation occurring in the South Caribbean deformed belt.

Weber et al. (2001) predicted that the Caribbean plate moves 20±3mm/year in a direction 86±2°. Data from two campaign GPS sites in Trinidad suggested that the Central Range fault currently accommodates most Caribbean-South American plate motion in Trinidad and that the plate boundary zone may be narrower than previously thought. Their angular-velocity vector predicts motion towards 90±2° along the seismically active east-striking El Pilar fault in Venezuela and pure dextral motion. In contrast, they inferred that transpression is active in Trinidad, where the active Central Range fault (average strike of 68°) is highly oblique to plate motion.

According to Perez et al. (2001), the Caribbean plate, along its southern boundary, slips at a rate of 20.5±2 mm/year with an azimuth of N84±2°E at 65°W, relative to the South-America plate. East of 68°W, the velocity field across the Caribbean/South American plate boundary is confined to a narrow shear zone and 80% of the surface deformation is contained within an 80-km-wide zone centered a few kilometers north of the El Pilar fault. The absence of significant motion at sites CRCS (Caracas) and CASI (San Casimiro) relative to CANO (La Canoa, a monolithic granite batholith in the Guayana Shield in Venezuela) indicates that the main locus of deformation is offshore. The details of the velocity field of the plate-boundary's westward widening are still unresolved.

Trenkamp et al (2002) found that the Caribbean plate is moving eastward at a rate of ~20 mm/yr with respect to South America. However, oblique E–SE convergence of 20 ± 2 mm/yr is occurring between the Caribbean island of San Andres and stable South America. Thus, the GPS data confirm the convergence between the Caribbean plate and northwestern South America, as proposed by several seismotectonic models (Pennington, 1981; van der Hilst and Mann, 1994; Perez et al., 1997a). Collision also appears to occur between the Costa Rica–Panama microplate and the N. Andean block, as the Costa Rica–Panama microplate is moving eastward, with respect to South America, ~10–22 mm/yr faster than the N. Andean block, which is moving northeastward with respect to South America along the Bocono–East Andes–Dolores Guayaquil megashear. Finally, the Nazca plate is moving eastward with respect to stable South America at a rate of 60 mm/yr.

Figure 3.4 summarizes the GPS data used in this study by showing velocity vectors from the three most recent GPS studies (Perez et al., 2001; Weber et al., 2001; Trenkamp et al., 2002), relative to stable South America. Altogether, these GPS data help define the relative motions among the four plates in the region.

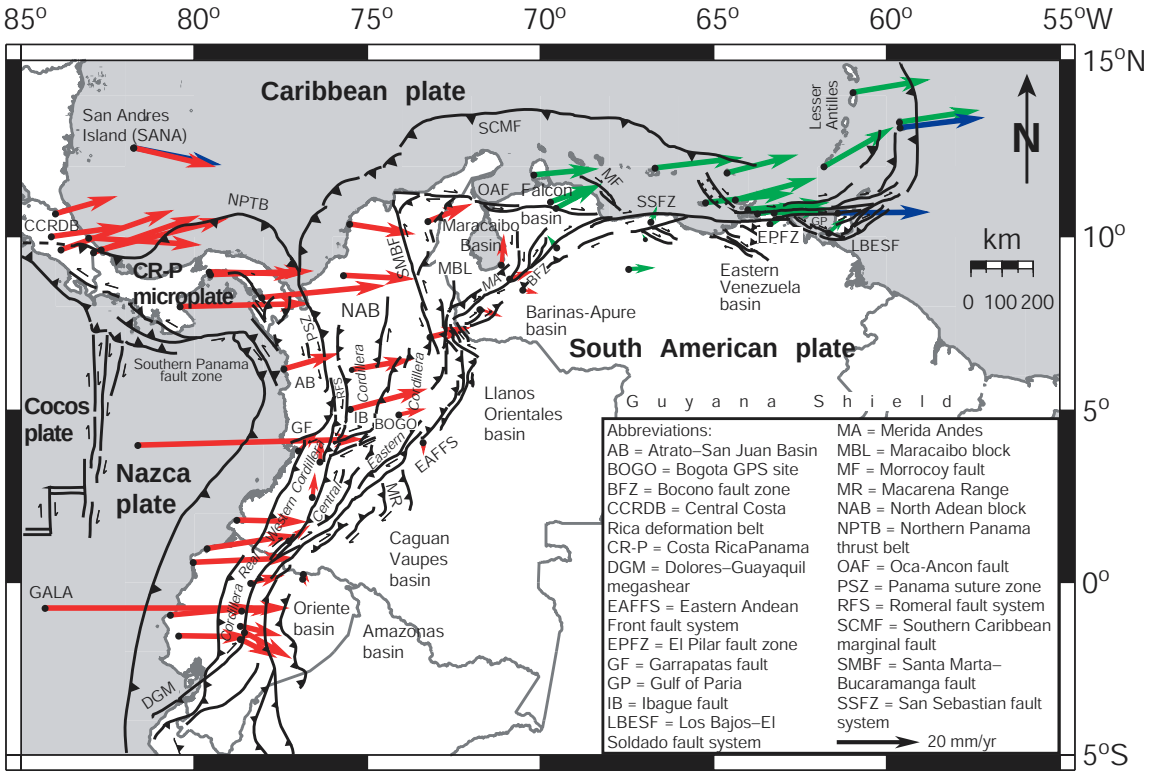

Figure 3.4: Major tectonic features of northern South America and GPS velocity vectors from different studies. All vectors denote velocities with respect to South America, and colors denote different studies. Location of Galápagos Island vector (GALA) has been shifted toward the east just so it can be shown in the study area (original location is at 90.3°W, 0.74°S).

3.5 REGIONAL STRESS

To clarify the state of stress in this region, the World Stress Map (WSM) database (Mueller et al., 2000) was carefully reviewed and edited and focal-plane mechanisms from well-defined plate boundaries were removed, as such events are not indicative of intraplate stresses (see Appendix 3.A for details). Overall, 116 of the 237 data points (quality A–C) in the region of interest were removed.

To supplement the WSM database, a thorough search for reliable focal mechanisms (FM's) in the region was done (Pennington, 1981; Kellogg and Bonini, 1982; Audemard and Romero, 1993; Garciacaro, 1997; Malavé, 1997; Perez et al., 1997a, b; Choy et al., 2000; Harvard CMT catalog 1976–present). Previous seismicity and focal mechanism studies of the tectonics of northern South America have suffered from a scarcity of data. The lack of national networks in the past has made it difficult to obtain focal mechanisms in the area. However, this issue is being gradually resolved and there is increasing availability of regional and teleseismic data. An exhaustive search of focal mechanisms in the literature has been done and at this point the available data allow a good coverage of the study area. FM's with magnitudes larger than 3 and with a maximum depth of 40 km were considered to assure that they reflect only crustal deformation. Eighty four data points were added to the original database.

Several microtectonic studies have been carried out in Venezuela and Colombia. Inversions of fault-striae sets are available from the Falcon basin (Audemard, 2001), eastern Venezuela (Beltrán and Giraldo, 1989), the Eastern Cordillera of Colombia and Bucaramanga (Taboada et al., 2000). Only the stress estimates obtained from Quaternary structures were selected. Six data points of quality A were added.

Observations of wellbore breakouts were used to further constrain the stress field in the study region. Stress-induced wellbore breakouts may form due to compressive wellbore failure that occurs within the region of maximum compressive stress around a wellbore. In a vertical well, the zone of compressive failure is centered at the azimuth of minimum horizontal far-field compression, because the compressive circumferential stress is greatest at this azimuth. This means that breakouts, when identified properly, provide a reliable means of determining the direction of the maximum horizontal stress (S_{Hmax}), as they systematically occur in the direction perpendicular to S_{Hmax} (Zoback and Zoback, 1991). Breakouts can best be identified with acoustic televiewer data (CBIL, UBI, etc.) (Zoback et al., 1985). Electrical imaging data (FMI, STAR, etc.) can also be used if the breakouts are well developed and if the image quality is good (Shamir et al., 1988). Image logs from 16 wells in the Barinas and Maturin basins in Venezuela (Figure 3.5) were analyzed. In addition, orientations of S_{Hmax} were incorporated from breakout

studies by Sanchez et al. (1999) in the Mara Oeste oil field, Venezuela, and by Willson et al. (1999) in the Cusiana oil field, Colombia, and the Pedernales oil field, Venezuela.

The evaluation of all these stress indicators and quality ranking was made according to Zoback and Zoback (1991). Altogether, a total of 97 well-constrained stress indicators were added from all the sources described (see Appendix 3.B for details).

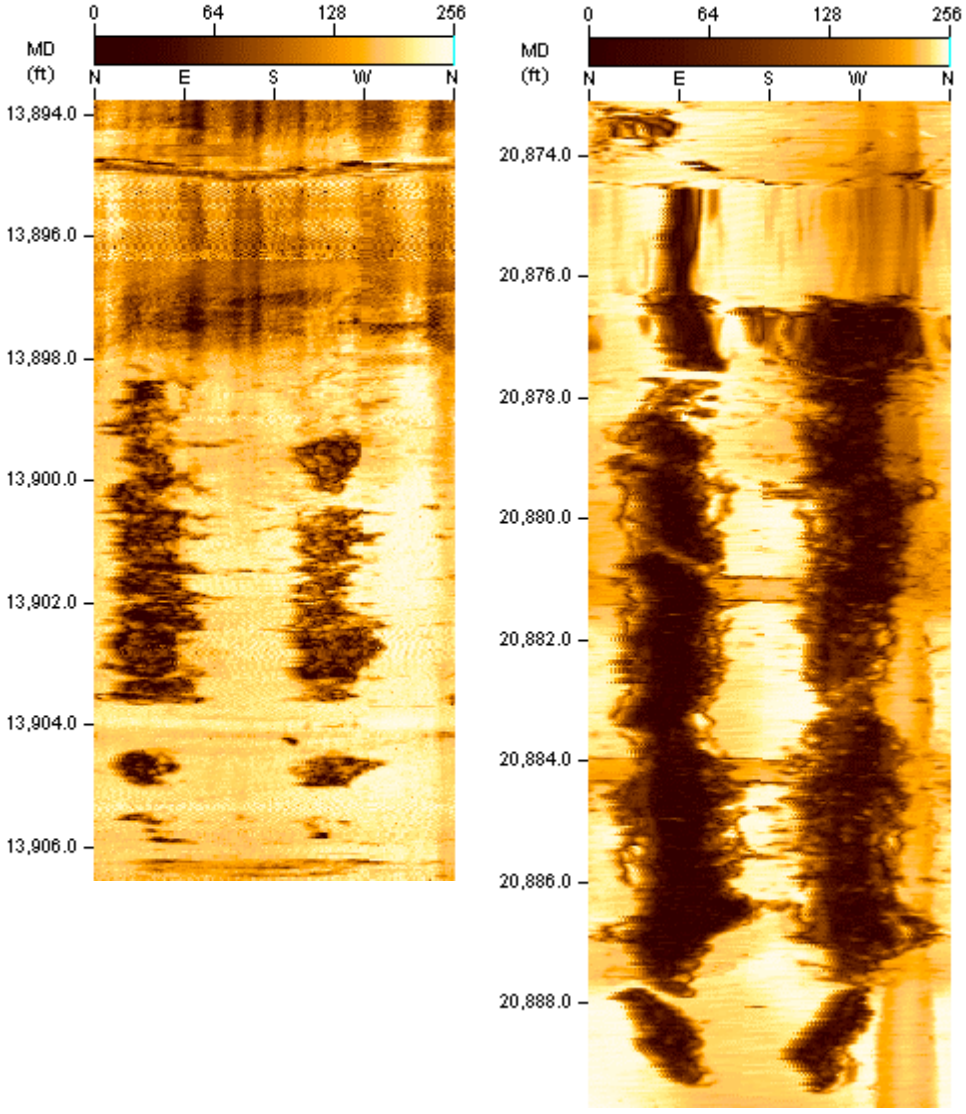

Figure 3.5: Image logs from two of the wells analyzed for this study. They both show the occurrence of breakouts and the direction of S_{Hmax} is a) 143° and b) 170°.

Table 3.1. Image logs used in this study that were obtained in Venezuela.

Location	Type of image log	# of logs obtained
Barinas basin	UBI	3
	CBIL	3
Maturin basin	UBI	7
	CBIL	3

3.6 DEFINITION OF STRESS PROVINCES

Figure 3.6 shows the integrated stress map of northern South America and includes all of the data described previously (see Appendix 3.C for the evolution of the stress map for this region over the last 7 years). In addition, Figure 3.6 also incorporates the major tectonic features of the area, which were synthesized from the work by Taboada et al. (2000), Gonzalez de Juana et al. (1980), Pennington (1981), Robertson and Burke (1989), Dashwood and Abbotts (1990), Mann et al. (1990), Beltrán (1993), Perez et al. (1997a), ECOPETROL (1998), Gutscher et al. (1999) and Mann (1999).The data are concentrated in the region corresponding to the N. Andean block, the Costa Rica–Panama microplate, and northeastern Venezuela. No data are available in the southern part of Venezuela or east of the Eastern Andean Front fault system in Colombia and Ecuador. These areas are a tectonically stable cratonic crust (i.e., the Guyana Shield) that is not undergoing deformation. The deformation in northern South America is for the most part taken up by the N. Andean block, suggesting that the interaction among the different plates of the region does not occur on discrete fault zones but throughout a broad deformation area, as suggested by several authors (e.g. Jordan, 1975; Trenkamp et al., 2002). Three stress provinces —areas of relatively uniform stress orientation and magnitude (Zoback and Zoback, 1980)— were defined in order to discuss variations of the stress field throughout the region: the Ecuadorian Andes, North Andes, and San Sebastian–El Pilar stress provinces (Figure 3.7).

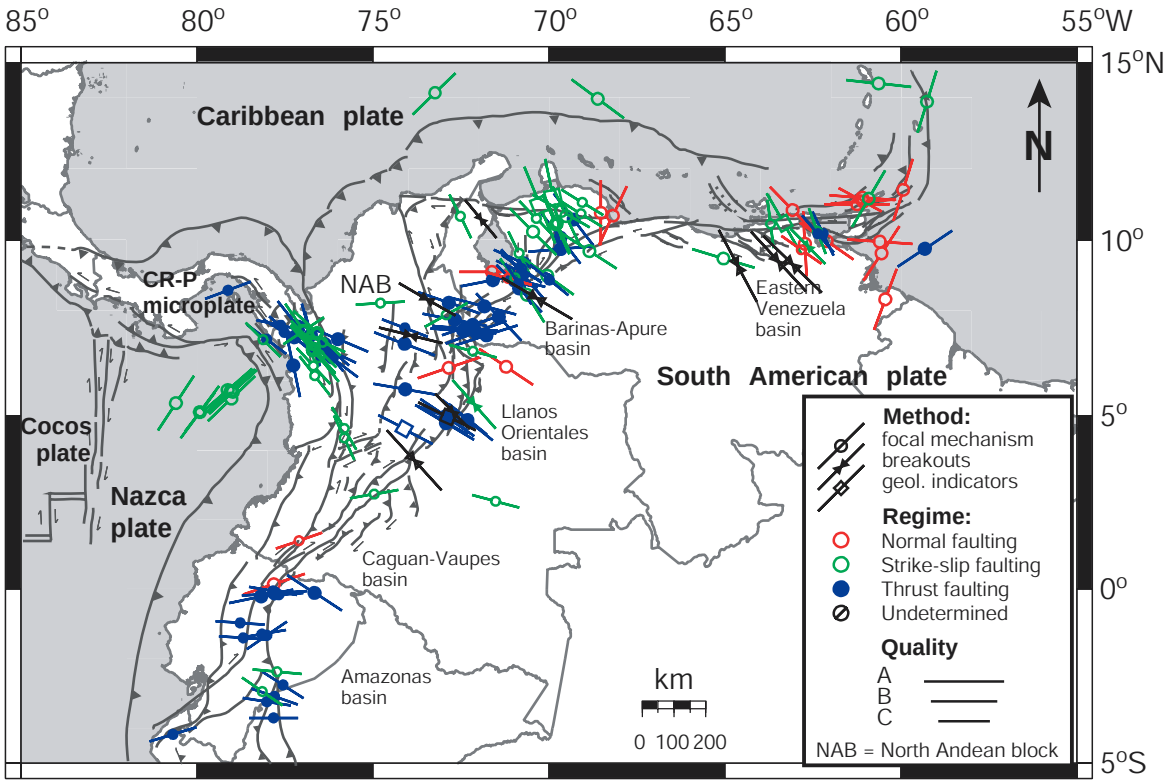

Figure 3.6: Integrated stress map of northern South America, showing observed directions of maximum horizontal compression in the crust. Symbol associated with each data point indicates type of stress indicator, and color indicates tectonic regime. Length of bars attached to each data point is a measure of its quality.

The Ecuadorian Andes stress province includes the Ecuadorian Andes and the southern part of the Colombian Andes up to the boundary between the Caguán-Vaupés basin and the Llanos Orientales basin east of the Eastern Cordillera of Colombia. The stress direction in this province shows maximum compression trending approximately E-W. The stress field is quite compressional as the majority of earthquakes are characterized by thrust faulting (with some strike-slip faulting). Two normal faulting earthquakes are thought to be associated with the high topography of the Andes (Zoback, 1992).

The North Andes stress province incorporates most of northwestern South America, covering the Atrato–San Juan basin, the Colombian Andes, and the Maracaibo block (Figure 3.4). Toward the Atrato–San Juan basin, the stress direction trends NW, and the focal mechanisms reveal both thrust and strike-slip faulting. The majority of the earthquakes occur in the northernmost part of the basin. Breakout data in this region also

exhibit a general NW trend of the S_{Hmax} axis. Willson et al. (1999) show that the Cusiana oil field is characterized by a strike-slip faulting stress state. In the northeasternmost part of the province, geologic indicators exhibit NNW-SSE compression, and the stress state is mainly strike-slip. Overall, there appear to be both a modest rotation of stress orientation and a decrease of relative stress magnitude from the southwest to northeast parts of this stress province.

The San Sebastian–El Pilar province includes the San Sebastian and the El Pilar fault systems and part of the Eastern Venezuela basin. Most of the earthquakes in the area result from strike-slip faulting and are considered to be part of the plate boundary between the Caribbean and South American plates. The events that directly occurred on either the San Sebastian, the El Pilar, or any other major, right-lateral strike-slip subsidiary faults were not included in the stress map but are kinematically consistent with the stress orientations inferred from the different stress indicators in the province. Geologic indicators in eastern Venezuela show NW-SE compression, and FM's from earthquakes due to strike-slip and normal faulting indicate this same compression direction. Willson et al. (1999) found that the stress state in the Pedernales oil field is strike-slip, which is consistent with slickensides analyzed by Beltrán and Giraldo (1989).

3.7 DISCUSSION AND CONCLUSIONS

As seen in Figure 3.7, the highly compressive stress field and E-W S_{Hmax} direction observed in the Ecuadorian Andes province clearly reflects the convergence of the Nazca and the South American plates. What is perhaps more interesting in Figure 3.7 is the clock-wise rotation of the S_{Hmax} direction of maximum horizontal compression observed going northward and eastward around northwestern South America, and the associated decrease in the relative magnitude of the principal stresses. In other words, in the North Andes stress province, the compression direction is generally NW-SE, and characterized by a transition from reverse to strike-slip faulting from south to north. In the San Sebastian-El Pilar stress province a still less compressive (normal-strike-slip faulting stress regime) is observed with a NW-SE oriented direction of maximum horizontal compression.

Near the Panama suture zone (Figure 3.4), the direction of compression may be influenced by the ongoing collision of the Costa Rica–Panama microplate with the N. Andean block. In Figure 3.8, the open arrow shows the direction of relative motion between the Costa Rica–Panama microplate and the N. Andean block (with respect to the reference station BOGO), as found by Trenkamp et al. (2002). However, the relative motion between the Caribbean and South American plates do not appear to be the reason for the rotation of the regional stress field in the areas further to the north and east in the North Andes stress province. As shown in Figure 3.4, the GPS data indicate that the convergence between the Caribbean plate (as indicated by the station SANA) and northwestern South America is E-SE.

Another possible origin of the stress rotation is the existence of the already subducted slab of the Caribbean plate. The shape of this slab can be determined from the depths of earthquakes as obtained from the National Earthquake Information Center (NEIC, 1973 to 2002) (Figure 3.8). The colored dots and dashed contour lines indicate the depths of the earthquakes. Note that the shape of the slab "wraps around" northwestern South America (for further information refer to Appendix 3.D). Furthermore, the maximum compression stress direction is parallel to the dip direction of the slab at depth and rotates as the slab changes orientation. This suggests that the clockwise rotation of the direction of maximum compression may result from the negative buoyancy of the already-subducted Caribbean plate beneath northwestern South America (Fleitout and Froidevaux, 1982; Turcotte and Schubert, 2002). It is worth noting that the change in the slab's dip direction in the Bucaramanga swarm area (BS in Figure 3.8) coincides with the step between the Eastern Andean front fault system and the Bocono fault zone (Figure 3.4).

In the vicinity of the Bucaramanga swarm (Figure 3.8), in the central part of the North Andes stress province, the top of the slab seems to reach ~100 km depth, continues almost horizontally for ~50 km and then resumes descending until it reaches a depth of ~200 km. The dip of the slab in the area just north of the Bucaramanga swarm is ~22° toward ~N100°E, which is also the direction of maximum compression in the area. Pennington (1981) identified a slab he called the Bucaramanga slab with a dip of 20°–25° toward N109°E; this slab is apparently continuous with the oceanic crust of the

Caribbean seafloor northwest of Colombia and the zone of deformation in and near the Panamanian isthmus. Toward the north of the Bucaramanga swarm, in an area ~200 km long (N-S), a well-defined Wadati-Benioff zone extending to 175 km depth has been identified. The dip of the slab is ~22° and its dip direction is ~N130°E, which is the same direction of maximum compression in the area. Moving northward, the dip direction of the slab rotates clockwise by ~15° as does the direction of maximum compression. Toward the Falcon basin in Venezuela, the slab as defined by seismicity reaches depths of 60–75 km. On the basis of tomographic data, van der Hilst and Mann (1994) observed a slab extending to 300 km. According to them, the Maracaibo slab is present in this area dipping 17° and its dip direction is N150°E, which is the same direction of maximum compression observed in the Falcon basin

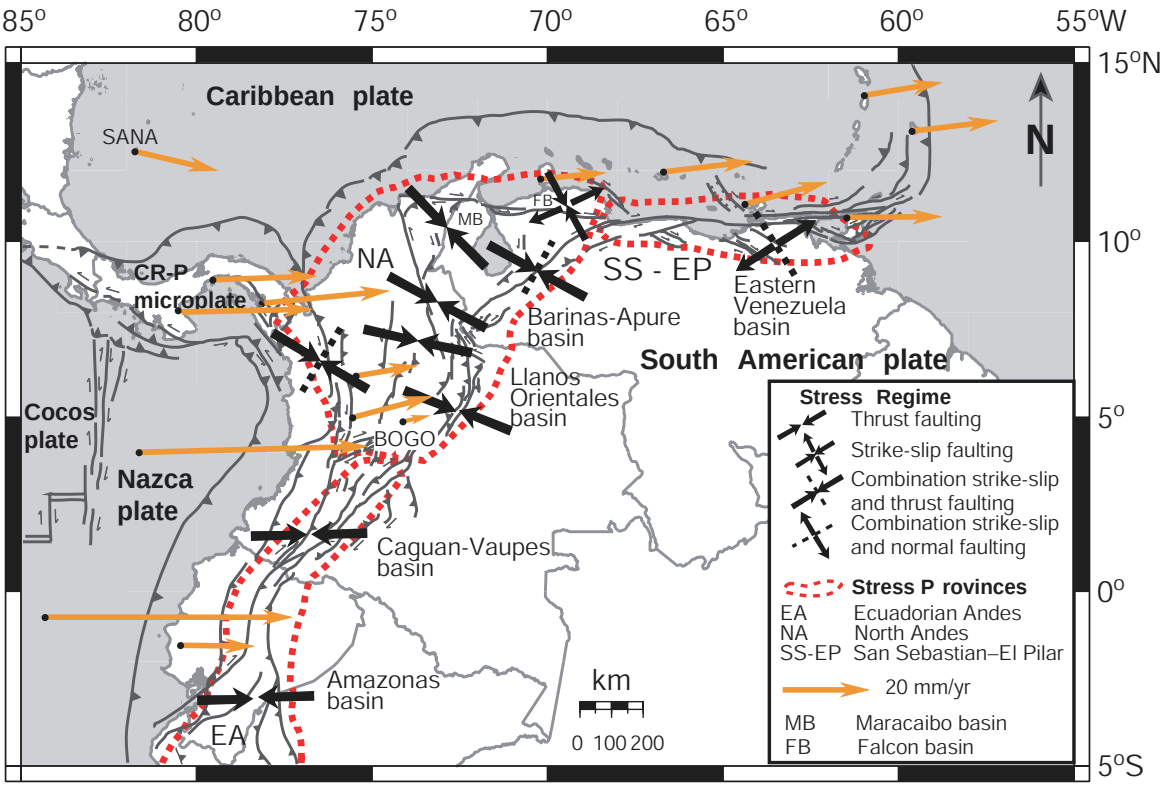

Figure 3.7: Generalized tectonic map of northern South America. Stress provinces are discussed in text.

It is noteworthy that fault-normal compression is observed along the right-lateral strike-slip Eastern Andean Front fault and the Bocono fault (this study; Giraldo, 1990). While these strike-slip fault systems principally accommodate the escape of the N. Andean block to the northeast, these faults have numerous sub-parallel thrust faults and fold axes along them. This situation is similar to what is observed along the San Andreas Fault in California (Zoback et al., 1987; Mount and Suppe, 1987) and may imply that these faults may also be low friction faults.

In summary, the stress field in northern South America varies systematically in both orientation and relative magnitude. It is most compressive in the Ecuadorian Andes province where the direction of maximum compression is approximately E-W, less compressive in the North Andes province with maximum compression approximately NW-SE, and least compressive in the San Sebastian–El Pilar province that shows a NE-SW direction of extension. This systematic change in the stress field appears to reflect both relative plate motions and the negative buoyancy of the subducted Caribbean slab. For further applications of this study see Appendix 3.E.

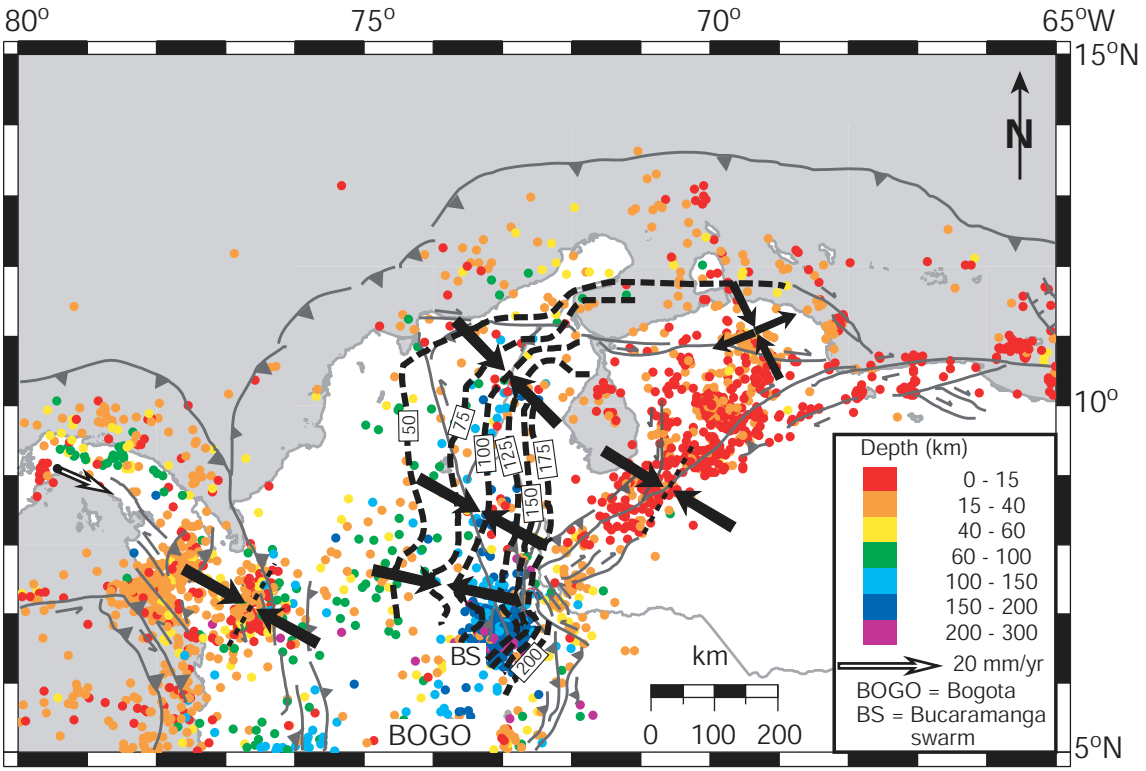

Figure 3.8: Map showing depth of regional seismicity. Contour lines are to top surface of inclined seismic zone in northwestern South America, and generalized stress directions are also shown (symbols as in Figure 3.7).

ACKNOWLEDGEMENTS

I thank the people in the Research and Technological Support Center of Petróleos de Venezuela (INTEVEP), a branch of the Venezuelan national oil company (PDVSA), who showed great interest in this research and kindly provided the image logs used in this study. I want to thank especially Eduardo Celis who was the motor to get this project going in INTEVEP. Thanks also to Marisela Sanchez and José Ramón Cabrera for their great and invaluable support during my visit to INTEVEP in 2001. I also thank the reviewers Alan Levander and Karl Fuchs for their valuable comments. The Generic Mapping Tool (GMT) was used to make the maps for this project. The Stanford Rock Physics and Borehole Geophysics Project (SRB) supported this study.

REFERENCES

Audemard, F., 2001, Quaternary tectonics and present stress tensor of the inverted northern Falcon basin, northwestern Venezuela: Journal of Structural Geology, v. 23, p. 431–453.

Audemard, F., and Romero, G., 1993, The Churuguara area—seismic evidence of contemporary activity of the Oca-Ancon system, *in* Proceedings of the Caribbean Conference on Natural Hazards: Volcanoes, Earthquakes, Windstorms, Floods, St. Augustine: Trinidad and Tobago, University of the West Indies, p. 21–32.

Beltrán, C., 1993, Mapa neotectónico de Venezuela: Funvisis, scale 1:2,000,000, 1 sheet.

Beltrán, C., and Giraldo, C., 1989, Neotectonic aspects of northeastern Venezuela, *in* VII Congreso Geológico Venezolano: Barquisimeto, Sociedad Venezolana de Geólogos, p. 1000–1010.

Choy, J., Palme, C., and Morandi, M., 2000, Observations about the tectonic stress state in the north of the Andes Merideños, Venezuela *in* Memorias del X Congreso Venezolano de Geofisica: Caracas, CD-ROM.

Dashwood, M., and Abbotts, I., 1990, Aspects of the petroleum geology of the Oriente basin, Ecuador, *in* Brooks, J., ed., Classic petroleum provinces: Geological Society [London] Special Publication 50, p. 89–117.

ECOPETROL (Empresa Colombiana de Petroleos), 1998, Opportunities for hydrocarbon exploration and production in Colombia: Santafe de Bogotá, D'Vinni Editorial, p. 13 and 34.

Fleitout, L., and Froidevaux, C., 1982, Tectonics and topography for a lithosphere containing density heterogeneities: Tectonics, v. 2, p. 315–324.

Garciacaro, E., 1997, Microseismicity, tectonics and seismic potential of the Bocono fault system [undergraduate thesis]: Caracas, Venezuela, Universidad Simón Bolivar, p. 27.

Giraldo, C., 1990, Determinación del campo actual de esfuerzos en la región Caribe a partir de datos sismológicos y neotectónicos: Caracas, Memorias del V Congreso Venezolano de Geofísica.

Gonzalez de Juana, C., Iturralde, J., and Picard, X., 1980, Geologia de Venezuela y de sus cuencas petrolifers: Caracas, Ediciones Foninves, v. 2, 1031 p.

Gutscher, M., Malavieille, J., Lallemand, S., and Collot, J., 1999, Tectonic segmentation of the North Andean margin: Impact of the Carnegie Ridge collision, Earth and Planetary Science Letters, v. 168, p. 255–270.

Harvard Seismology – Centroid Moment Tensor (CMT) catalog, 1977 to present, http://www.seismology.harvard.edu/CMTsearch.html (July 2002)

Jordan, T., 1975, The present-day motions of the Caribbean plate: Journal of Geophysical Research, v. 80, p. 4432–4439.

Kellogg, J., and Bonini, W., 1982, Subduction of the Caribbean plate and basement uplifts in the overriding South American plate: Tectonics, v. 1, p. 251–276.

Malavé, G., 1997, Seismicity of western Venezuela [Ph.D. thesis]: Mexico City, Universidad Nacional Autónoma de México, p. 108–109.

Mann, P., 1999, Caribbean sedimentary basins: Classification and tectonic setting from Jurassic to present, *in* Mann, P., ed., Caribbean basins: Amsterdam, Elsevier, p. 3–31.

Mann, P., Schubert, C., and Burke, K., 1990, Review of Caribbean neotectonics, *in* Dengo, G., and Case, J.E., eds., The Caribbean region: Boulder, Colorado, Geological Society of America, Geology of North America, v. H, p. 307–338.

Mount, V.S., and Suppe, J., 1987, State of stress near the San Andreas fault: Implications for wrench tectonics: Geology, v. 15, p. 1143–1146.

Mueller, B., Reinecker, J., Heidbach, O., and Fuchs, K., 2000, The 2000 release of the World Stress Map (available online at www.world-stress-map.org).

NEIC (National Earthquake Information Center), 1973 to present, http://neic.usgs.gov/neis/epic/epic.html (July 2002)

Pennington, W., 1981, Subduction of the Eastern Panama basin and seismotectonics of northwestern South America: Journal of Geophysical Research, v. 86, p. 10,753–10,770.

Perez, O., and Aggarwal, Y., 1981, Present-day tectonics of the southeastern Caribbean and northeastern Venezuela: Journal of Geophysical Research, v. 86, p. 10,791–10,804.

Perez, O., Jaimes, M., and Garciacaro, E., 1997a, Microseismicity evidence for subduction of the Caribbean plate beneath the South American plate in northwestern Venezuela: Journal of Geophysical Research, v. 102, p. 17,875–17,882.

Perez, O., Sanz, C., and Lagos, G., 1997b, Microseismicity, tectonics and seismic potential in southern Caribbean and northern Venezuela: Journal of Seismology, v. 1, p. 15–28.

Perez, O., Bilham, R., Bendick, R., Velandia, J., Hernandez, N., Moncayo, C., Hoyer, M., and Kozuch, M., 2001, Velocity field across the southern Caribbean plate boundary and estimates of Caribbean/South American plate motion using GPS geodesy 1994–2000: Geophysical Research Letters, v. 28, p. 2987–2990.

Robertson, P., and Burke, K., 1989, Evolution of southern Caribbean plate boundary, vicinity of Trinidad and Tobago: American Association of Petroleum Geologists Bulletin, v. 73, p. 490–509.

Russo, R.M., Speed, R.C., Okal, E.A., Shepherd, J.B. and Rowley, K.C., 1993, Seismicity and tectonics of the Southeastern Caribbean: Journal of Geophysical Research, v. 98, p. 14229-14319.

Sanchez, M., Vasquez, A., Van Alstine, D., Butterworth, J., Garcia, J., Carmona, R., Poquioma, W., and Ramones, M., 1999, SPE 54008 Applications of geomechanics in the development of the naturally fractured carbonates of the Mara Oeste field, Venezuela *in* 1999 SPE Latin American and Caribbean Petroleum Engineering Conference: Caracas, CD-ROM.

Taboada, A., Rivera, L., Fuenzalida, A., Cisternas, A., Philip, H., Bijwaard, H., Olaya, J., and Rivera, C., 2000, Geodynamics of the northern Andes: Subductions and intracontinental deformation (Colombia): Tectonics, v. 19, p. 787–813.

Trenkamp, R., Kellogg, J., Freymueller, J., and Mora, H., 2002, Wide plate margin deformation, southern Central America and northwestern South America, CASA GPS observations: Journal of South American Earth Sciences, v. 15, p. 157–171.

Turcotte, D., and Schubert, G., 2002, Geodynamics (2nd edition): New York, Cambridge University Press, 456 p.

van der Hilst, R., and Mann, P., 1994, Tectonic implications of tomographic images of subducted lithosphere beneath northwestern South America: Geology, v. 22, p. 451–454.

Weber, J., Dixon, T., DeMets, C., Ambeh, W., Jansma, P., Mattioli, G., Saleh, J., Sella, G., Bilam, R., and Perez, O., 2001, GPS estimate of relative motion between the Caribbean and South American plates, and geologic implications for Trinidad and Venezuela: Geology, v. 29, p. 75–78.

Wessel, P., and W. H. F. Smith, New version of the Generic Mapping Tools released, EOS Trans. Amer. Geophys. U., vol. 76, pp. 329, 1995.

Willson, S., Last, N., Zoback, M., and Moos, D., 1999, SPE 53940 drilling in South America: A wellbore stability approach for complex geologic conditions *in* 1999 SPE Latin American and Caribbean Petroleum Engineering Conference: Caracas, CD-ROM.

Zoback, M.L., 1992, First- and second-order patterns of stress in the lithosphere: The World Stress Map Project: Journal of Geophysical Research, v. 97, p. 11703–11728.

Zoback, M.L., and Zoback, M.D., 1980, State of stress of the conterminous United States: Journal of Geophysical Research, v. 85, p. 6113–6156.

Zoback, M.D., and Zoback, M.L., 1991, Tectonic stress field of North America and relative plate motions, *in* Slemmons, D.B. et al., eds., Neotectonics of North America: Boulder, Colorado, Geological Society of America, Decade Map, v. 1, p. 339–366.

Zoback, M.D., Zoback, M.L., Mount, V., Suppe, J., Eaton, J., Healy, J., Oppenheimer, D., Reasenberg, P., Jones, L., Raleigh, C., Wong, I., Scotti, O., and Wentworth, C., 1987, New evidence on the state of stress of the San Andreas fault system: Science, v. 238, p. 1105–1111.

APPENDIX 3.A. QUALITY CONTROL OF WSM DATABASE

As mentioned earlier, all plate boundary earthquake focal mechanisms were removed. In addition, I also took a look at the following inconsistencies in the database:

1. Two normal events at the Boca del Tocuyo, Venezuela. According to Perez et al (1997a), these are normal events with a strike-slip component and they are already reported in the WSM database, that is, these events are reported twice.

2. The event from 19th May of 1970 has been given several solutions and the widely accepted one is given by Dewey (1972) (S_{Hmax} azimuth = 302°) and not by Kafka and Weidner (1981) (S_{Hmax} azimuth = 58°) which is precisely the one plotted by the WSM.

3. Two possible focal mechanism solutions have been proposed for the main event of the 1986 Churuguara seismic sequence: thrust and strike-slip. According to Audemard and Romero (1993) the thrust fault solution does not fit the regional tectonic setting so they calculated two well-constrained focal mechanisms for the main event and its aftershocks and obtained two strike-slip composite focal mechanisms. The solution that is reported in the WSM database is the thrust fault one.

4. Two breakouts in the Llanos Basin (COL10 and COL11 in the WSM database), Colombia, reported by Castillo and Mojica (1990). These data points are reported as average breakout orientations from the lower and upper parts of the Guayuriba-2 well respectively. However, they should be eliminated from the database because they represent keyseats instead of breakouts, as can be deduced from their paper.

Table 3.A.1. Data from the WSM database that was revised

#	ISO	Lat	Long	Azi	Type	Regime	Depth [km]	Comments
1	VEN27, VEN45	11.1	-68.18	179	FMS	SS, NF	15	Boca del Tocuyo events
1	VEN28, VEN47	11.14	-68.2	169	FMS	SS, NF	15	Boca del Tocuyo events
2	VEN3	10.99	-68.92	68	FMS	SS	6	Event of May 19th, 1970
3	VEN22	10.84	-69.24	143	FMS	TF	15	Churuguara event
4	COL10	3.18	-73.41	115	BOC	U	2.2	Guayuriba keyseats
4	COL11	3.18	-73.41	176	BOC	U	1.3	Guayuriba keyseats

APPENDIX 3.B. DATA SUBMITTED TO THE WSM DATABASE

Table 3.B.1 (this and next 5 pages): Focal mechanism data. 84 data points were submitted to the WSM Database.

#	Site	Lat	Long	Azi.	Type	h	Q	Reg.	Locality	Date	Met.	S1Az	S1Pl	S2Az	S2Pl	S3Az	S3Pl	References
1	VEN	10.7	-67	134	FMC	15	B	SS	Central coast of Venezuela	1985, 87, 94	FM	134						Perez et al., 1997b
2	VEN	10.8	-65.5	124	FMC	15	B	SS	Central coast of Venezuela	1990	FM	124						Perez et al., 1997b
3	VEN	9.9	-68.7	123	FMC	15	B	SS	Yaracuy State	1985, 87, 90	FM	123						Perez et al., 1997b
4	VEN	10.2	-67.9	44	FMC	15	B	SS	Carabobo State	1995	FM	44						Perez et al., 1997b
5	VEN	10.2	-67.9	109	FMC	15	B	SS	Carabobo State	33116	FM	109						Perez et al., 1997b
6	VEN	10.2	-67	7	FMC	15	B	SS	Aragua State	1986	FM	7						Perez et al., 1997b
7	VEN	8.4	-70.9	148	FMC	20	B	SS	Merida State	1984	FM	148						Perez et al., 1997a
8	VEN	9.2	-69.9	126	FMC	20	B	SS	Trujillo State	1986	FM	126						Perez et al., 1997a
9	VEN	9.9	-69.5	94	FMC	20	B	SS	Lara State	1986	FM	94						Perez et al., 1997a
10	VEN	10.3	-69.8	106	FMC	20	B	SS	Lara State	1988	FM	106						Perez et al., 1997a
11	VEN	11.1	-68.18	179	FMC	15	B	SS	Coast of Falcon State	31137	FM	179						Perez et al., 1997a
12	VEN	11.14	-68.2	169	FMC	15	B	SS	Coast of Falcon State	31167	FM	169						Perez et al., 1997a
13	VEN	10.9	-72.4	23	FMS	36	C	NS	Zulia State	691020	FM	23	49	90	9	10	36	Pennington. 1981
14	COL	6.4	-77.5	85	FMS	8	C	NF	West coast of Colombia	700926	FM	85	39	85	51	175	0	Pennington. 1982

#	Site	Lat	Long	Azi.	Type	h	Q	Reg.	Locality	Date	Met.	S1Az	S1Pl	S2Az	S2Pl	S3Az	S3Pl	Reference
15	COL	6.5	-77.4	110	FMS	6	C	NF	West coast of Colombia	700927	FM	110	63	110	27	20	0	Pennington, 1983
16	COL	6	-77.5	100	FMS	13	C	NF	West coast of Colombia	701216	FM	100	59	100	31	10	0	Pennington, 1984
17	PAN	8.8	-79.1	69	FMS	16	C	TS	South of Panama	710120	FM	69	3	151	73	159	17	Pennington, 1985
18	COL	7.8	-77.6	102	FMS	12	C	TF	Northwest of Colombia	740713	FM	102	27	116	62	15	7	Pennington, 1986
19	COL	7.2	-77.8	78	FMS	40	C	TF	Northwest of Colombia	750125	FM	78	33	90	57	169	3	Pennington, 1987
20	VEN	10.1	-69.6	158	FMS	36	C	SS	Lara State	750405	FM	158	0	68	14	68	76	Pennington, 1988
21	COL	7.6	-77.5	122	FMS	30	C	TS	Northwest of Colombia	751121	FM	122	14	19	42	45	44	Pennington, 1989
22	ECU	0.8	-79.8	118	FMS	9	C	TS	Ecuador	760409	FM	118	22	45	35	3	47	Pennington, 1990
23	COL	7.4	-78	127	FMS	3	C	TF	Northwest of Colombia	760711	FM	127	25	133	65	37	0	Pennington, 1991
24	ECU	2.2	-79	125	FMS	12	C	TF	Near coast of Ecuador	760810	FM	125	29	125	61	35	0	Pennington, 1992
25	COL	5	-78.2	134	FMS	33	C	NF	Near West coast of Colombia	761111	FM	134	53	126	37	36	0	Pennington, 1993
26	COL	7.3	-76.3	114	FMS	33	C	SS	Northwest of Colombia	770831	FM	114	33	61	43	176	29	Pennington, 1994
27	VEN	10.6	-67.3	127	FMS	0	C	SS	Falcon State	670730	FM	127	4	15	85	218	1	Pennington, 1995
28	VEN	10.9	-68.9	122	FMS	15	C	SS	Falcon State	700519	FM	302	47	145	43	33	1	Pennington, 1996
29	VEN	9.25	-70.38	264	FMS	14	B	TF	Lara State	650719	MI	264	0			354	11	Malave, 1997
30	VEN	11	-72.38	334	FMS	8	B	SS	Zulia State	691020	MI	334	27			65	3	Malave, 1997
31	VEN	7.51	-72.08	260	FMS	12	B	TF	Merida State	700127	MI	260	14			357	26	Malave, 1997

#	Site	Lat	Long	Azi.	Type	h	Q	Reg.	Locality	Date	Met.	S1Az	S1Pl	S2Az	S2Pl	S3Az	S3Pl	Reference
32	VEN	10.01	-69.67	337	FMS	10	B	TF	Lara State	750405	MI	337	9			245	12	Malave, 1997
33	VEN	7.21	-72.17	95	FMS	15	B	TF	Tachira State	800502	MI	95	26			227	54	Malave, 1997
34	VEN	7.65	-72.11	93	FMS	11	B	TF	Tachira State	820704	MI	93	1			2	18	Malave, 1997
35	VEN	10.02	-69.91	293	FMS	15	B	TF	Lara State	910817	MI	293	22			26	7	Malave, 1997
36	VEN	7.35	-72.11	104	FMS	11	B	TF	Tachira State	940531	MI	104	7			223	76	Malave, 1997
37	VEN	8.13	-72.47	118	FMS	28	B	TF	Tachira State	811018	MI	118	10			214	29	Malave, 1997
38	VEN	9.9	-68.7	123	FMC	15	B	SS	Andes	1984	FM	123	4			33	4	Garciacaro, 1997
39	VEN	7.92	-71.43	276	FMC	15	B	SS	Andes	1983	FM	276	18			185	1	Garciacaro, 1997
40	VEN	8.13	-72	287	FMC	15	B	SS	Andes	1981	FM	287	30			177	30	Garciacaro, 1997
41	VEN	8.3	-71.16	148	FMC	15	B	TF	Andes	1981	FM	148	2			43	81	Garciacaro, 1997
42	VEN	8.26	-71.1	155	FMS	10	B	TF	Andes	841102	FM	155	3			255	73	Garciacaro, 1997
43	VEN	7.52	-72.09	72	FMS	12	B	TF	Andes	941109	FM	72	5			181	74	Garciacaro, 1997
44	VEN	7.83	-71.75	136	FMC	10	B	TF	Andes	1979 - 1980	FM	136	11			15	70	Garciacaro, 1997
45	VEN	8.52	-72.34	104	FMS	10	B	TF	Andes	811018	FM	104	29			284	61	Garciacaro, 1997
46	VEN	9	-71.25	284	FMC	20	B	TF	Andes	1984	FM	284	7			174	70	Garciacaro, 1997
47	VEN	9	-71.06	284	FMS	29	B	TF	Andes	680513	FM	284	7			174	70	Garciacaro, 1997

#	Site	Lat	Long	Azi.	Type	h	Q	Reg.	Locality	Date	Met.	S1Az	S1Pl	S2Az	S2Pl	S3Az	S3Pl	Reference
48	VEN	10.802	-69.36	336.1	FMC	15	B	SS	Churuguara, Falcon State	860718	FM	336.1	11.6			70.1	10.9	Audemard and Romero, 1993
49	VEN	11.04	-69.44	299.5	FMC	15	B	SS	Churuguara, Falcon State	July - Sept. 1986	FM	299.5	5.7			36.1	48.7	Audemard and Romero, 1993
50	VEN	9.54	-70.77	253	FMS	13	B	TF	Andes	930316	FM	253	4			353	67	Choy et al., 2000
51	VEN	9.67	-70.67	41	FMS	22	B	TS	Andes	931231	FM	41	11			144	51	Choy et al., 2000
52	VEN	9.45	-70.74	261	FMS	0	B	SS	Andes	940411	FM	261	11			166	32	Choy et al., 2000
53	VEN	9.76	-70.63	238	FMS	5	B	SS	Andes	940708	FM	238	4			145	38	Choy et al., 2000
54	VEN	9.75	-70.63	223	FMS	0	B	TF	Andes	940710	FM	223	24			337	44	Choy et al., 2000
55	VEN	9.76	-70.67	154	FMS	14	B	NS	Andes	950315	FM	154	46			258	13	Choy et al., 2000
56	VEN	9.83	-70.74	209	FMS	16	B	TF	Andes	960218	FM	209	1			300	57	Choy et al., 2000
57	VEN	9.72	-70.65	51	FMS	25	B	SS	Andes	980808	FM	51	6			144	23	Choy et al., 2000
58	VEN	9.23	-70.74	114	FMS	0	B	TF	Andes	920315	FM	114	15			325	73	Choy et al., 2000
59	VEN	9.35	-70.65	127	FMS	14	B	TS	Andes	921013	FM	127	15			19	50	Choy et al., 2000
60	VEN	9	-71.07	107	FMS	13	B	TF	Andes	980222	FM	107	11			341	71	Choy et al., 2000
61	VEN	9.21	-70.76	311	FMS	8	B	NF	Andes	980223	FM	311	60			119	29	Choy et al., 2000
62	VEN	8.87	-71.12	101	FMS	15	B	TF	Andes	980320	FM	101	11			346	65	Choy et al., 2000

#	Site	Lat	Long	Azi.	Type	h	Q	Reg.	Locality	Date	Met.	S1Az	S1Pl	S2Az	S2Pl	S3Az	S3Pl	Reference
63	VEN	9	-70.91	142	FMC	9	B	TF	Andes	-	FM	142	14			13	69	Choy et al., 2000
64	VEN	8.98	-70.89	328	FMC	13	B	TF	Andes	-	FM	328	5			67	60	Choy et al., 2000
65	VEN	8.84	-70.85	136	FMC	6	B	TF	Andes	-	FM	136	7			348	81	Choy et al., 2000
66	VEN	8.79	-70.78	307	FMS	6	B	TF	Andes	-	FM	307	22			108	68	Choy et al., 2000
67	VEN	8.81	-70.82	289	FMS	6	B	SS	Andes	-	FM	289	0			199	4	Choy et al., 2000
68	VEN	9.28	-70.43	353	FMS	27	B	TS	Andes	980123	FM	353	12			252	44	Choy et al., 2000
69	VEN	9.74	-69.83	69	FMS	18	B	SS	Andes	500803	FM	69	23			160	4	Choy et al., 2000
70	VEN	9.58	-70.21	129	FMS	0	B	NF	Andes	980228	FM	129	58			20	13	Choy et al., 2000
71	VEN	9.71	-69.76	338	FMS	0	B	NF	Andes	980311	FM	338	57			154	32	Choy et al., 2000
72	VEN	9.69	-69.78	323	FMS	0	B	NF	Andes	980311	FM	323	59			152	30	Choy et al., 2000
73	VEN	9.63	-70.01	6	FMS	2	B	NS	Andes	980530	FM	6	52			118	17	Choy et al., 2000
74	VEN	9.037	-69.985	309	FMS	25	B	TF	Andes	750305	FM	309	3			50	75	Choy et al., 2000
75	VEN	9.29	-70.05	170	FMS	1	B	TF	Andes	980710	FM	170	6			70	60	Choy et al., 2000
76	VEN	10.61	-63.47	353	FMS	11	B	SS	Eastern Venezuela	740612	FM	353	63			190	26	Russo et al. 1993
77	VEN	10.6	-62.93	310	FMS	16	B	SS	Eastern Venezuela	860611	FM	310	16			46	22	Russo et al. 1993
78	VEN	10.58	-63.45	305	FMS	33	B	SS	Eastern Venezuela	741029	FM	305	42			44	11	Russo et al. 1993
79	VEN	10.53	-63.36	163	FMS	11	B	TS	Eastern Venezuela	810623	FM	163	13			49	60	Russo et al. 1993

#	Site	Lat	Long	Azi.	Type	h	Q	Reg.	Locality	Date	Met.	S1Az	S1Pl	S2Az	S2Pl	S3Az	S3Pl	Reference
80	VEN	10.45	-62.45	160	FMS	12	B	TS	Eastern Venezuela	840820	FM	160	7			61	50	Russo et al. 1993
81	COL	5.97	-74.05	280	FMS	35.4	B	SS	Central Colombia	820117	MI	280	0	10	59	190	31	Harvard CMT
82	COL	4.58	-75.75	329	FMS	27.7	B	SS	Central Colombia	990125	MI	329	32	139	58	236	4	Harvard CMT
83	COL	4.31	-75.74	337	FMS	33.8	B	SS	Central Colombia	990125	MI	337	32	153	58	246	2	Harvard CMT
84	COL	8.58	-74.83	266	FMS	34.1	B	SS	Central Colombia	010908	MI	266	9	31	75	174	12	Harvard CMT

Table 3.B.2: Geologic indicators data.

#	Site	Lat	Lon	Azi	Q	Reg.	Locality	Date	Num.	S1Az	S1Pl	S2Az	S2Pl	S3Az	S3Pl	Rock - Age	References
1	VEN	11.29	-69.7	354.5	A	TS	Coro, Falcon State	2001	8	355	52	254.3	7.8	158	36.9	Sedimentary – Plio-Quaternary	Audemard, 2001
2	VEN	10.99	-70.2	331.2	A	SS	Sabaneta, Falcon State	2001	29	350	9.5	110	71.5	257	15.7	Sedimentary – Plio-Quaternary	Audemard, 2001
3	VEN	10.6	-63	135	B	SS	Sucre State - El Pilar	1989	N/A	135	N/A	N/A	N/A	N/A	N/A	Sedimentary – Quaternary	Beltran and Giraldo, 1989
4	VEN	10.4	-63.7	135	A	SS	Sucre State - El Pilar	1989	N/A	135	N/A	N/A	N/A	N/A	N/A	Sedimentary – Quaternary	Beltran and Giraldo, 1990
5	COL	5.1	-72.6	114	A	U	Eastern Cordillera	2000	10	114	36	3	26	245	43	Gravel – Quaternary	Taboada et al., 2000
6	COL	4.72	-74	300	A	TF	Eastern Cordillera	2000	19	300	5	30	3	153	84	Lagoonal deposit – Quaternary	Taboada et al., 2000

Table 3.B.3: Stress-induced wellbore breakouts data

#	SITE	Lat	Lon	Azi	h	Q	Reg.	Locality	Date	Num.	SD	Tot. Length	SD Weight	References
1	VEN	9.6	-63.5	154	~4 km	A	U	Maturin Basin	2002	582	7.45	285	Length	Colmenares and Zoback, 2003
2	VEN	9.5	-62.9	149.2	~4 km	A	U	Maturin Basin	2002	194	7.17	48.36	Length	Colmenares and Zoback, 2003
3	VEN	9.33	-64.4	149.6	~4 km	A	U	Maturin Basin	2002	20	8.41	1.19	Length	Colmenares and Zoback, 2003
4	VEN	8.435	-70.1	139.2	~3 km	A	U	Barinas Basin	2002	120	7.7	20.8	Length	Colmenares and Zoback, 2003
5	VEN	10.7	-72.1	140	N/A	B	U	Mara Field, Zulia State	1999	N/A	N/A	N/A	N/A	Sanchez et al., 1999
6	COL	5	-72.7	138	4.6	C	SS	Cusiana	1999	N/A	N/A	N/A	N/A	Willson et al., 1999
7	VEN	10	-62.3	135	1.7	C	SS	Pedernales	1999	N/A	N/A	N/A	N/A	Willson et al., 1999

APPENDIX 3.C. EVOLUTION OF THE STRESS MAP OF NORTHERN SOUTH AMERICA SINCE 1999

As a result of this project, to some extent, the WSM data coverage of northwestern South America has changed significantly. From a couple of data points in the database of 1997 (Figure 3.C.1), it improved notably for the release of 2000 (Figure 3.C.2), already containing part of our collaboration and the inclusion of the Harvard CMT database in the WSM database. The release of 2004, also containing part of our collaboration (Figure 3.C.3) does not seem to have changed much from the release of 2000 for the study area. However, some of the problematic points have been eliminated (the Guayuriba key seats). For the release of the 2005 WSM database, all of the new data provided by this study will hopefully be included in the database. It is important to note that all these maps still contain focal mechanisms from well-defined plate boundaries while the integrated stress map generated by this study does not contain this kind of events.

Figure 3.C.3 shows that in its current state, the WSM is much more extensive for northern South America and provides a better basis to make tectonic interpretations. The way it was in 1999 was not suitable for making any analysis. This study has definitely improved the possibilities for potential future analysis in this region of the world.

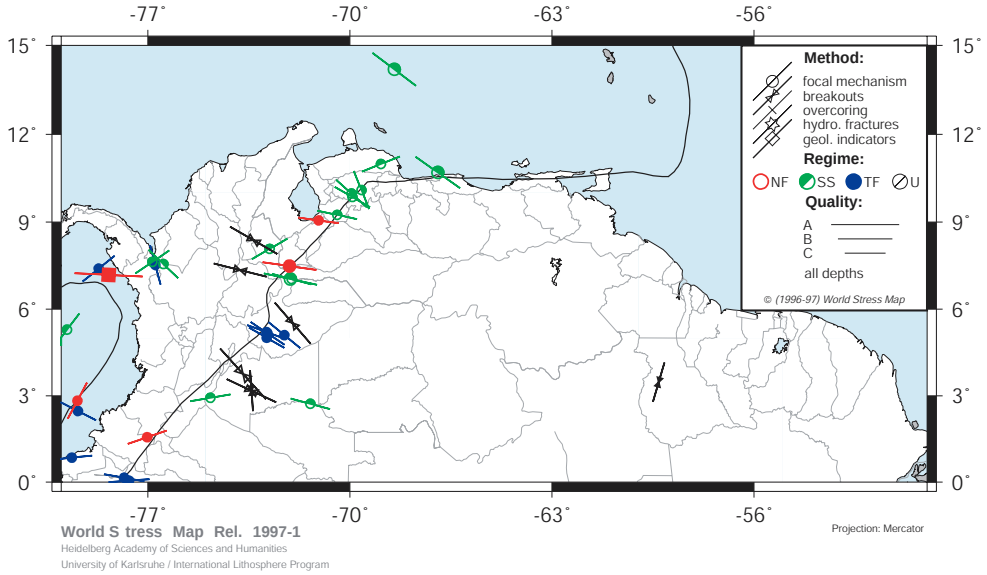

Figure 3.C.1: Stress map of northern South America using the 1997-1 database from the WSM. This map was downloaded from the WSM website in March of 1999.

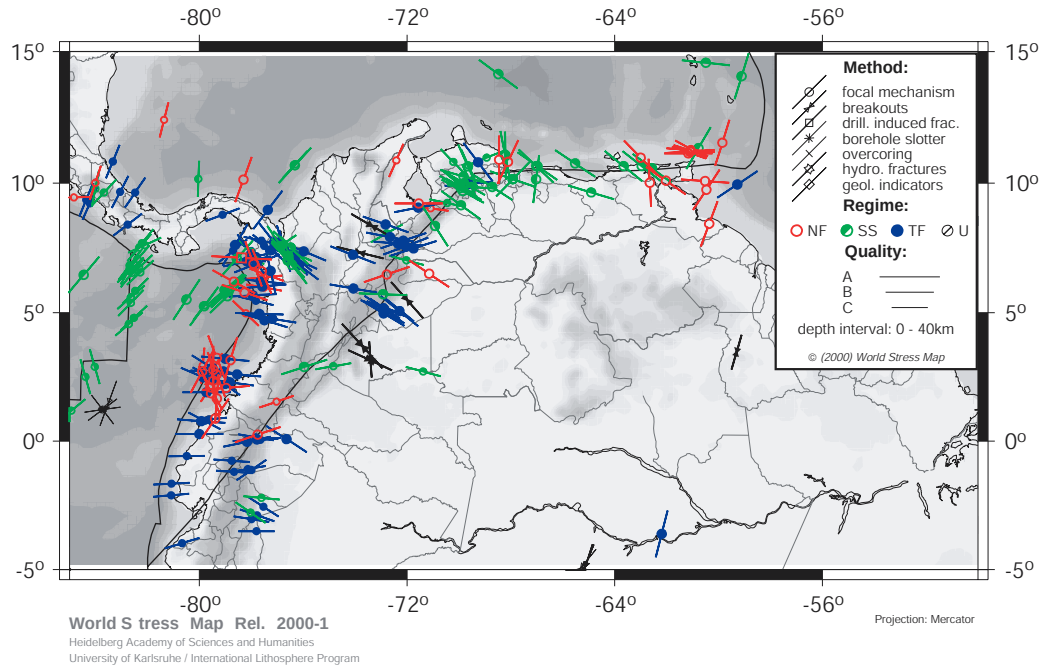

Figure 3.C.2: Stress map of northern South America using the 2000-1 database from the WSM. This map was downloaded from the WSM website in April of 2001.

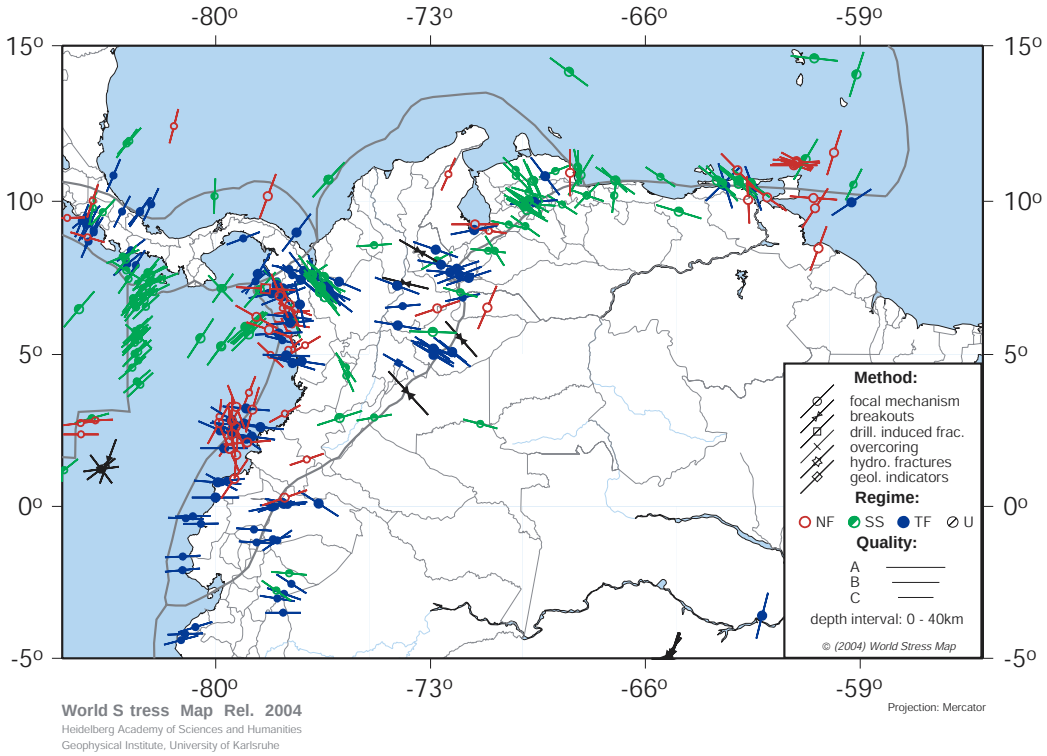

Figure 3.C.3: Stress map of northern South America using the 2004 database from the WSM. This map was downloaded from the WSM website on September 2004. Note that the plate boundary in northwestern Venezuela corresponds to the interpretation made by Perez et al., 1997a (Figure 3.2b).

APPENDIX 3.D. INTERPRETATION OF THE SLAB BENEATH NORTHWESTERN SOUTH AMERICA

The shape and extent of the slab beneath Northwestern South America (shown in Figure 3.8) was determined from the depths of earthquakes as obtained from the National Earthquake Information Center (NEIC, 1973-2002). Twelve (12) seismic cross sections were made, as shown in Figures 3.D.1 - 3.D.4 and each profile is equivalent to a box 100 km wide which projects all the data points contained in it along the lettered line (A to L).

Each profile, except for profile L shows the interpretation of the top of the slab. Profile L is an interesting cross section that mainly shows that there is no seismicity beneath 60 km along the Merida Andes of Venezuela. However, seismicity deepens towards the Southwest and it concentrates on what has been called the Bucaramanga Swarm (group of "blue" earthquakes in Figure 3.D.1 and in profiles H to L in Figures 3.D.3 and 3.D.4).

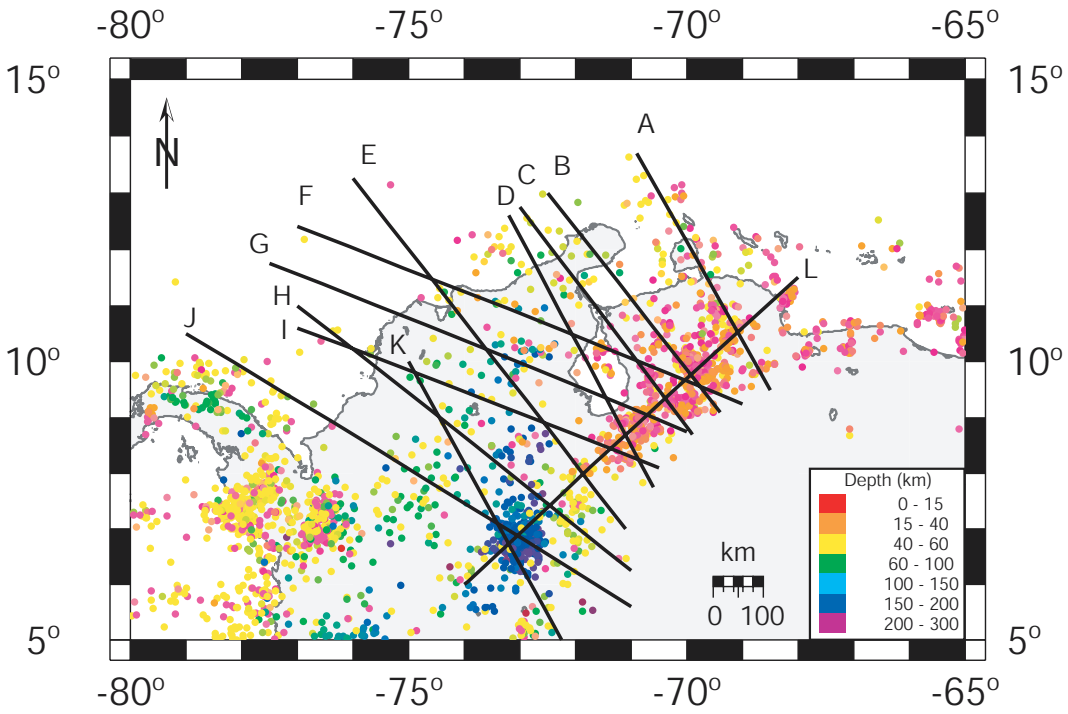

Figure 3.D.1: Depth of regional seismicity and location of cross sections shown in Figures 3.D.2 – 3.D.4.

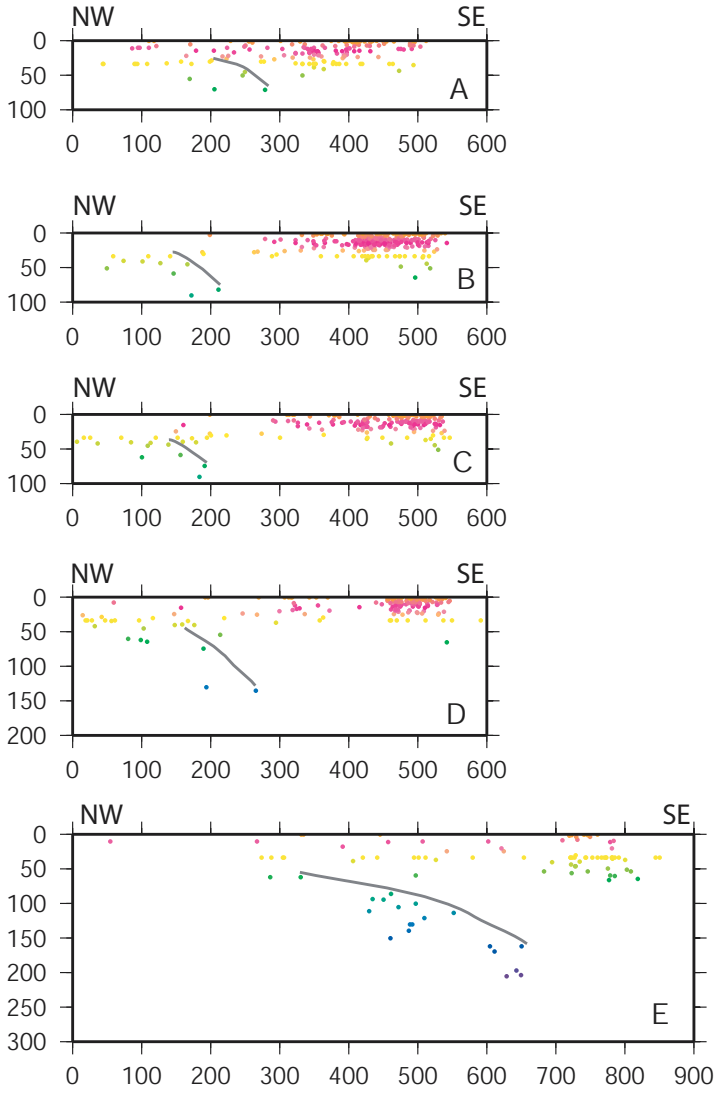

Figure 3.D.2: Cross sections A to E showing depth of regional seismicity and interpretation of top of the slab. For location of cross sections see Figure 3.D.1.

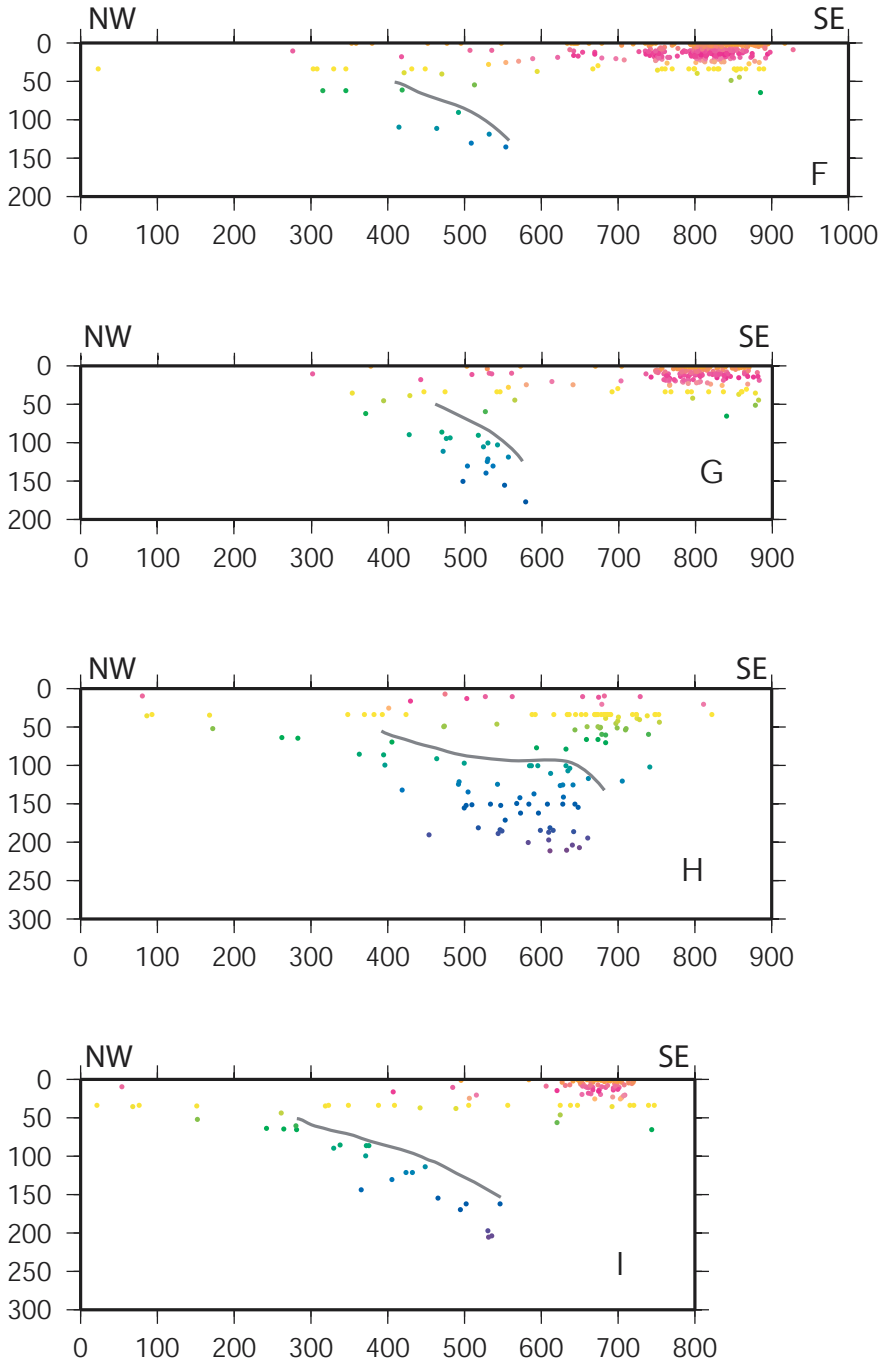

Figure 3.D.3: Cross sections F to I showing depth of regional seismicity and interpretation of top of the slab. For location of cross sections see Figure 3.D.1.

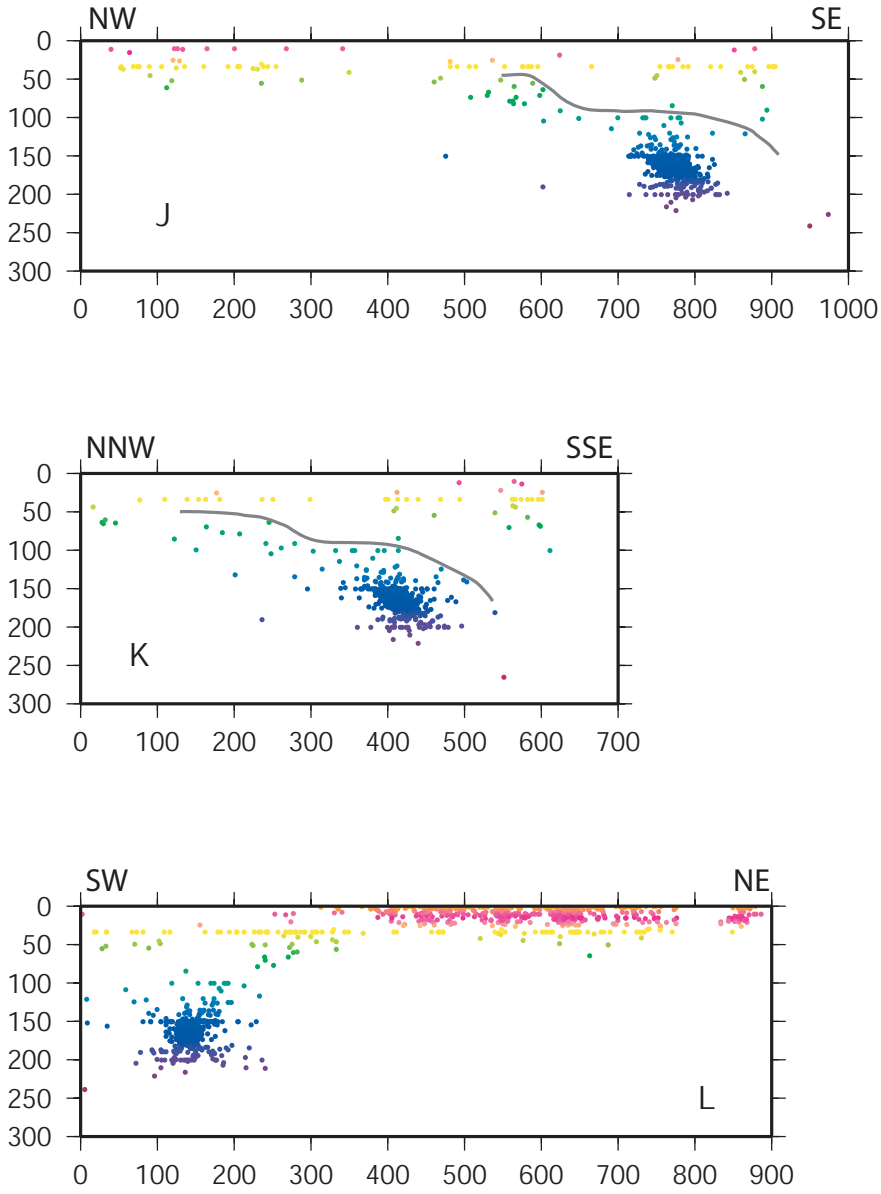

Figure 3.D.4: Cross sections J to L showing depth of regional seismicity and interpretation of top of the slab. For location of cross sections see Figure 3.D.1.

APENDIX 3.E. POTENTIAL APPLICATION OF THIS WORK TO THE OIL INDUSTRY

Depending on their location, the oil basins of the region are under different stress regimes. This regional study allows me to infer the stress regime of the oil basins located in areas where there is few or no data. Knowing the stress field of an oil field is very important when assessing issues related to wellbore stability, optimization of production from fractured reservoirs and understanding the sealing or leaking behavior of faults.

As can be seen in Figure 3.E.1, the oil fields of the Oriente basin in Ecuador are subjected to a compressive E-W stress field which rotates clockwise becoming NW-SE towards the north-northeastward direction, where the Colombian oil basins are located (North Andes province), for example, the Llanos, Magdalena Valley and Cesar-Rancheria basins. This prevalent NW-SE trending stress field, as well as its compressive-strike-slip nature can also be observed in the Maracaibo, Guajira, Catatumbo and Barinas basin. Even though I did not obtain data from oil wells in the Apure basin, from Figure 3.E.1 it can be inferred that the oil fields in this region are under NW-SE compression as well. With respect to the San Sebastian – El Pilar province, the breakout data from the oil fields of the region (Maturin basin) indicate compression in the NW-SE direction but the magnitude of the stresses, as indicated by focal mechanisms is normal-strike-slip, that is, less compressive than in the North Andes province.

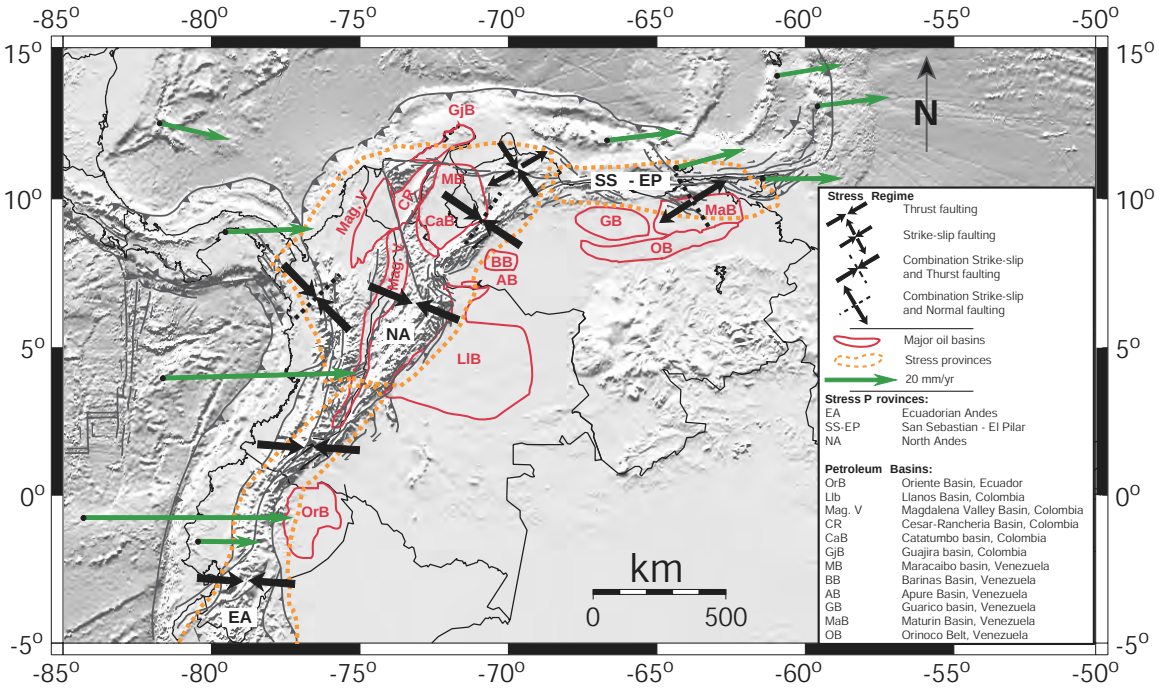

Figure 3.E.1. Generalized stress map of northern South America with major oil basins of the region. The stress provinces shown in the figure are discussed in the text.

Chapter 4.

Geomechanics and the Effectiveness of Wellbore Completion Methods of Coalbed Methane (CBM) Wells in the Powder River Basin: Implications for Water and Gas Production

This chapter will be submitted with Mark D. Zoback as co-author to the AAPG Bulletin.

4.1 ABSTRACT

The shallow depth and relatively low cost of Coalbed Methane (CBM) wells in the Powder River basin (PRB) has resulted in widespread use of open-hole/single horizon completion procedures. A common completion technique used by most operators in the PRB is to drill to the top of the coal seam, case and cement the wellbore and then drill the coal section. After drilling, the coal section is under-reamed to enlarge the hole and to minimize the effects of any formation damage. In many cases, water is then pumped into the wellbore to "clean it out" and "enhance" production. After analyzing pressure and flow rate data during these operations, it is clear that "water-enhancement" activities result in hydraulic fracturing of the coal. To determine whether vertical hydraulic fracture growth might extend into adjacent formations (and potentially result in both excess CBM water production and inefficient depressurization of coals), water-enhancement test data from approximately 550 wells have been analyzed to obtain the magnitude of the least principal stress (S_3) in the coal seams. These data indicate that vertical fracture growth (S_3 corresponds to the minimum horizontal stress) does occur in many parts of the basin whereas the hydrofrac growth appears to be horizontal (S_3 corresponds to the overburden stress) in other areas. In addition, water production from wells with horizontal fractures is minimal and excessive water production is always associated to wells with vertical hydraulic fractures. In these wells with exceptionally high water production, the time at which gas production starts is significantly delayed relative to wells with vertical fractures and low water production, which are excellent gas producers. In general, wells with vertical fractures produced more gas than wells with horizontal fractures. Wells with vertical fractures tend to be excellent gas producers, which implies that the face cleats in the coals must be efficiently connected by the induced vertical fracture. It has also been identified that horizontal hydraulic fracturing is typical towards the Sheridan area. This may be a significant finding, as water injection wells are perhaps needed in the near future in this region because the water has a high content of sodium and will need to be properly disposed. Thus, knowing that there is no vertical connection between the coal seam that is being produced and the sand layers where the water may be injected is particularly important for the operators of the area if water injection activities are

undertaken here. It appears that coal thickness affects the S_3 magnitudes. In general, in areas where a coal seam has a thickness greater than 60 feet S_3 is equivalent to the minimum horizontal stress, and therefore fractures propagate in the vertical direction. This implies that by identifying the areas where a coal seam is thicker than 60 ft, areas of vertical fracture propagation would also be identified. In order to minimize CBM water production, recommendations for better well completion practices have been outlined here. In areas of known vertical fracture propagation it is necessary to limit the injection during the water enhancement tests in order to prevent propagation of induced fractures into the overlying water-bearing formations. In areas where S_3 is unknown, a minifrac (~2 bpm for ~2 min) should be done to determine the magnitude of S_3 and thus whether fracture propagation would be vertical or horizontal. If S_3 corresponds to the overburden, horizontal fracture propagation will occur and the water enhancement activities can proceed as usual. As many wells with horizontal fractures tend to be poor gas producers, it is also suggested that such wells are hydraulically fractured (and propped) to enhance gas production. If the shut-in pressure is significantly less than the overburden, vertical hydraulic fracture growth is implied and significantly reduced pumping is advised. This would be beneficial from the perspective of minimizing produced waters and decreasing the time for initial gas production.

4.2 INTRODUCTION

Most coalbed methane in the United States has been produced from the San Juan basin of New Mexico and Black Warrior basin of Alabama. In recent years, the Powder River Basin has gained in importance as production and number of producing wells has increased tremendously (Figure 4.1).

The Powder River Basin of Wyoming and Montana is the site of the fastest growing domestic natural gas play, mostly from the development of coalbed methane from the Wyodak and Big George coal beds of the Fort Union formation. Nearly 4 billion cubic feet per day of coalbed methane are currently being produced in the US, with about 20% of it coming from the Powder River Basin. Within the next 10 years, as much as 75% of the growth in coalbed methane production in the U.S. is expected to occur in this region. Along with the growth in CBM production has been the growth in produced

water, as part of dewatering and depressurizing the coal formations, which enables the coals to release their adsorbed methane. Coalbed methane wells in the Powder River Basin are generally pumped constantly, removing as much as 400 barrels/day/well (De Bruin et al., 1999). Figure 4.2 shows the production history of a coalbed methane well in the basin. This figure shows that even after gas production is initiated, large volumes of water are still being produced. Production from water bearing coal seams can yield significant volumes of water, enough to make it difficult or infeasible to dewater the formation sufficiently to initiate coalbed methane flow (EPA, 2002). Even though the water is generally of potable quality in the center of the basin, it becomes more saline towards the north and south. Therefore, the disposal of such great amounts of water produced by coalbed methane wells is a major environmental issue, especially in areas where the water produced has a high content of sodium.

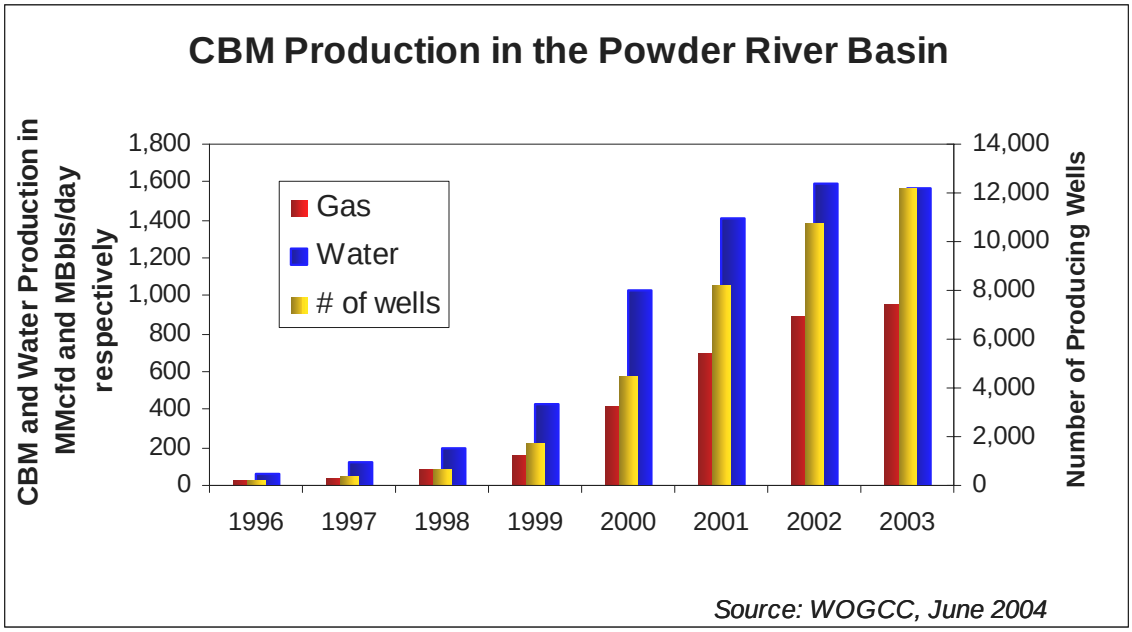

Figure 4.1: CBM and water production and number of producing wells in the PRB since 1996 until 2004.

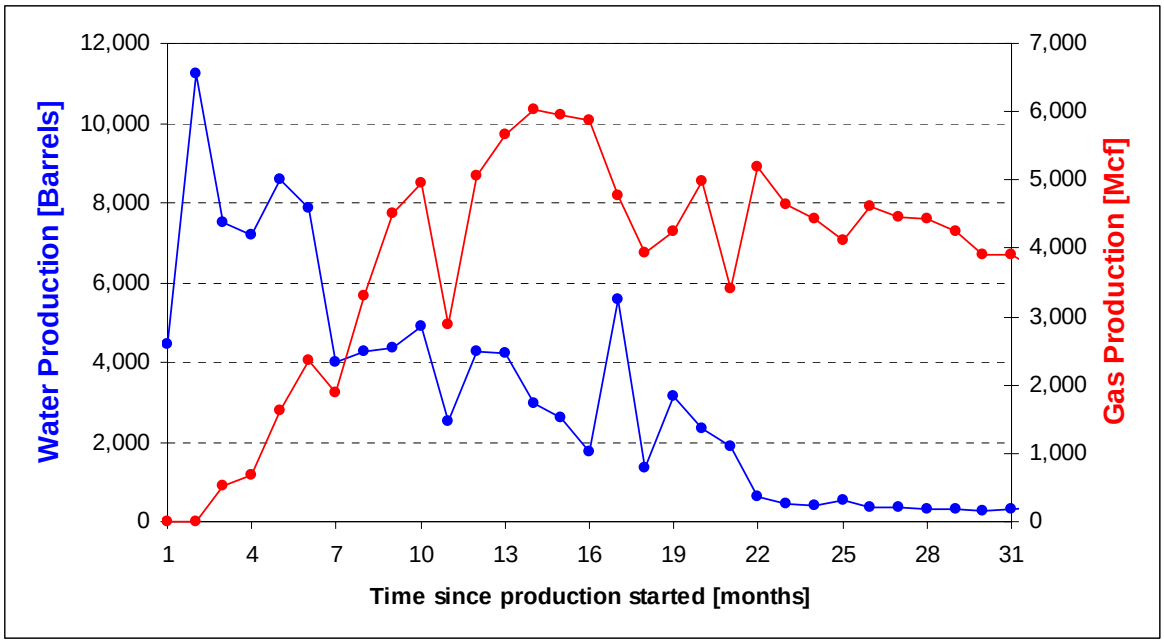

Figure 4.2: Water and gas production of a CBM well in the PRB. Source WOGCC, 2004.

At the moment production is concentrated along two main bands in the basin (Figure 4.3). Development towards the Sheridan area has started but it is not as developed as in Campbell and Johnson counties of Wyoming. Coalbed methane production has migrated towards the western part of the basin, compared to its initial times (1980's to early 1990's) when production was concentrated in the Campbell County. Since ~12,500 wells have been drilled to date, with 50,000 more wells expected in the next decade, water disposal constitutes a major environmental challenge. At the present, 150 barrels of water are produced per well per day, with 50,000 wells in the basin, water production will rise to ~7.5 million barrels per day. The goal of this study is to evaluate wellbore completion practices to determine if there are ways to produce less CBM water and still achieve adequate coal depressurization for CBM production. Minimizing water production would have appreciable beneficial consequences.

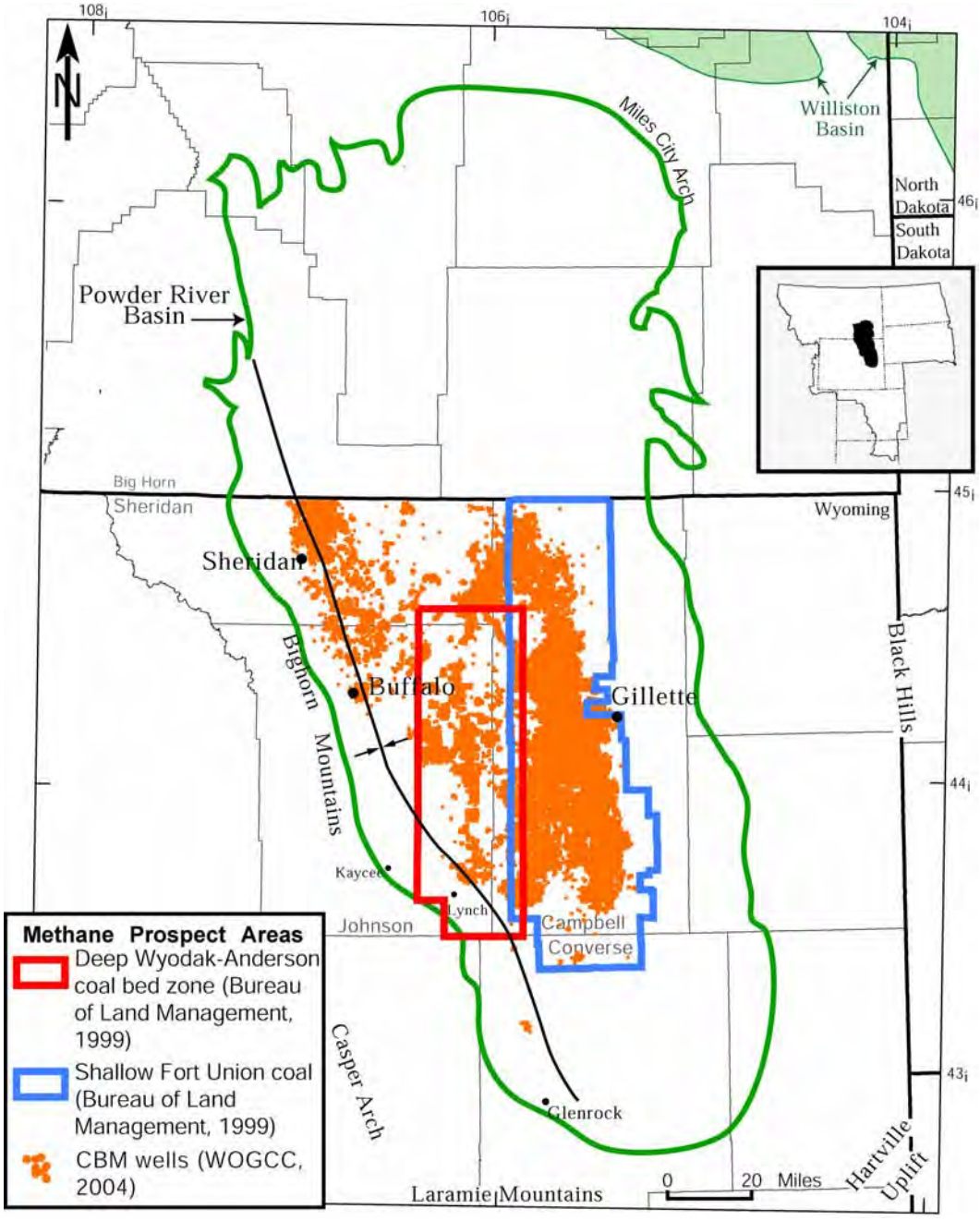

Figure 4.3: Location of the PRB showing counties, cities, CBM wells and methane prospect areas (modified from Flores and Bader, 1999)

4.3 ORIGIN OF COALBED METHANE

During the early stages of coalification of buried peat, biogenic methane is generated as a by-product of bacterial respiration. Aerobic bacteria first metabolize any free oxygen left in the plant remains and surrounding sediments. If sulfates are present, methane generation will not dominate until after sulfate-reducing species of anaerobic bacteria have metabolized the sulfates. In environments where brackish or fresh waters are low in sulfates, methane production begins immediately after the oxygen is depleted (Rice and Claypool in De Bruin and Lyman, 1999). When the temperature of a coal reaches about 50°C, and after a sufficient amount of time, most of the biogenic methane is generated, approximately two-thirds of the original moisture is expelled, and the coal attains an approximate rank of subbituminous (Rightmire in De Bruin and Lyman, 1999).

As the temperature increases above 50°C, through increased depth of burial or increased geothermal gradient, thermogenic processes start and additional water plus carbon dioxide and nitrogen, are generated as coalification proceeds to the rank of high volatile bituminous (Figure 4.4). Maximum generation of carbon dioxide, with little methane generation, occurs at about 100°C. Thermogenic generation of methane begins in the higher ranks of the high volatile bituminous coals, and at about 120°C generation of methane exceeds generation of carbon dioxide. Maximum generation of methane from coal occurs at about 150°C. With even higher temperatures and higher ranked coals, methane is still generated, but at somewhat lower volumes (Rightmire in De Bruin and Lyman, 1999).

Gas storage in coal beds is more complex than in most conventional carbonate and sandstone reservoirs. According to Yee, Seidle, and Hanson (De Bruin et al., 1999), coalbed methane is stored in four ways: 1) as free gas within the micropores and fractures (cleats); 2) as dissolved gas in water within the coal; 3) as adsorbed gas held by molecular attraction on maceral, micropore, and cleat surfaces; and 4) as absorbed gas within the molecular structure of the coal. It is important to note that the percentage of adsorbed methane generally increases with increasing pressure and coal rank, while coals at shallower depths with good cleat development contain significant amounts of free and dissolved gas.

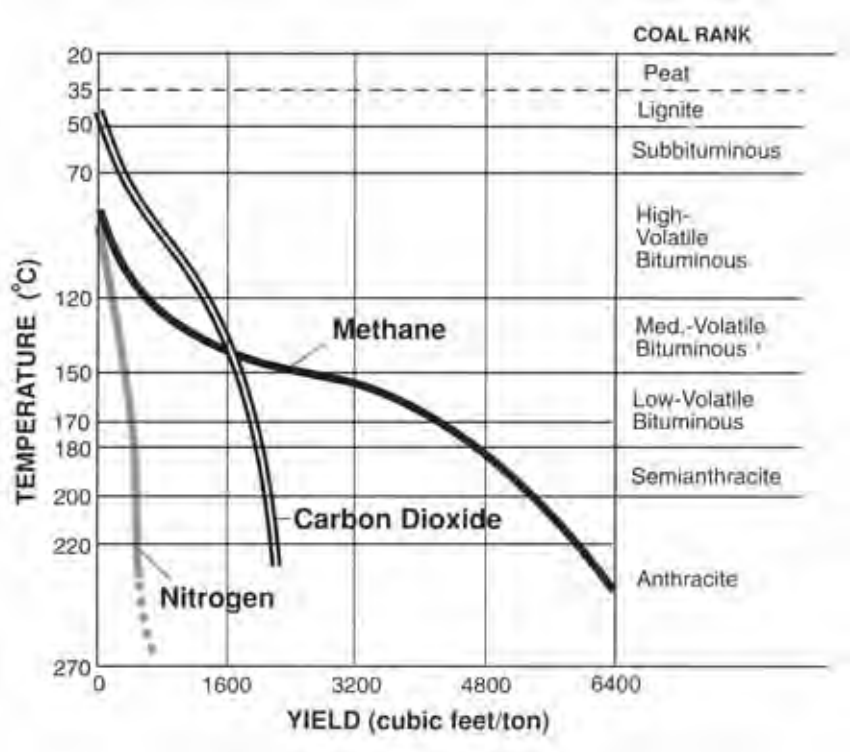

Figure 4.4: Calculated curves of gases generated from coal during coalification. (Modified from Rightmire in DeBruin, R. and Lyman, R, 1999)

Most of the coal in the Powder River Basin is subbituminous in rank, which is indicative of a low level of maturity. Some lignite, lower in rank, has also been identified. The thermal content of the coals found in the Powder River Basin is typically 8,300 BTU per pound (Randall in EPA, 2002). Coal in the Powder River Basin was formed at relatively shallow depths, at relatively low temperatures. Most of the methane generated under these conditions is biogenic, which means that it was formed by bacterial decomposition of organic matter. The coals from the Wasatch and Fort Union Formations tend to be less thermally mature than the Tertiary coal beds located in the deeper parts of the Wind River, Bighorn, Hanna and Green River coal fields of Wyoming (De Bruin and Lyman, 1999). Consequently, coal in the Powder River Basin contains less methane per unit volume than many other coal deposits in other parts of the country. The gas is typically more than 95% methane, the remainder being mostly nitrogen and carbon dioxide. This resource was overlooked for many years because it was thought to be too shallow for the production of significant amounts of methane. However, the relatively low gas contents of Powder River Basin coal is compensated by the thickness of the coal deposits. Because of the thickness of the deposits and their accessibility, commercial

development of the coalbed methane has been found to be economical. In the Powder River Basin, two different coalbed methane sources are commonly developed: (1) gas extraction from methane-charged dry sand layers overlying or interbedded with the coals, and (2) conventional methane extraction from the water saturated coal seams (EPA, 2002).

4.3.1 General Coal Properties

The elastic modulus for the non-coal rock ranges from 2.0 x 10^6 psi to 5.0 x 10^6 psi, compared to approximately 0.5 x 10^6 psi for coal. Similarly, the Poisson's ratio for non-coal rocks varies from 0.1 to 0.28, with coal ranging from 0.23 to in excess of 0.40 (Figure 4.5). Coal is a weak, friable material that readily fails in compression. It is weakest at ranks ranging from high-volatile A bituminous to low-volatile bituminous, as shown in Figure 4.6. The unconfined compressive strength decreases to a minimum as the coal rank increases and the carbon content reaches 70 to 80 percent (daf). Strength then increases in the anthracitic ranks. (Jones, Bell and Schraufnagel, 1998).

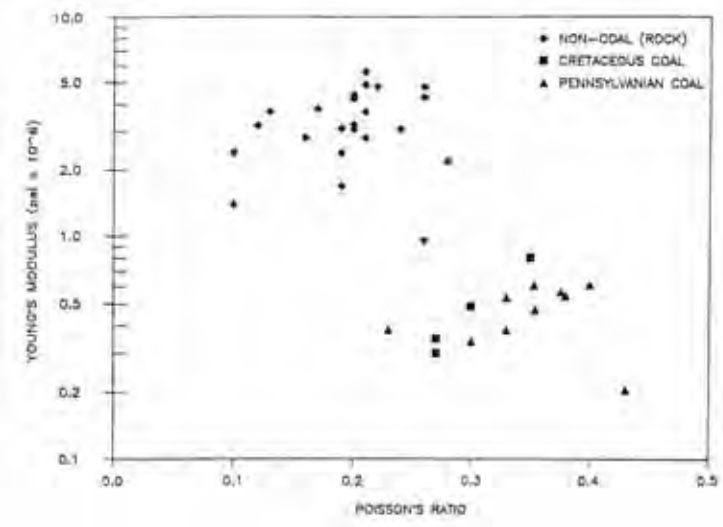

Figure 4.5: Mechanical properties of coal and non-coal rock. Source: Jones, A. , Bell, G. and R. Schraufnagel, 1988.

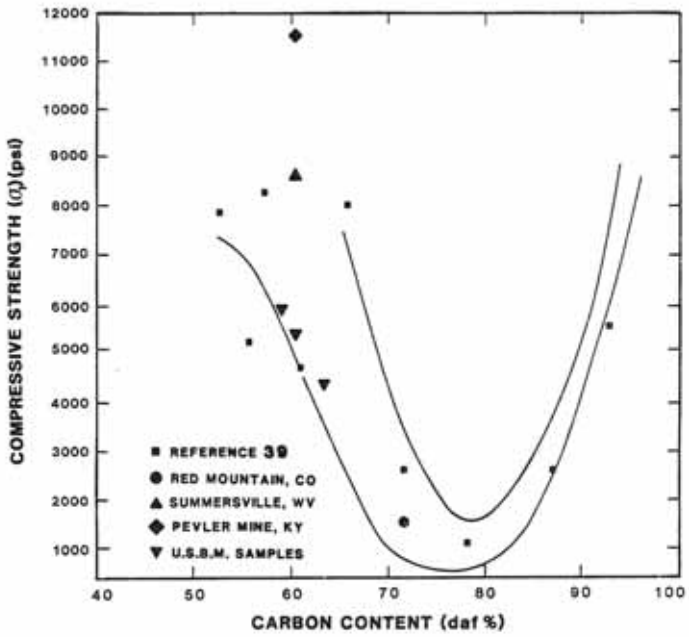

Figure 4.6: Comparison of unconfined compressive strength with volatile matter content (modified from Pomeroy and Foote, 1960). Source: Jones, A. , Bell, G. and R. Schraufnagel, 1988.

4.4 GEOLOGY

The Powder River Basin is bounded to the east by the Black Hills uplift, to the west by the Big Horn uplift and Casper Arch, to the south by the Laramie and Hartville uplifts, and to the north, it is separated from the Williston Basin by the Miles City Arch and the Cedar Creek Anticline (Figure 4.7). The long axis of the basin is generally aligned NW-SE, and is 18,000 feet deep (Figures 4.7 and 4.8). Sediments range from Paleozoic at the bottom through Mesozoic to Tertiary at the top of the basin. The basin is a large asymmetrical syncline with its axis near the west side of the basin (Figure 4.8).

Several periods of deposition by marine and fluvial-deltaic processes have occurred within the basin during the Cretaceous and Tertiary periods. These Cretaceous and lower Tertiary rocks have a total thickness of up to 15,000 feet (Montgomery, 1999).

Coal is found in the Paleocene Fort Union and Eocene Wasatch Formations (Figure 4.9). Most of the coal beds in the Wasatch Formation are continuous and thin (six feet or less) although, locally, thicker deposits have been found (DeBruin et al., 2000). The Fort Union Formation (Paleocene) extends over 22,000 square miles in the Powder River Basin in Wyoming and Montana. It is overlain by the Wasatch Formation (Eocene)

and underlain by the Lance Formation (Upper Cretaceous) in the central part of the basin, and is more than 5,200 ft thick along the basin axis. In ascending stratigraphic order, the Fort Union Formation is divided into the Tullock, Lebo, and Tongue River Members. The Tullock Member is 740 ft thick, the Lebo Member 2,600 ft thick, and the Tongue River Member 1,860 ft thick. The Fort Union Formation outcrops on the eastern side of the basin, east of the city of Gillette, and on the western side of the basin, north and south of Buffalo. Most of the coalbeds in this formation are part of the upper Tongue River Member (Figure 4.9), which is typically 1,500 to 1,800 feet thick, and up to a composite total of 350 feet of coal can be found in various beds. The thickest of the individual coal beds is over 200 feet (Flores and Bader, 1999). As can be seen in Figure 4.9, the coal beds are interspersed with sandstone, conglomerate, siltstone, mudstone and limestone. Most coalbed methane wells in the Powder River Basin are in the Tongue River Member of the Fort Union Formation, in the Wyodak-Anderson coal zone, which contains up to 32 different coal beds according to some authors (Ayers, 1986), including the Big George in the central part of the basin (Flores and Bader, 1999). Most of the coal beds are found within 2,500 feet of the ground surface. The Wyodak coal bed gets progressively deeper and thicker toward the west. The thickness of the Wyodak coal bed ranges from 42 to 184 feet. Most of the coalbed methane wells in the Powder River Basin are within the Wyodak coal zone near the City of Gillette. The Big George coalbed is located in the central and western portion of the Powder River Basin. Although the Big George is stratigraphically higher than the Wyodak, owing to the structure of the basin, the Big George, in the center portion of the basin, is deeper than the Wyodak at the eastern margin of the basin.

The stratigraphic correlation of coal beds composing the Wyodak-Anderson coal zone is complex. Part of the problem originated from the use of the same names by various investigators for coal beds that are not stratigraphically correlative within the Powder River Basin. In addition, many local names were applied to coal beds in isolated areas, beds that were later physically correlated across the basin. Compounding these problems, no biostratigraphic studies were conducted to confirm or refute these physical correlations basinwide. One solution to these stratigraphic correlation problems was to lump all the coal beds and associated rocks into a single coal zone. This coal zone was named the Wyodak-Anderson coal zone by Averitt in 1975 and was correlated basinwide

by Glass in 1990. It has also been called the Wyodak coal, or the Anderson and Canyon coal beds coalesced (Flores and Bader, 1999).

The complexity of correlation is displayed by splitting and merging of the Wyodak-Anderson coal zone according to Flores and Bader (1999). Splitting of coal beds in the Wyodak-Anderson coal zone generates two beds (the lower Wyodak bed comprising the merged Canyon and Werner coals, and the upper Wyodak bed comprising the merged Smith, Swartz, and Anderson coal), three beds (Anderson or Dietz 1, Dietz 2, and Dietz 3), five beds (lower and upper Anderson and lower, middle, and upper Canyon beds), six beds (Smith, Swartz, Anderson, upper and lower Canyon, and Werner beds), or as many as eleven beds (Sussex beds). Overall, successive splitting and merging of beds in this coal zone basinwide, from overlapped, offset, zigzag, and shingled segments, results in older Wyodak-Anderson coal beds (for example, the Big George coal) in the west-central part of the basin than on the basin margins (for example, Smith, Anderson, Dietz, Canyon, School, and Badger coal) (Flores and Bader, 1999). Figure 4.10 shows the number of coal beds found in different areas in the PRB.

4.4.1 Note about Big George Coal

The Big George coal, as defined and interpreted by Flores and Bader (1999), is the amalgamation of different coals, and is between 45 and 200 feet thick. The Big George, as so defined, exists only in the central part of the basin, that is, it directly indicates the location. According to what the operators of the basin have called Big George, this coal seam ranges from 5 feet to 200 feet in thickness, which does not coincide with the interpretation of Flores and Bader (1999). However, the interpretation of the operators and what they report to the Wyoming Oil and Gas Conservation Commission (WOGCC) has been adopted because making the reconciliation between the operators' interpretation and the interpretation of the USGS is an extremely daunting, if not impossible task and beyond the scope of this study.

It is very important to mention that the identification of coal seams in this study has been taken from what the operators report to the WOGCC website. Therefore, certain names may not coincide with Flores and Bader's interpretation of coals in the basin. However, a complete basin-wide reconciliation between all the different names for a

certain coal bed does not exist yet so the WOGCC interpretation was chosen as a guide. Currently, efforts are taking place to reconcile the coal nomenclature (Jones, 2004), but, until these reconciliations are completed, some ambiguity remains regarding coal beds classified as Big George by different sources. In an attempt to reduce some of the uncertainty, Gamma Ray (GR) logs were analyzed, where available, to establish correlations across wells of the Big George and the Wyodak coals since they are thick and have a distinct GR response. Based on this analysis, I feel confident that the operators' definition and interpretation of these coal beds is consistent (see the section on "Water and Gas Production Throughout the Basin" for a more detailed description of the GR analysis). This GR based distinction of coal beds is harder, if not impossible, for the thinner coals. Nevertheless, the possible confusion in definition of these coal beds should be kept in mind for future analyses.

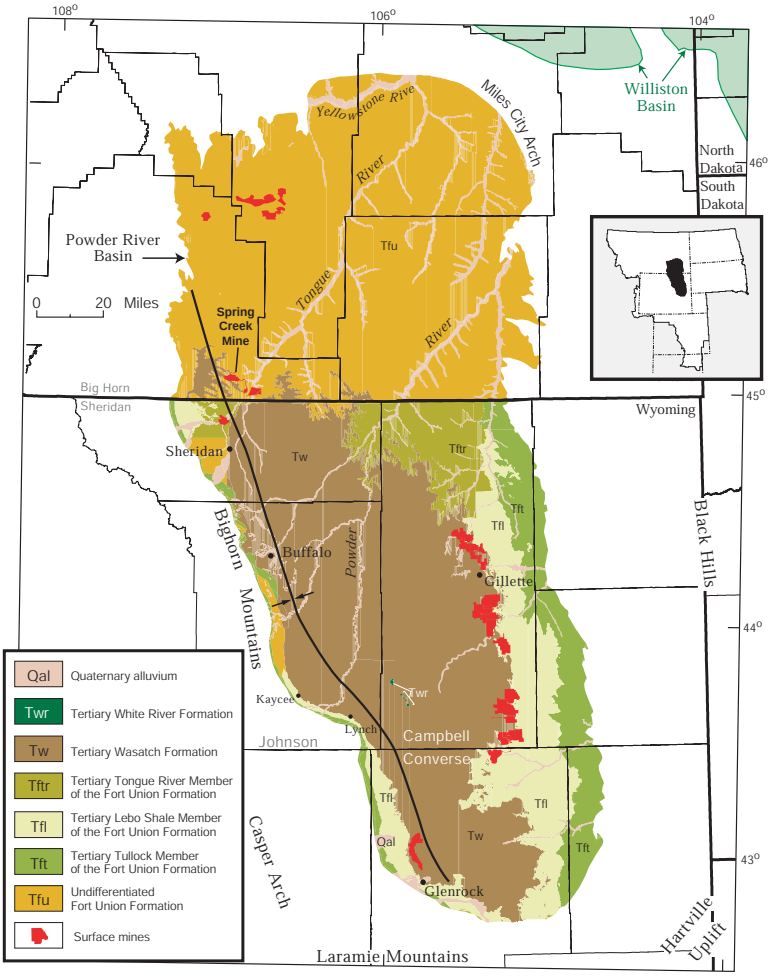

Figure 4.7: Generalized geologic map showing the extent of the Powder River Basin in Wyoming and Montana. Also shown are county boundaries, geological structures, mines, and cities (modified from Flores and Bader, 1999)

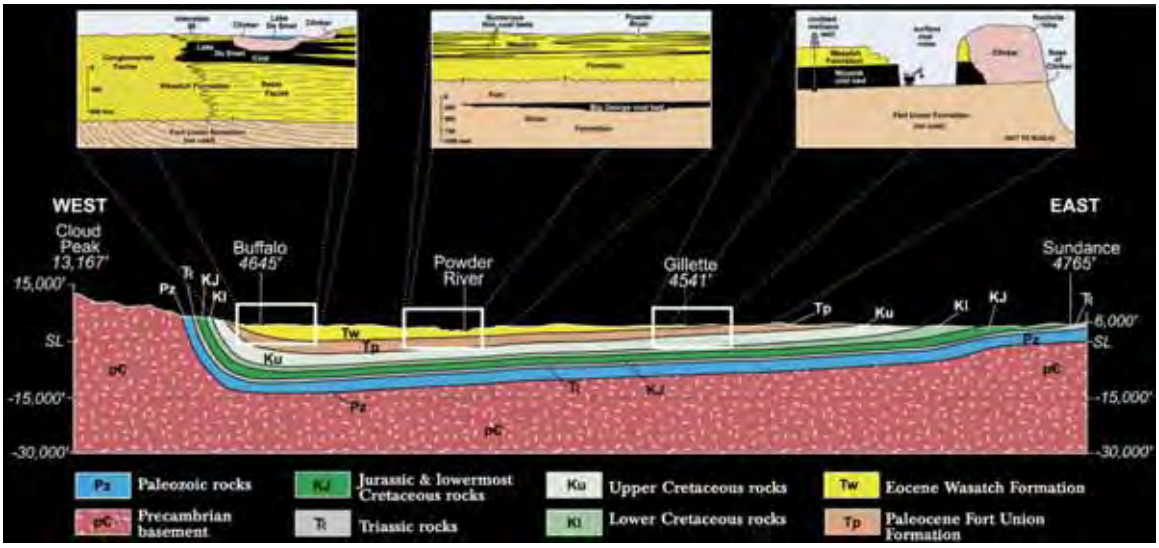

Figure 4.8: Conceptual Cross Section of the Powder River Basin (West-East) (DeBruin et al., 2004).

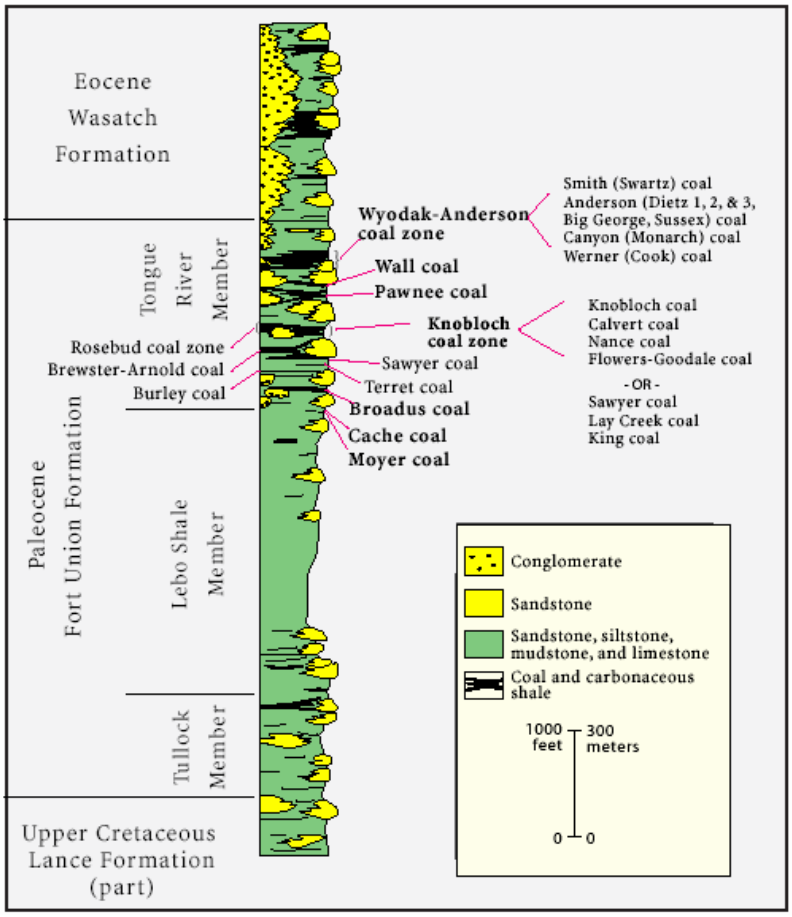

Figure 4.9: Composite stratigraphic column showing the Upper Cretaceous Lance Formation (part), and Tertiary Fort Union and Wasatch Formations in the Powder River Basin, Wyoming and Montana. Major coal beds and zones in the Fort Union Formation are identified. Coal zones or beds targeted for coalbed methane are bold. (Rice et al., 2000)

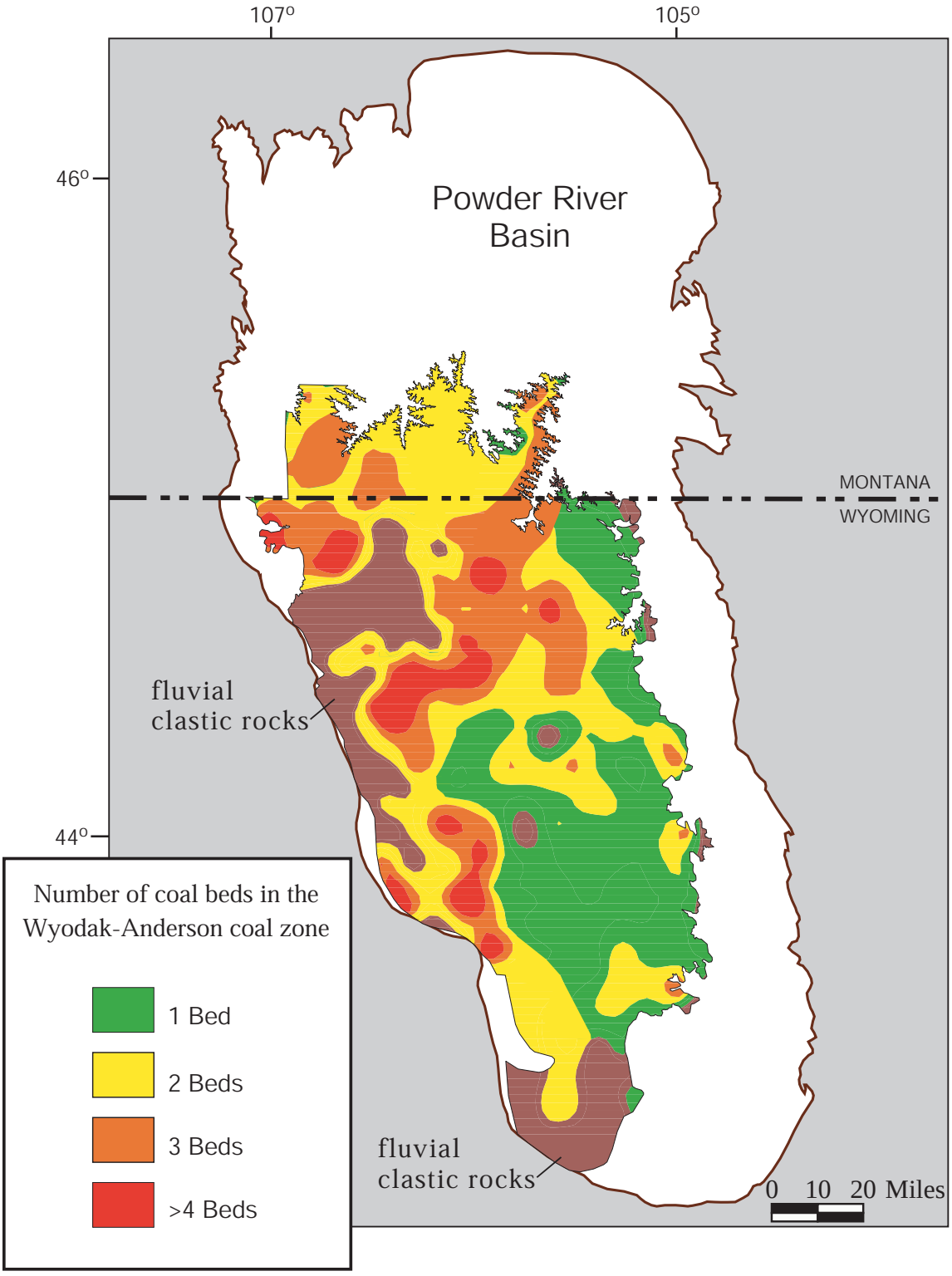

Figure 4.10: Distribution of the number of coal beds in the Wyodak-Anderson coal zone in the Powder River Basin. (Modified from Flores and Bader, 1999)

4.5 DRILLING AND COMPLETION OVERVIEW

The following is a standard drilling and completion procedure followed by the operators (Figure 4.11a) in the Powder River Basin when under-reaming the coal seam:

The well is spudded with a 14 ¾" surface bit and drilled to ten percent (10%) of the total well depth or a minimum of 95 feet (29 m). Then, a surface casing (10 ¾") is put in place and cemented. After cementing the surface casing, operators drill the next hole section down to the top of the coal. This section is drilled with water as a drilling fluid; sometimes gel is added to make the water more viscous, which improves the cleaning capacity of the drilling fluid. As a result, more debris can be transported out of the well. A seven inch production casing is then put in place and cemented. The operators pay special attention to achieve a good high quality cement job for this casing shoe, in order to prevent the coalbed methane from escaping the well, and also to prevent communication with overlying aquifers. Because of this, a cement bond log is run to ensure the quality of the cement job.

Initially, the coal section and an extra 10 feet (3 m) below the coal, are drilled with a 6 ¼" bit. The drill fluid used is identical to the previous hole section (water with gel). After finishing the 6 ¼" hole through the coal, a gamma ray log is run, in order to accurately locate the extent of the coal seam. After logging, the diameter of the coal section is enlarged with an under-reamer to a final diameter of 14". When there is more than one economical coal seam, operators under-ream the bottom coalbed and perforate the upper ones (Figure 4.11b). Afterwards, the coal is water-enhanced. This procedure implies the pumping of 2500 gpm or 60 bpm of water into the coal during approximately 15 minutes. It is possible that during this process the coal is hydraulically fractured. Some operators use a 5 ½" slotted liner in the open hole section of the well, as shown in Figure 4.11a. This slotted liner is used to prevent debris migrating up the hole and blocking the flow. To finalize the completion of the well, a submersible water pump and the wellhead are installed. The tubing, with a submersible electric water pump, is inserted to allow the water to flow from the bottom of the hole. CBM exits the well through the annulus formed by the casing and the tubing. The well is capped to control the flow of methane gas. Wells are often dewatered for several months before producing significant quantities of methane gas (Figure 4.12).

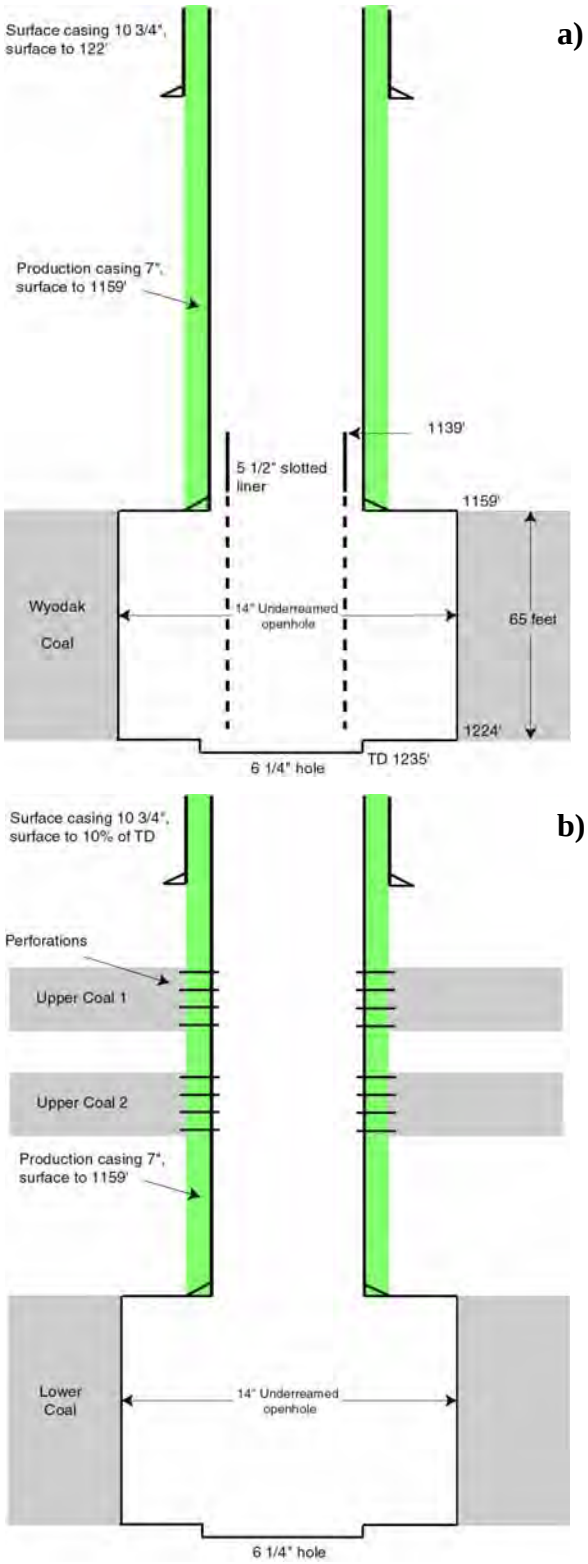

Figure 4.11: a) Standard completion method in the CBM wells in the Powder River Basin using under-reaming. Some operators prefer not to use the slotted liner. b) If there are several productive coal seams, this is the completion method used by the operators, under-reaming the lower seam and perforating the upper ones.

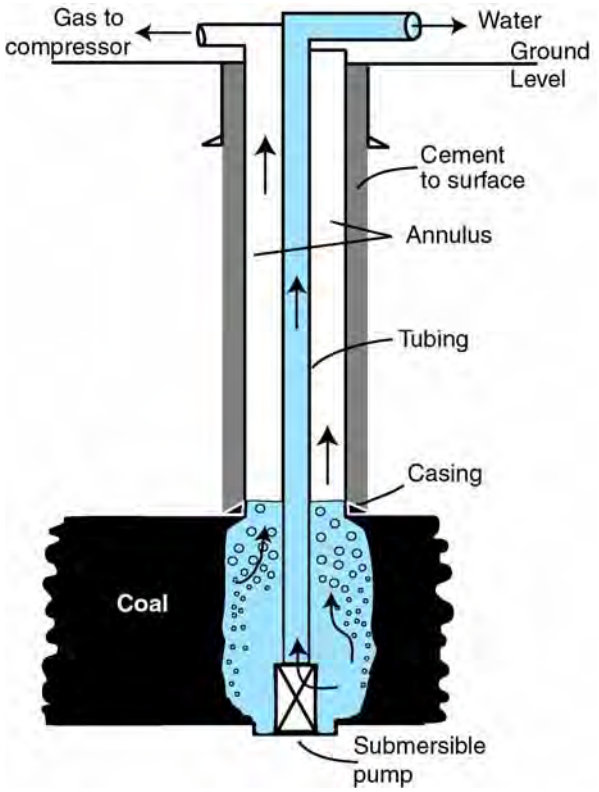

Figure 4.12: Schematic diagram showing open-hole completion technique for a typical coalbed methane well. Modified from DeBruin et al., 2004.

4.5.1 Hydraulic Fracturing in the PRB

During the early years of CBM development in the Powder River Basin (1980's to early 1990's), gas exploration and development companies completed wells with and without hydraulic fracture techniques. Early wells were completed without fracturing treatments, particularly wells targeting gas reserves in coals interspersed between sandstone layers. However, the Quarterly Review (in EPA, 2002) reported that in one well, Rawhide 15-17, located north of Gillette, Wyoming, an "open frac" hydraulic fracturing was performed using 13,000 lbs of 12/20-mesh sand in 3,500 gallons of gelled water. Several wells installed in the early 1990s by Betop, Inc. were fractured using 4,000 to 15,000 gallons of a solution with 2% potassium chloride (KCl) in water. Sand was used to prop the fractures open in five of these wells (Quarterly Review in EPA 2002). However, hydraulic fracturing experienced little success in this basin. It was argued that fractured wells produced poorly because the permeable, shallow sub-

bituminous coals collapsed under the pressure of the overburden after they were dewatered.

The Powder River Basin contains coals of high permeability. Consequently, drilling fluid (typically water) is lost when drilling the coal beds. Many times drilling mud is used to prevent loss of circulation. Because of this high permeability, most coalbed wells in the Fort Union formation can be drilled and completed without the use of hydraulic fracturing. In the past, water or sand/water mixtures have been used to fracture the coal (EPA, 2002).

The operators in the PRB routinely perform a procedure called "water-enhancement" and it is intended to create pathways in the coal for easier flow of water and gas into the well. This procedure results in the fracturing of the coal. In Figure 4.13a a water-enhancement test plot from the Powder River Basin is shown. The upper and lower panels show the flow rate in gpm (gallons per minute) and barrels/min respectively. The middle panel shows the pressure-time history while the water was being pumped into the well. When a fracture is produced during the water-enhancement procedure, the pressure-time history from the water-enhancement test (middle panel in Figure 4.13a) is similar to the pressure-time history of an extended Leak-off Test (Figure 4.13b). The water-enhancement test data shows that large volumes of water are pumped into the coal while the pressure remains constant. This indicates the formation of a hydraulic fracture and its propagation. The extent of a hydraulic fracture is controlled by the pumping pressure and the variation of the least principal stress with depth. I have also confirmed that such "enhancement" activities result in hydraulic fracturing of the coal through direct interviews with the different operators in the Powder River Basin.

Even though hydraulically fracturing the coal might be intended to render good results for CBM production, if such a fracture is vertical and extends up into adjacent strata, it could result in both excess CBM water production and inefficient depressurization of coals. As can be seen in Figure 4.14, if the hydraulic fracture propagates vertically through the coal seam and through a confining unit, then the migration of groundwater toward the producing well occurs. Avoiding this can result in great benefits for the operators and the environment.

To determine the direction of propagation of a hydraulic fracture it is necessary to know the magnitude of the least principal stress (S_3) since a hydraulic fracture will

always propagate perpendicular to the orientation of S_3 (Figure 4.15). Therefore, if S_3 corresponds to the minimum horizontal stress, this indicates that the hydraulic fracture propagates in a vertical plane and if S_3 corresponds to the overburden stress, this indicates that the hydraulic fracture will propagate in the horizontal plane. Even though the water enhancement tests in the PRB are not made with the intention of determining the magnitude of S_3, they are a useful resource since it is possible to determine such magnitude from these tests (see following section).

It has been suggested that after a relatively short period of production (several months), an appreciable amount of the water produced from CBM wells may come from the formations adjacent to the coal seams (personal communication with several operators, 2002-2003). It seems that one factor possibly exacerbating this is the vertical growth of hydraulic fractures during the drilling and completion of CBM wells. I will test this by analyzing the relationship between hydraulic fracture orientation and water and gas production.

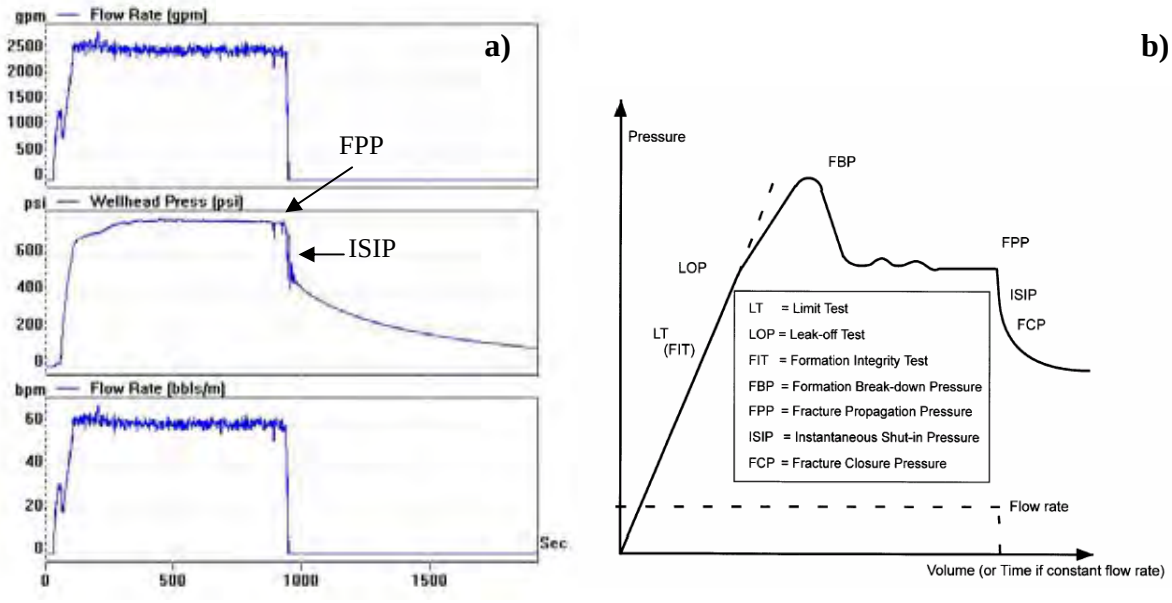

Figure 4.13. a) Water-enhancement test from a CBM well in the PRB. b) Schematic illustration of an extended Leak-off Test (after Gaarenstroom et al. in Zoback et al., 2003).

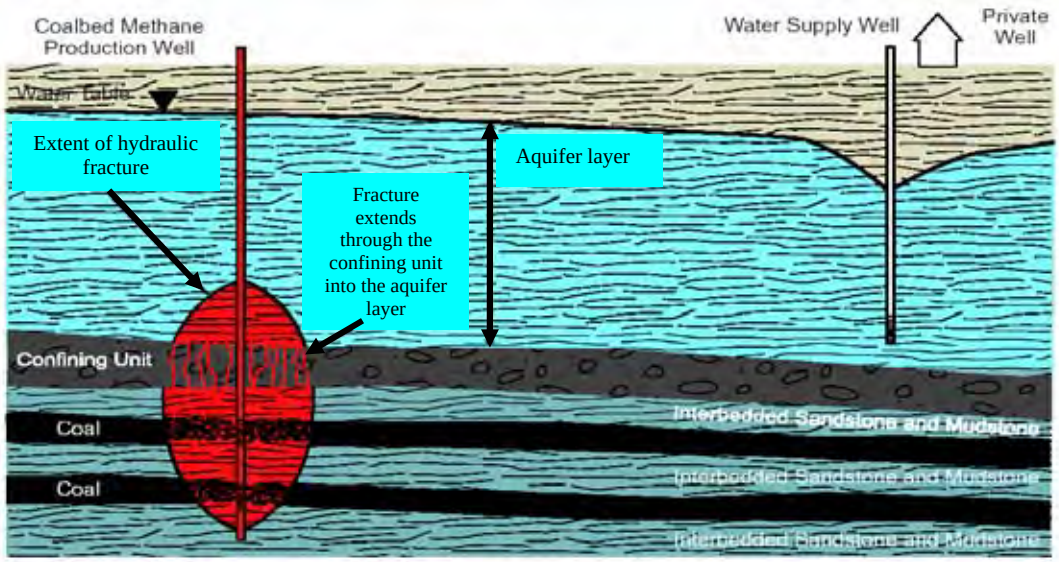

Figure 4.14: Vertical growth of a hydraulic fracture (EPA, 2002).

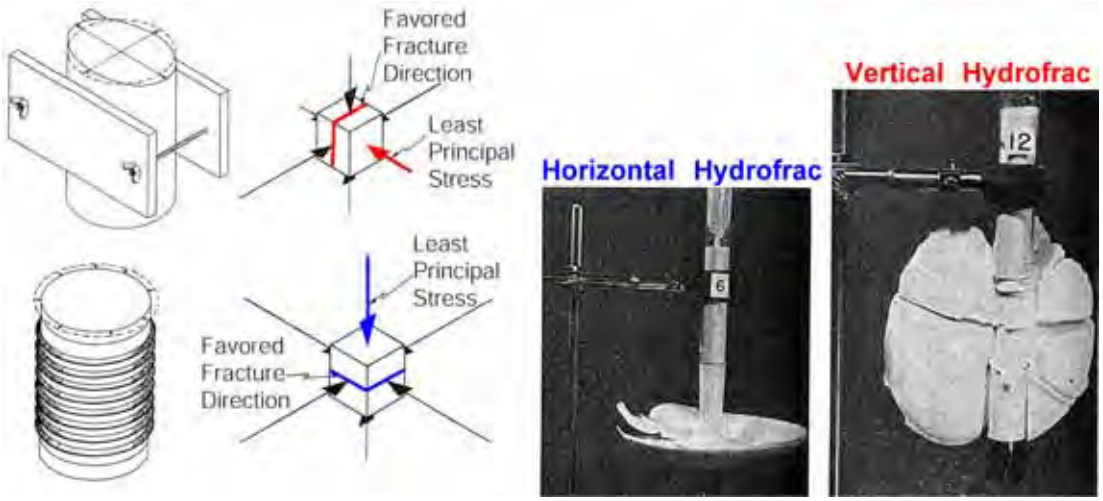

Figure 4.15. Hydraulic fractures always propagate perpendicular to the orientation of the least principal stress.

4.6 LEAST PRINCIPAL STRESS (S_3) IN THE POWDER RIVER BASIN

4.6.1 Data Analysis per Area

As mentioned earlier, the magnitude of the least principal stress can be obtained from the water-enhancement tests. Figure 4.13a shows that at the surface the Fracture Propagation Pressure (FPP) is 750 psi and the Instant Shut-in Pressure (ISIP) is 600 psi. To determine the magnitude of the least principal stress at the depth of this test, it is necessary to add the pressure in the wellbore due to the column of wellbore fluid.

To date, I have analyzed water-enhancement tests from 550 wells, and obtained the magnitude of the least principal stress (S_3) for 372 of these wells. The wells locations of are shown in Figure 4.16. Figures 4.17 to 4.20 show the analyzed data, which have been grouped by location (areas A, B, B1, B2, C and D shown in Figure 4.16). The colors represent the producer coal interval in the respective wells, the black line is the overburden stress or S_v and the gray line corresponds to the hydrostatic pressure or P_{hyd} (0.44 psi/ft).

The magnitude of S_v can be calculated by integration of rock densities from the surface to the depth of interest, z, that is

$$S_v = \int \rho(z) g dz \approx \bar{\rho} g z$$

where $\rho(z)$ is the density as a function of depth, g is the gravitational acceleration constant and $\bar{\rho}$ is mean overburden density. Since density logs were not available, a mean overburden density was assumed equal to 2.3 g/cc, which reflects the different lithologies that can be found above the coal (i.e. mudstones, shales, sandstones).

It is important to note that in some of the figures that follow, the ISIP's fall above the line denoting the overburden stress, which indicates that the magnitude of S_3 is greater than the magnitude of the overburden. Possible causes are the shallow depth of the measurements or the large volumes of water used in the water-enhancement test. At shallow depths the overburden might not be one of the principal stresses and therefore the ISIP's could be larger than the overburden. With respect to the other possible cause, since water enhancement tests are not originally intended to determine the magnitude of S_3, the

large flow rate used in the tests could create friction effects that might disguise the actual magnitude of S_3. To reduce the uncertainty in determining the magnitude of S_3, water-enhancement tests made at lower flow rates (1 – 4 bpm instead of 60 bpm) would be more suitable for the determination of the least principal stress.

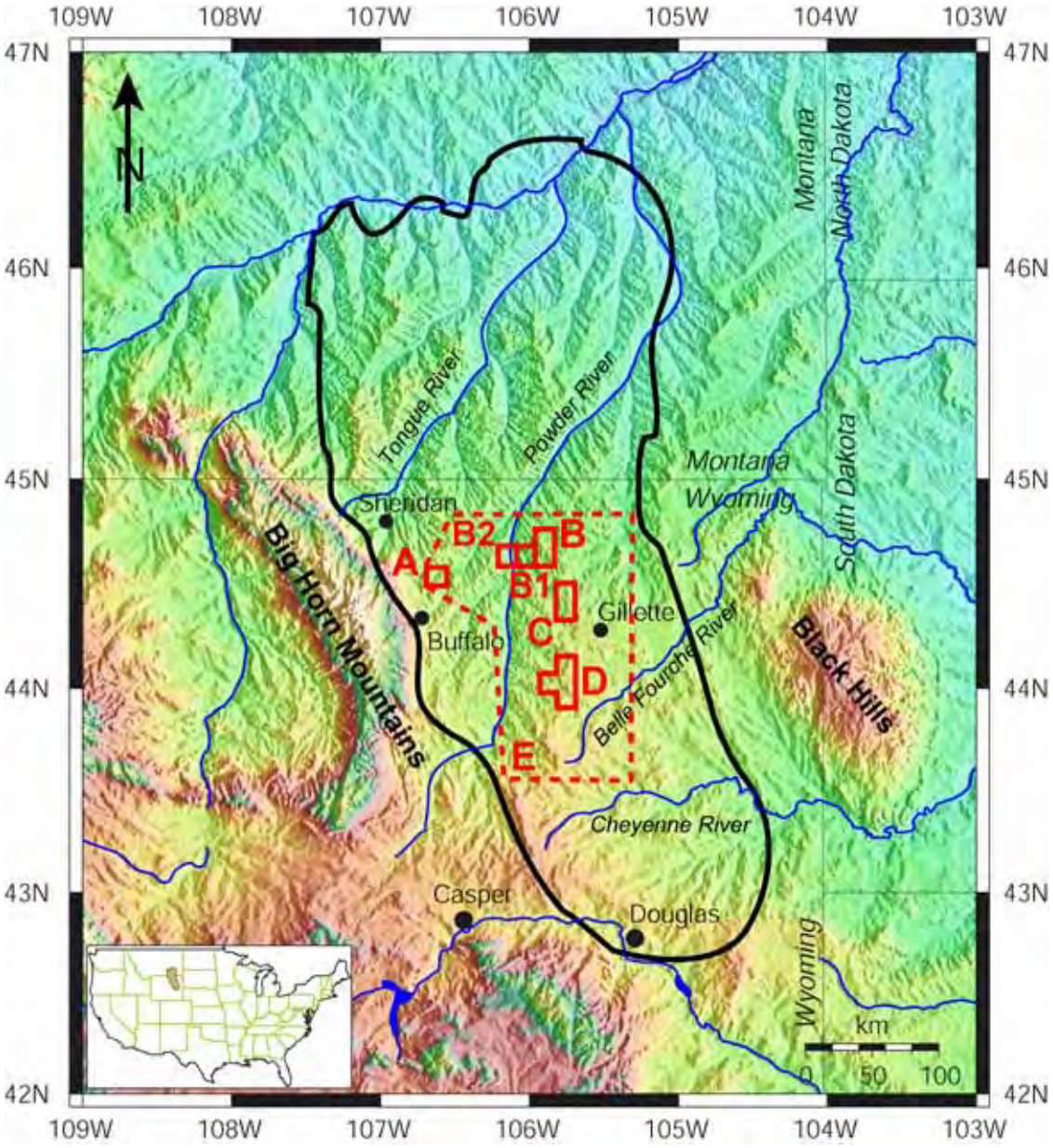

Figure 4.16: Water-enhancement tests data from 550 wells were obtained from the locations delineated by red lines. The letters identify the grouping of the fields in the areas I analyzed. The data from Figures 4.17 to 4.20 all come from areas A to D. The dashed red line encompasses the total area (E) from where all the data were obtained.

In the following paragraphs, I will present the least principal stress and overburden versus depth data separated by the different areas indicated on Figure 4.16 (to see more data of S_3 vs depth, please refer to Appendix 4.A):

Area A

All the data from the 12 wells in Area A come from the Roland coal, which is at a depth between 600 and 800 ft (Figure 4.17a). The magnitude of the least principal stress is approximately equal to the overburden. Therefore, since the overburden corresponds to the least principal stress, the hydraulic fractures produced in this area propagate in a horizontal plane. This may be a significant finding, as water injection wells are perhaps needed in the near future in this region because the water has a high content of sodium and will need to be properly disposed. Thus, knowing that there is no vertical connection between the coal seam that is being produced and the sand layers where the water may be injected is particularly important for the operators of the area if water injection activities are undertaken here.

Area B

The data in Area B is from 50 wells that are producing from either the Anderson, Cook, Canyon, Smith, Stray or Wall coals (Figure 4.17b). Down to a depth of 850 feet (Anderson, Cook, Canyon, Smith, and Stray coals), the magnitude of the least principal stress appears to correspond to the overburden, which indicates horizontal propagation of the hydraulic fractures. This implies that the coals just mentioned are not connected to adjacent formations, an important aspect to know if injection is needed in this area. In the Wall coal, between 850 ft and 1200 ft, the magnitude of the least principal stress is generally below the overburden. Therefore, for the Wall coal, most hydraulic fractures would appear to propagate in the vertical direction.

Area B1

Area B1 is just to the West of Area B and all 9 wells are in the Anderson coal. Water enhancement tests from these wells indicate that the least principal stress is clearly the minimum horizontal stress (Figure 4.18a) as it is well below the vertical stress.

Therefore, the fractures propagate vertically. It is important to note that for these wells the Anderson coal is about 200 ft deeper than in area B.

Area B2

West of area B1, stress data from the Anderson coal in Area B2 shows that the least principal stress can either be the overburden (5 wells) or the minimum horizontal stress (13 wells), as can be seen in Figure 4.18b. This indicates that both types of hydraulic fractures are produced in this area. At this location, the Anderson coal spans from a depth of ~500 ft to 1000 ft deep.

Area C

South of Area B, the magnitude of the least principal stress from 13 wells in the Anderson and Canyon coals in Area C corresponds to the minimum horizontal stress (Figure 4.18c). Thus, vertical hydraulic fracturing is expected in this region. In Area C the Anderson coal spans between 600 and 1000 ft, similar to Area B2.

Area D

In Area D the data come from 61 wells in the Big George and Wyodak coals. For the Big George coal, all the wells located in T47N R75W and most of the wells in T46N R74W (Figure 4.19c) have water enhancement tests that indicate that the least principal stress corresponds to the minimum horizontal stress, i.e. the fractures would be expected to propagate vertically (Figure 4.19a). All the wells located in T47N R74W and some of the wells located in T46N R74W (Figure 4.19c) show that the magnitude of the least principal stress corresponds to the overburden, i.e. the fractures propagate horizontally (Figure 4.19b). For the Wyodak coal a geographic differentiation is also seen. As can be observed in Figure 4.20a, in the wells located in sections 1, 2, 11, 12, 13, 14, 23, 24, 26 and 36 of T48N R74W (Figure 4.20c), the fractures propagate vertically. In sections 15 and 21, of the same township (Figure 4.20c), the fractures are expected to propagate horizontally (Figure 4.20b).

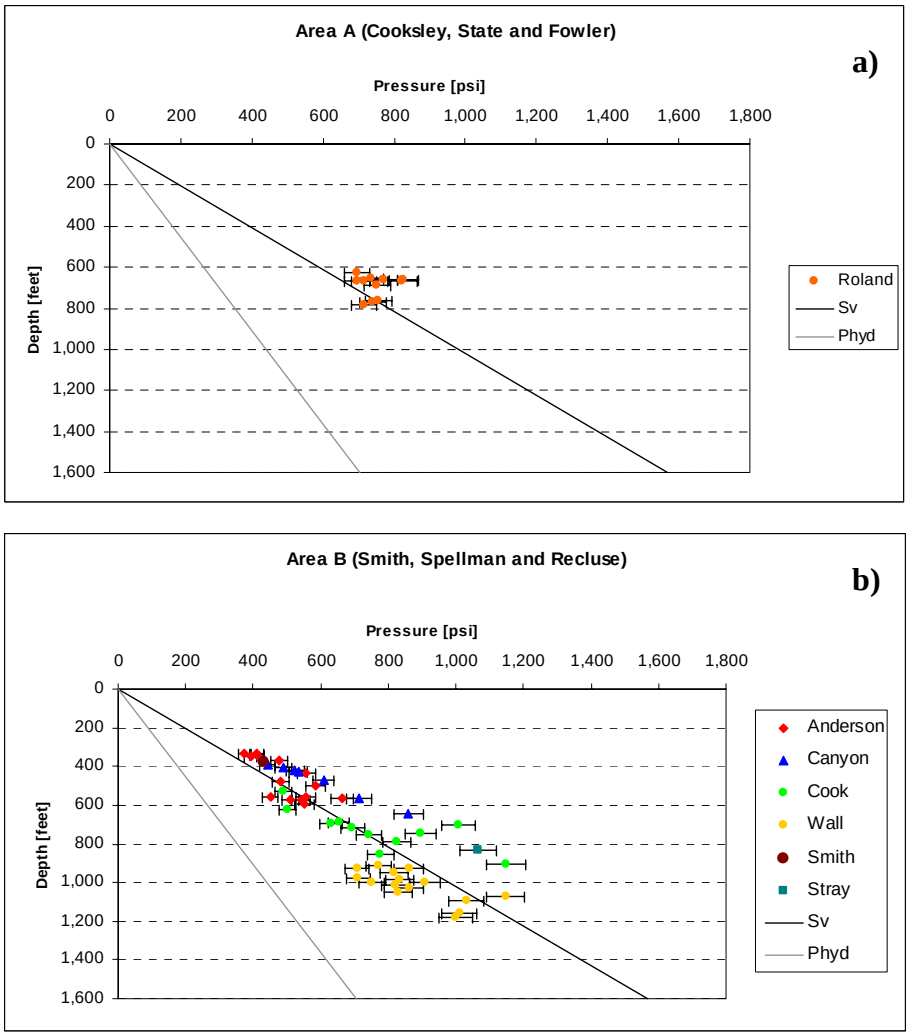

Figure 4.17: Magnitude of S_3 in the Powder River Basin vs. depth. The data has been plotted per geographic location and the color denotes the coal seam where the test was performed. a) Area A and b) Area B. The location of areas A and B can be seen in Figure 4.16.

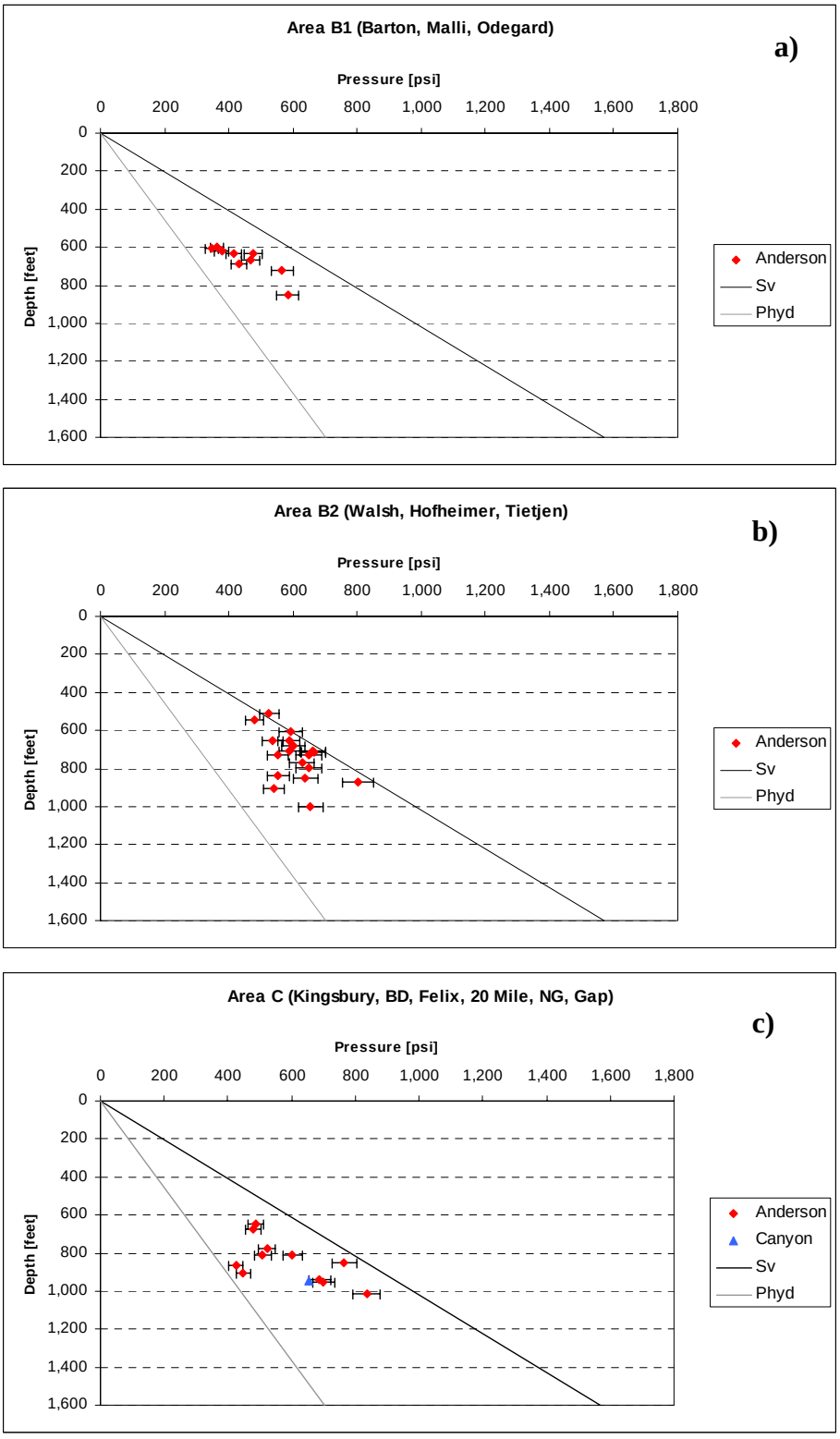

Figure 4.18: Magnitude of S_3 in the Powder River Basin vs. depth. The data has been plotted per geographic location and the color denotes the coal seam where the test was performed. a) Area B1, b) Area B2 and c) Area C. The location of these areas can be seen in Figure 4.16.

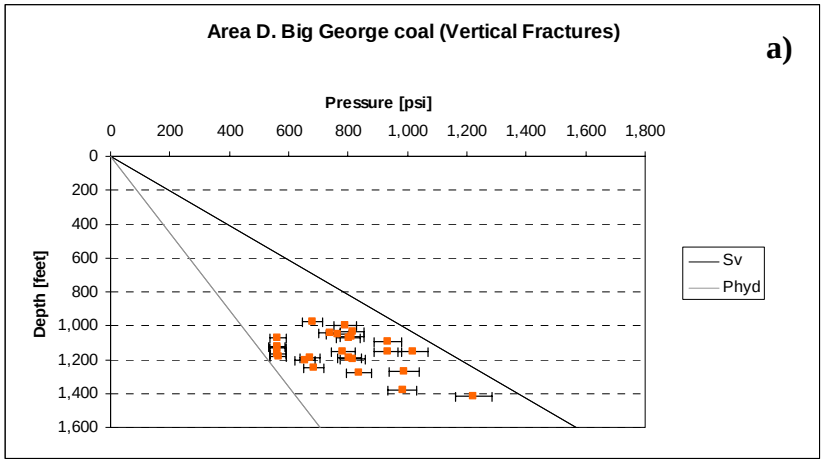

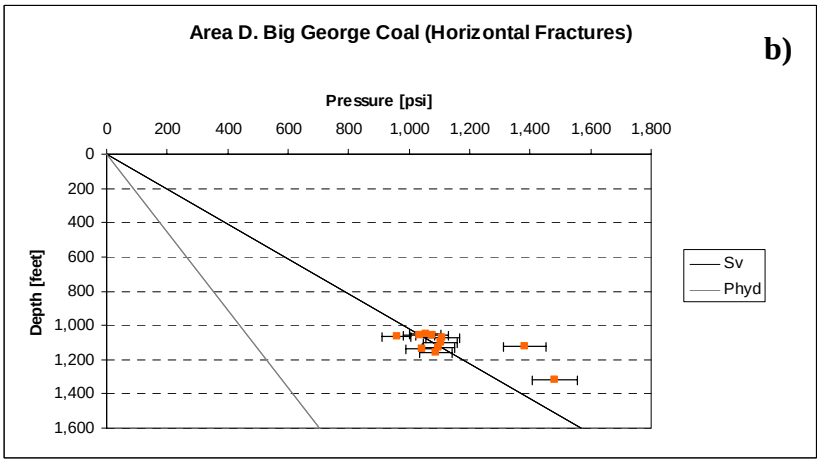

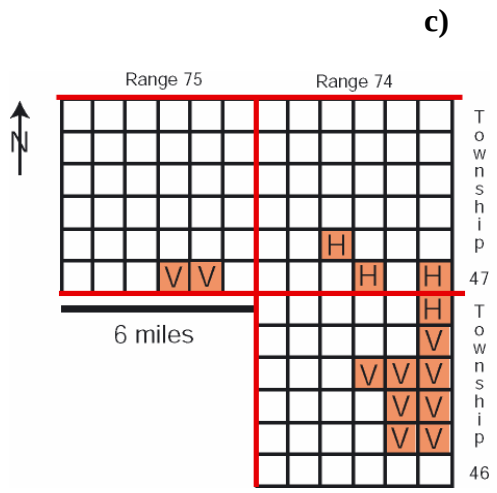

Figure 4.19: Magnitude of S_3 in the Powder River Basin vs. depth for the Big George coal in Area D. a) S_3 corresponds to the minimum horizontal stress, b) S_3 corresponds to the vertical stress and c) Occurrence of horizontal (H) and vertical (V) hydraulic fractures in Area D. The location of this area can be seen in Figure 4.16.

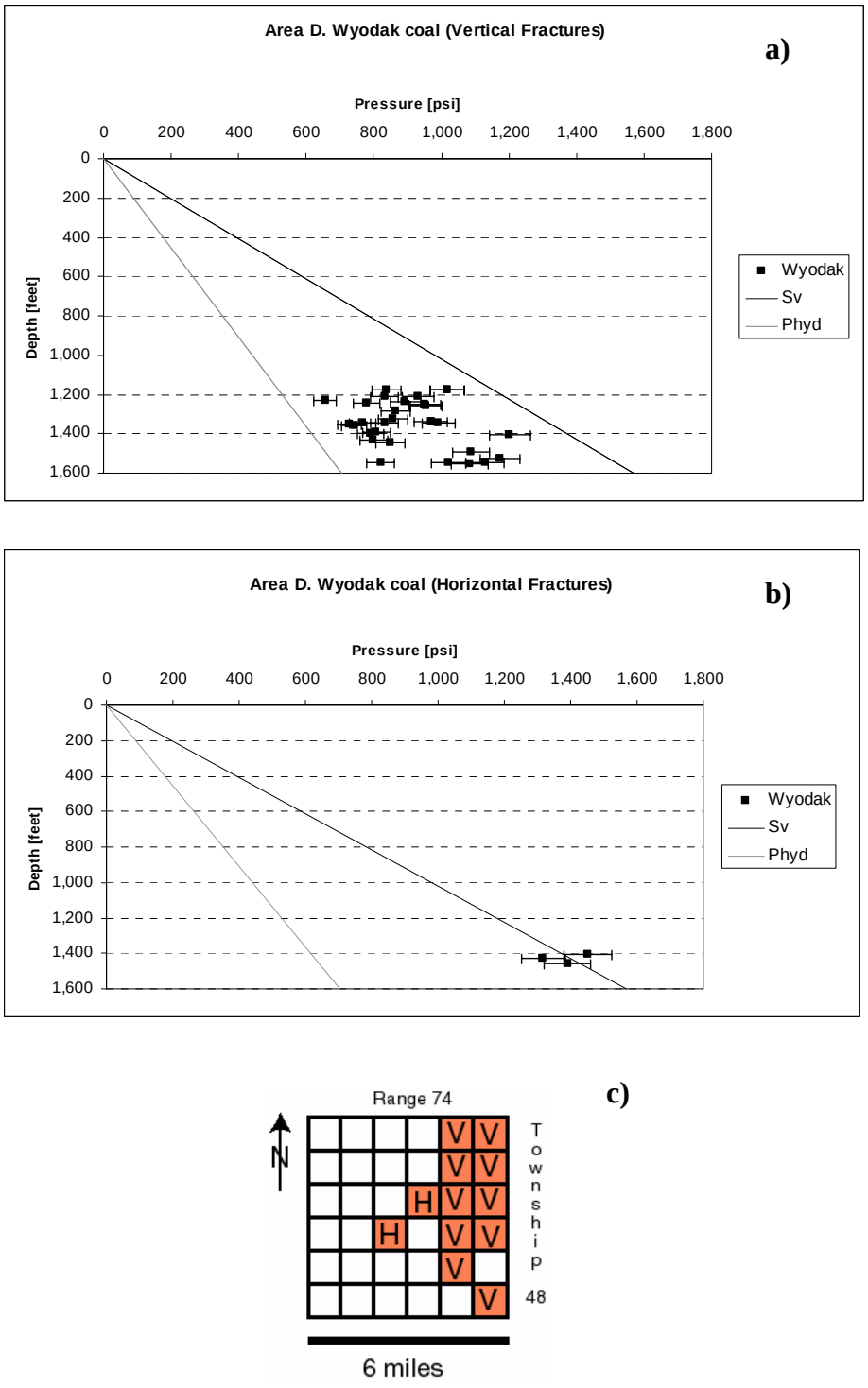

Figure 4.20: Magnitude of S_3 in the Powder River Basin vs. depth for the Wyodak coal in Area D. a) S_3 corresponds to the least horizontal stress, b) S_3 corresponds to the vertical stress and c) Occurrence of horizontal (H) and vertical (V) hydraulic fractures in Area D. The location of this area can be seen in Figure 4.16.

4.6.2 Variation of the Least Principal Stress (S_3) Across the Basin

As mentioned earlier, the magnitude of the least principal stress has been determined from water-enhancement tests for wells targeting different coal seams in the basin. Maps of the occurrence of vertical and/or horizontal fractures in the central part of the basin have been made for each coal. However, water-enhancement test data have come only from ~550 wells, representing 4% of the total amount of wells in the Powder River Basin. Therefore, more data are needed to make the maps more complete.

In Figures 4.21 to 4.27, the blue color represents areas where the fractures are horizontal, that is $S_3 = S_V$ ($S_3/S_V = 1$). The red shades represent areas where the fractures are vertical, that is $S_3 = S_{hmin}$, ($S_3/S_V < 1$). These maps were made using the interpolation tool from GMT (the Generic Mapping Tool; Wessel and Smith, 1995). The areas that do not have any points, are areas where there is no control over the interpolation and should be interpreted carefully, hence, the question marks. The interpolation for each coal was made with the numbers of points outlined in Table 4.1. Many of the wells (data points) are situated very close to each other, so the symbols for some wells overlap, or plot on top of each other.

From Figures 4.21 to 4.27 it can be seen that vertical and horizontal fractures occur in many areas of the basin. However, it seems that north of the cities of Gillette and Buffalo, horizontal fracturing is more common than vertical fracturing. It appears that for places where the coal is thinner, there is more possibility of horizontal fracturing. For instance, in Big George (Figure 4.22) and Wyodak (Figure 4.27), which are thick coals, areas with vertical fractures are more common than areas with horizontal fractures. Conversely, for Anderson, Canyon, Cook, Werner and Wall, which are thinner coals, areas with horizontal fractures seem to be more common. It is important to mention that Figure 4.24 was obtained by combining the data of Cook and Werner coals since these two coals are the same but have received different names at one time or another.

The reliability of the maps could be improved if not only more least principal stress data are acquired but also if a consensus on the naming of coals could be reached to ensure a consistent classification.

These maps are potentially very useful for future developments in the basin. The operators could use the maps as tools to easily identify areas where potential fractures could propagate in the vertical or horizontal plane. If the operators know in advance that they would cause vertical fracture growth with their enhancement techniques, they could then limit the amount of water they use in the tests to hopefully limit the extent of vertical fracture propagation.

Table 4.1. Number of data points used to make the interpolation of S_3/S_V for each coal seam.

Coal seam	**# of data points**
Anderson	79
Big George	76
Canyon	44
Cook	14
Wall	38
Werner	9
Wyodak	91

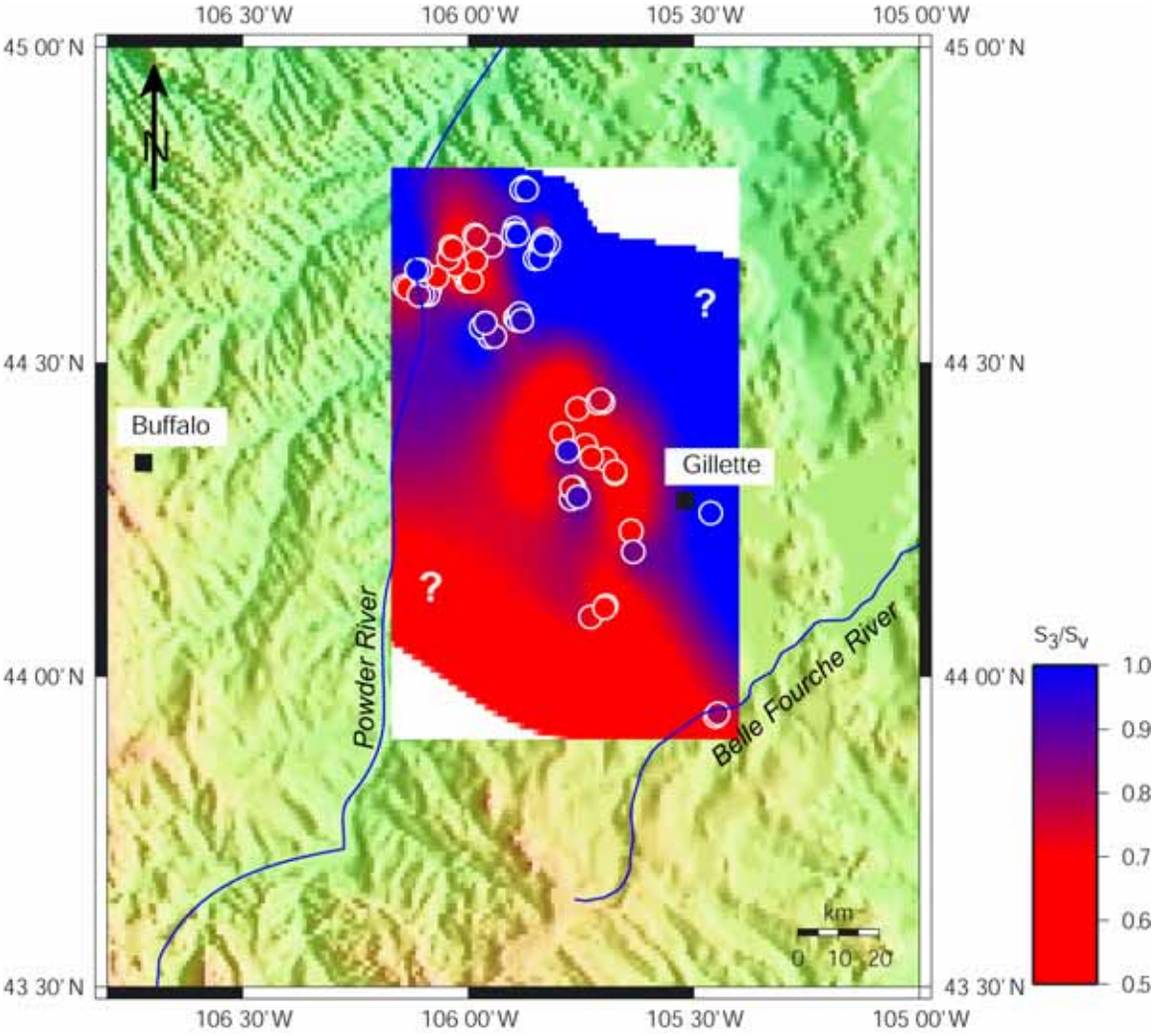

Figure 4.21: Map showing variation of S_3/S_v for the Anderson coal. The circles are actual data points. If $S_3/S_v = 1$, horizontal fractures are expected. If $S_3/S_v < 1$, vertical fractures are expected.

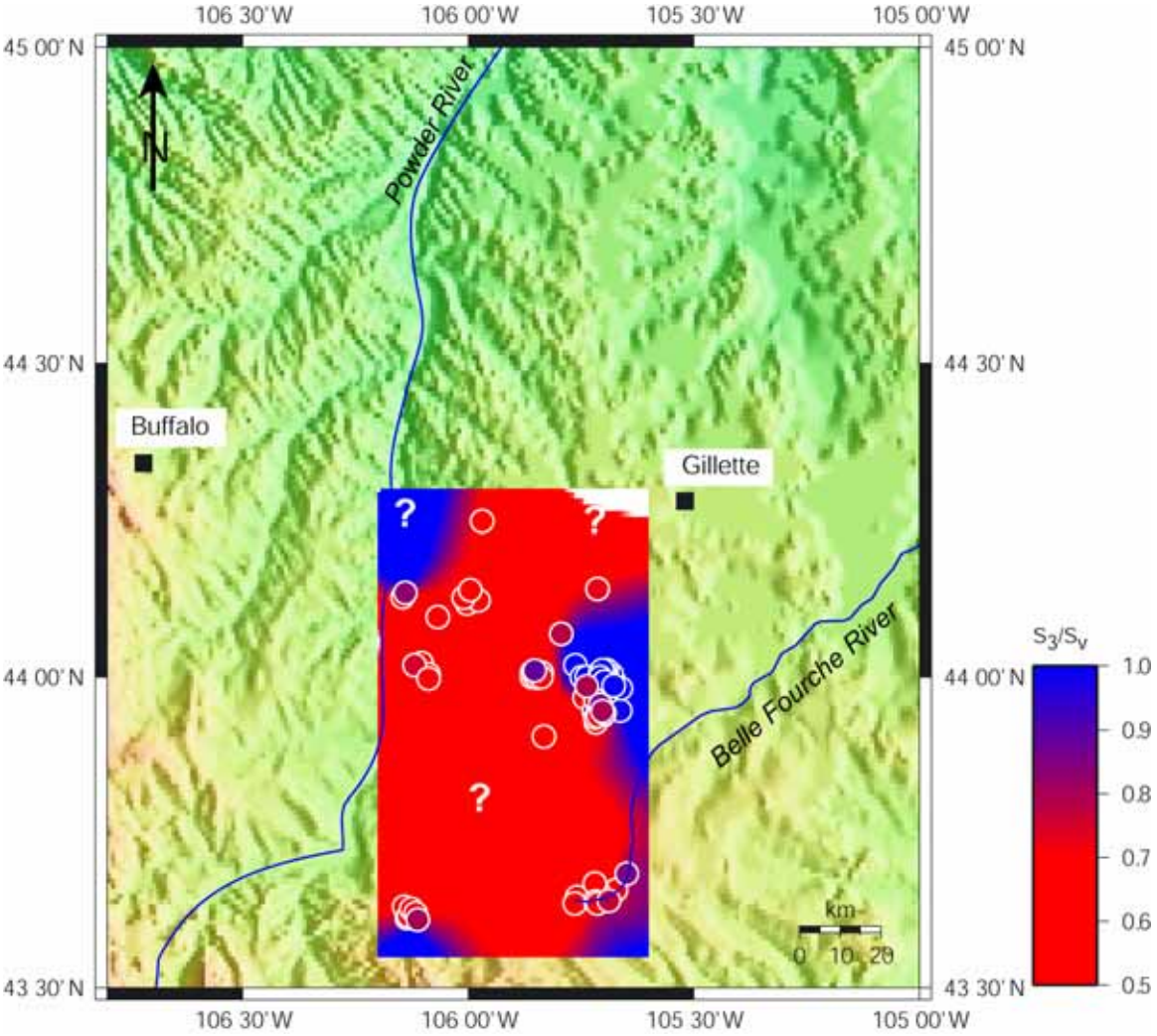

Figure 4.22: Map showing variation of S_3/S_v for the Big George coal. Explanation as in Figure 4.21.

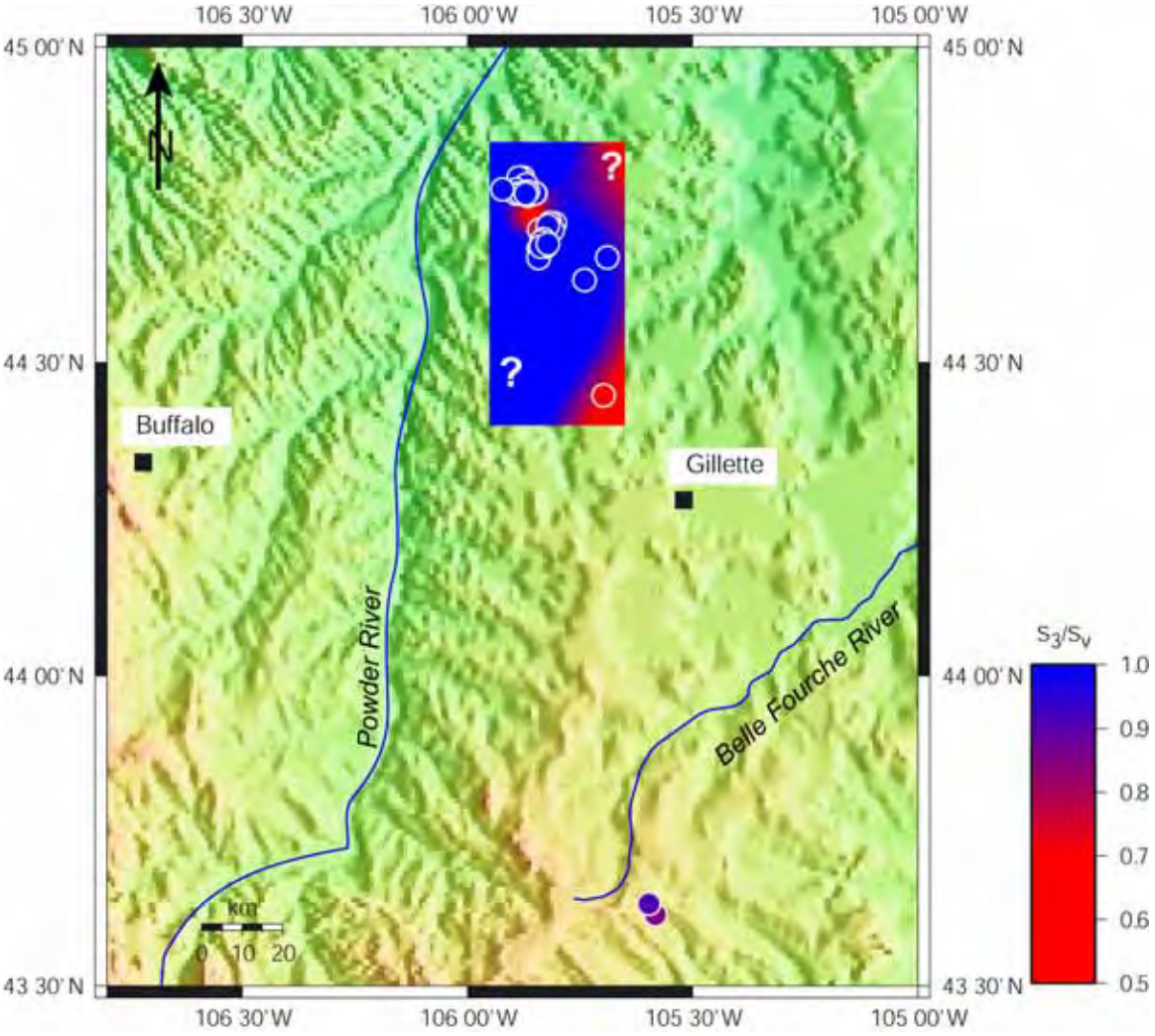

Figure 4.23: Map showing variation of S_3/S_v for the Canyon coal. Explanation as in Figure 4.21.

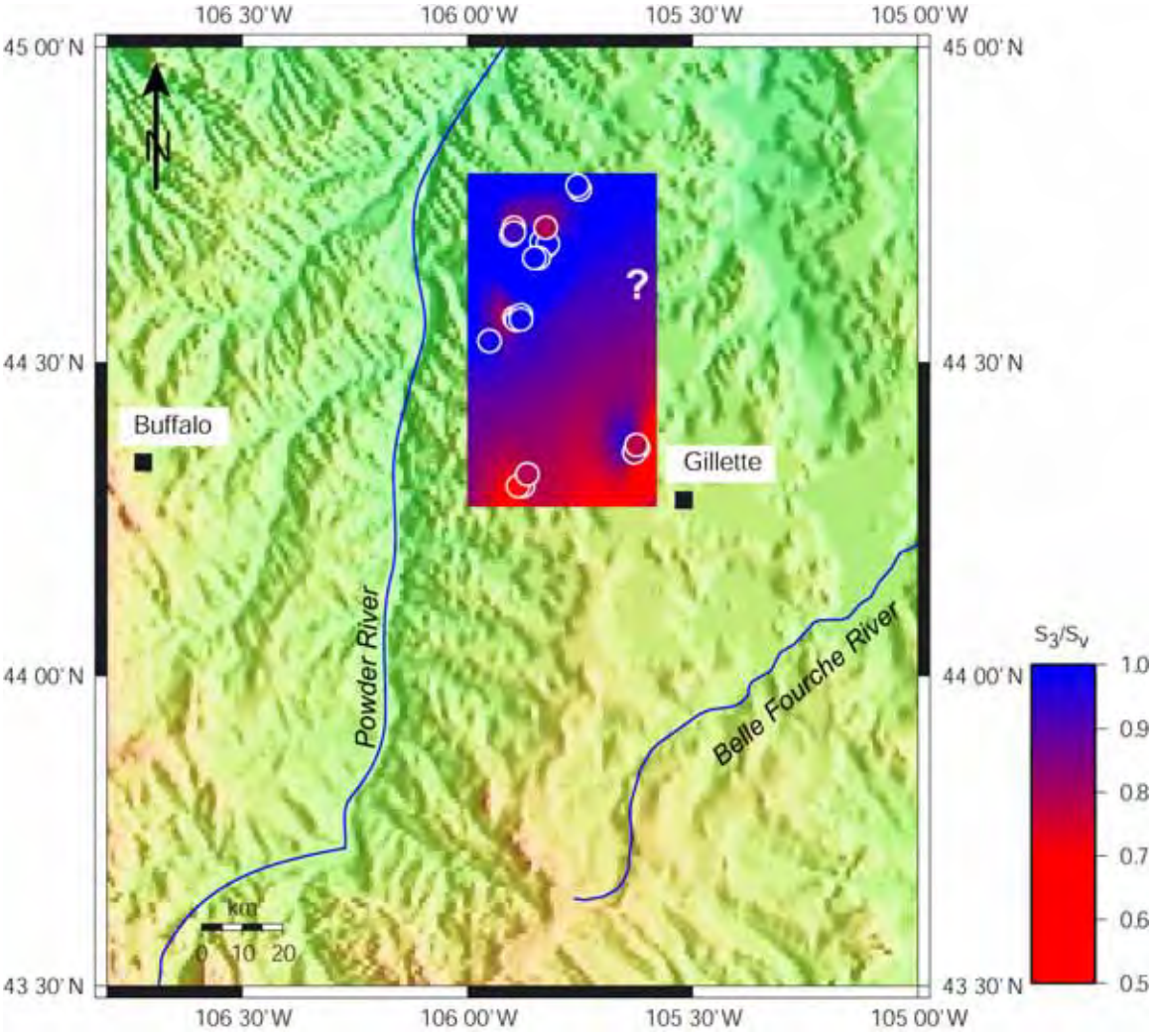

Figure 4.24: Map showing variation of S_3/S_v for the Cook-Werner coal. Explanation as in Figure 4.21.

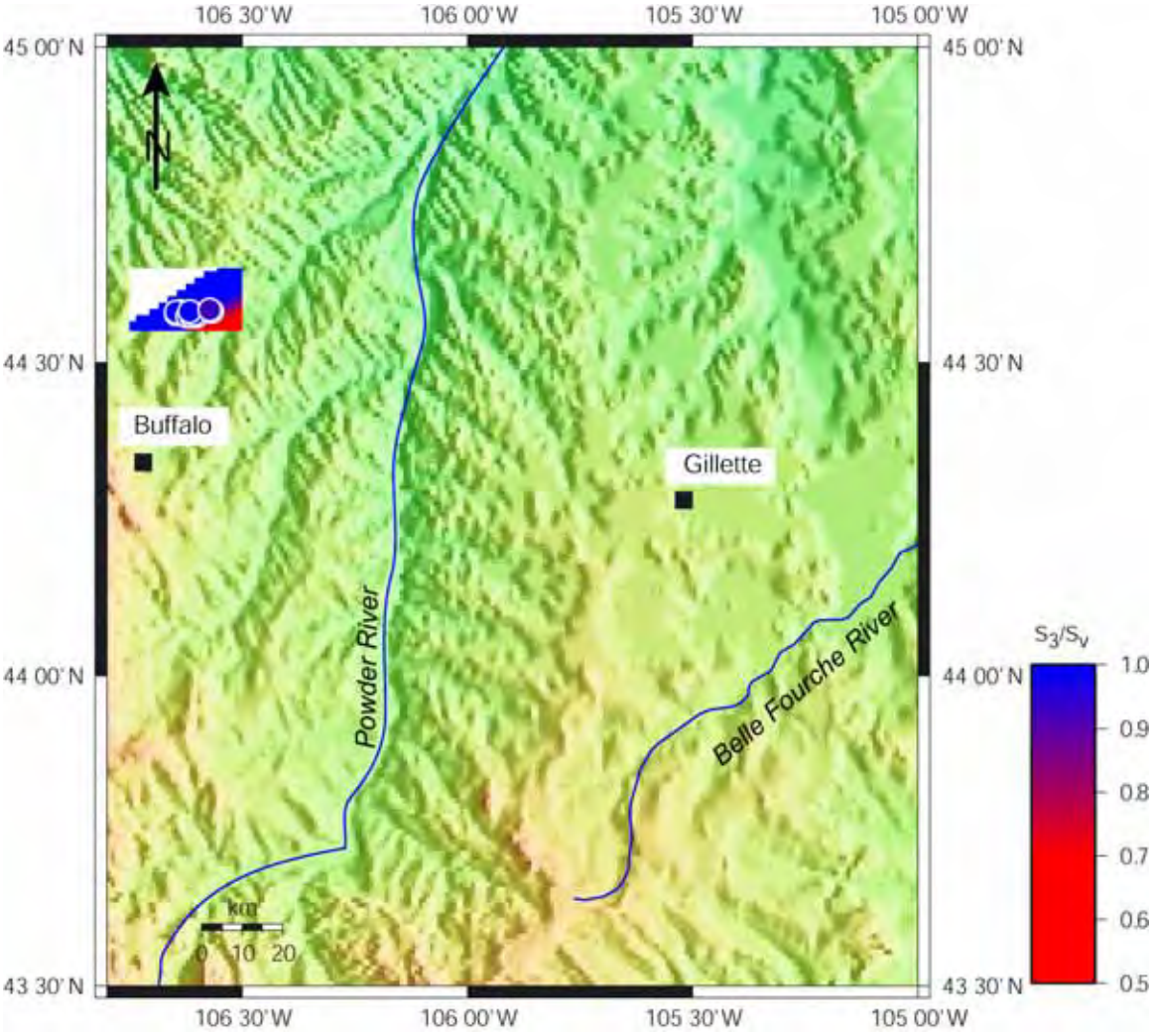

Figure 4.25: Map showing variation of S_3/S_v for the Roland coal. Explanation as in Figure 4.21.

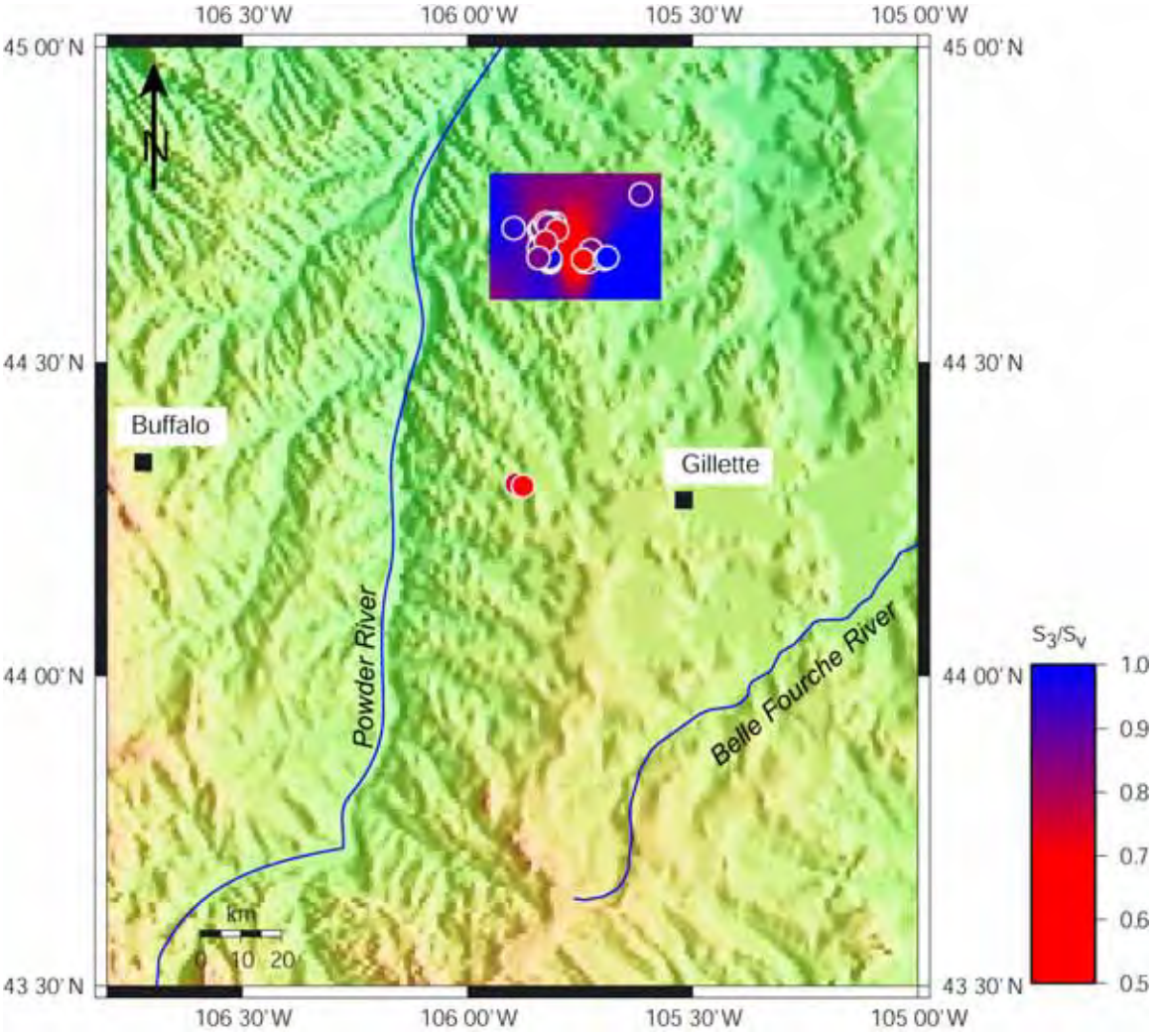

Figure 4.26: Map showing variation of S_3/S_v for the Wall coal. Explanation as in Figure 4.21.

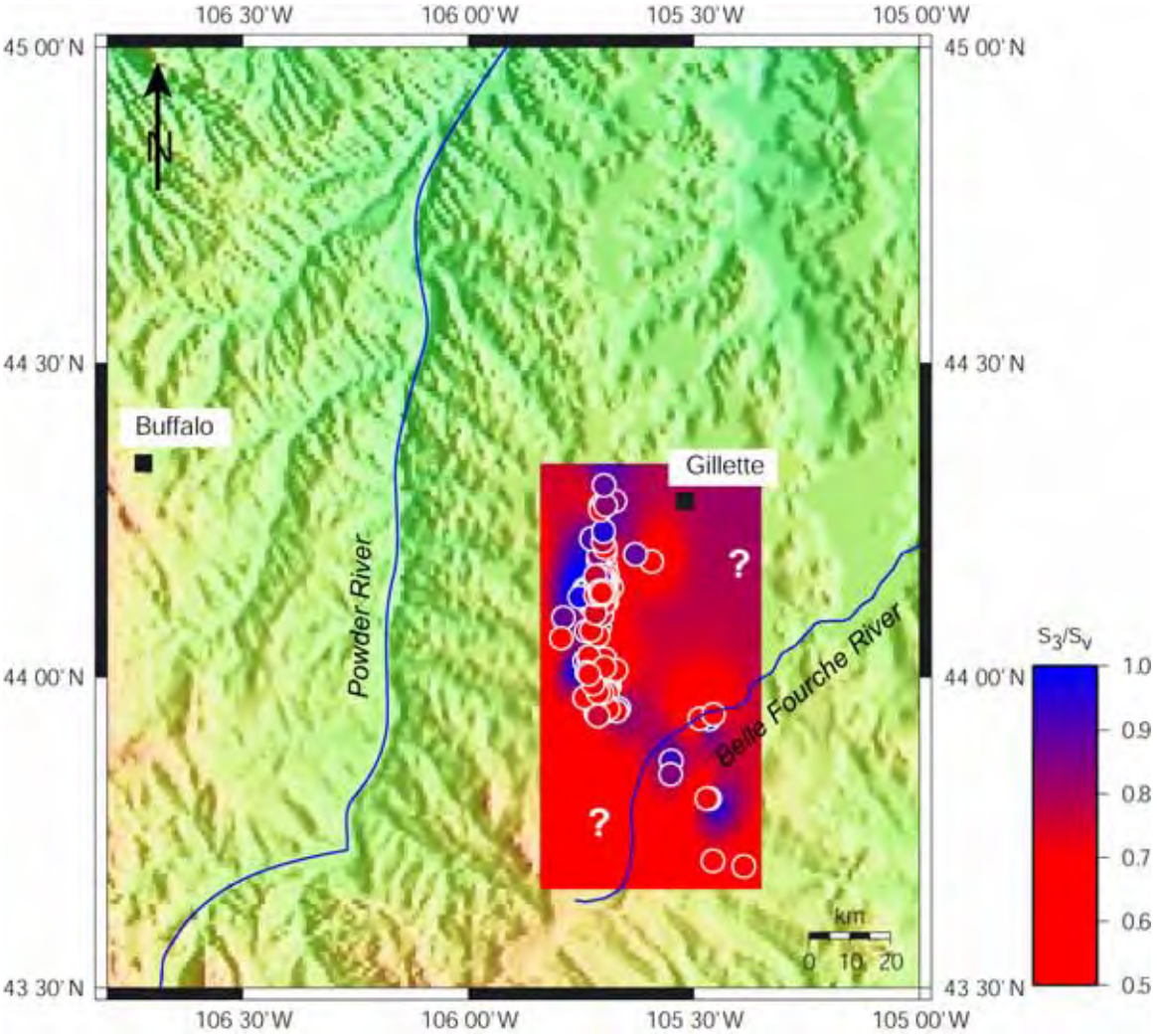

Figure 4.27: Map showing variation of S_3/S_v for the Wyodak coal. Explanation as in Figure 4.21.

4.6.3 Possible Causes for the Variation of S_3 in the Basin

Thickness

The differential stress appears to be larger in thicker coals than in thinner coal beds (Figures 4.28, 4.30 and 4.31). This means that in thicker coals the difference between the overburden and the least principal stress is large and the propagation of fractures occurs in the vertical direction. For thinner coals, the difference between S_V and S_3 is smaller and S_V is often the least principal stress, in which case fractures propagate in the horizontal direction.

For thinner coals it is possible to obtain magnitudes of S_3 equivalent to S_V and also equivalent to the minimum horizontal stress. However, the difference between S_V and the minimum horizontal stress is not large, i.e. assuming that S_V is S_1, the differential stress is small. For thicker coals the magnitude of the least principal stress is equivalent to the minimum horizontal stress and the difference between S_3 and S_V is large, which indicates that the differential stress is also large.

For the Big George coal there seems to be a direct relationship between thickness and the magnitude of S_3 (Figure 4.28). In fact, when the Big George coal is thicker than 47 feet, only vertical fractures occur in this coal. Mapping the thickness of the Big George coal (Figure 4.29) and comparing it with the map of S_3/S_V (Figure 4.22) it can be seen that the region in the central part of the map is most probably a vertical-fracture-prone area because the thickness of the Big George coal at this location is much greater than 47 feet (for more information see Appendix 4.D).

For the other coals (Anderson, Canyon, Wall and Wyodak), the magnitude of S_3/S_V is less than 0.9 at thickness greater than 60 ft, which implies that only fractures propagating in the vertical plane will occur at thickness greater than 60 ft in these coals. There is not enough data available to make any interpretations about thickness and fracturing in the Werner coal.

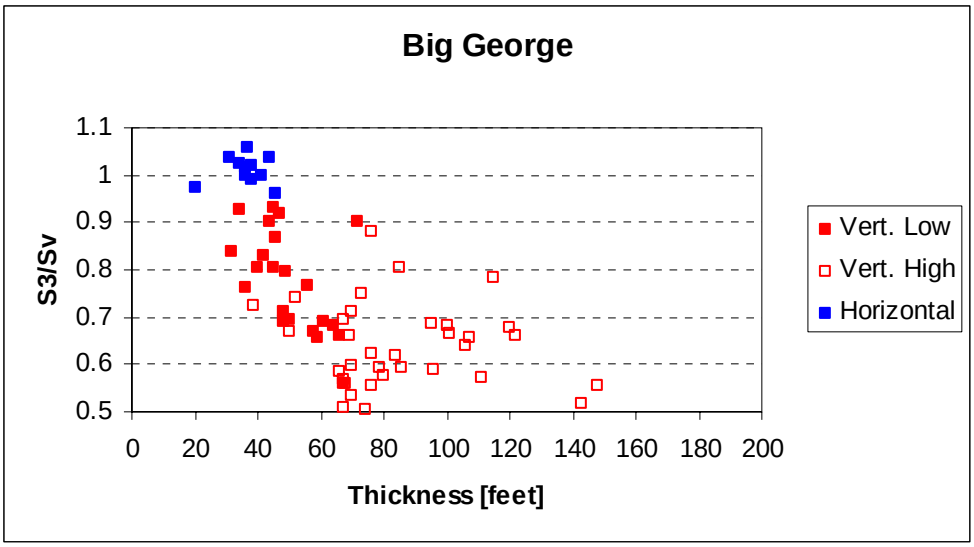

Figure 4.28: S_3/S_V vs thickness for Big George coal.

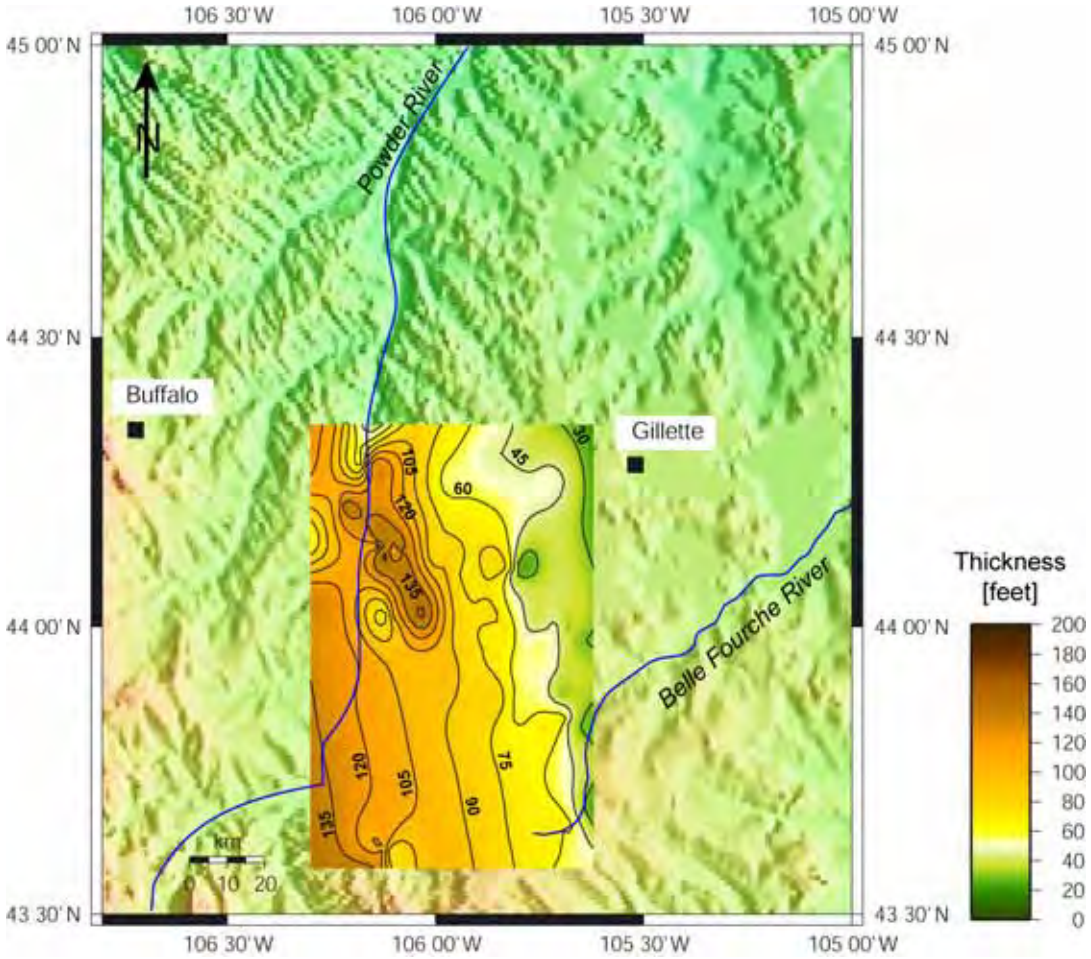

Figure 4.29: Thickness of Big George. Note that towards the center of the map, Big George is thicker.

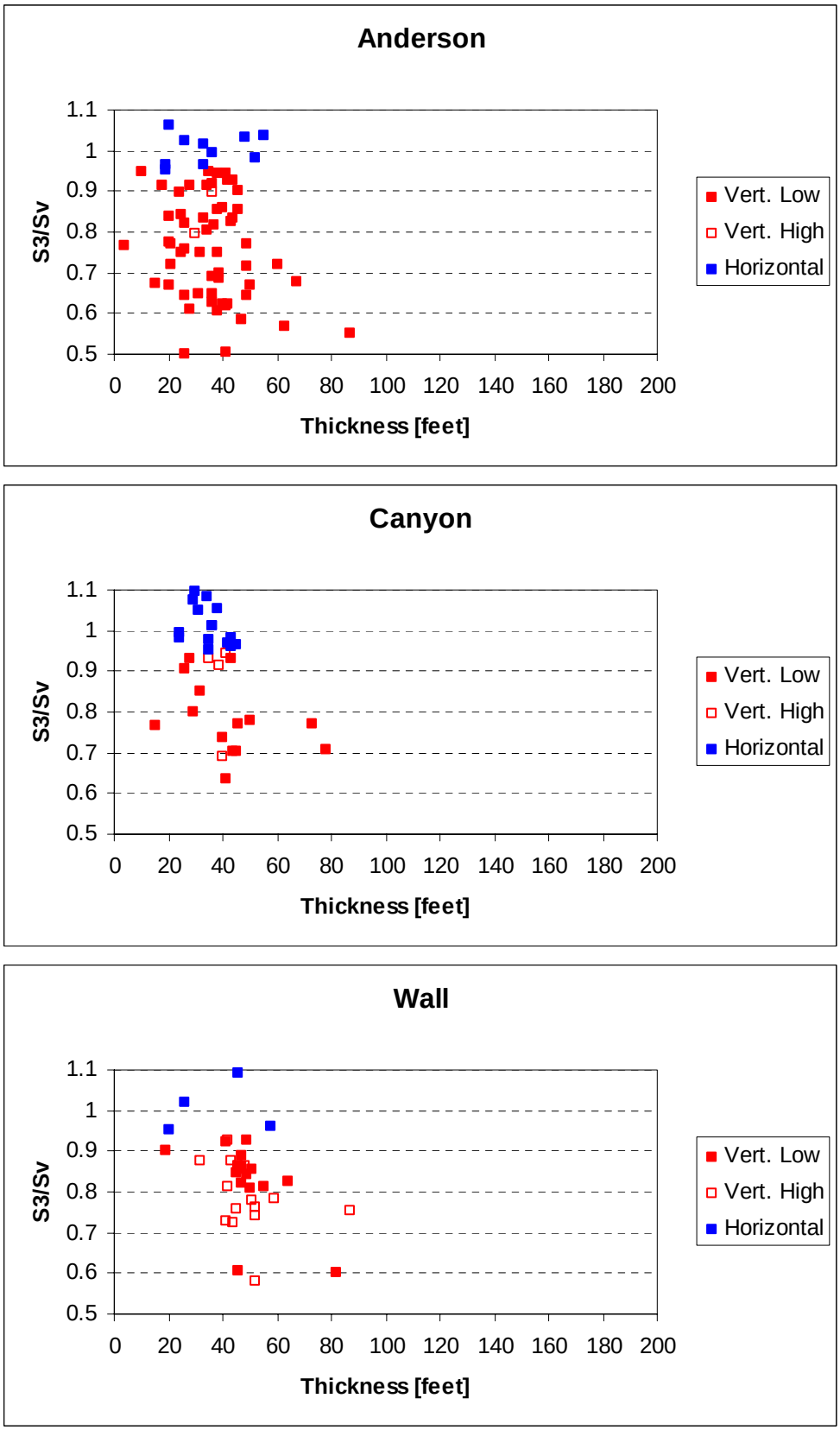

Figure 4.30: S_3/S_V versus thickness for Anderson, Canyon and Wall coals.

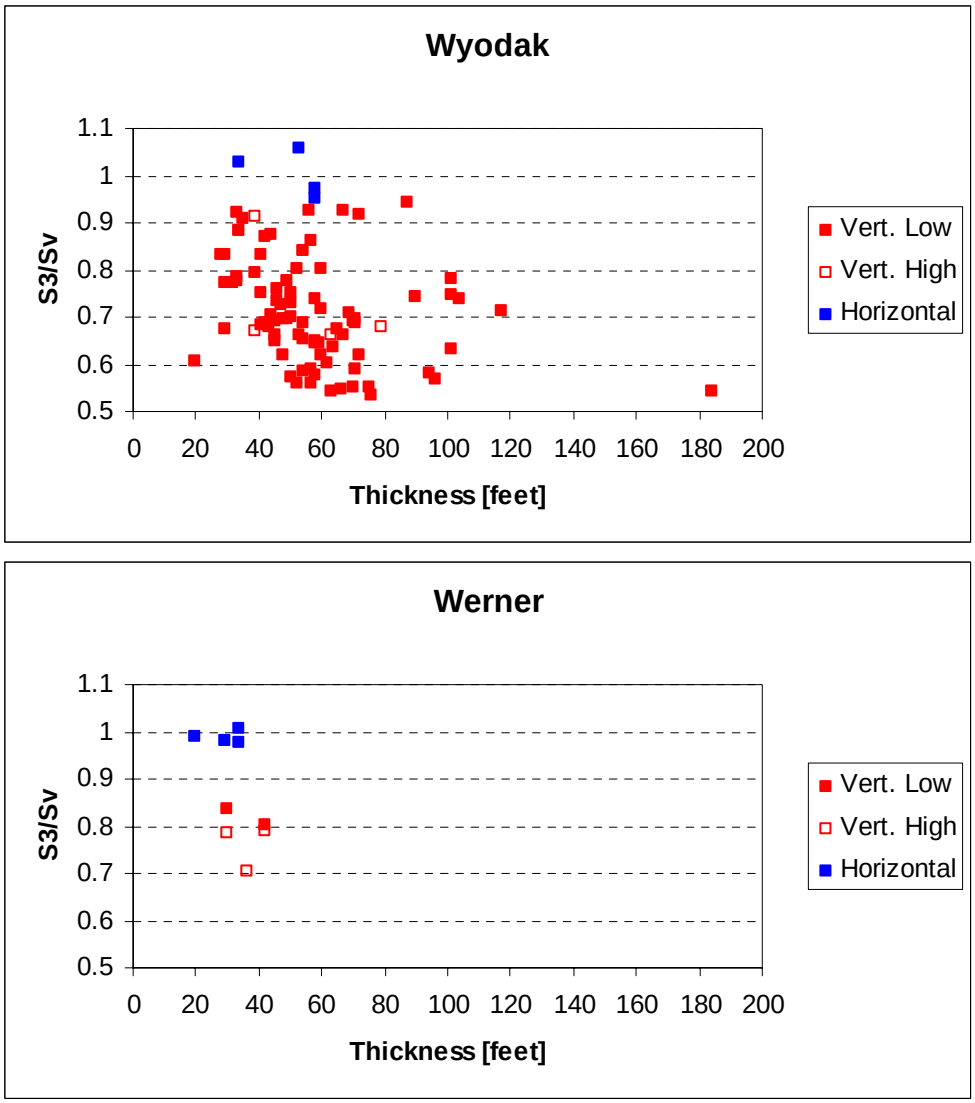

Figure 4.31: S_3/S_V versus thickness for Wyodak and Werner coals.

Pore Pressure Changes

Even though changes in pore pressure might not necessarily imply large changes in the magnitude of S_3, it was necessary to investigate this hypothesis. Figures 4.32 and 4.33 show a map with interpolated values of P_{obs}/P_{hyd} (observed pressure over hydrostatic pressure) for the Big George and Wyodak coals respectively. The magnitude of S_3/ S_V is also shown. If $P_{obs} = P_{hyd}$ then $P_{obs}/P_{hyd} = 1$ but if $P_{obs} < P_{hyd}$ then $P_{obs}/P_{hyd} < 1$ indicating subhydrostatic conditions.

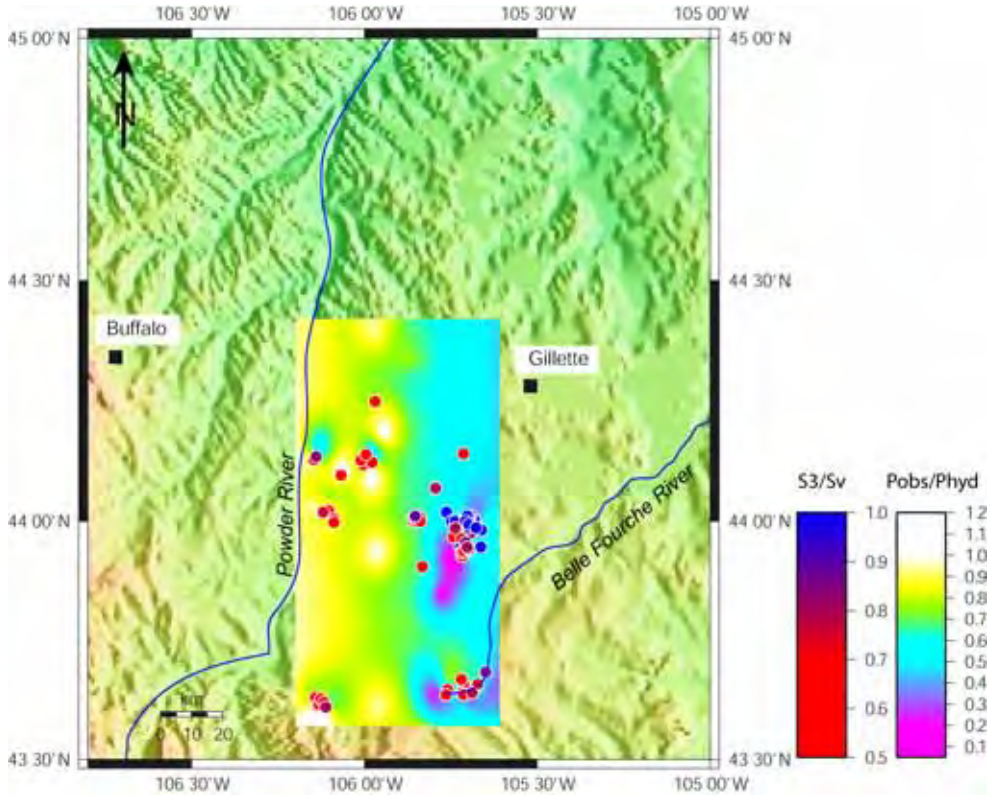

Figure 4.32: Pore pressure interpolation for Big George coal. Data points denote value of S_3/S_v.

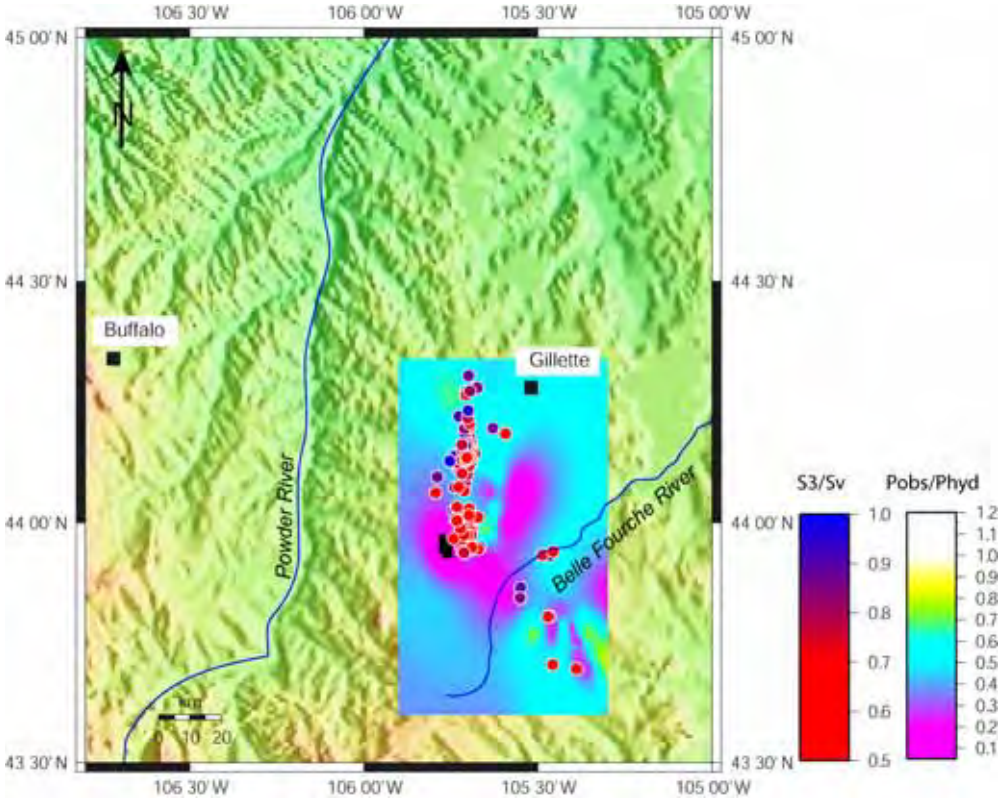

Figure 4.33: Pore pressure interpolation for Wyodak coal. Same as in Figure 4.32.

As well numbers have increased in the basin, depressurization of the Wyodak-Anderson coal bed has also increased (Meyer, 1999). This explains why the Big George coal is almost entirely in subhydrostatic conditions, with the exception of small areas in the central part of the region. It can also be seen that the Big George coal becomes more subhydrostatic towards the East, where coalbed methane operations started a decade ago. However, vertical fractures and horizontal fractures occur under no specific pore pressure condition. Vertical fractures occur in places under subhydrostatic, as well as hydrostatic conditions. For the Wyodak coal, the ratio of P_{obs}/P_{hyd} does not exceed 0.7, which means that the entire coal in this area is under subhydrostatic conditions. However, it is possible to have both vertical and horizontal fractures.

From the above analysis it is apparent that there is no correlation between the magnitude of S_3 and pore pressure. Further analysis is required on a more comprehensive data set in order to confirm this conclusion.

4.7 RELATIONSHIP BETWEEN HYDRAULIC FRACTURE ORIENTATION AND WATER AND GAS PRODUCTION

As shown in section 4.6, the magnitude of the least principal stress and therefore the type of hydraulic fracture, varies across the basin. If the vertical hydraulic fractures propagate into an aquifer layer (and if these fractures remain open through time), a hydraulic connection between the coal and the aquifer layer would be established. As a result, a large water production and either a delay in gas production or a lower gas production rate in wells with vertical fractures is expected, compared to wells with horizontal fractures. The water and gas production data for each well is reported by the operators to the WOGCC once the well has been put in production. The analysis was made depending on the availability of these data. Thus, there are more wells with least principal stress data than with water and gas production data.

The plots in this section show average gas production in Mcf/month versus average water production in barrels/month (see Figure 4.34). Each symbol represents a well and the color indicates the orientation of the hydraulic fracture, i.e. red is for vertical fractures and blue is for horizontal ones. Figure 4.31 shows that within each coal seam there seems to be more wells with vertical fractures than with horizontal fractures. It can

also be seen that wells with horizontal fractures always produce low water volumes (less than 7,000 barrels/month). In addition, large water production is always associated to wells with vertical fractures. It is important to note that wells with vertical fractures can produce low water volumes and/or large water volumes. However, wells with vertical fractures producing large volumes of water are poor gas producers, while wells with vertical fractures producing small volumes of water tend to be excellent gas producers (i.e. a well produce more than 3,000 Mcf/month). It is important to keep in mind that the presented data come only from a subset of wells in the basin. Nevertheless, the fact that the relationships are consistent among the different coals seams, increases the confidence in these findings.

When looking at Figure 4.34, it is interesting to note that wells with horizontal fractures, even if they are good gas producers, never get to produce as much gas as wells with vertical fractures (Appendix 4.B shows maps of water and gas production for the Big George coal). The only exception to this is the Werner coal. However, the data for this coal come from only 9 wells, which is not sufficient to make any comparisons.

In the following paragraphs, I will discuss the regional trends of water and gas production for the individual coals. As can be seen in Figure 4.34, the Anderson coal in general is not a big water producer. Only three wells produce more than 7000 barrels/month. From the 71 wells I analyzed in the Anderson coal, 27% have horizontal fractures and 73% have vertical fractures. 79% of the water production and 78% of the gas production is produced by wells with vertical fractures, which means that fracture geometry has hardly any impact on water and gas production in this coal. Only ~15% of the wells with vertical fractures in the Anderson coal actually produce large amounts of water.

For the Canyon coal, 34 wells were analyzed, of which 47% have vertical fractures. It is interesting to note that the water production for this coal is almost identical for wells with vertical fractures and wells with horizontal fractures. However, 69% of the gas production comes from wells with vertical fractures, which suggests that wells with vertical fractures are better gas producers than wells with horizontal fractures.

For the Wall coal, 36 wells were analyzed. 81% of these wells have vertical fractures and produce 91% of the water and 86% of the gas. Wells with vertical fractures

that produce large amounts of water represent 39% of all the wells and they produce 60% of the water and 44% of the gas from the Wall coal.

For the Big George coal, 74 wells were analyzed, of which 82% have vertical fractures. In total, wells with vertical fractures produce 95% of the water and 99% of the gas. It is important to point out that only half of the wells with vertical fractures are responsible for the bulk of water production (85% of the total amount of produced water) but these large water producers still only account for 45% of the total amount of gas produced from the Big George coal. The remaining 54% of gas production is produced by wells with vertical fractures with a low water production.

Eighty five (85) wells were analyzed from the Wyodak coal and 91% had vertical fractures. From this 91%, 5% had high water production. It is curious to note that even though the Big George coal and the Wyodak coal are similar in thickness, their gas and water production differ greatly. For the wells in the Wyodak coal, those with vertical fractures and large water production are only responsible for 13% of the total amount of water produced from this coal. This means that 78% of the water is produced by wells with vertical fractures and low water production, and these same wells produce 92% of the gas from the coal. This seems to imply that the high water production from wells in the Big George coal is not just related to thickness, since the Wyodak coal has a similar thickness and yet, does not produce as much water. At the same time, the Wyodak coal is a better gas producer, perhaps because the depressurization of the coal is more efficient, or because its gas content may be much higher than the Big George coal. As can be seen in Figure 4.34, wells in the Big George coal produce a maximum of 4000 Mcf/month while the wells in the Wyodak coal can produce 10,000 Mcf/month. Even the large water producers in the Wyodak coal do not produce as much water as those in the Big George coal (23,000 barrels/month compared to 43,000 barrels/month respectively). A possible explanation for the high water production by Big George wells can be given by comparing Gamma Ray logs between the Big George and Wyodak coals. The Gamma Ray log in what has been called the Big George coal by the operators and therefore by the WOGCC has a blocky signal that is easily identifiable in all the wells analyzed. Conversely, in the Wyodak coal, the Gamma Ray signal shows more variations, suggesting that interbedded shale stringers lie within this coal (Figure 4.35). The shales might be acting as flow barriers impeding the flow of water towards the well. If the water

cannot flow to the well, then depressurization does not occur. This process is expected to reduce gas production unless the shale stringers also contain gas thereby contributing to the overall gas production from the Wyodak coals. Thus, the presence of shale may explain why the Wyodak coal is not a big water producer and at the same time produces large amounts of gas. The shale stringers in the Wyodak coal can also be acting as barriers for fracture propagation and since the Big George does not have such barriers, the fractures might be propagating into adjacent formations allowing for a hydraulic connection.

The Big George coal is an amalgamation of the Anderson and Canyon coals, however, it does not produce as much gas as the individual Anderson and Canyon coal beds (Figure 4.34). Possibly, the free gas that used to be present in the various coals has escaped out of the coal towards overlying formations (sands, shales). It is known that some sands across the basin contain gas, which are economically extractable (EPA, 2002). Therefore, the idea of the Big George coal being under-saturated of methane is a plausible one. This could be another possible factor responsible for the Big George coal producing less gas than the Wyodak coal. In addition, if the Big George coal is hydraulically connected to overlying formations it is being dewatered inefficiently and this could also account for the lower gas production.

Figure 4.34: (next pages) Average gas production versus average water production for Anderson, Canyon, Wall, Werner, Wyodak and Big George coals. The gas production scale for all the plots is the same from 0 to 12,000 Mcf/month. The water production scale is the same for all the coals except for Big George coal and it is from 0 to 25,000 and from 0 to 45,000 barrels/month, respectively.

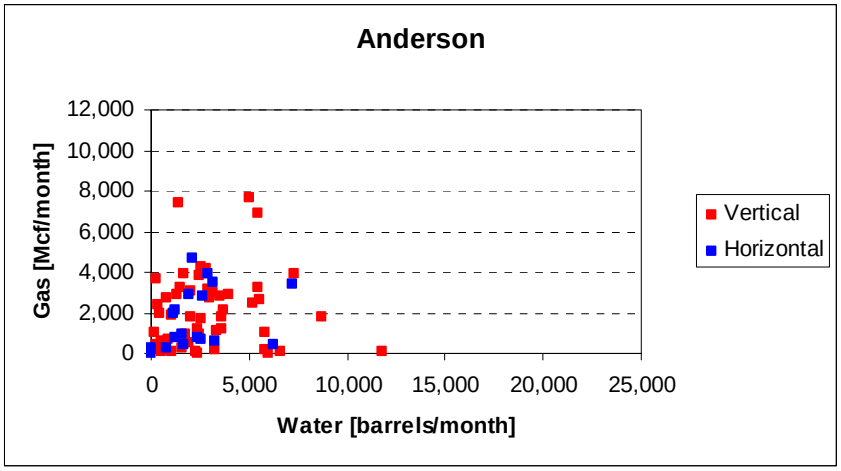
Anderson
Gas [Mcf/month]
12,000
10,000
8,000
6,000
4,000
2,000
0
0
5,000
10,000
15,000
20,000
25,000
Water [barrels/month]
Vertical
Horizontal

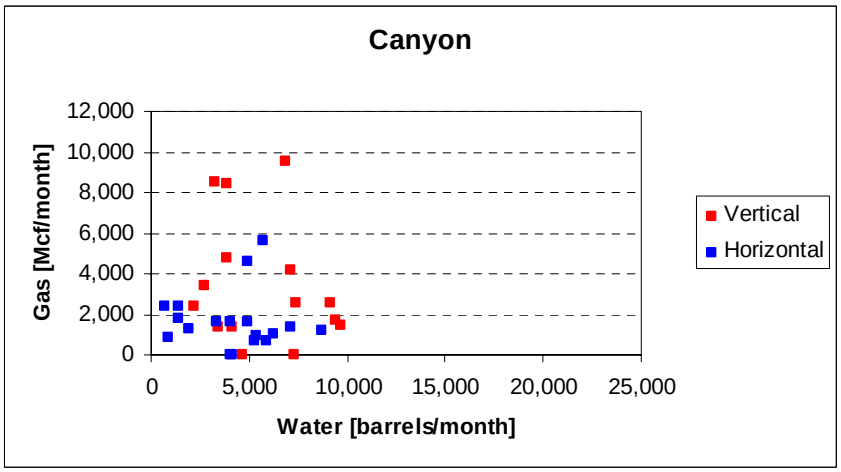
Canyon
Gas [Mcf/month]
12,000
10,000
8,000
6,000
4,000
2,000
0
0
5,000
10,000
15,000
20,000
25,000
Water [barrels/month]
Vertical
Horizontal

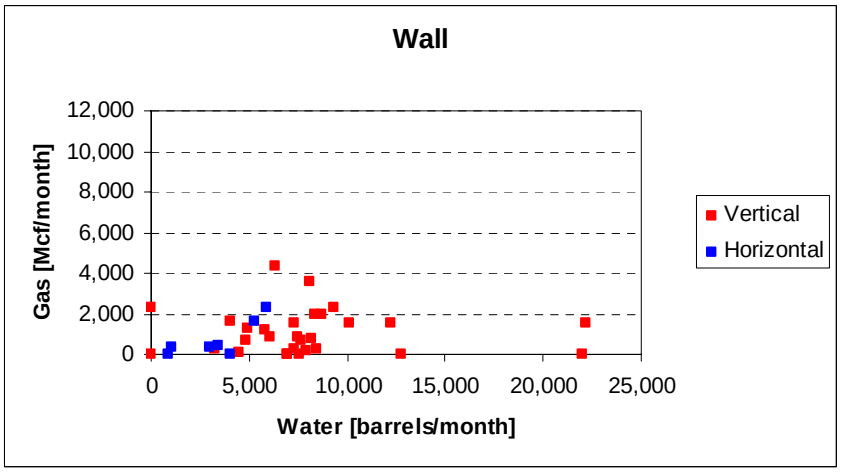
Wall
Gas [Mcf/month]
12,000
10,000
8,000
6,000
4,000
2,000
0
0
5,000
10,000
15,000
20,000
25,000
Water [barrels/month]
Vertical
Horizontal

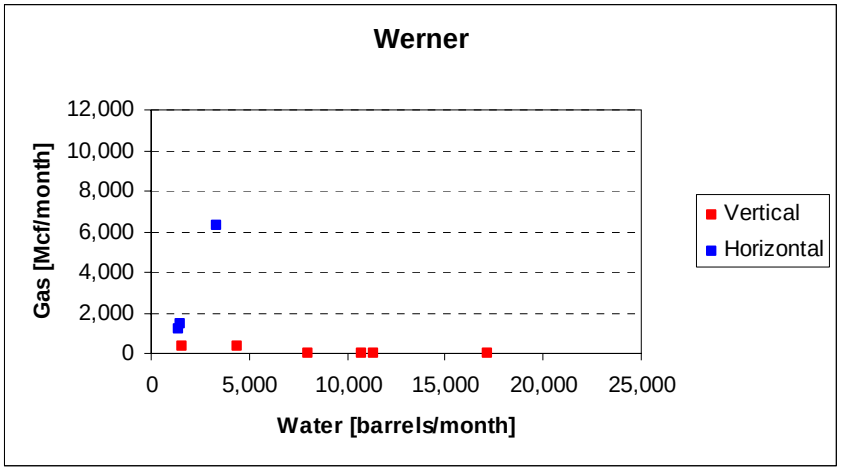
Werner
Gas [Mcf/month]
12,000
10,000
8,000
6,000
4,000
2,000
0
0
5,000
10,000
15,000
20,000
25,000
Water [barrels/month]
Vertical
Horizontal

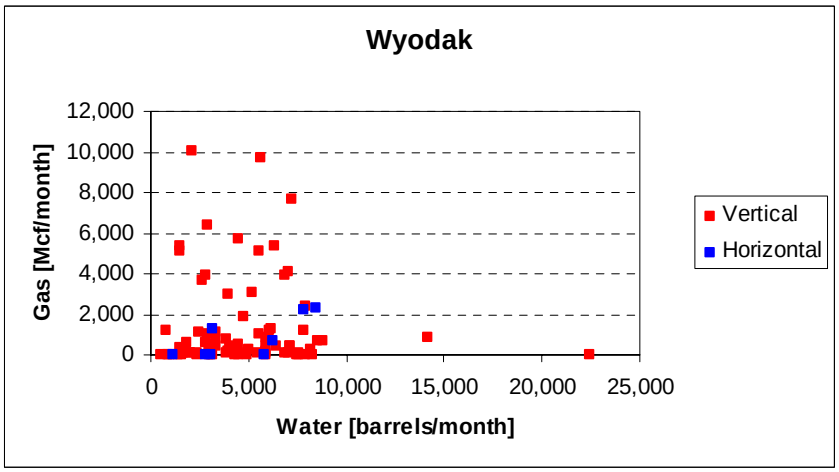
Wyodak
Gas [Mcf/month]
12,000
10,000
8,000
6,000
4,000
2,000
0
0
5,000
10,000
15,000
20,000
25,000
Water [barrels/month]
Vertical
Horizontal

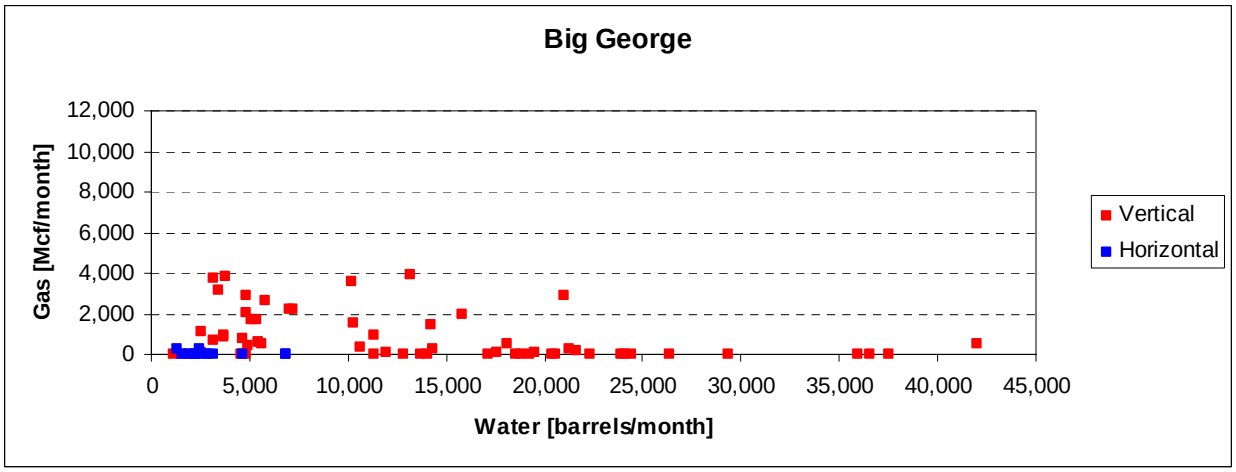
Big George
Gas [Mcf/month]
12,000
10,000
8,000
6,000
4,000
2,000
0
0
5,000
10,000
15,000
20,000
25,000
30,000
35,000
40,000
45,000
Water [barrels/month]
Vertical
Horizontal

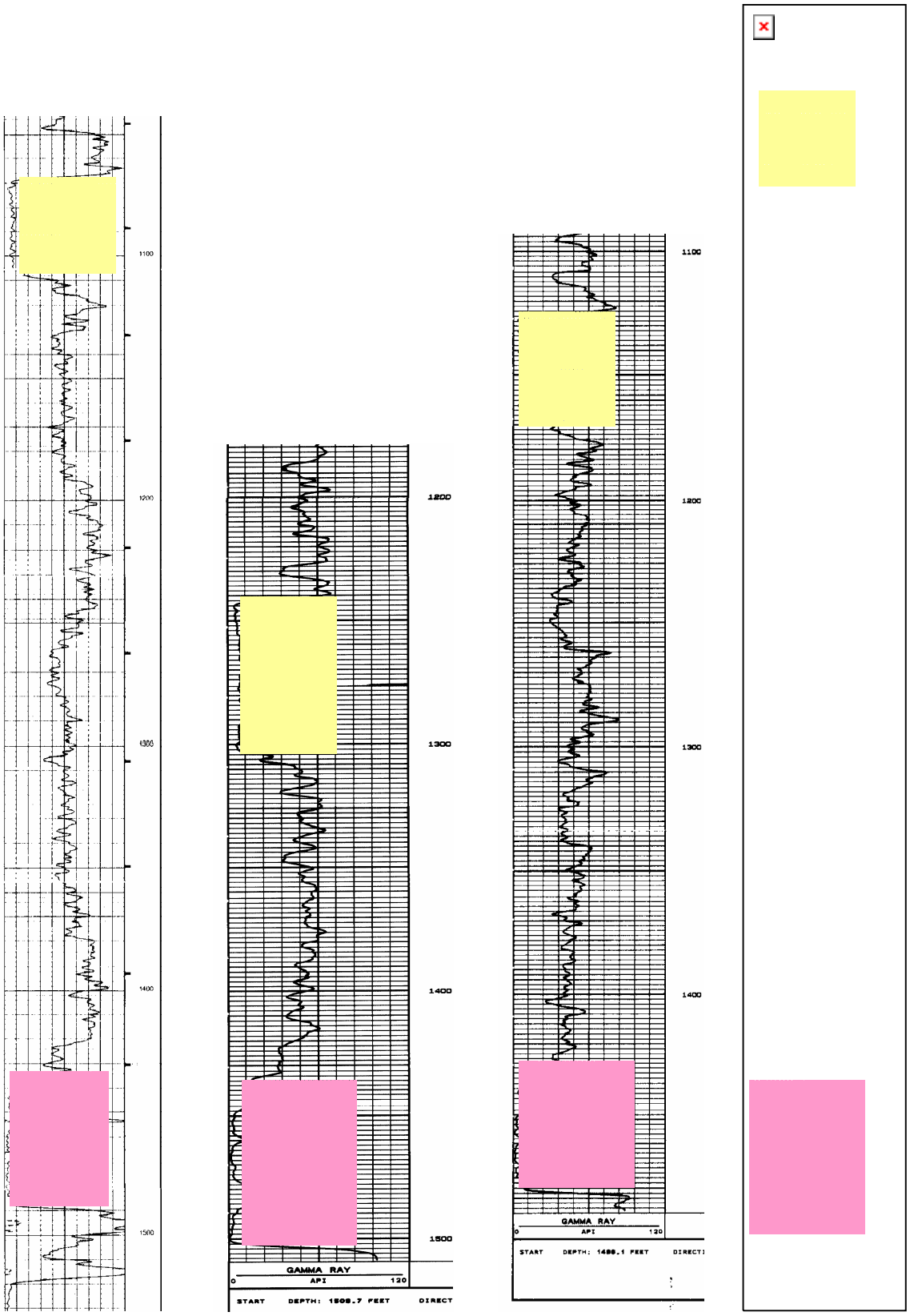

Figure 4.35: Gamma Ray logs showing Big George (yellow) and Wyodak (pink) for wells: 534670, 539081, 539123, 545693 respectively. Source: WOGCC website.

4.7.1 Water and Gas Production in Specific Areas of the Basin

In this section, the wells for a given coal are analyzed in an area-specific manner to determine if the relationships seen in the previous section are not only regional but can also apply to smaller areas (to see more data of water production and gas production versus time, please refer to Appendix 4.C). Figures 4.36 to 4.47 show plots of water and gas production (barrels and Mcf respectively) for each area that has been analyzed. The plots also indicate whether the data come from wells with vertical or horizontal hydraulic fractures. All the wells show water and gas production since the time production started; in this way it is easier to establish comparisons among wells. The water and gas production data for all the wells were obtained from the WOGCC website.

Area D (Big George coal)

There is a marked contrast in water production depending on the type of hydraulic fracture produced in the Big George coal as can be seen in Figures 4.36 and 4.37 (data for wells with horizontal, and vertical fractures, respectively). Wells with vertical fractures produce more water than wells with horizontal fractures. In fact, 71% of the CBM water from the Big George coal is produced by only 32% of the wells (those enclosed in the blue dashed box in Figure 4.37), all of which are characterized by vertically propagating hydraulic fractures. The same wells that produce 71% of the CBM water in this area, have been in production for at least 16 months and still show no gas production. Actually, gas production seems to only occur in wells (with horizontal or vertical fractures) that produce less than 10,000 barrels of water in a given month. Wells with vertical fractures that produce low water volumes are excellent gas producers. Even though for some of these wells gas production is delayed between 4 to 14 months, it can also be seen that these wells produce 12 times more gas than wells with horizontal fractures. Therefore, wells with vertical fractures that produce low water volumes are better gas producers than wells with horizontal fractures.

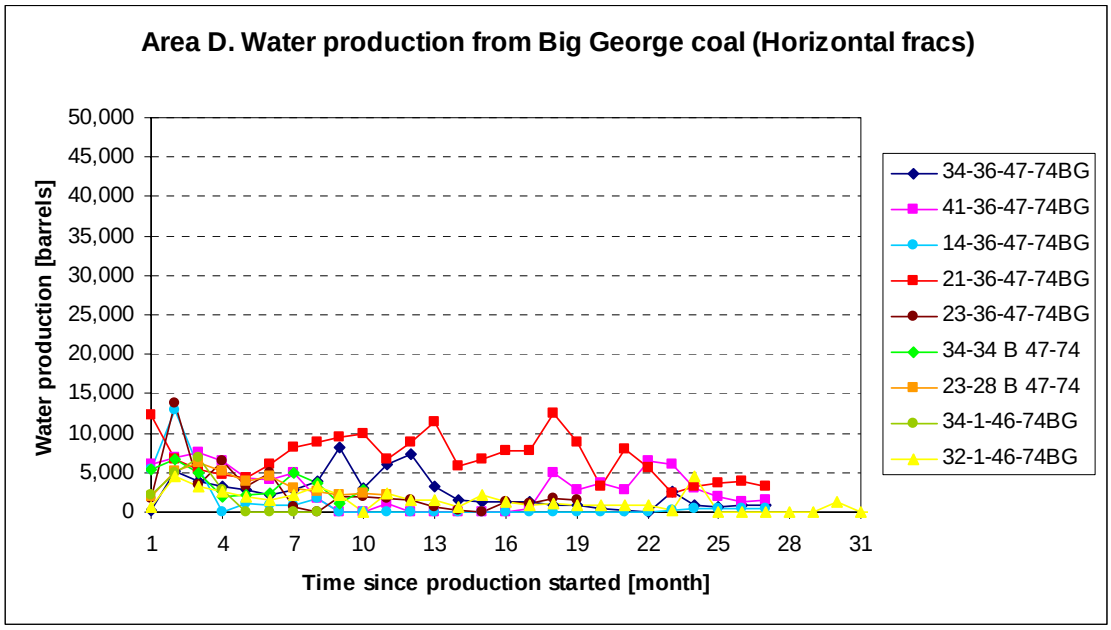

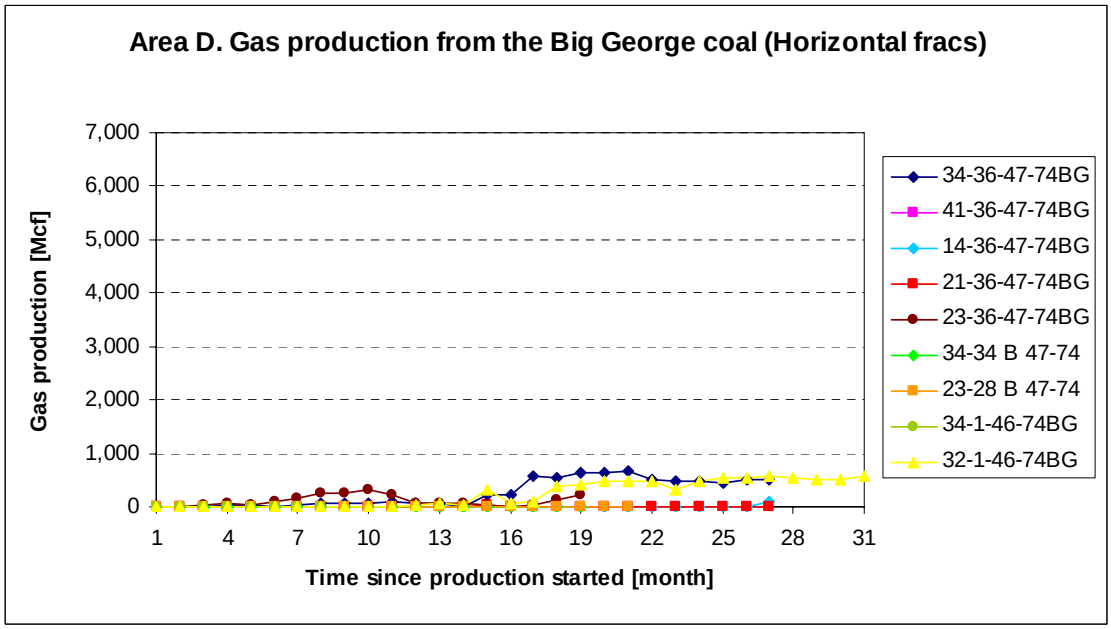

Figure 4.36: Water and gas production from the Big George coal for wells with horizontal fractures in Area D. a) Water production and b) Gas production. Water production is low and gas production is immediate but low (compare to gas production from wells with vertical fractures in Figure 4.37b).

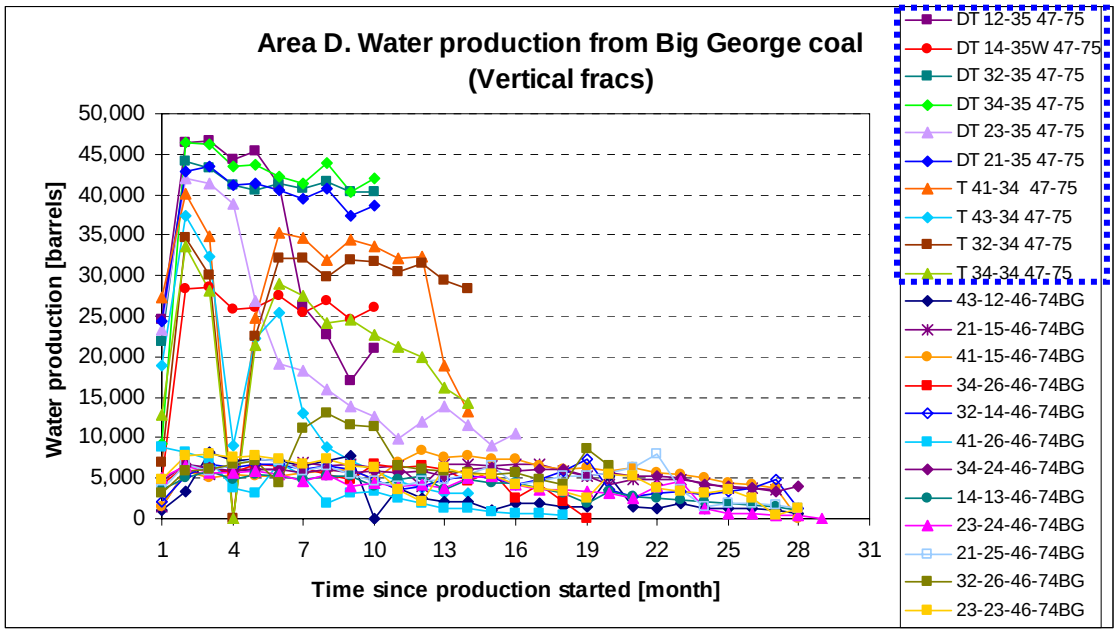

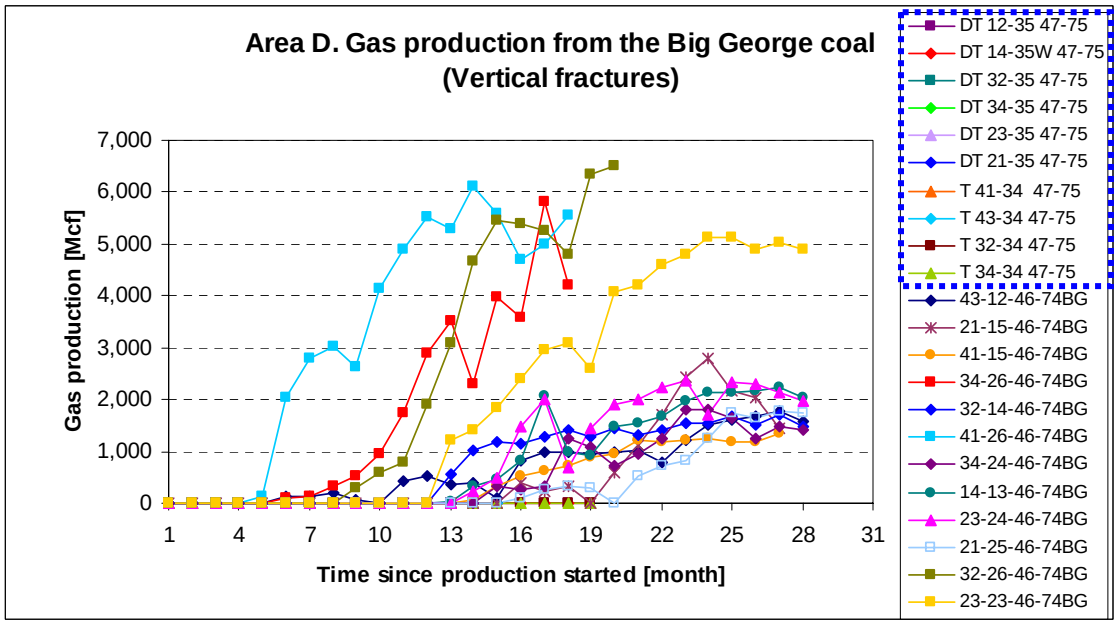

Figure 4.37: Water and gas production from the Big George coal for wells with vertical fractures in Area D. a) Water production and b) Gas production The water production in wells with vertical fractures is about 7 to 10 times larger than that of the wells with horizontal fractures (Figure 4.36). All the wells enclosed by the dashed blue box produce more than 10,000 barrels in a month and have not produced any gas. For wells producing less than 10,000 barrels in a month of water gas production is large but delayed by at least 5 months.

Area D (Wyodak Coal)

For the Wyodak coal (Figures 4.38 and 4.39), the difference in water production between wells is not as large as in the Big George coal. However, the average water rate in wells with horizontal fractures is at least 2000 barrels/month lower than for the wells with vertical fractures. In this area, few wells with vertical fractures are producing gas, but they produce more gas than wells with horizontal fractures (e.g. 7 Mcf, 173 Mcf and 68 Mcf by the 19th month). These wells might not be depressurized enough for methane to desorb but it will be interesting to compare gas production between the wells with horizontal fractures and wells with vertical fractures in the future. It would not be surprising if wells with vertical fractures end up producing more gas than wells with horizontal fractures, already four of the wells with vertical fractures are producing more gas than wells with horizontal fractures.

Area B2 (Anderson coal)

In area B2, the water production of wells with horizontal fracturing (Figure 4.40) ranges from ~0 barrels to 6000 barrels, with only one well having an anomalous water production rate of 12000 barrels after 9 months of being in production (3-34-54-77). In general, the gas production of these wells increases with time, as can be seen in Figure 4.40, and the maximum gas production was ~9000 Mcf in well 1-35-54-77.

Wells with vertical fractures (Figure 4.41) that reached a water production rate of more than 6,000 barrels/month in the first 12 months, either have delays in gas production of about 12 months (e.g. 5-35-54-77, 3-35-54-77, 11-26-54-77, 15-35-54-77) or show no gas production at all (e.g. 13-28-54-77 and 3-33-54-77). Interestingly, wells with vertical fractures that have water production rates lesser than 6,000 barrels/month, produce gas immediately, reaching a gas production of 6000 Mcf in the first 12 months of production (15-34-54-77, 15-24-54-77, 1-22-54-77).

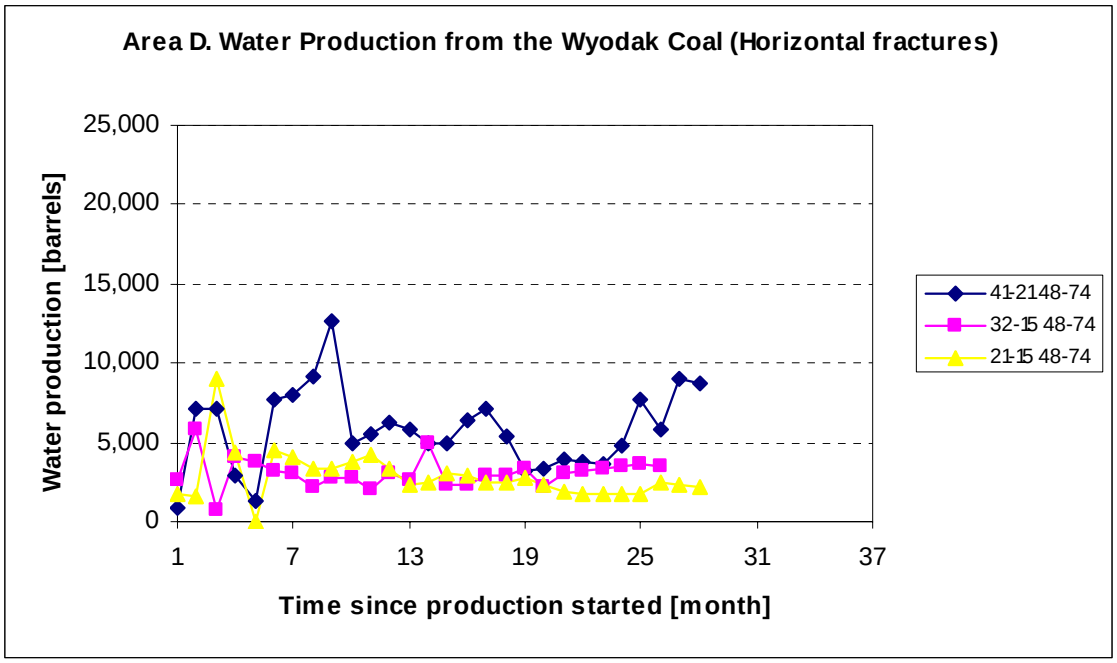

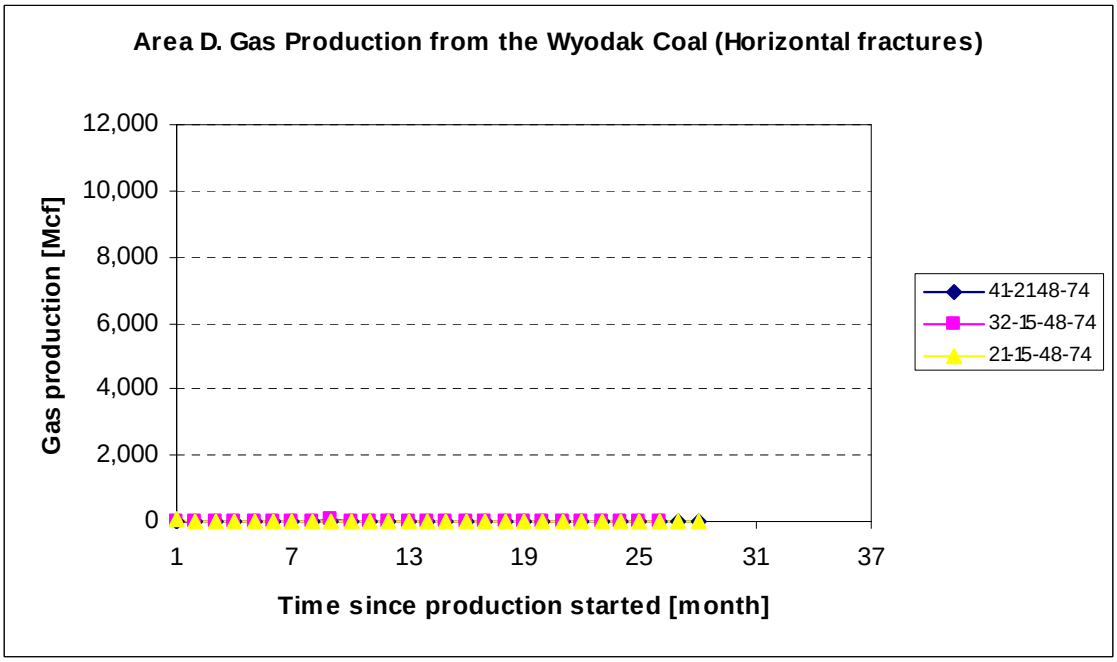

Figure 4.38: Water and gas production from the Wyodak coal for wells with horizontal fractures in Area D. a) Water production and b) Gas production. Note that even though water production is low, gas production is nearly zero.

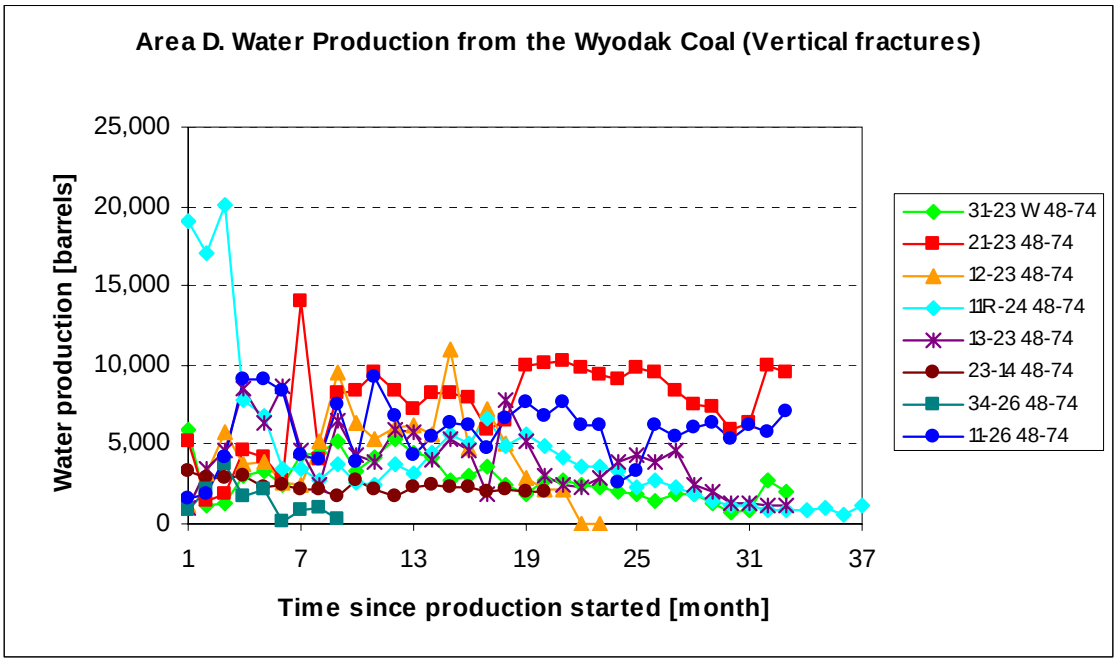

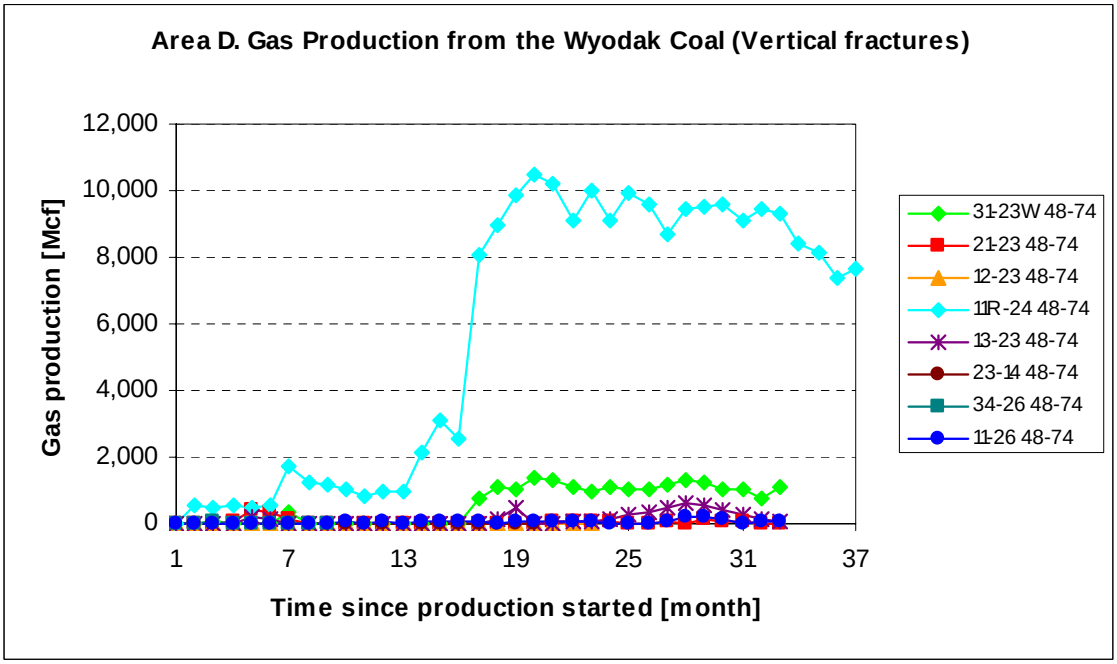

Figure 4.39: Water and gas production from the Wyodak coal for wells with vertical fractures in Area D. a) Water production and b) Gas production.

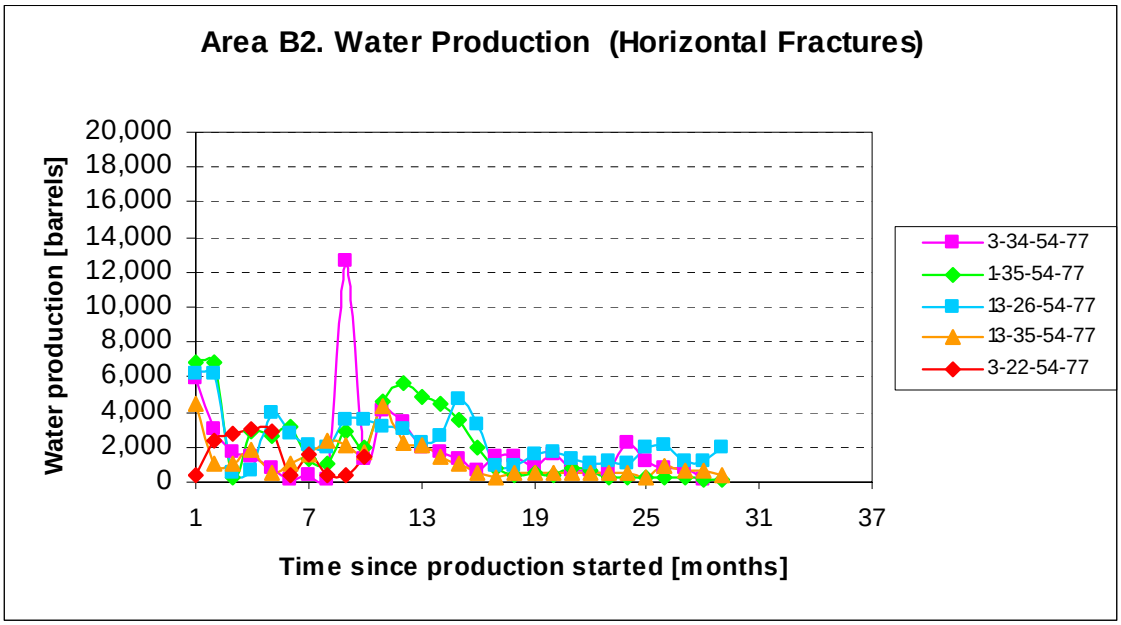

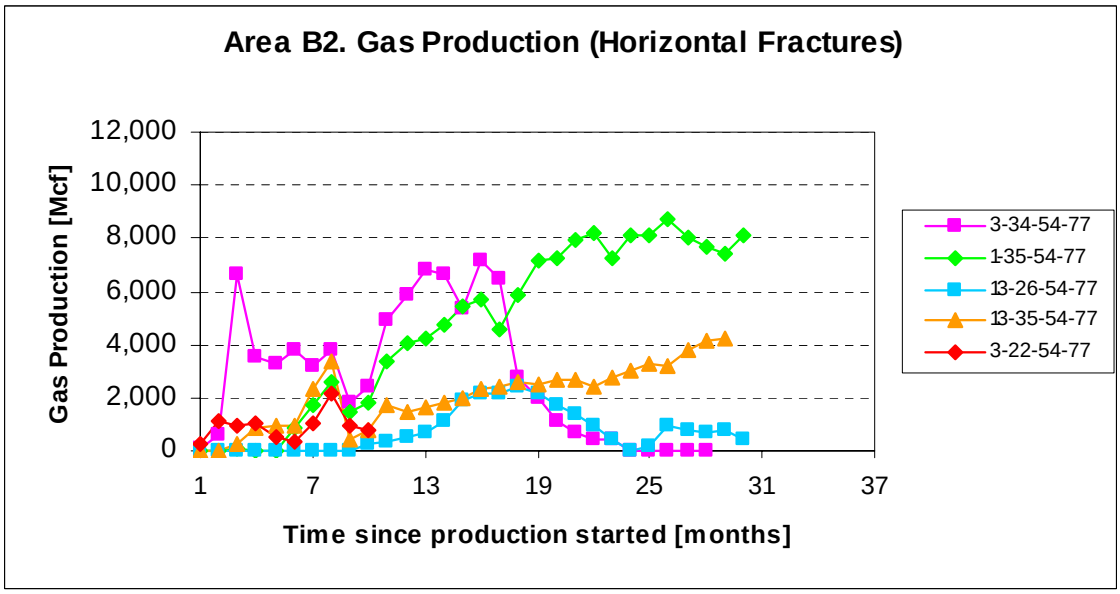

Figure 4.40: Water and gas production from the Anderson coal for wells with horizontal fractures in Area B2. a) Water production and b) Gas production

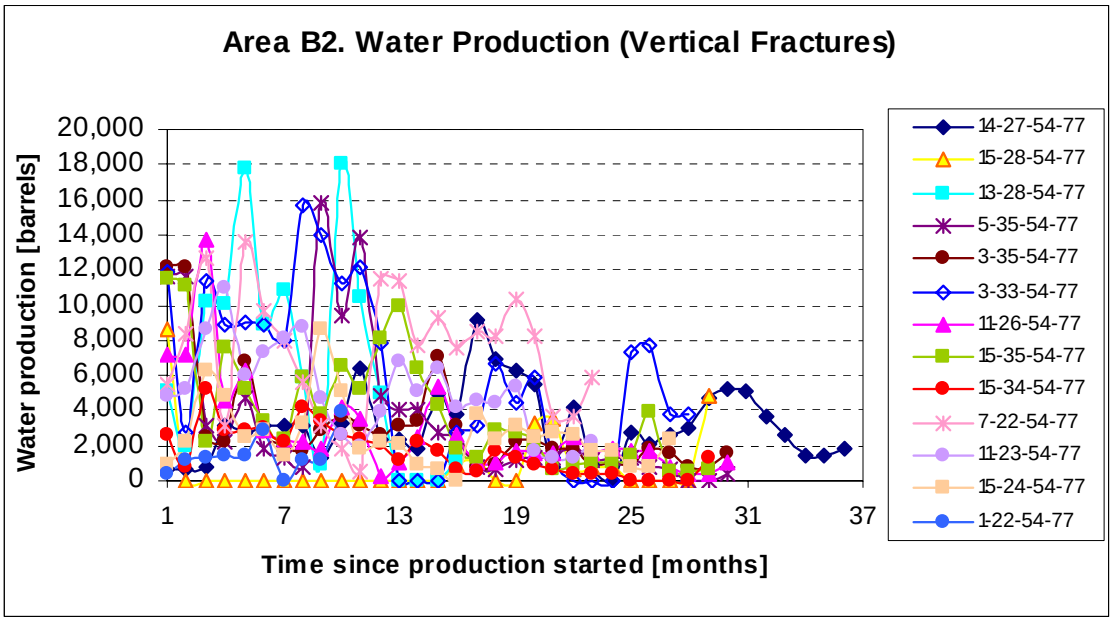

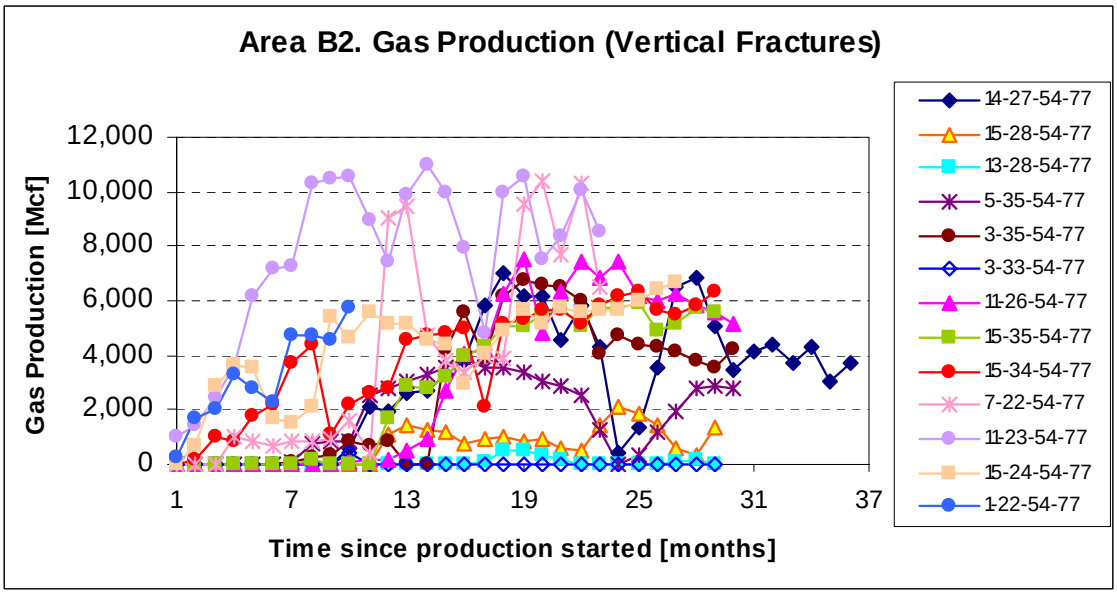

Figure 4.41: Water and gas production from the Anderson coal for wells with vertical fractures in Area B2. a) Water production and b) Gas production

Area B1 and B (Anderson coal)

Water production of more than 8,000 barrels/month in the first 7 months is more common in wells with vertical fractures (Figure 4.42) than in wells with horizontal fractures (Figure 4.43). Even though water production is greater in wells with vertical fractures in area B1 than in wells with horizontal fractures in area B, gas production is immediate and in general, they all have similar trends in gas production, which increases up to the 13th month of production and then declines over time. However, wells with vertical fractures produce at least 3000 Mcf/month but they also reach 4,000 and even 11,000 Mcf/month compared to the steady and lower gas production from the wells with horizontal fractures (between 1,000 and 4,000 Mcf/month). Since gas production in the wells with vertical fractures was not affected by water production, that is, production of large water volumes did not imply a delay in gas production, the large water volumes produced here in the first 7 months might just have been part of a normal dewatering process. After all, these wells do not produce as much water as the wells with vertical fractures in area B2 (Figure 4.41). It is interesting to note that wells with vertical fractures are better gas producers than wells with horizontal fractures as has also been found for the Big George coal.

Area B (Wall Coal)

As can be seen in Figures 4.44 and 4.45, there is a marked difference in water production between wells with horizontal fracturing and some of the wells with vertical fracturing. The wells Smith 5-1W, 5-18W, 11-1W, 14-1W and 6-1W (Figure 4.45) produce almost 4 times more water than the two wells with horizontal fractures (Figure 4.44). These wells with high water production also produce the least amount of gas among all the wells with vertical fractures, e.g. Smith 14-1 (Figure 4.45). In some cases, gas production is delayed by at least 15 months and water production can be as high as 15,000 barrels. Interestingly, Smith 3-1 W (Figure 4.45), which has vertical fractures, has an average water production of only 5,000 barrels/month, similar to the wells with horizontal fractures (Figure 4.44), and its gas production is high (~10,000 Mcf). A possible explanation for what is observed in Smith 3-1W is that the vertical fracture may

not be extending into the aquifer layer, so water production from the aquifer layer is not being tapped, preventing high water production.

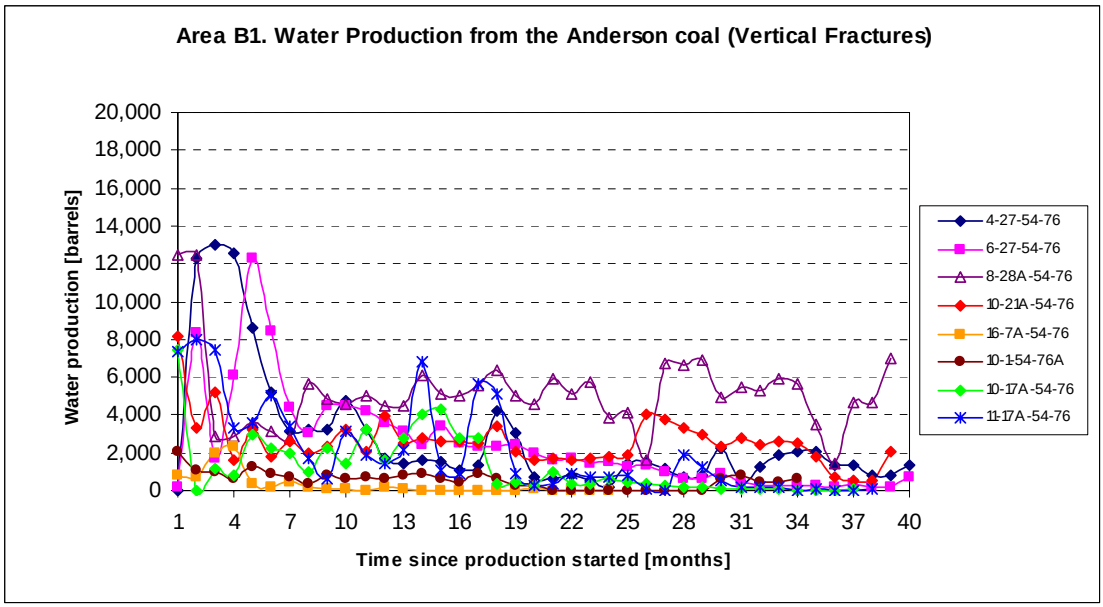

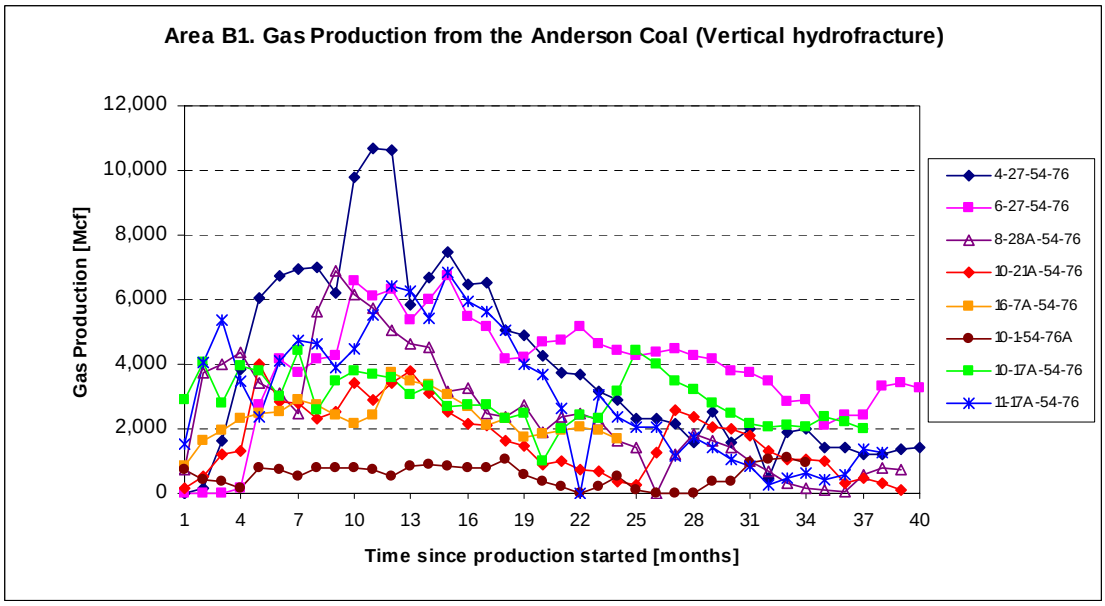

Figure 4.42: Water and gas production from the Anderson coal for wells with vertical fractures in Area B1. a) Water production and b) Gas production

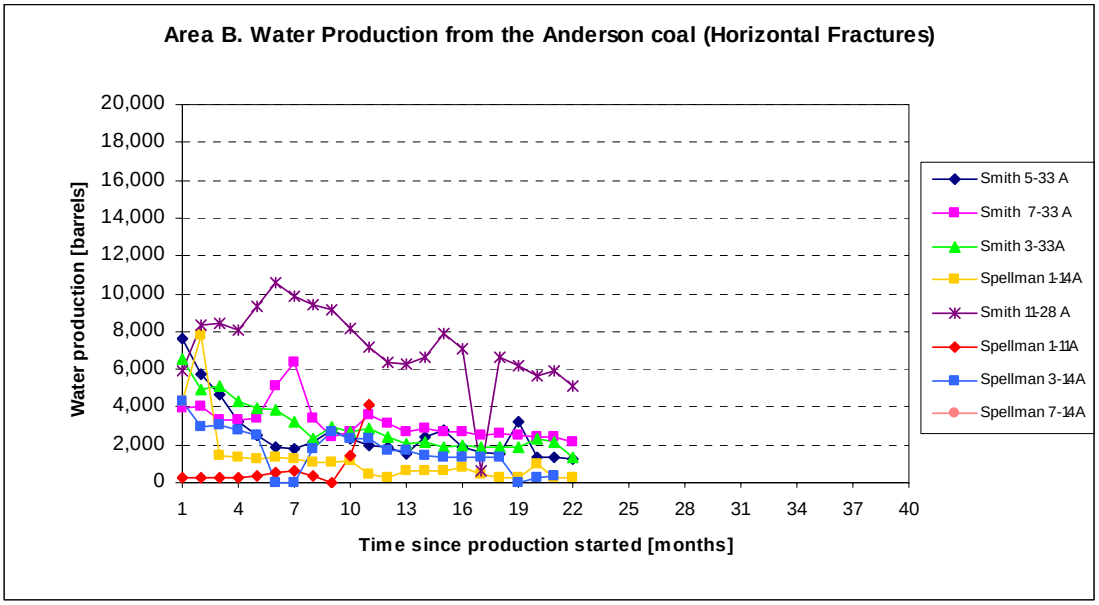

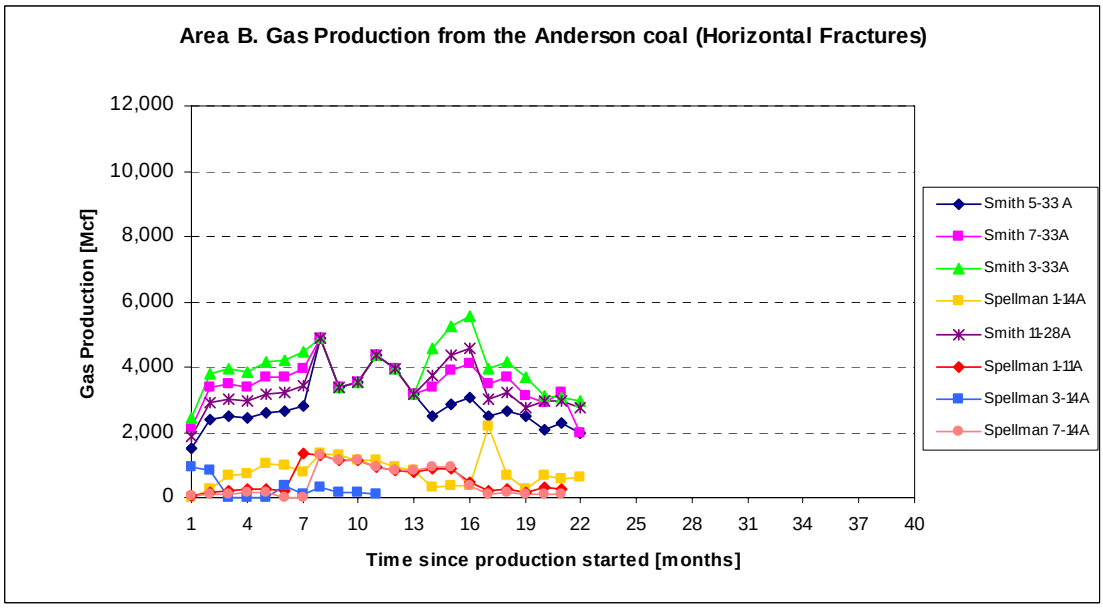

Figure 4.43: Water and gas production from the Anderson coal for wells with horizontal fractures in Area B. a) Water production and b) Gas production

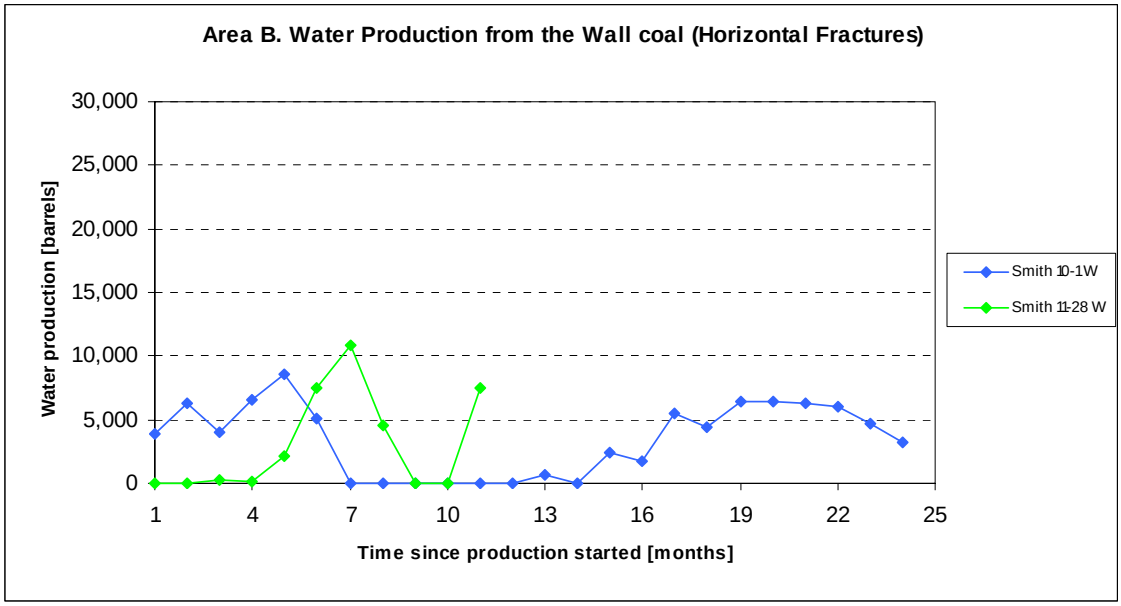

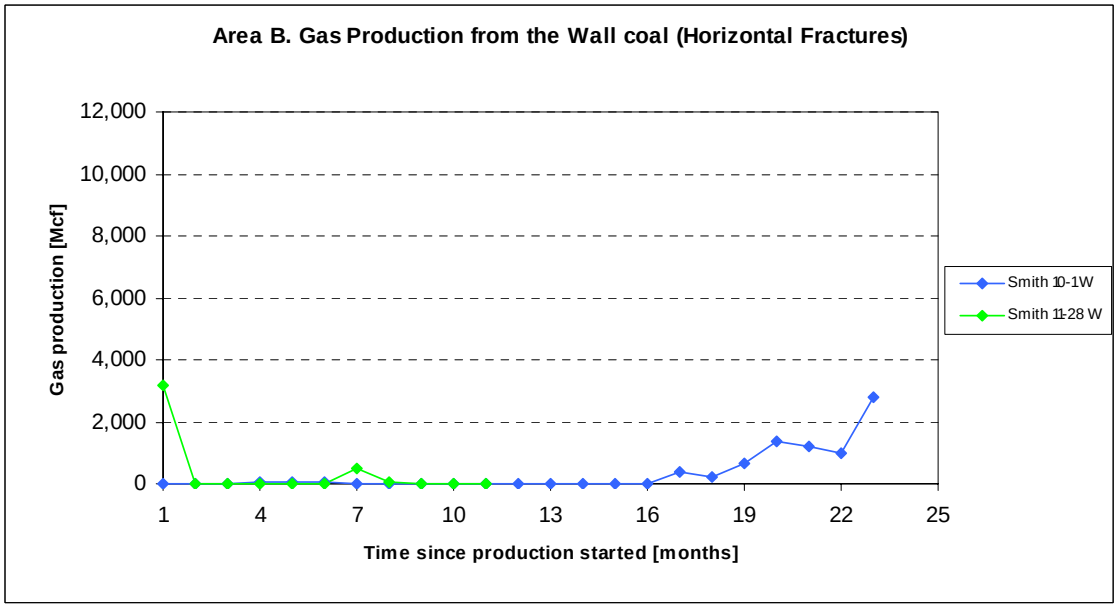

Figure 4.44: Water and gas production from the Wall coal for wells with horizontal fractures in Area B. a) Water production and b) Gas production

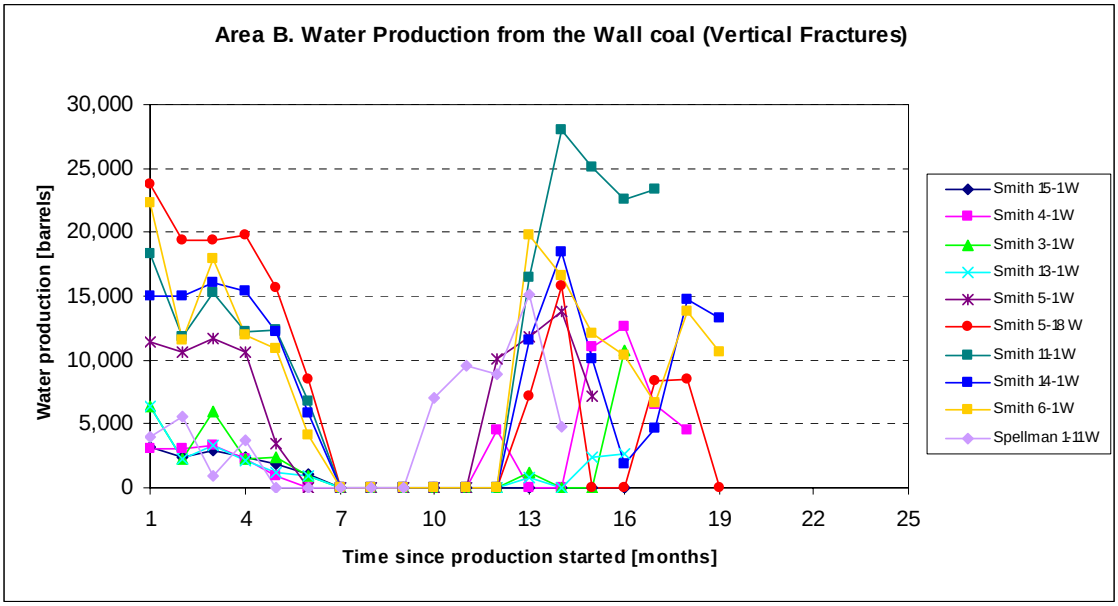

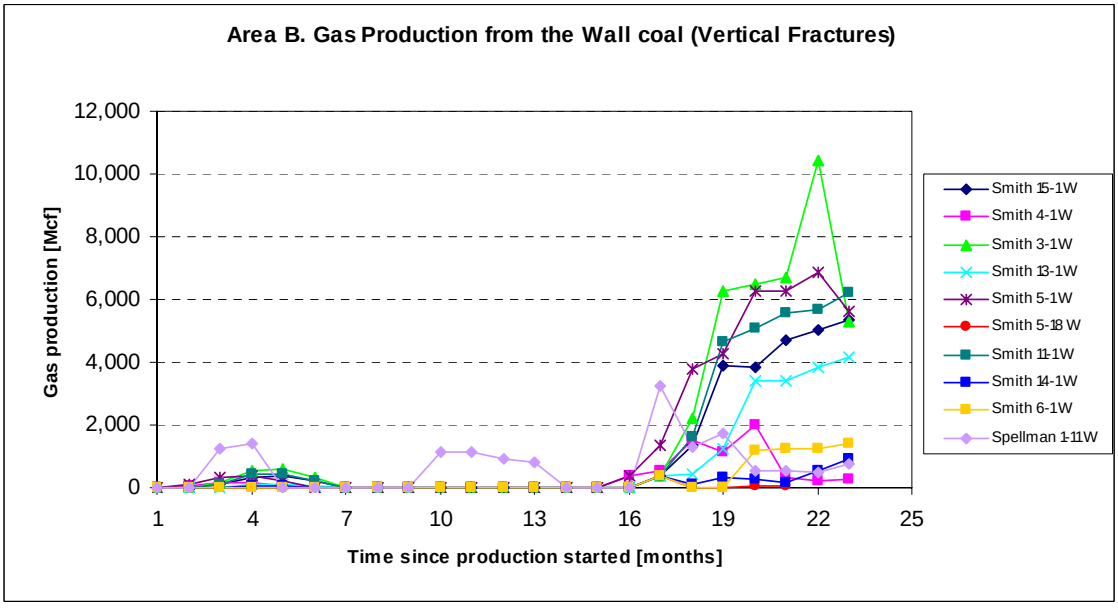

Figure 4.45: Water and gas production from the Wall coal for wells with vertical fractures in Area B. a) Water production and b) Gas production

Area C (Anderson Coal)

Even though water production rates are not too high in these wells, it can still be seen that in wells with lower water production, more gas is produced (Figure 4.46). However, the maximum gas production reached in this area (4500 Mcf for well 9-27-51-74) is about half of what is being produced in area B2 (Figure 4.41) for the same coal (the Anderson coal). In addition, most of the wells in Area C are only producing an average of 1000 Mcf/month, which is relatively low compared to the gas production in areas B1 and B2 (Figures 4.42 and 4.41). This could be due to inefficient depressurization of the coal, or the Anderson coal could be undersaturated of methane in this area.

Area A (Roland Coal)

Figure 4.47 shows that the water production from the Roland coal in area A started at ~1,000 barrels/month and increased to between 2,500 and 6,000 barrels/month for the different wells, with some periods of zero production interspersed. These wells show no gas production. I am unable to compare this water production with other wells because none of the other wells I have analyzed are producing from the Roland coal.

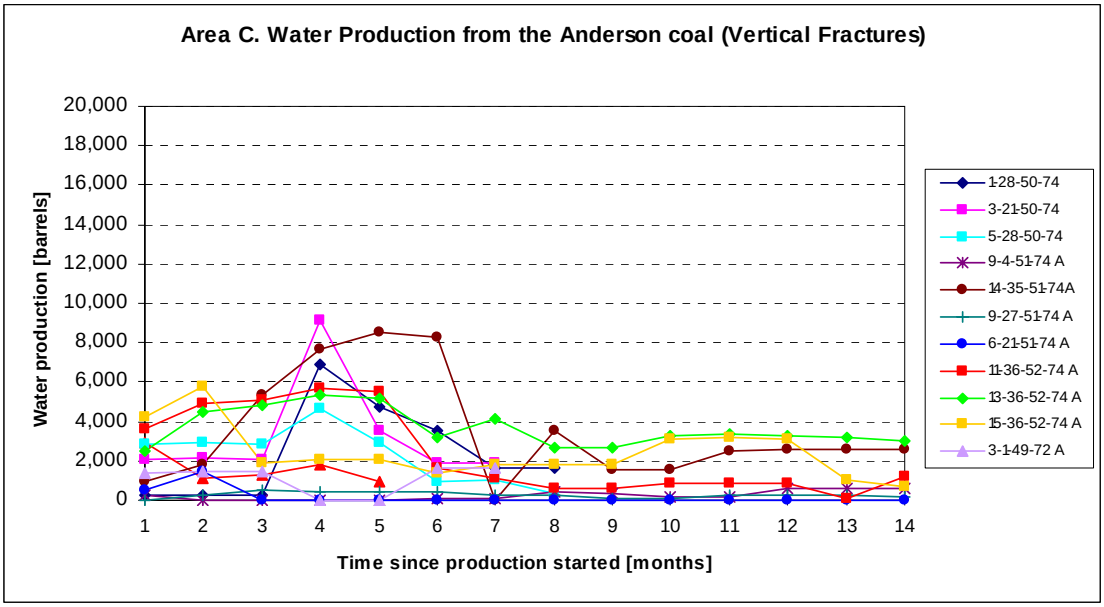

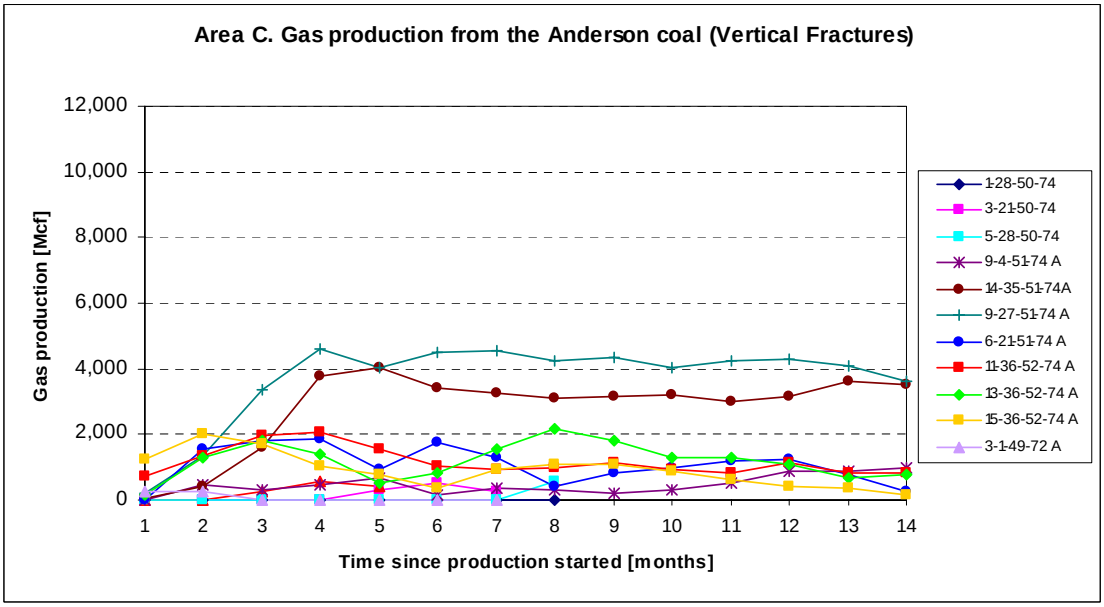

Figure 4.46: Water and gas production from the Anderson coal for wells with vertical fractures in Area C. a) Water production and b) Gas production.

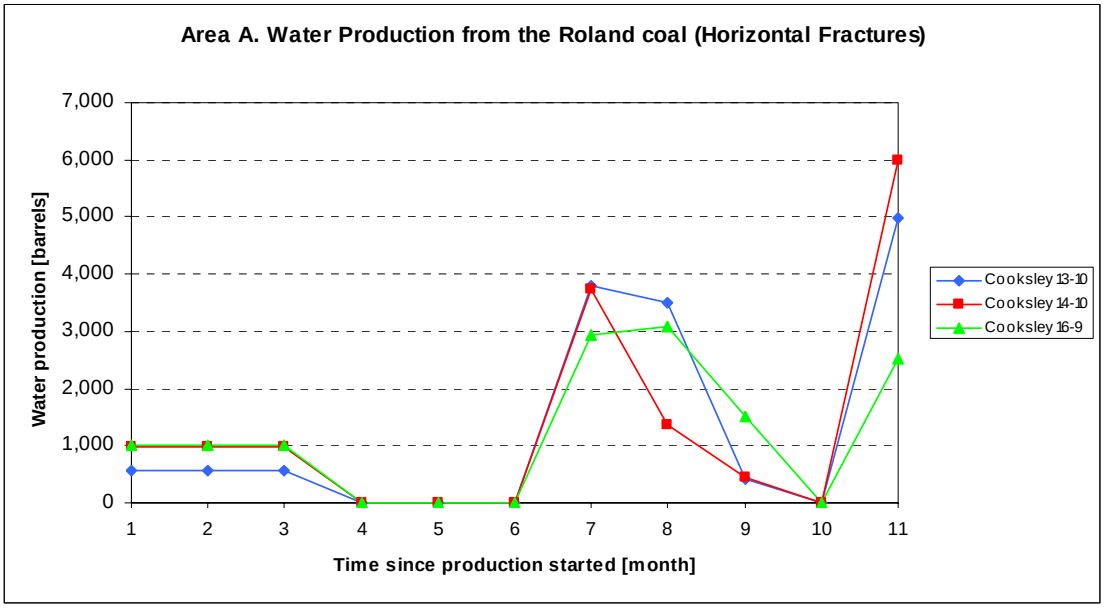

Figure 4.47: Water production from the Roland coal in Area A. In this area, the hydraulic fractures propagate in a horizontal plane.

4.7.2 How does the Relation Between Hydraulic Fracture Orientation and Cleat System Affect the Water and Gas Production?

Fluid flow in coalbeds occurs through the natural fractures, or cleats. Cleats are systematic, orthogonal fracture systems that commonly are perpendicular to bedding. They commonly form during coalification, and the face (dominant) cleat orientation reflects the far-field stress present during their formation. Tectonic, postcoalification fractures also may be present. The face cleat is more continuous than the subordinate butt cleat and in general, cleat density is greatest in thin, bright, low-ash coals (Ayers, 2002). Cleats are perpendicular to the bedding of the coal seam.

Wells with induced vertical hydraulic fractures are, in general, better gas producers than wells with induced horizontal hydraulic fractures. Therefore, the vertical fractures must have a strike nearly perpendicular to the strike of the face cleats, which would imply an efficient connection of several face cleats through the vertical hydraulic fracture. Wells with horizontal hydraulic fractures that produce relatively good amounts of gas (more than 3,000 Mcf/month), must be producing free gas and gas from the cleats, which get connected by the horizontal hydraulic fracture. However, horizontal fractures

do not seem to be the most efficient pathway for flow of methane from the coal into the well.

There are wells with horizontal hydraulic fractures in the Anderson and Canyon coals that produce more gas than wells with horizontal fractures in the Big George and Wyodak coals. Interestingly, the Anderson and Canyon coals are thinner and shallower than the Big George and Wyodak coals. The cleat density may be larger in the thinner coals than in the thicker coals and the amount of free gas is generally higher in shallower coals than in deeper coal. These could explain why horizontal fractures in thinner coals are better conduits than in thicker coals and therefore, this could also explain why wells with horizontal fractures in thinner coals are better gas producers than wells with horizontal fractures in thicker coals.

4.8 IN AREAS OF VERTICAL HYDRAULIC FRACTURING: WHY DO SOME WELLS HAVE LARGE WATER PRODUCTION AND OTHERS LOW WATER PRODUCTION?

One of the goals of this study is to understand why some wells with vertical fractures have excessive water production, while water production is low in adjacent wells. I have identified three different factors that may be responsible for this observation: stratigraphy, thickness and depth.

4.8.1 Stratigraphy

Excess CBM water production could result from the propagation of the vertical fractures into overlying strata, creating a hydraulic connection between the formations. Gamma ray logs from a number of wells with vertical fractures in Area D have been analyzed. It was expected that wells with vertical fractures and excessive water production would be overlain by sand bodies, which behave as aquifers, and would therefore yield a large amount of water once the coals began to be dewatered. With respect to the wells with vertical fractures and low water production, it was expected that the coals in these wells were overlain by shales, which have low permeability, and therefore yield less water than sands.

Some of the wells with vertical fractures and large water production rates have sand bodies overlying the coal. However, other wells with vertical fractures and large water production rates have shales overlying the coal. Furthermore, wells with vertical fractures and low water production rates were either overlain by shales or sands. Thus, no obvious relationship between stratigraphy and water production can be established. In the future, the availability and analysis of a more extensive gamma ray log dataset may yet reveal whether a relationship does exist between vertical fracture growth and stratigraphy.

4.8.2 Thickness

As can be seen in Figure 4.48, there is a general trend that the thicker the Big George coal, the greater the water production. However, at a given thickness, say 70 feet, the average water production for different wells ranges from 0 to 40,000 barrels/month. For the Wyodak coal (Figure 4.48), water production is generally low, despite the large thickness of the coal seam. Even where the coal is thicker than 100 feet, the average water production is less than 8,000 barrels/month. This implies that coal seam thickness is not an obvious indicator for the amount of water a coal will end up producing.

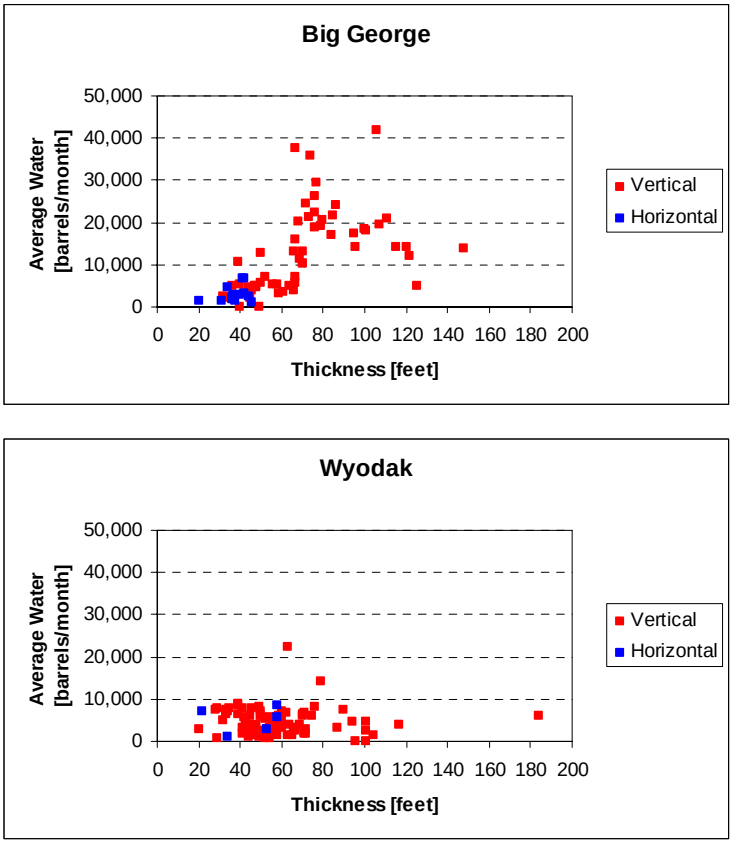

Figure 4.48. Average water production versus thickness for the Big George coal (upper panel) and the Wyodak coal (lower panel).

4.8.3 Depth

Figure 4.49 shows a plot of water production versus depth for the Big George coal seam. The plot shows that wells with vertical fractures and high water production rates occur at any depth between 750 and 1,500 feet. Therefore, there appears to be no direct correlation between high water production and depth.

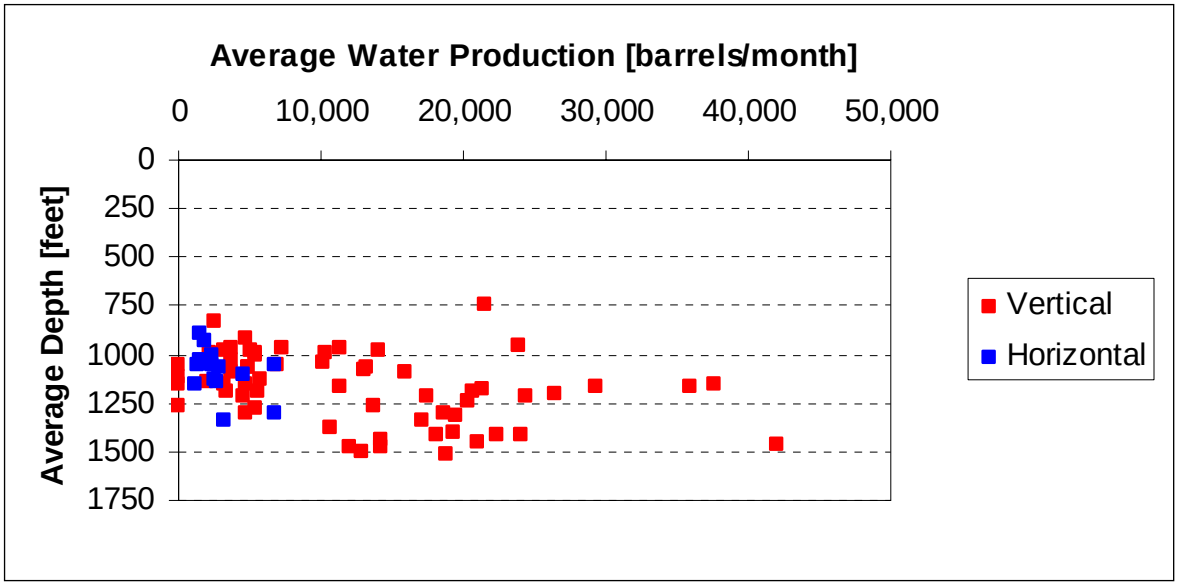

Figure 4.49: Average water production versus depth for the Big George coal.

None of the investigated factors (stratigraphy, coal thickness, depth) appear to affect the amount of water that is produced in wells with vertical fractures. At this time and considering the factors just mentioned, the prediction of water production in these wells is still not viable.

4.9 PORE PRESSURE AND GAS PRODUCTION

It is known that methane desorbs from the coal once the pressure in the coal decreases. The aim of this section is to investigate the amount of depressurization required for methane desorption to occur. The data presented in this section come from the Big George coal. Figure 4.50 shows the water and gas production data for each well and also the changes in delta pressure with time. Delta pressure is equivalent to hydrostatic pressure minus observed pressure, which indicates that with time, the observed pressure should be lower due to the dewatering (and depressurizing) of the coal and therefore the delta pressure should increase.

Well SRU2 (Figure 4.50a) shows a change of ~200 psi in delta pressure with ongoing depletion, due to water production, but even after three years it is still not producing any gas. Even though depressurization is implied, the large water production

rate (~35,000 barrels/month) indicates that depressurization might not be taking place effectively. The coal at this site may be in connection with overlying strata.

For well Roush (Figure 4.50b), a change in delta pressure of ~30 psi was not enough for the methane to desorb from the coal. The change in 30 psi occurred during the first year of production and gas production started a year after that. Dewatering for eighteen months was necessary for this well to start producing gas.

Within three months, delta pressure changed by 10 psi for well Spittler, (Figure 4.50c) just before dewatering began. In this well, gas production was immediate and it apparently reached a peak production of 9341 Mcf after 18 months and then gas production declined. Water production started at ~6000 barrels, increased to 40,000 barrels in the first three months and then declined steadily. By the time gas production peak was reached, the water production was 4500 barrels.

Well Oh, in Figure 4.50d, has horizontal fractures and is located in T46 R73, adjacent to Area D. In its first 6 months of production, the delta pressure changed by 25 psi. However, this well has been in production for 4 years and gas production has still not begun. This indicates that the initial change in pore pressure was not large enough for the methane to be desorbed. In addition, delta pressure might still not be increasing sufficiently for the methane to desorb at all. This well confirms the previous findings, that is, wells with horizontal fractures in the Big George coal produce low water volumes and gas production is low or absent.

For some wells, a 25 psi change in pressure is enough for the gas to desorb, while for others it is not large enough. In fact, even a large change like 200 psi in the case of SRU2 was not large enough for the methane to desorb. It appears that something more complicated might be taking place in this well. The coal at this site may be in hydraulic connection with adjacent strata, which would explain the large volumes of water produced and the absence of gas production.

Figure 4.50: (next pages) Plots of water and gas production versus time and delta pressure (hydrostatic pressure minus observed pressure) for different wells in the Big George coal.

a)

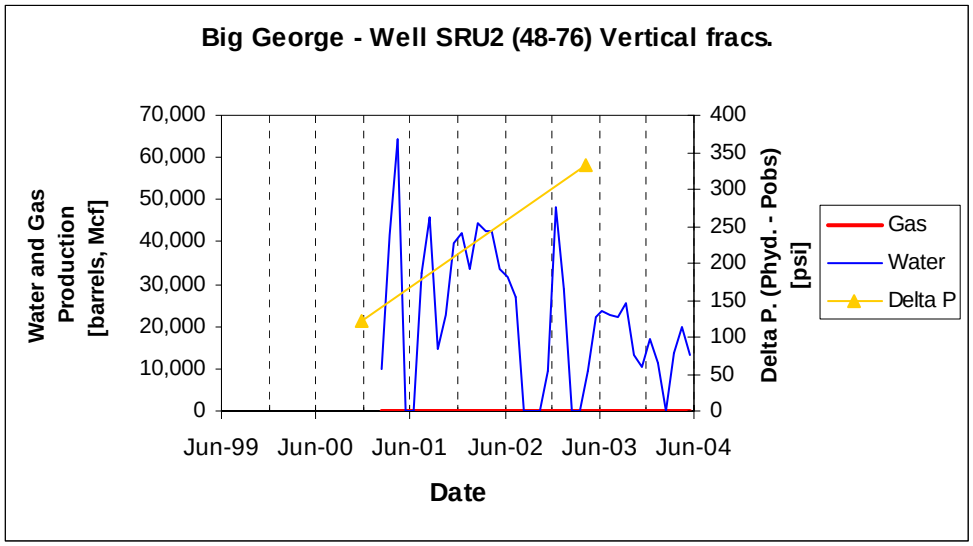

b)

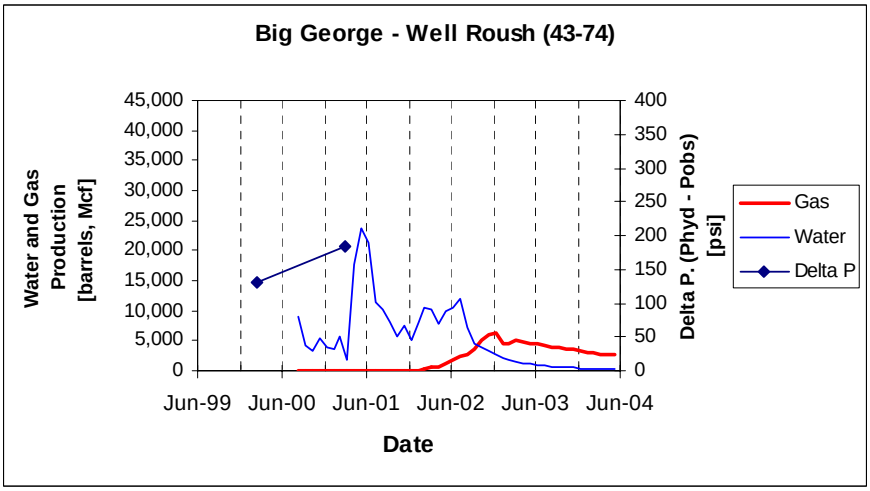

c)

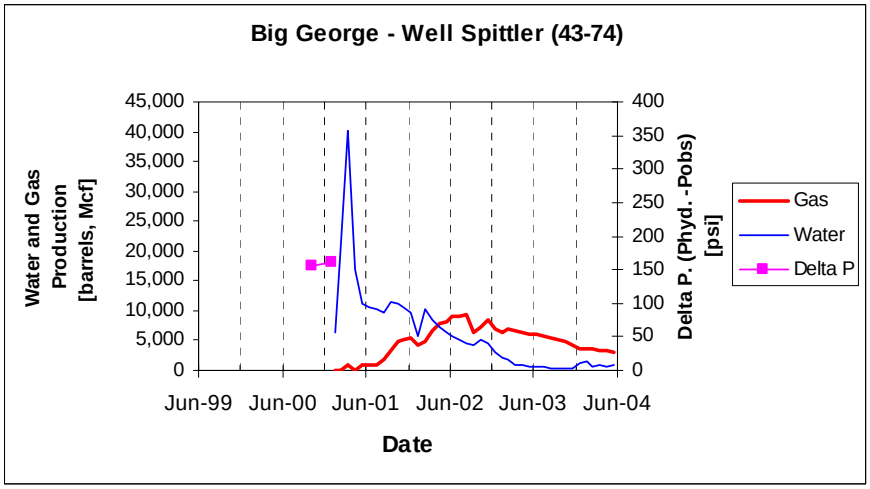

d)

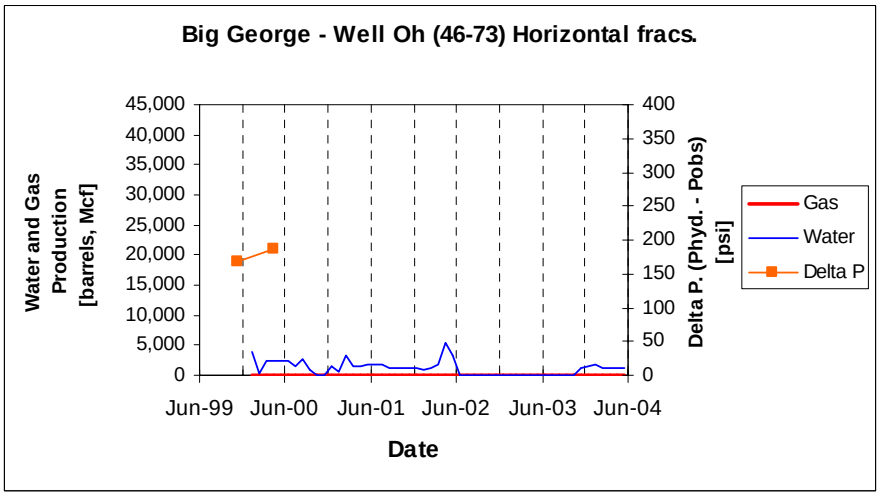

4.10 TEMPORAL AND SPATIAL VARIATIONS IN PORE PRESSURE

Figure 4.51 is a crossplot of P_{obs}/P_{hyd} versus time when the measurement was made and shows no correlation between changes in pore pressure and time for the Big George coal. Figure 4.52 shows a map of interpolated P_{obs}/P_{hyd} with data points over the top. Each symbol represents the year in which the pore pressure (P_p) measurement was taken. There seems to be more of a spatial trend than a temporal trend. The magenta-blue areas ($P_{obs}/P_{hyd} < 1$) are defined not only by data points from 1999 but also from 2004,

whereas the yellow-white ($P_{obs}/P_{hyd} \geq 1$) areas are not only defined by data points from 2004, but also from 1998-2002. This may indicate that P_p not only depends on time (when dewatering began) but also on the area (there may be interaction with other formations).

Figure 4.53a shows elevation with respect to delta pressure for Big George coal. In general, if a fluid level remains at constant elevation while the topography increases, the pore pressure at the depth of the water table will be more subhydrostatic at the location of highest elevation, compared to the pore pressure at depth in the location of lower topography. This means that if elevation increases, delta pressure should also increase, i.e. the pore pressure should become more subhydrostatic. The data presented in this figure do not show this trend when considered as a whole. However, according to the trends observed in Figure 4.53a, it is possible to establish four different groups of these data (Figure 4.53b). For Group 1 there seems to exist a correlation between elevation and pore pressure since pore pressure tends to become more subhydrostatic with the increase in elevation. However, for Groups 2, 3 and 4, pore pressure becomes more subhydrostatic at constant elevation. In Figure 4.53c, fluid elevation is plotted against Delta Pressure and what can be seen here is that for Group 1 fluid elevation remains constant while delta pressure increases (i.e., pore pressure becomes more subhydrostatic). For Groups 2, 3 and 4 fluid elevation decreases at the same time that pore pressure becomes more subhydrostatic. These findings are summarized in Figure 4.54a, where the brown line corresponds to elevation and the blue line corresponds to the fluid elevation. By determining the location of these wells in the basin I was able to identify that the wells belonging to Group 1 are all located on slopes of hills, the wells from Group 2 are located on a plateau, the ones from Group 3 are in the Powder River valley and the wells from Group 4 are located on a ridge (Figure 4.54b). In summary, wells located on the slopes become more subhydrostatic with elevation because the fluid level remains constant. In addition, wells located in plateaus, river valleys and ridges become more subhydrostatic at constant elevation because the fluid level decreases. Usually, the water table reflects the topography in a more subdued way. However, these data allow one to realize that the water table does not follow the topography in the studied region, which might be indicating the impact of anthropogenic activities (e.g. domestic water wells, mining, CBM operations) in the groundwater system.

With the limited amount of P_p data obtained, it has not been possible to find a clear correlation between P_p and depth, thickness or elevation (Figure 4.55). A possible explanation for this lack in trend in pore pressure is that the coal may not be a hydraulically isolated formation. The coals may be in communication with other formations resulting in a masked magnitude of the "coal" pore pressure. Since there may be a hydraulic connection between the coals and adjacent formations, the pore pressure magnitude obtained in the coal may be the pore pressure that results from the hydraulic interplay of all the formations hydraulically connected at a certain location in the basin. Figure 4.56 shows an example in which the delta pressure has varied by 150 psi even though production has not started. This well is located in T46N R74W (in Area D). An important observation about this well is that gas production starts before water production, which may originate from desorbed gas due to depressurization. The average water production is 2082 barrels/month and the average gas production is 1416 Mcf/month. S_3 data is not available for this specific well but the S_3 data from wells in this same field and in the same section (and adjacent sections) indicate that $S_3 = S_{hmin}$, corresponding to vertical fracture propagation. Thus, this well reinforces what has been observed before, that is, wells with vertical fractures that produce low water volumes produce gas immediately. However, the reason why the pore pressure varies before the dewatering phase starts is unknown and deserves attention. Production-induced pore pressure changes may perhaps affect the magnitude of S_3 as well. However, further analysis is needed to understand how the reservoir works, its connection and correlation with adjacent formations and how the drawdown from one well affects the pore pressure in other wells and whether this inflicts a change in S_3.

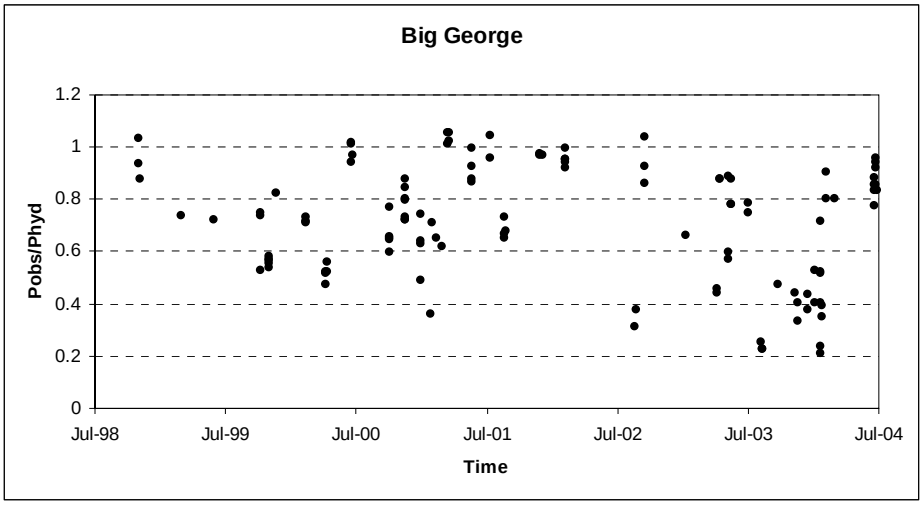

Figure 4.51: Crossplot of P_{obs}/P_{hyd} vs Time.

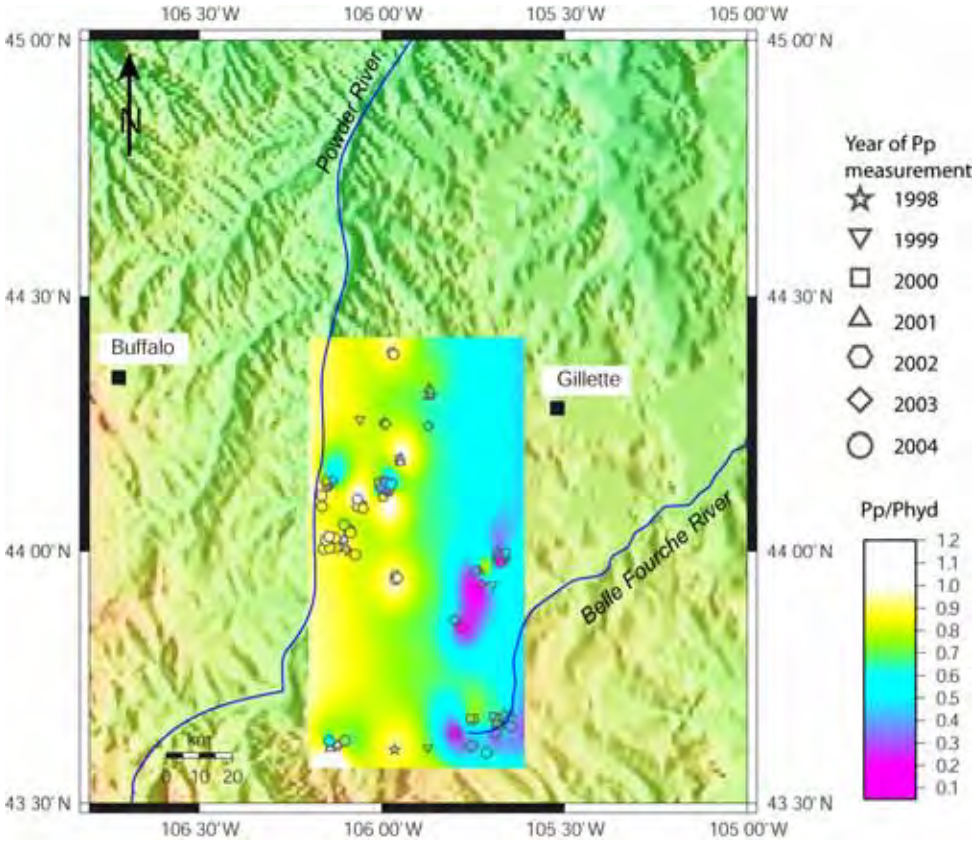

Figure 4.52: Map of P_{obs}/P_{hyd} for Big George coal; symbols represent the year at which the pore pressure measurement was done.

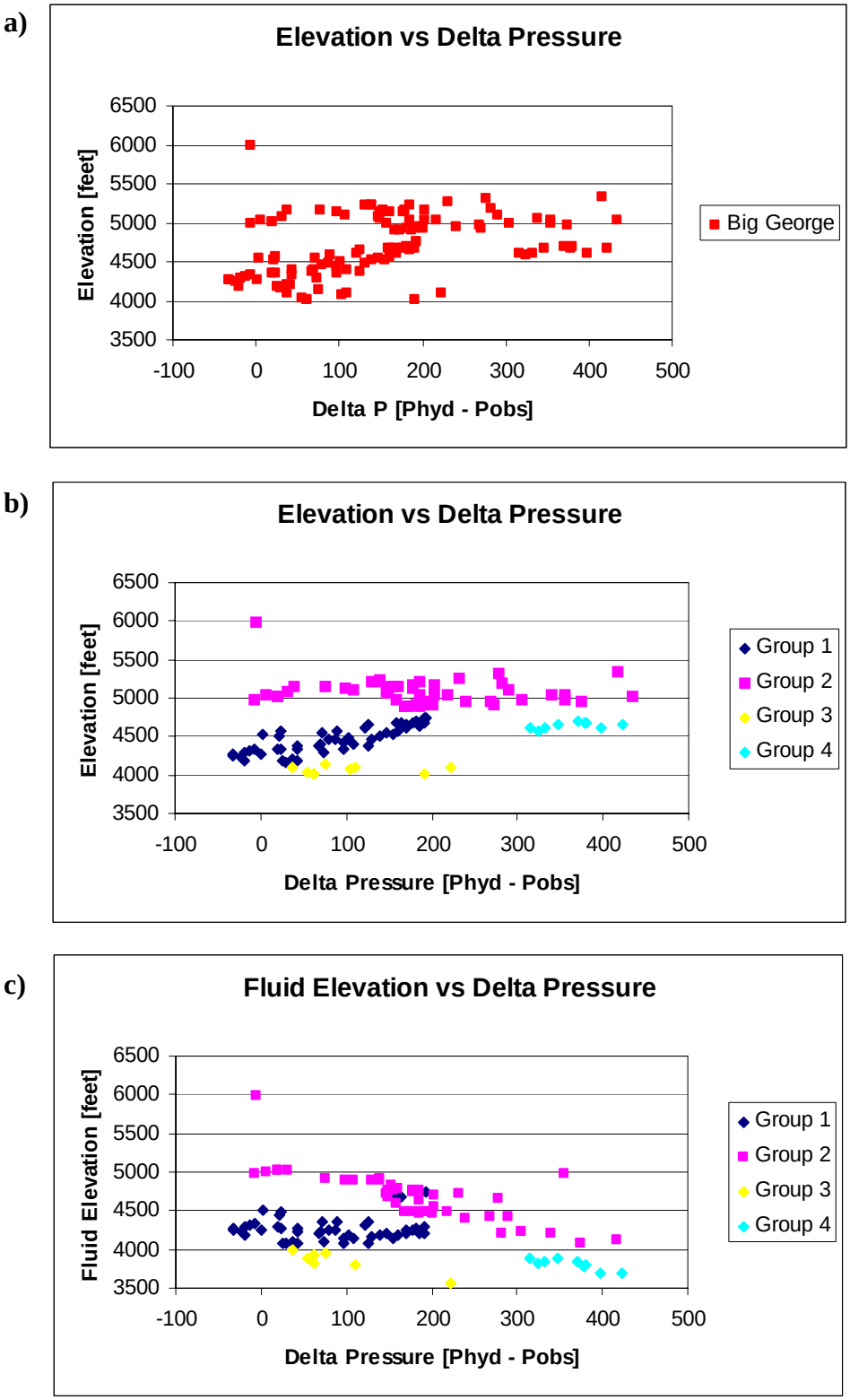

Figure 4.53: Elevation vs Delta Pressure for Big George coal: a) Ungrouped data, b) Same data grouped in 4 different groups. c) Fluid Level vs Delta Pressure for the 4 groups.

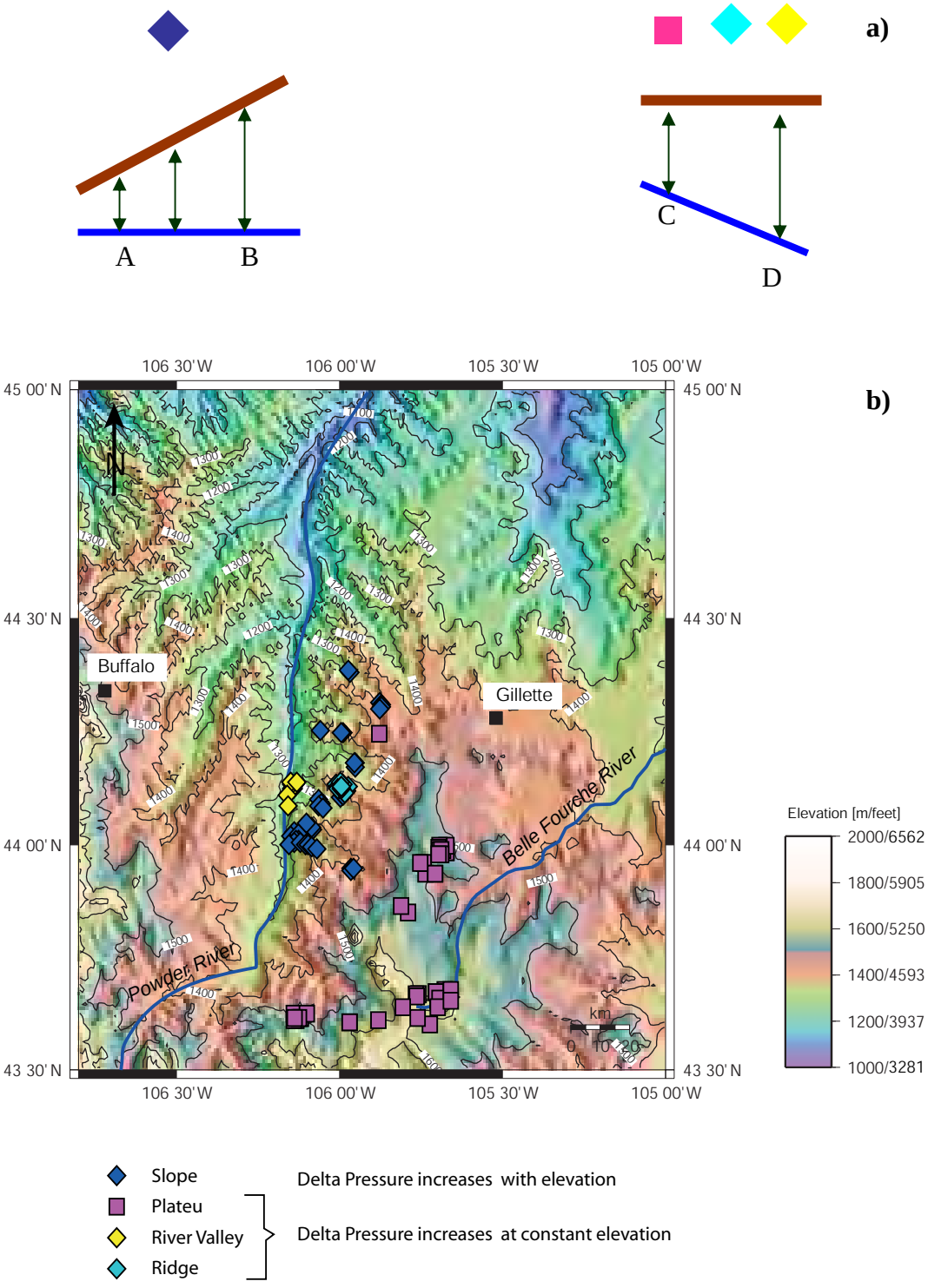

Figure 4.54. a) Variations of fluid elevation and topography for Groups 1 (on the left) and Groups 2, 3 and 4 (on the right). For Group 1 the pore pressure at point B is more subhydrostatic than at point A; for Groups 2, 3 and 4 the pore pressure at point D is more subhydrostatic than at point C. b) Location of the wells that conform the different groups. The elevation contours are in meters.

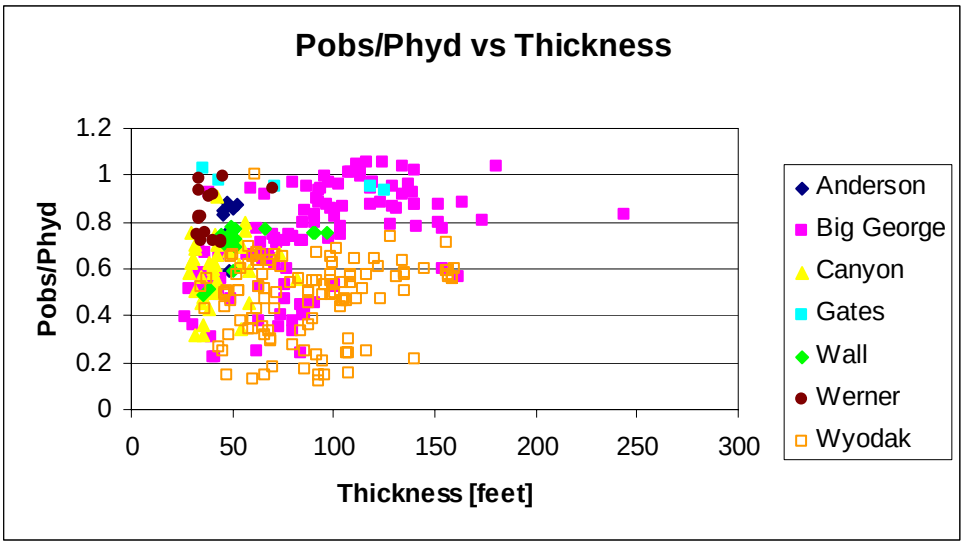

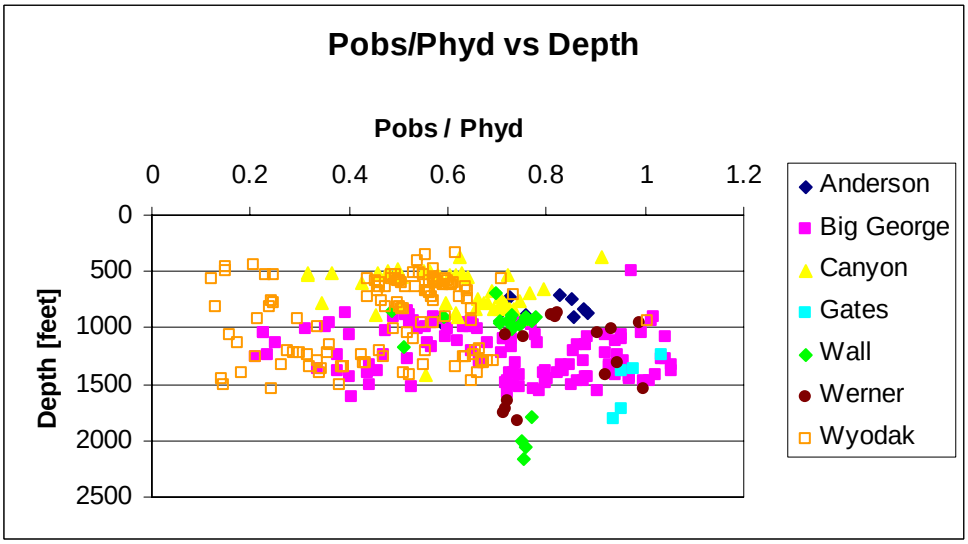

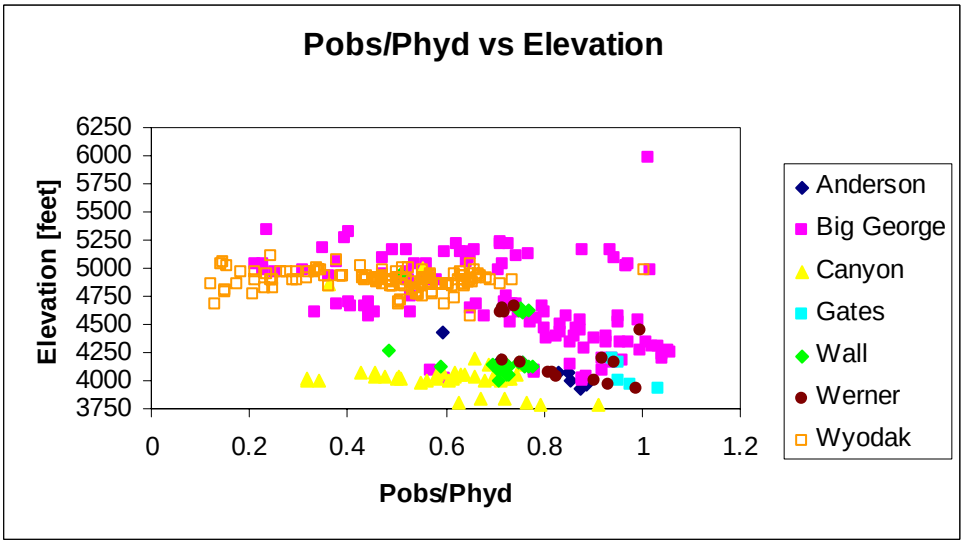

Figure 4.55: P_{obs}/P_{hyd} vs Thickness, Depth and Elevation for Big George coal.

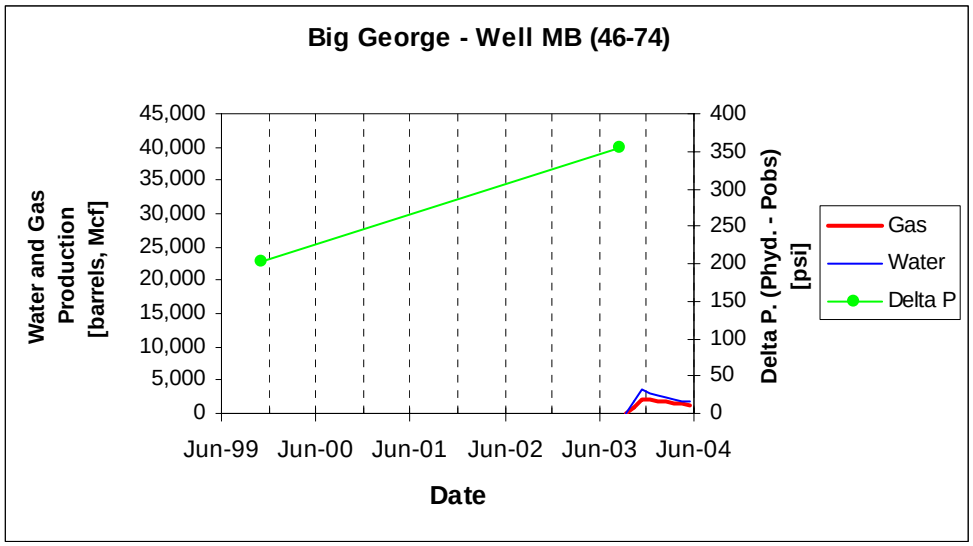

Figure 4.56: Logically, changes of pressure occur after dewatering starts. However, in this well the pore pressure changes before production starts.

4.11 RECOMMENDATIONS TO ACHIEVE BEST WELL COMPLETION PRACTICES

In this study, I have demonstrated that *i*) water-enhancement activities during wellbore completion results in hydraulic fracturing of the coal, *ii*) all of the wells with exceptionally high water production are associated with vertical fracture propagation, *iii*) in these same wells, there are very significant delays in gas production, apparently due to inefficient depressurization of the coals, *iv*) approximately half of the wells characterized by vertical hydraulic fracturing are also characterized by excessive water production.

In areas of known vertical fracture propagation it is necessary to limit the injection during the water enhancement tests in order to prevent propagation of induced fractures into the overlying water-bearing formations. In areas of unknown least principal stress an alternative to the "standard" wellbore completion methods is suggested to limit the number of wells characterized by excessive water production and delayed gas. Water-enhancement procedures should be done in two steps. In the first step, a minifrac (~2 bpm for ~2 min) should be done to determine the magnitude of the least principal stress and thus whether fracture propagation would be vertical or horizontal. If the least horizontal stress corresponds to the overburden (approximately 1 psi/ft), it is safe to assume that horizontal fracture propagation will occur and the water enhancement

activities can proceed at whatever rate and duration the operator chooses. Because many wells with horizontal fractures tend to be poor gas producers, such wells could be hydraulically fractured (and propped) to enhance gas production without risk of significantly affecting the rate of water production. If the shut-in pressure is significantly less than the overburden (~0.6 – 0.9 psi/ft), vertical hydraulic fracture growth is implied and significantly reduced pumping is advised. This would be beneficial from the perspective of minimizing produced waters and decreasing the time for initial gas production.

Mapping the thickness of a coalseam could also be used to predict the direction in which a fracture will propagate. As was shown in Figures 4.28 – 4.31, hydraulic fractures propagate in the vertical plane in coals as thick or thicker than 60 feet. Therefore, if the thickness of the coal is greater than 60 feet, the water enhancement test should be done with a reduced amount of water to prevent vertical hydraulic fracture propagation.

4.12 SUMMARY AND CONCLUSIONS

Through analysis of water-enhancement tests performed in CBM wells of the Powder River Basin, it is clear that the "water-enhancement" activities result in hydraulic fracturing of the coal and possibly the adjacent strata, resulting in perhaps both excess CBM water production and inefficient depressurization of coals.

The magnitude of the least principal stress has been compiled for 372 wells, and this has demonstrated that both vertical and horizontal hydraulic fracture propagation occurs within the basin. Where the least principal stress is vertical, hydraulic fracture growth is horizontal and water production is minimal. Where the least principal stress is horizontal, fracture growth is vertical and water production is significantly greater for some wells. It is important to note that all of the wells with exceptionally high water production are always associated with vertical fracture growth. In these same wells, there are significant delays in gas production, perhaps due to inefficient depressurization of the coals. However, wells with vertical fractures that produce low water volumes are excellent gas producers (they produce more than 3,000 Mcf/month) and are better gas producers than wells with horizontal fractures. Since wells with vertical fractures are, in

general, excellent gas producers, it is inferred that the face cleats in the coals must be efficiently connected by the induced vertical fracture.

It has been identified that horizontal hydraulic fracturing is typical towards the Sheridan area. This may be a significant finding, as water injection wells are perhaps needed in the near future in this region because the water has a high content of sodium and will need to be properly disposed. Thus, knowing that there is no vertical connection between the coal seam that is being produced and the sand layers where the water may be injected is particularly important for the operators of the area if water injection activities are undertaken here.

While the reason for the variation in the magnitude of S_3 has not been determined it does appear that coal thickness affects the S_3 magnitudes. In general, in areas where a coal seam has a thickness greater than 60 feet S_3 is equivalent to the minimum horizontal stress, and therefore fractures propagate in the vertical direction. By knowing the areas where a coal seam is thicker than 60 ft, propagation of a vertical fracture into adjacent formations could be avoided by scaling down the water-enhancement procedure.

In order to minimize produced CBM waters, recommendations for better well completion practices have been outlined. In areas of known vertical fracture propagation it is necessary to limit the injection during the water enhancement tests in order to prevent propagation of induced fractures into the overlying water-bearing formations. In areas of unknown least principal stress an alternative to the “standard” wellbore completion methods has been suggested to limit the number of wells characterized by excessive water production and delayed gas. A minifrac (~2 bpm for ~2 min) should be done to determine the magnitude of the least principal stress and thus whether fracture propagation would be vertical or horizontal. If the least horizontal stress corresponds to the overburden, horizontal fracture propagation will occur and the water enhancement activities can proceed at whatever rate and duration the operator chooses. As many wells with horizontal fractures tend to be poor gas producers, it is also suggested that such wells are hydraulically fractured (and propped) to enhance gas production. If the shut-in pressure is significantly less than the overburden, vertical hydraulic fracture growth is implied and significantly reduced pumping is advised. This would be beneficial from the perspective of minimizing produced waters and decreasing the time for initial gas production.

ACKNOWLEDGEMENTS

Thanks to Conoco-Phillips, Marathon Oil – Pennaco Energy, Williams and Wolverine Energy for kindly providing the data used in this study. Thanks especially to Chris Hogle and Gabriel D'Arthenay for their kindness and interest in this work. Apache Corporation, Conoco-Phillips and Marathon-Pennaco (sponsors of the Western Resources Project Foundation), supported this study.

REFERENCES

Ayers, W., 2002, Coalbed gas systems, resources, and production and a review of contrasting cases from the San Juan and Powder River basins: AAPG Bulletin, **86**, pp. 1853-1890.

DeBruin, R. and Lyman, R., 1999, Coalbed Methane in Wyoming *in* Wyoming Geological Association Guidebook "Coalbed Methane and the Tertiary Geology of the Powder River Basin, Wyoming and Montana", pp. 61-72.

DeBruin, R., Lyman, R., Jones, R. and Cook, L., 2004, Coalbed Methane in Wyoming. Wyoming State Geological Survey, Information Pamphlet 7 (second revision).

Flores, R. M. and Bader, L. R., 1999, Fort Union Coal In The Powder River Basin, Wyoming And Montana: A Synthesis *in* U.S. Geological Survey Professional Paper 1625-A, Resource Assessment Of Selected Tertiary Coal Beds And Zones In The Northern Rocky Mountains And Great Plains Region, 1999.

Jones, N., Overview of an Interactive Geologic, hydrologic and water quality database and model for the northern Powder River Basin *in* Proceedings of the First Annual Coalbed Natural Gas Research, Monitoring, and Applications Conference, Laramie, Wyoming, Aug. 17 – 19, 2004, p. 25 – 26.

Jones, A. , Bell, G. and R. Schraufnagel, 1988, A review of the physical and mechanical properties of coal with implications for coal-bed methane well completion and

production in Coal-Bed Methane, San Juan Basin. Rocky Mountain Association of Geologists, pp. 169-181.

Meyer, J., 1999, General Draw-Down Map – Wyodak / Anderson Coal Bed, 1980 to 1998 *in* Wyoming Geological Association Guidebook "Coalbed Methane and the Tertiary Geology of the Powder River Basin, Wyoming and Montana", pp. 87-88.

United States Environmental Protection Agency, 2002. DRAFT Evaluation of Impacts to Underground Sources of Drinking Water by Hydraulic Fracturing of Coalbed Methane Reservoirs (EPA 816-D-02-006) http://www.epa.gov/safewater/uic/ /cbmstudy/docs.html (April, 2003)

Wessel, P., and W. H. F. Smith, New version of the Generic Mapping Tools released, EOS Trans. Amer. Geophys. U., vol. 76, pp. 329, 1995.

Wyoming Oil and Gas Conservation Commission (WOGCC) http://wogcc.state.wy.us (August 2004)

Zoback, M.D., Barton, C.A., Brudy M., Castillo, D.A., Finkbeiner, T., Grollimund, B., Moos, D.B, Peska, P., Ward, C.D. and Wiprut, D.J., 2003, Determination of stress orientation and magnitude in deep wells: International Journal of Rock Mechanics and Mining Sciences, **40**, 1049-1076.

APPENDIX 4.A. DATA OF LEAST PRINCIPAL STRESS VS DEPTH

Figure 4.A.1 is a helpful resource to visualize the exact location of the data. It also provides information about some of the major operators in the Powder River Basin.

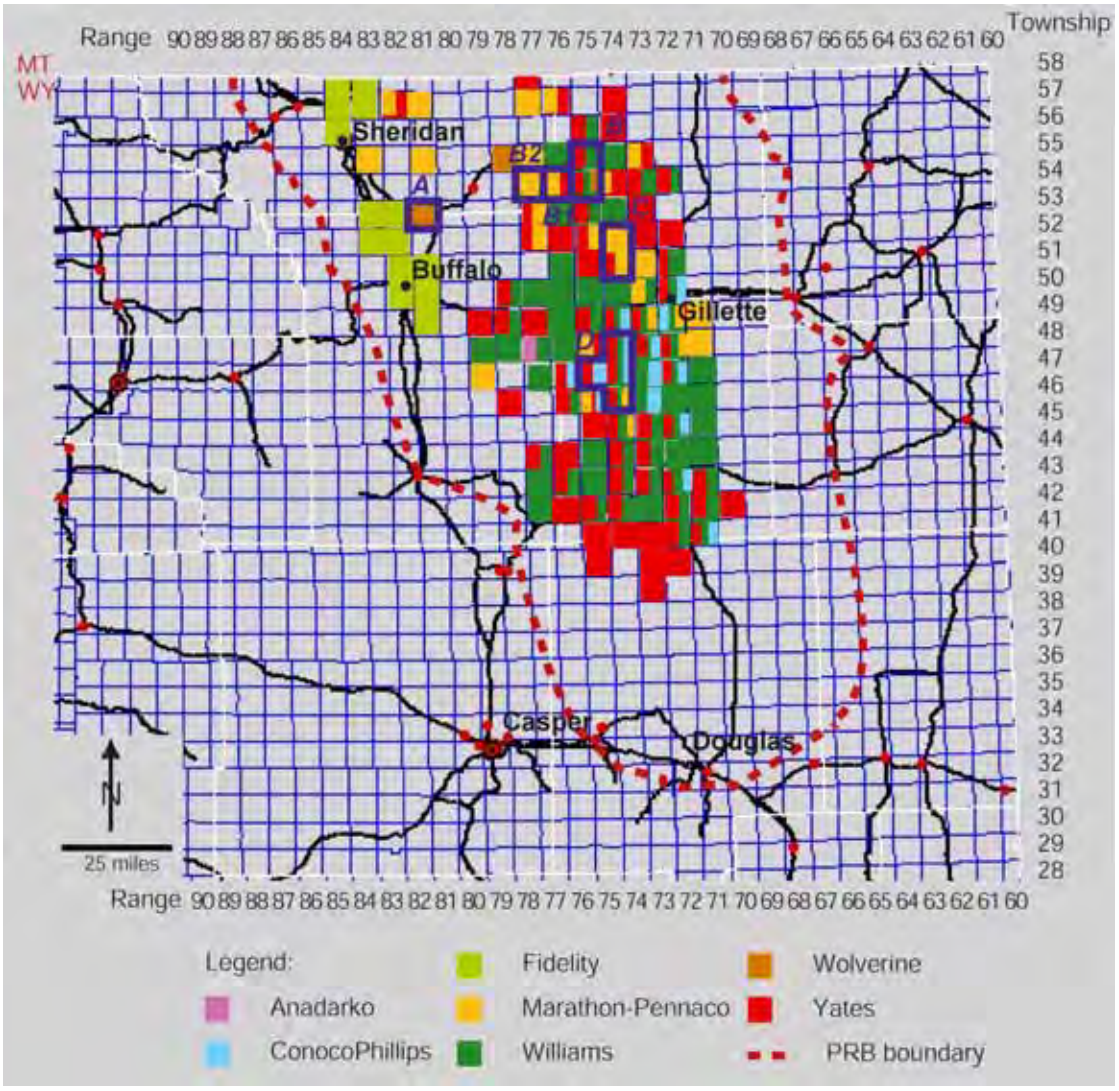

Figure 4.A.1: Map of the Wyoming part of the Powder River basin showing the townships and some of the companies operating in the basin.

Figure 4.A.2: (next seven pages) Plots showing the magnitude of the least principal stress vs depth throughout the basin. The color denotes the coal seam where the test was performed. For reference, the overbuden stress and the hydrostatic pressure have also been plotted. The black line corresponds to the overburden or vertical stress and the gray line corresponds to the hydrostatic pressure. Use Figure 4.A.1 for location.

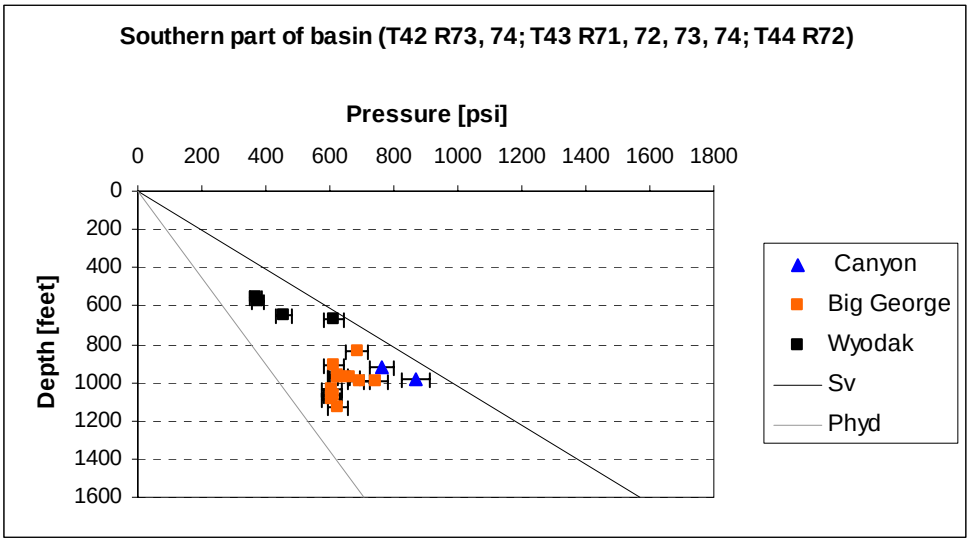

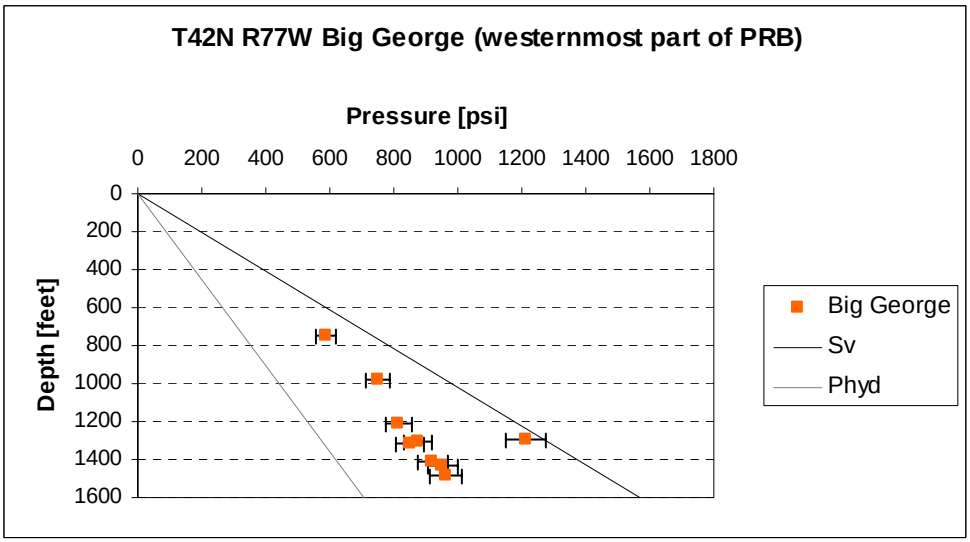

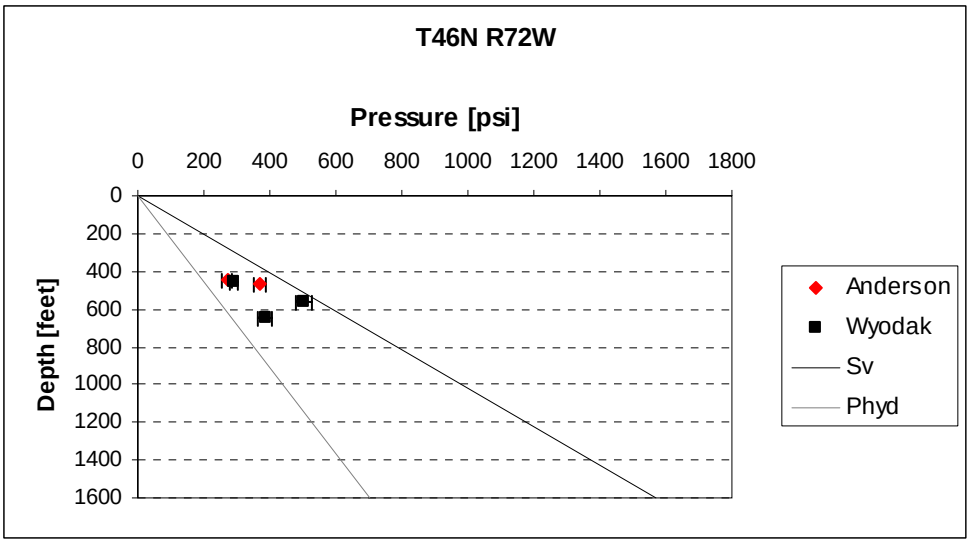
T46N R72W
Pressure [psi]
0 200 400 600 800 1000 1200 1400 1600 1800
Depth [feet]
0 200 400 600 800 1000 1200 1400 1600
Anderson
Wyodak
Sv
Phyd

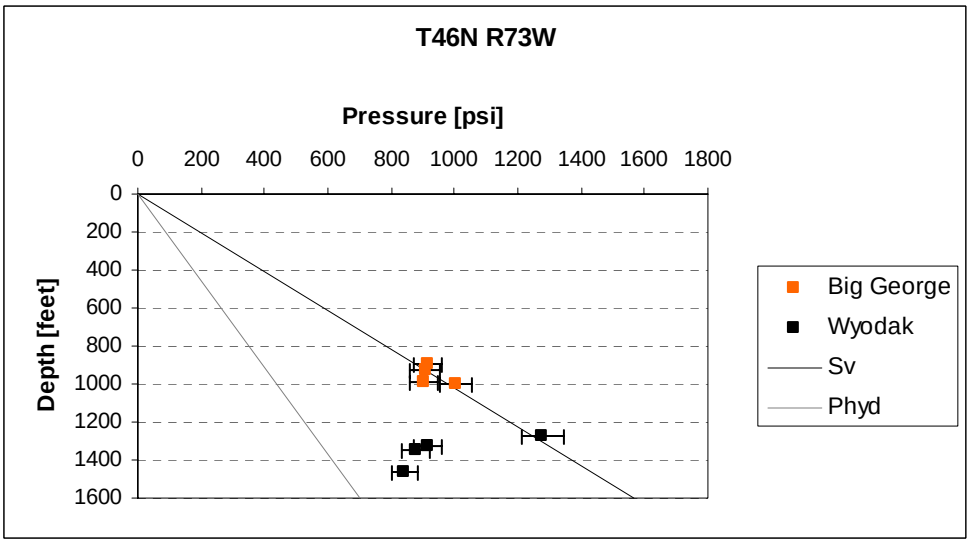
T46N R73W
Pressure [psi]
0 200 400 600 800 1000 1200 1400 1600 1800
Depth [feet]
0 200 400 600 800 1000 1200 1400 1600
Big George
Wyodak
Sv
Phyd

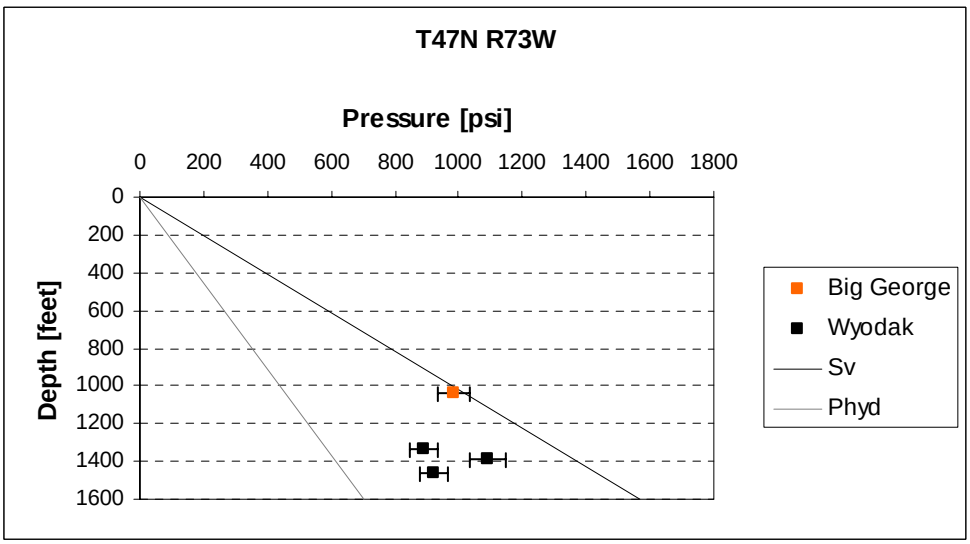
T47N R73W
Pressure [psi]
0 200 400 600 800 1000 1200 1400 1600 1800
Depth [feet]
0 200 400 600 800 1000 1200 1400 1600
Big George
Wyodak
Sv
Phyd

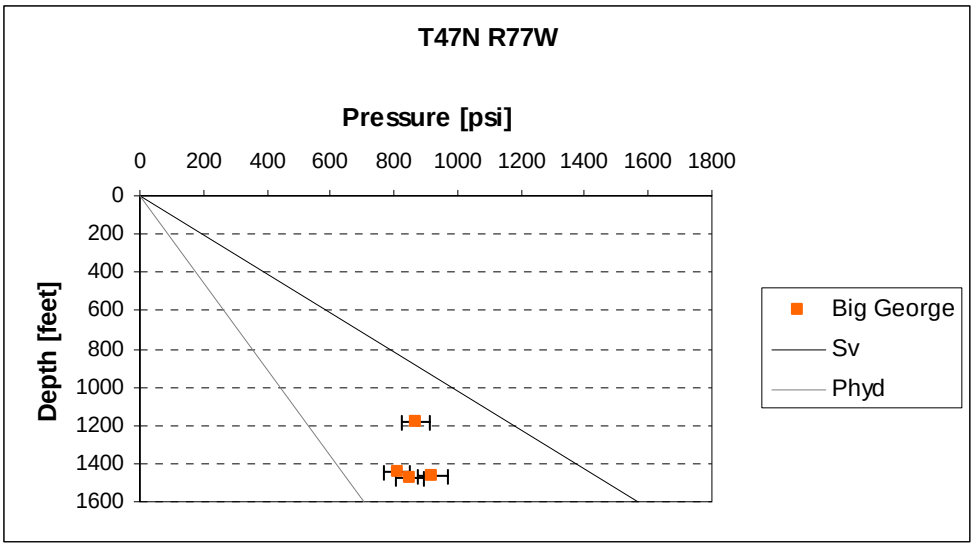
T47N R77W
Pressure [psi]
0 200 400 600 800 1000 1200 1400 1600 1800
Depth [feet]
0 200 400 600 800 1000 1200 1400 1600
Big George
Sv
Phyd

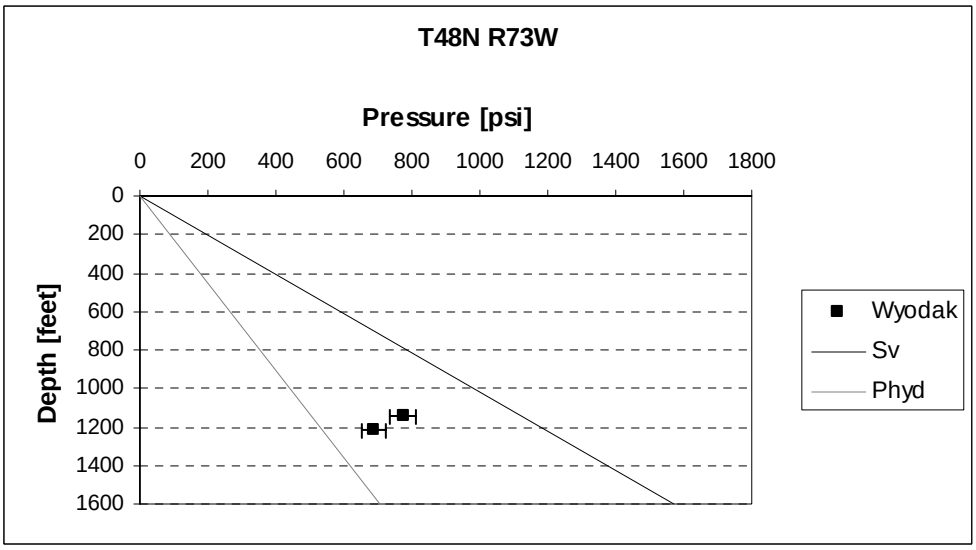
T48N R73W
Pressure [psi]
0 200 400 600 800 1000 1200 1400 1600 1800
Depth [feet]
0 200 400 600 800 1000 1200 1400 1600
Wyodak
Sv
Phyd

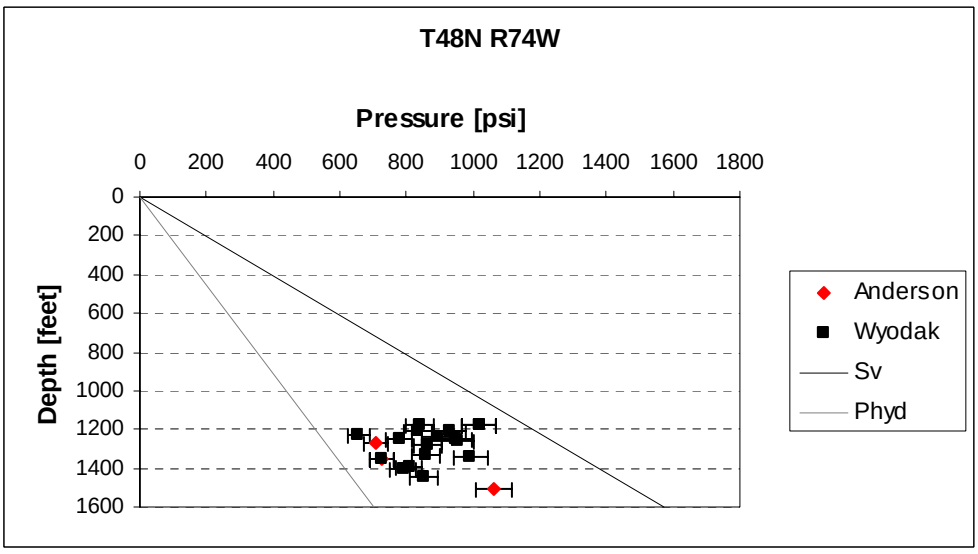
T48N R74W
Pressure [psi]
0 200 400 600 800 1000 1200 1400 1600 1800
Depth [feet]
0 200 400 600 800 1000 1200 1400 1600
Anderson
Wyodak
Sv
Phyd

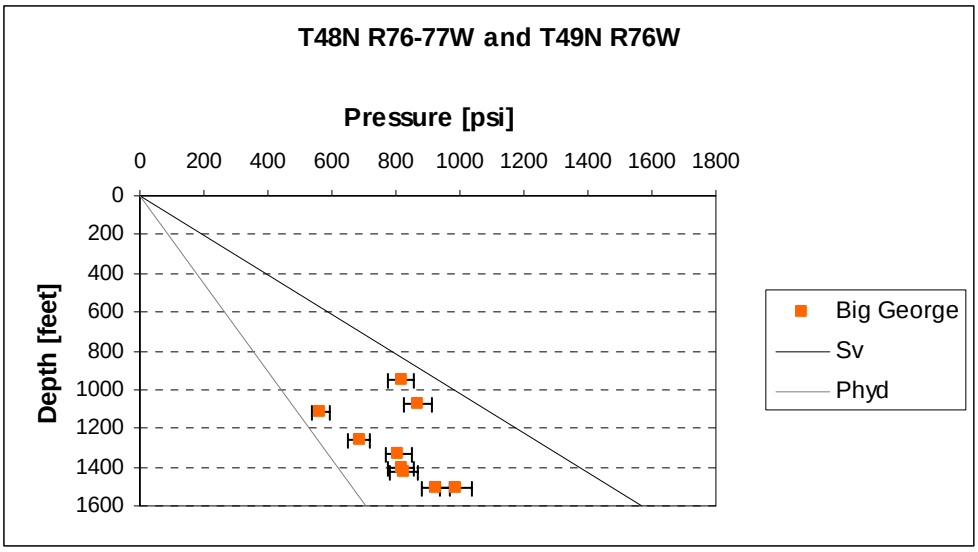
T48N R76-77W and T49N R76W
Pressure [psi]
0 200 400 600 800 1000 1200 1400 1600 1800
Depth [feet]
0 200 400 600 800 1000 1200 1400 1600
Big George
Sv
Phyd

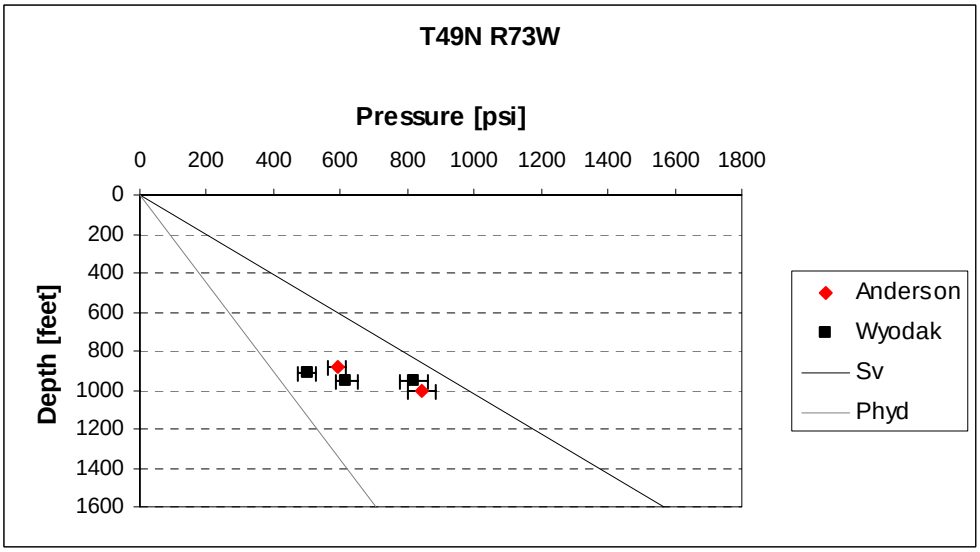
T49N R73W
Pressure [psi]
0 200 400 600 800 1000 1200 1400 1600 1800
Depth [feet]
0 200 400 600 800 1000 1200 1400 1600
Anderson
Wyodak
Sv
Phyd

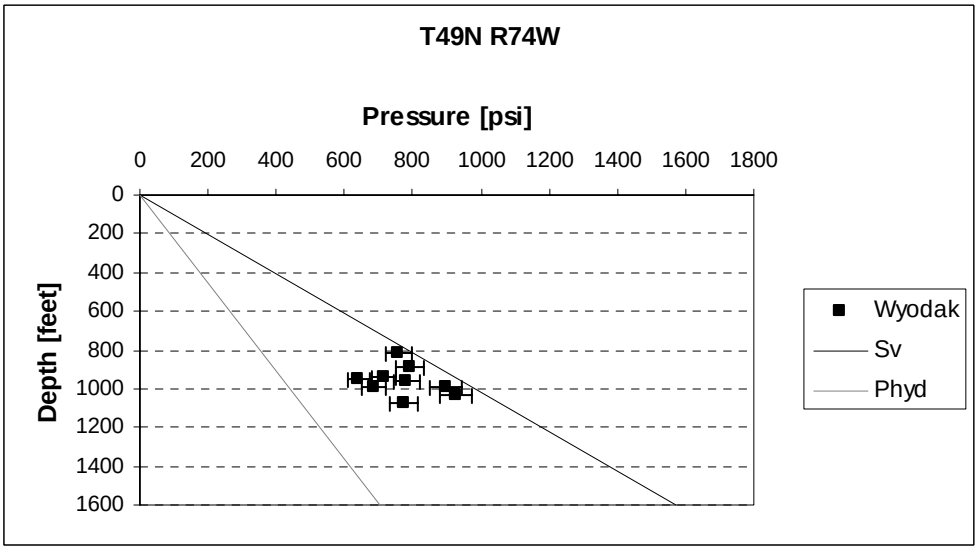
T49N R74W
Pressure [psi]
0 200 400 600 800 1000 1200 1400 1600 1800
Depth [feet]
0 200 400 600 800 1000 1200 1400 1600
Wyodak
Sv
Phyd

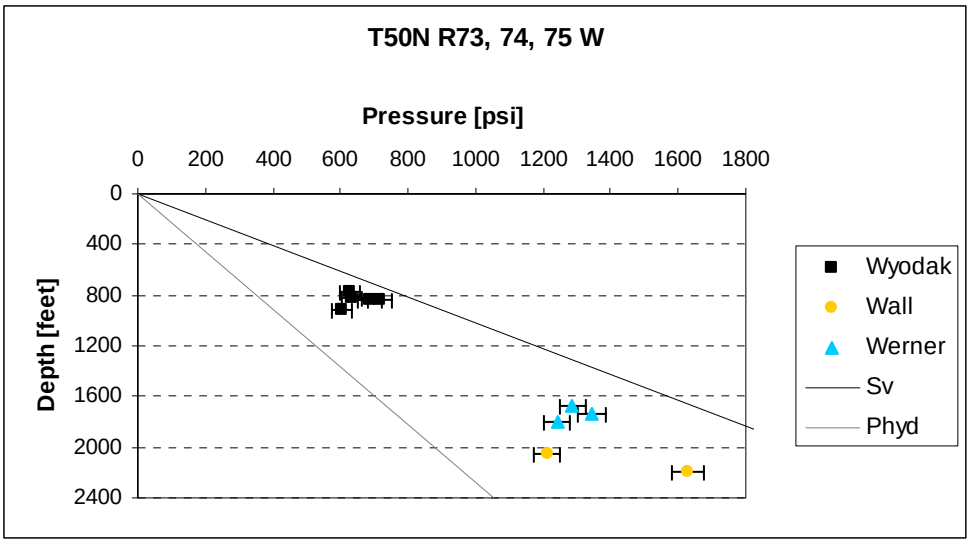
T50N R73, 74, 75 W
Pressure [psi]
0 200 400 600 800 1000 1200 1400 1600 1800
Depth [feet]
0 400 800 1200 1600 2000 2400
Wyodak
Wall
Werner
Sv
Phyd

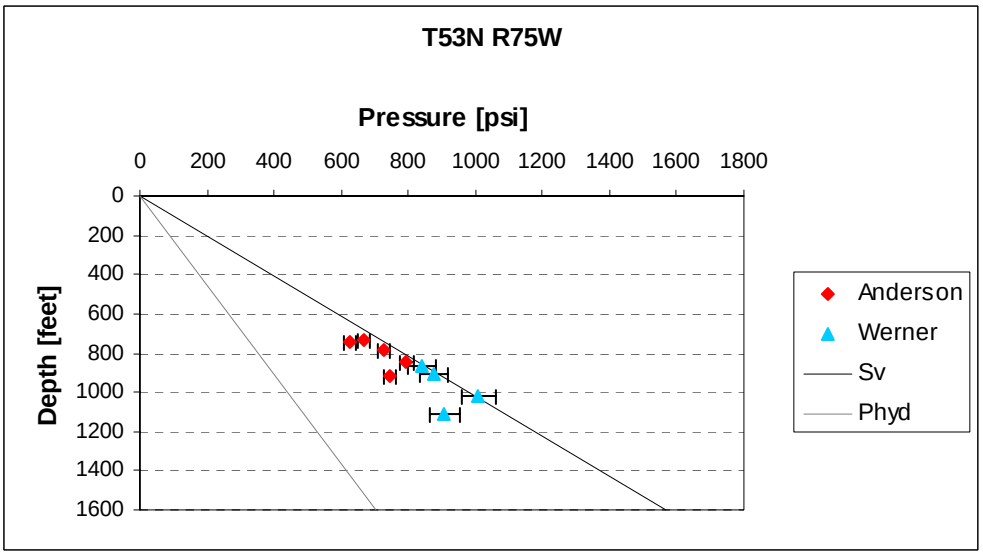
T53N R75W
Pressure [psi]
0 200 400 600 800 1000 1200 1400 1600 1800
Depth [feet]
0 200 400 600 800 1000 1200 1400 1600
Anderson
Werner
Sv
Phyd

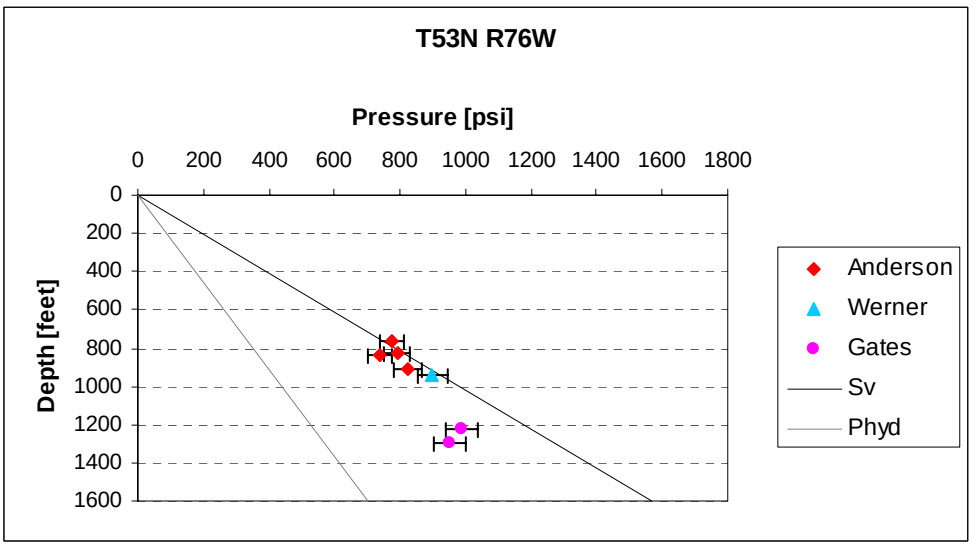
T53N R76W
Pressure [psi]
0 200 400 600 800 1000 1200 1400 1600 1800
Depth [feet]
0 200 400 600 800 1000 1200 1400 1600
Anderson
Werner
Gates
Sv
Phyd

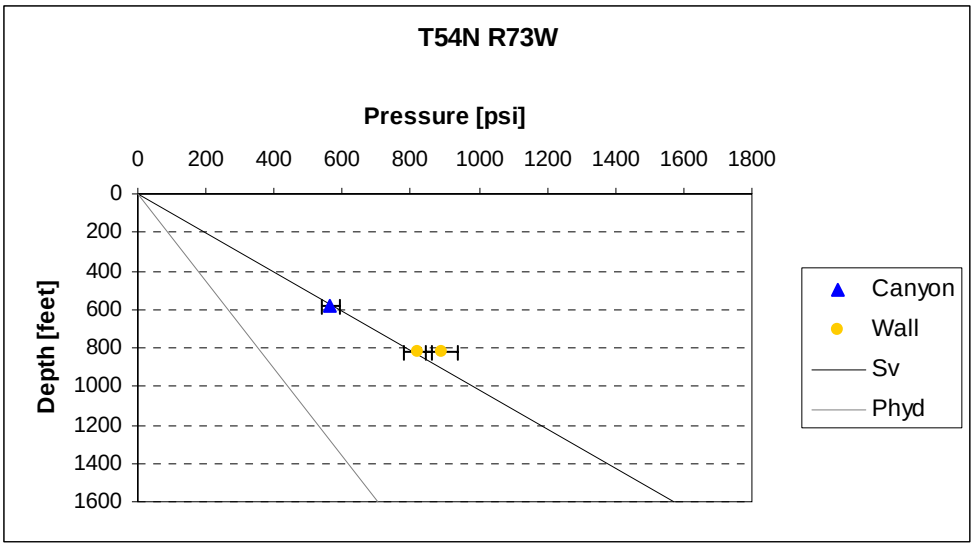
T54N R73W
Pressure [psi]
0 200 400 600 800 1000 1200 1400 1600 1800
Depth [feet]
0 200 400 600 800 1000 1200 1400 1600
Canyon
Wall
Sv
Phyd

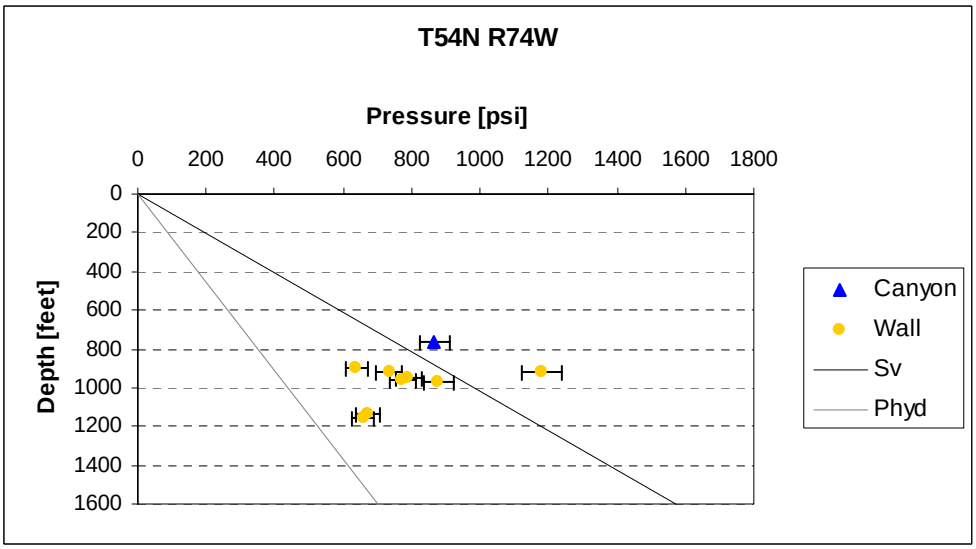
T54N R74W
Pressure [psi]
0 200 400 600 800 1000 1200 1400 1600 1800
Depth [feet]
0 200 400 600 800 1000 1200 1400 1600
Canyon
Wall
Sv
Phyd

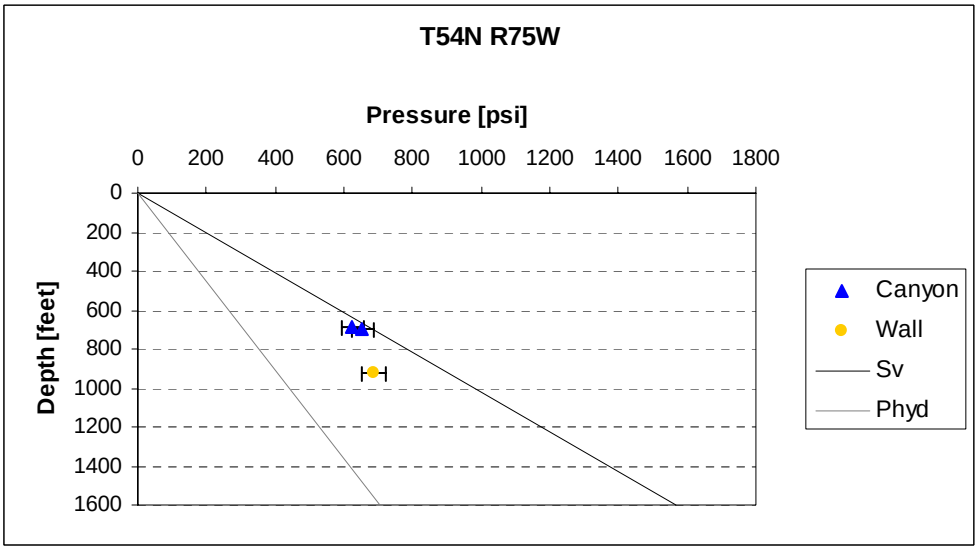
T54N R75W
Pressure [psi]
0 200 400 600 800 1000 1200 1400 1600 1800
Depth [feet]
0 200 400 600 800 1000 1200 1400 1600
Canyon
Wall
Sv
Phyd

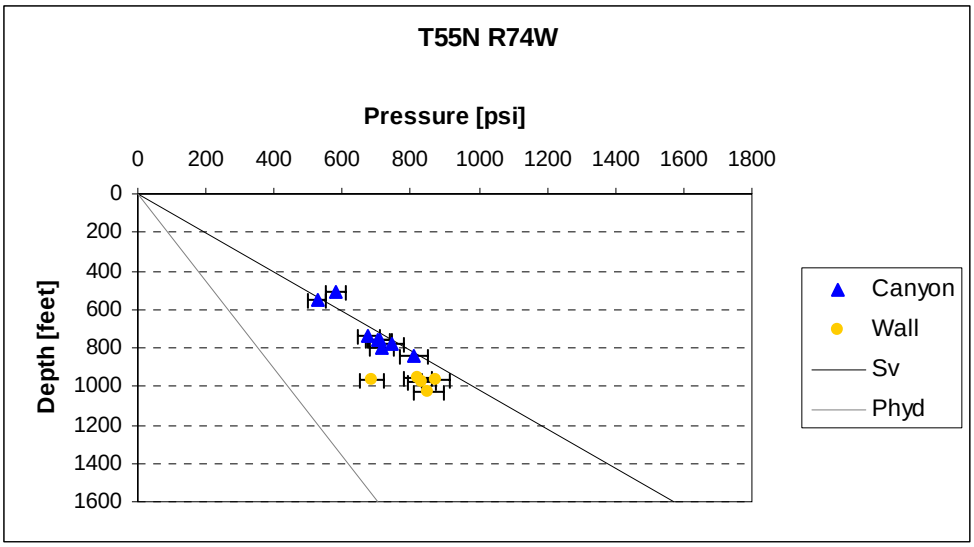
T55N R74W
Pressure [psi]
0 200 400 600 800 1000 1200 1400 1600 1800
Depth [feet]
0 200 400 600 800 1000 1200 1400 1600
Canyon
Wall
Sv
Phyd

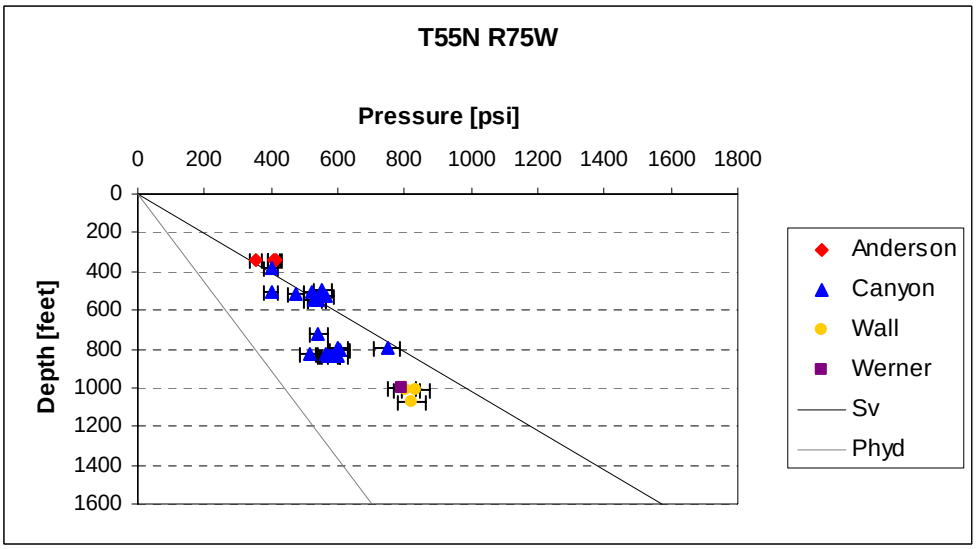
T55N R75W
Pressure [psi]
0 200 400 600 800 1000 1200 1400 1600 1800
Depth [feet]
0 200 400 600 800 1000 1200 1400 1600
Anderson
Canyon
Wall
Werner
Sv
Phyd

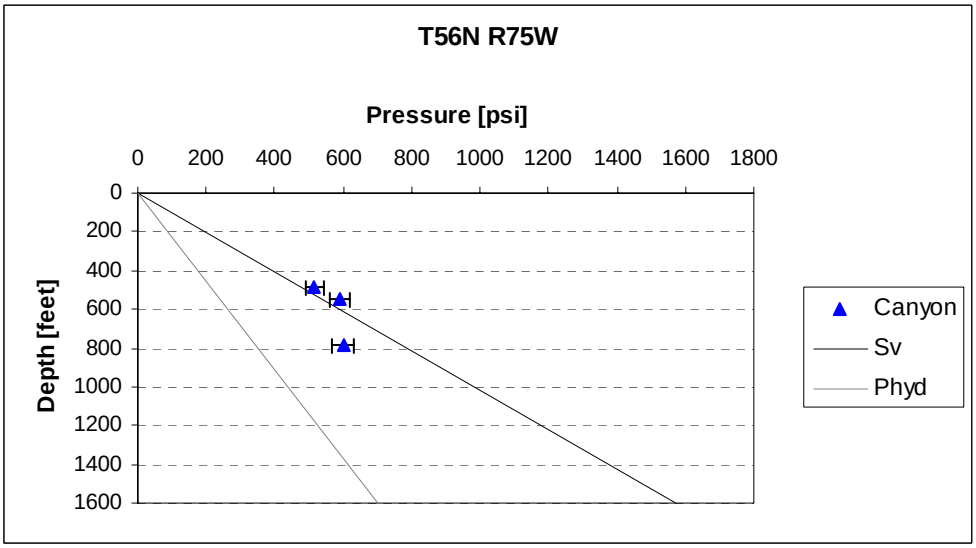
T56N R75W
Pressure [psi]
0 200 400 600 800 1000 1200 1400 1600 1800
Depth [feet]
0 200 400 600 800 1000 1200 1400 1600
Canyon
Sv
Phyd

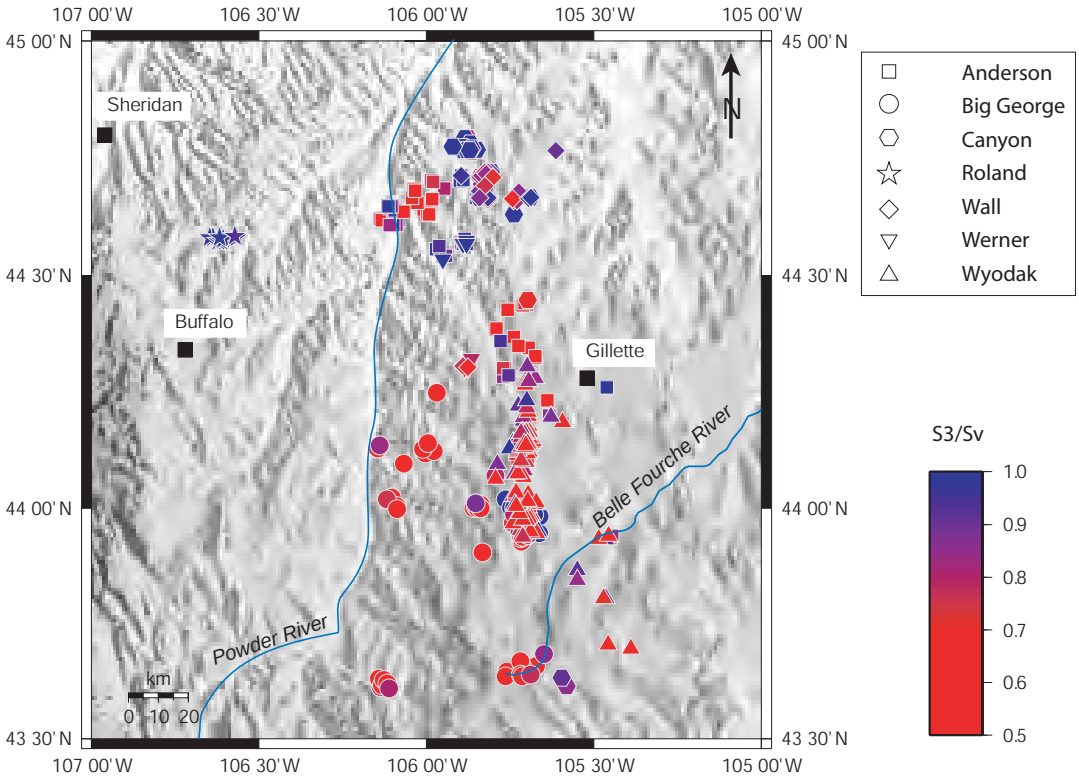

Figure 4.A.3: Summary figure showing the magnitude of S_3/S_V for seven coals, represented by different symbols, in the central part of the basin. Note that symbols overlap.

APPENDIX 4.B. WATER AND GAS PRODUCTION MAPS FOR BIG GEORGE COAL

These maps were created with extra data points of water and gas production in order to make a better interpolation using GMT. The data points encircled in white correspond to S3/Sv. This map helps visualize areas of small and large water production. As can be seen, data points in blue, (S3/Sv = 1, horizontal fractures) are always associated with the blue regions interpolated from the water production data. The data points indicating vertical fractures are associated with both small and large water production. Combining the map with the previous findings, it is possible to predict the gas production of wells with vertical fractures. Wells with vertical fractures in low water production areas will be producing high amounts of gas, but wells with vertical fractures in large water production areas will be producing almost no gas. Figure 4.B.2 confirms the above conclusions. All the white data points in Figure 4.B.2 indicate zero gas production.

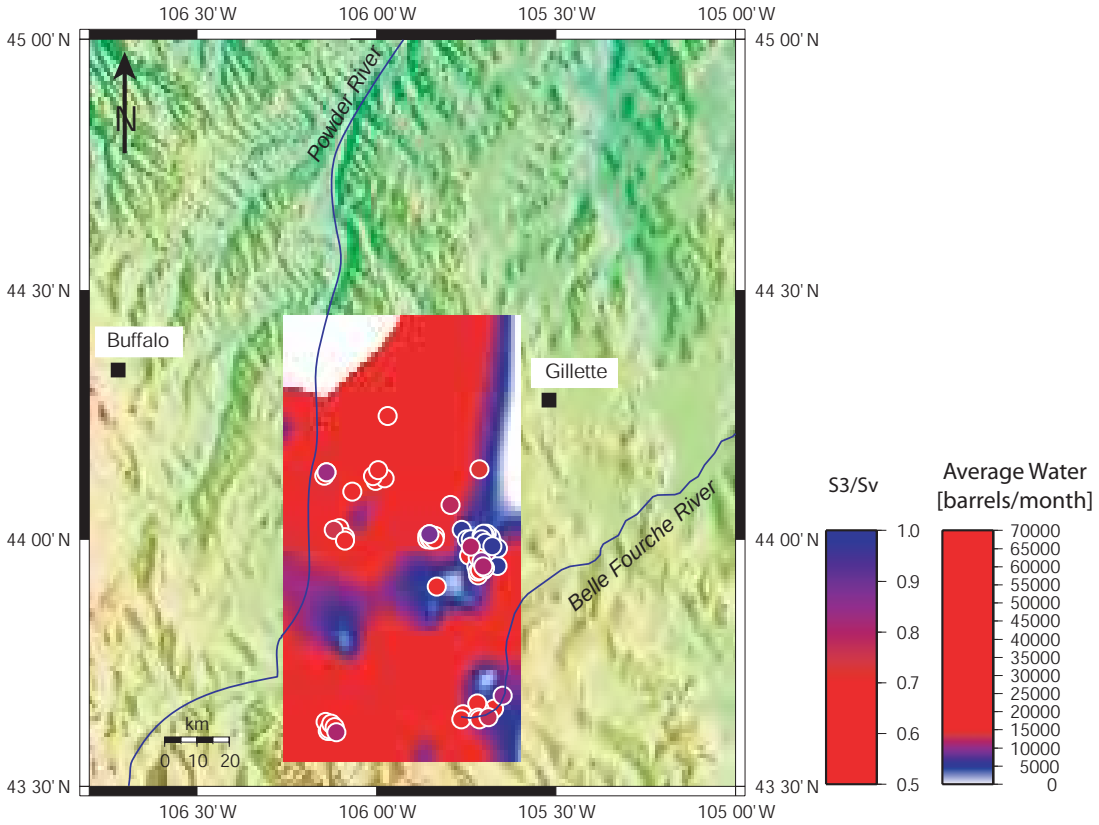

Figure 4.B.1: Interpolation for average water production and data points of S_3/S_V for Big George coal.

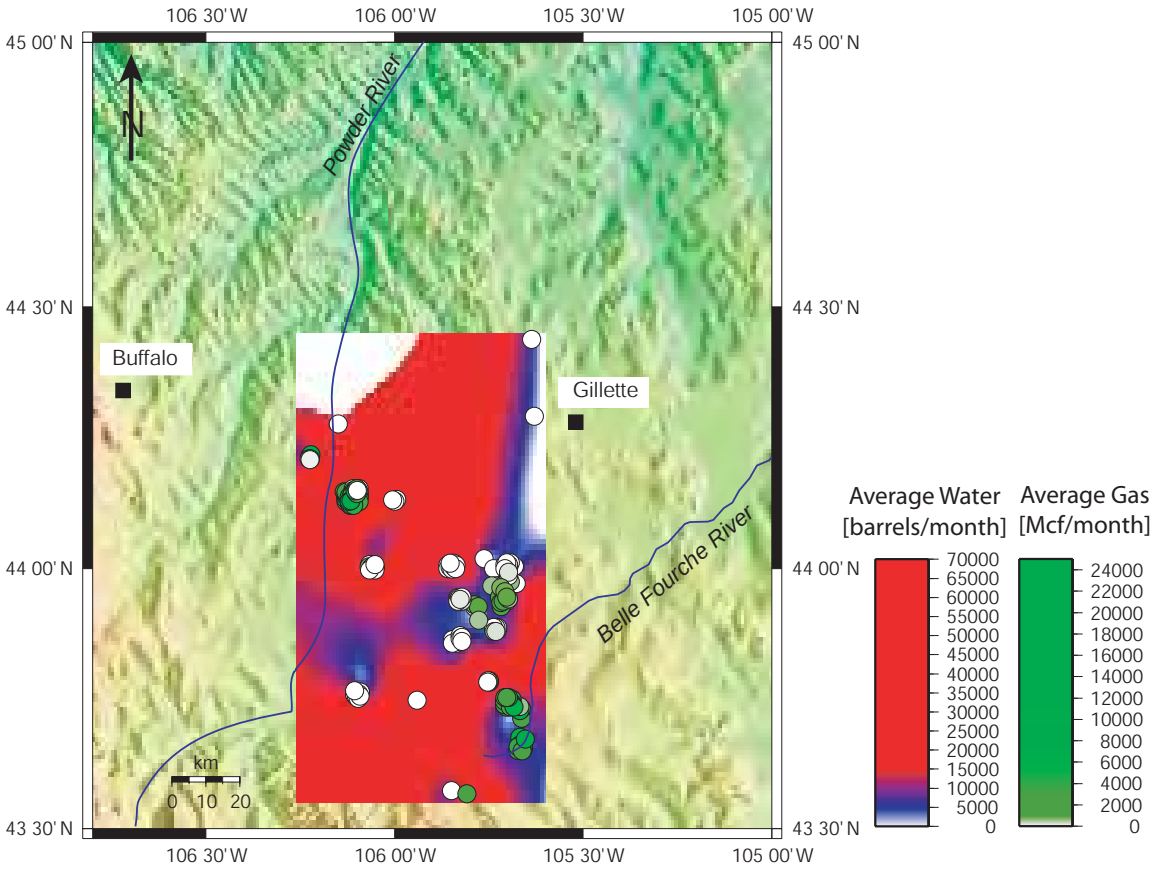

Figure 4.B.2: Interpolation of water production with gas production data points for Big George coal.

APPENDIX 4.C. WATER AND GAS PRODUCTION DATA

In this Appendix, plots of water and gas production versus the time since production started for the additional wells analyzed are presented.

Figure 4.C.1: (next 19 pages) Plots of water production (upper panel) and gas production (lower panel) throughout the basin with respect to the time that the wells have been in production. All the plots have the same scale, that is, water production is from 0 to 40,000 barrels, gas production is from 0 to 20,000 Mcf and time since production started is from 0 to 52 months. This will help to establish comparisons among townships. For location refer to Figure 4.A.1.

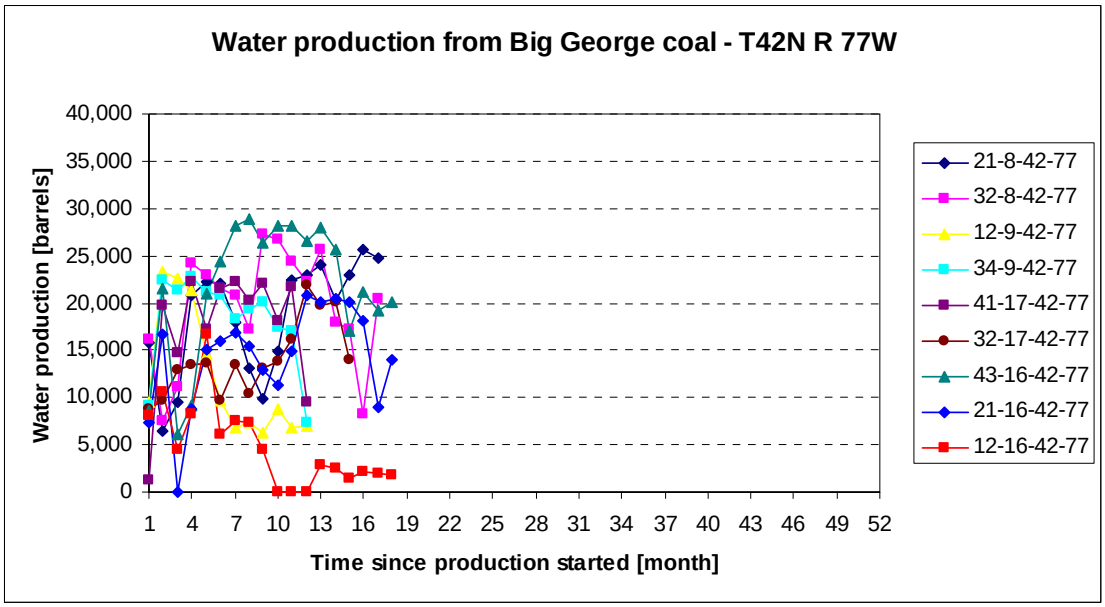

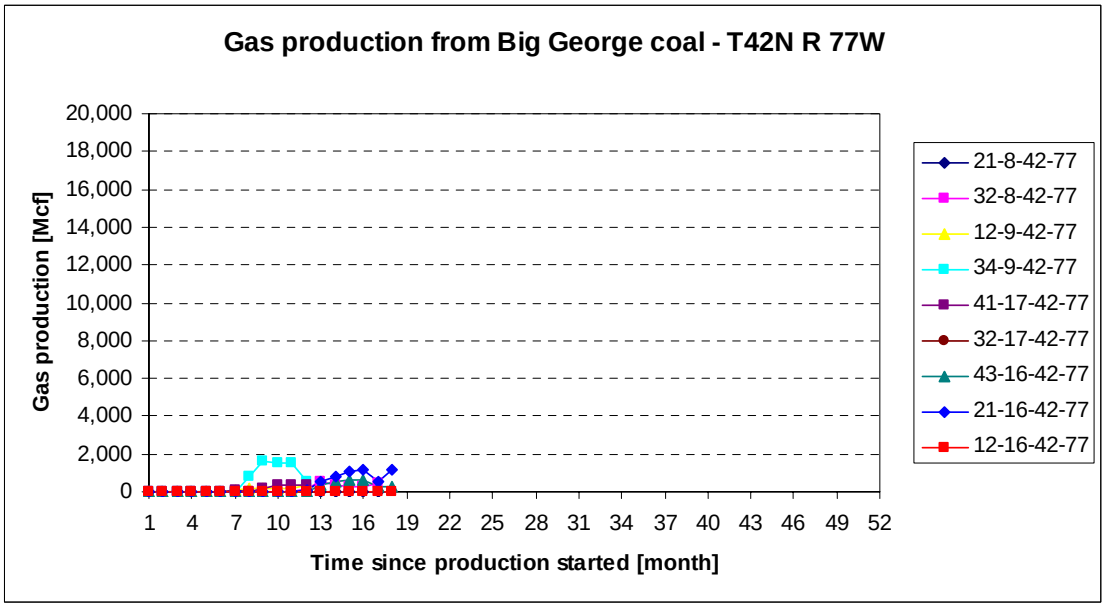

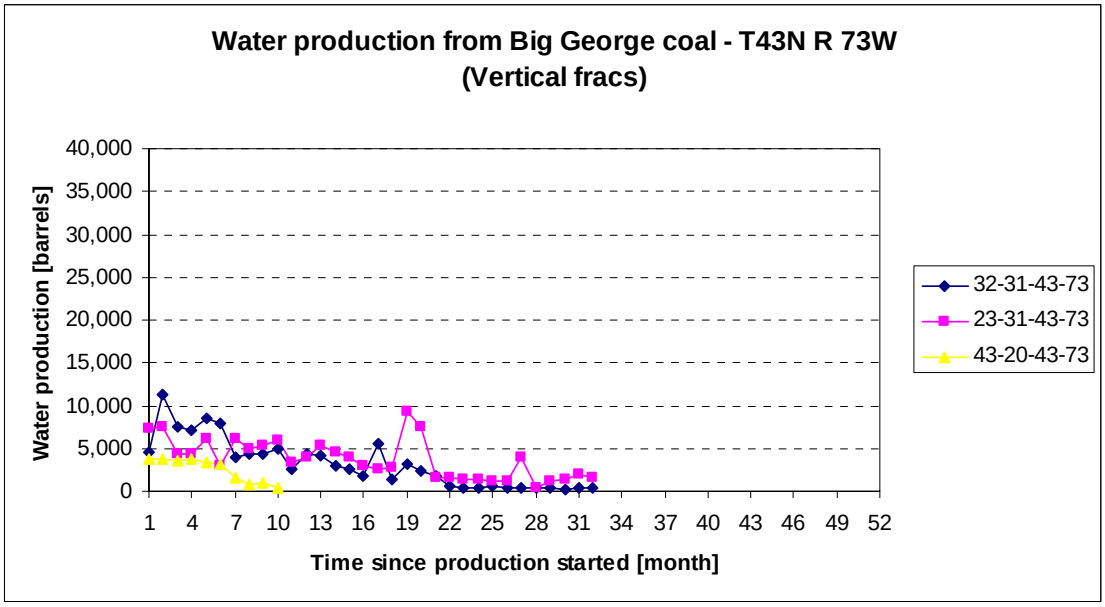
Water production from Big George coal - T43N R 73W
(Vertical fracs)
Water production [barrels]
40,000
35,000
30,000
25,000
20,000
15,000
10,000
5,000
0
1 4 7 10 13 16 19 22 25 28 31 34 37 40 43 46 49 52
Time since production started [month]
32-31-43-73
23-31-43-73
43-20-43-73

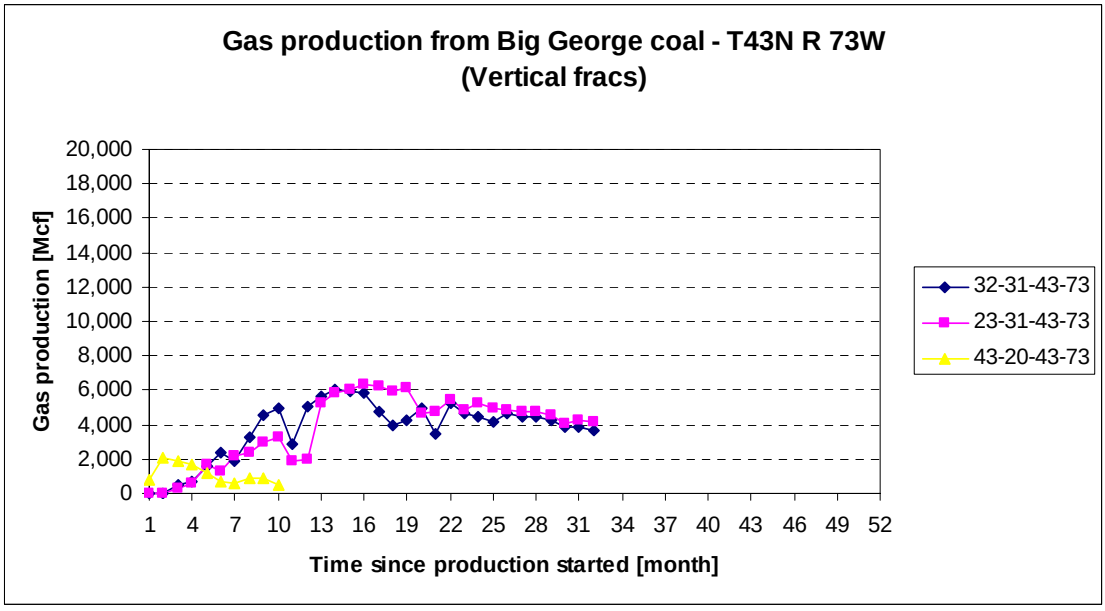
Gas production from Big George coal - T43N R 73W
(Vertical fracs)
Gas production [Mcf]
20,000
18,000
16,000
14,000
12,000
10,000
8,000
6,000
4,000
2,000
0
1 4 7 10 13 16 19 22 25 28 31 34 37 40 43 46 49 52
Time since production started [month]
32-31-43-73
23-31-43-73
43-20-43-73

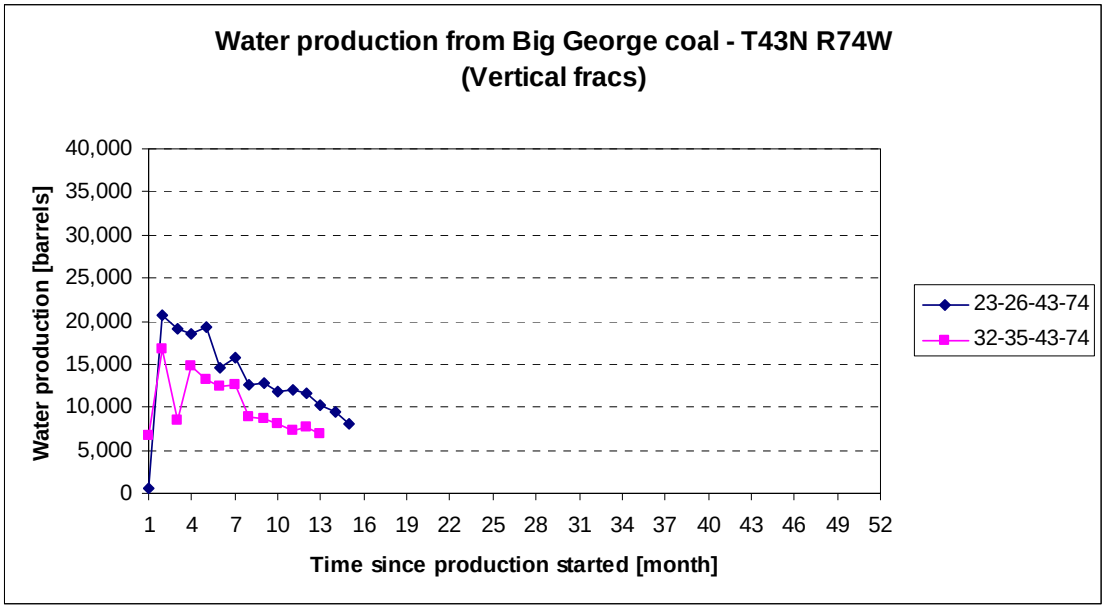
Water production from Big George coal - T43N R74W
(Vertical fracs)
Water production [barrels]
40,000
35,000
30,000
25,000
20,000
15,000
10,000
5,000
0
1 4 7 10 13 16 19 22 25 28 31 34 37 40 43 46 49 52
Time since production started [month]
23-26-43-74
32-35-43-74

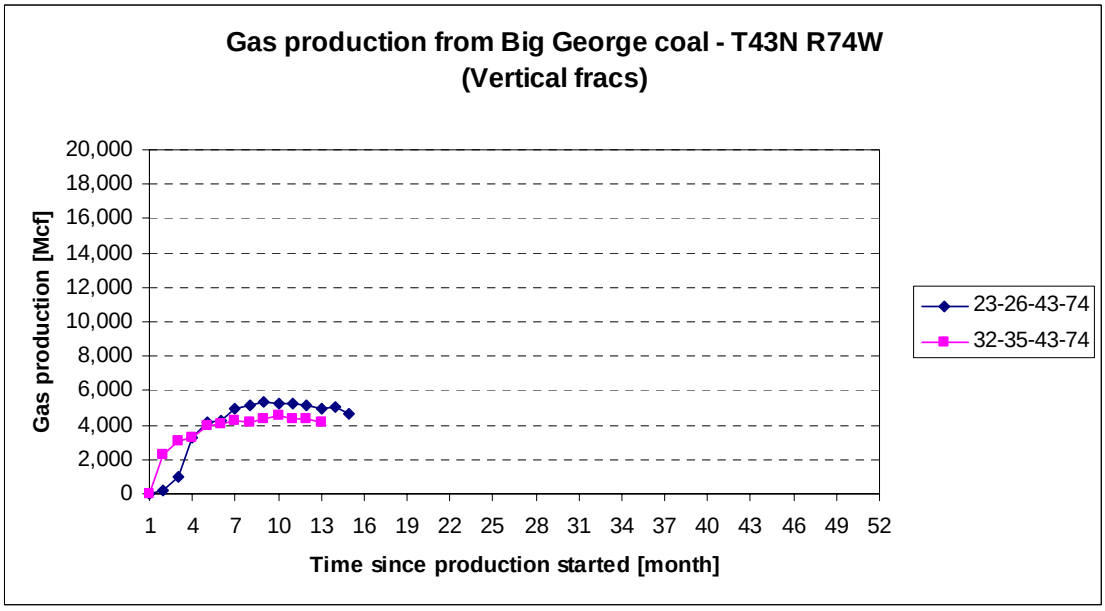
Gas production from Big George coal - T43N R74W
(Vertical fracs)
Gas production [Mcf]
20,000
18,000
16,000
14,000
12,000
10,000
8,000
6,000
4,000
2,000
0
1 4 7 10 13 16 19 22 25 28 31 34 37 40 43 46 49 52
Time since production started [month]
23-26-43-74
32-35-43-74

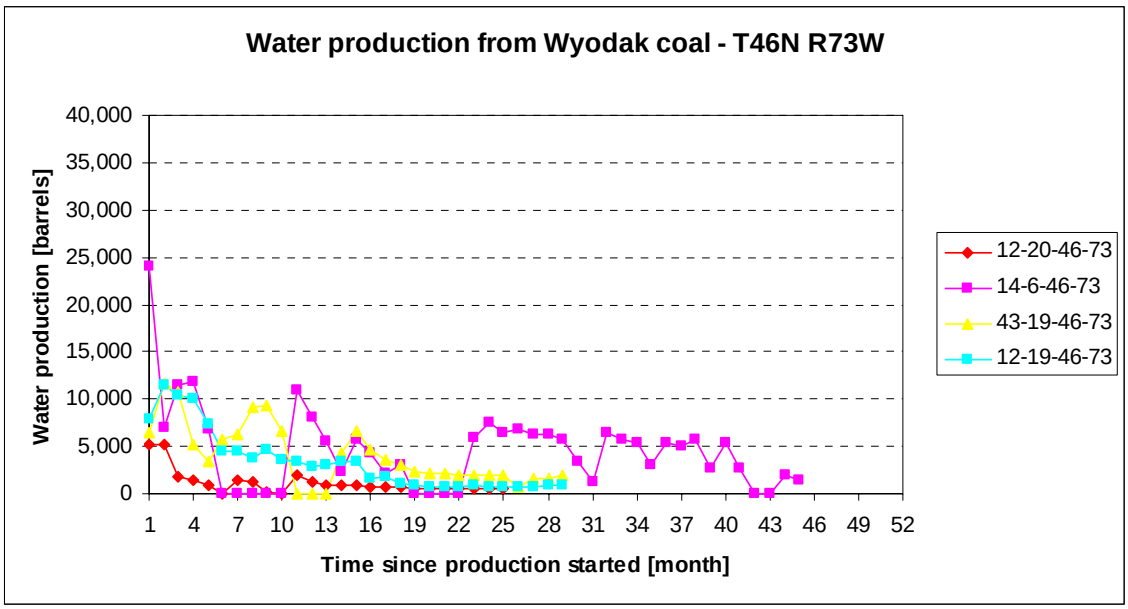
Water production from Wyodak coal - T46N R73W
Water production [barrels]
40,000
35,000
30,000
25,000
20,000
15,000
10,000
5,000
0
1 4 7 10 13 16 19 22 25 28 31 34 37 40 43 46 49 52
Time since production started [month]
12-20-46-73
14-6-46-73
43-19-46-73
12-19-46-73

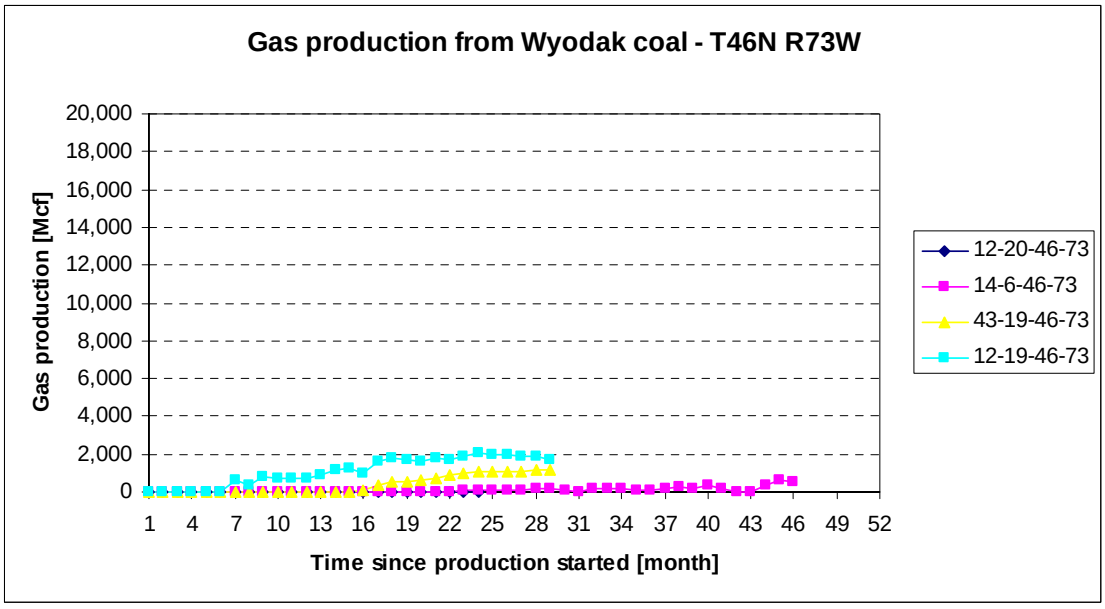
Gas production from Wyodak coal - T46N R73W
Gas production [Mcf]
20,000
18,000
16,000
14,000
12,000
10,000
8,000
6,000
4,000
2,000
0
1 4 7 10 13 16 19 22 25 28 31 34 37 40 43 46 49 52
Time since production started [month]
12-20-46-73
14-6-46-73
43-19-46-73
12-19-46-73

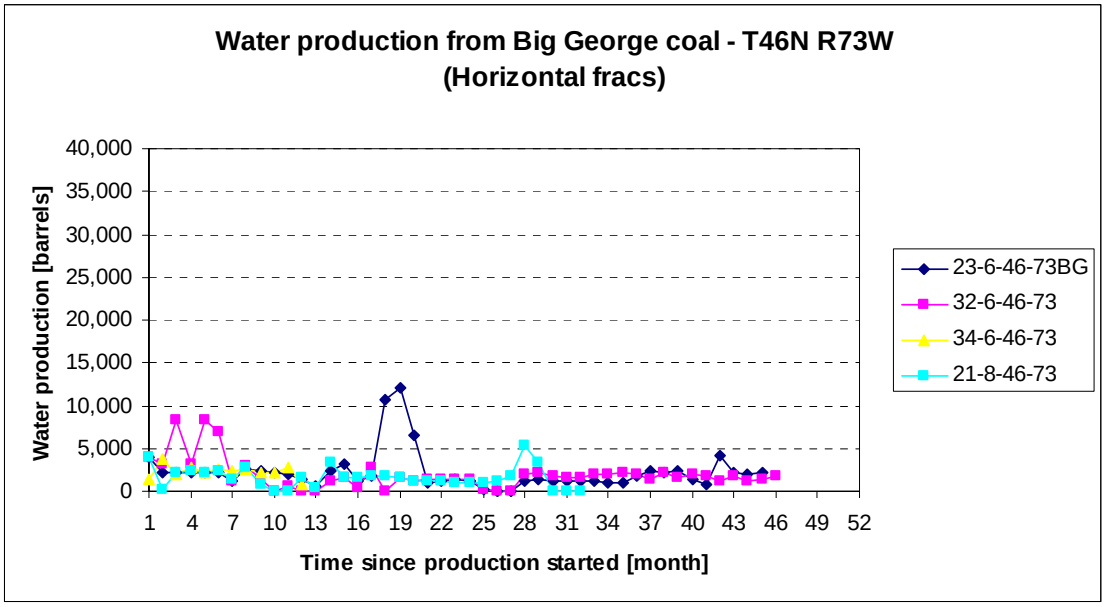
Water production from Big George coal - T46N R73W
(Horizontal fracs)
Water production [barrels]
40,000
35,000
30,000
25,000
20,000
15,000
10,000
5,000
0
1 4 7 10 13 16 19 22 25 28 31 34 37 40 43 46 49 52
Time since production started [month]
23-6-46-73BG
32-6-46-73
34-6-46-73
21-8-46-73

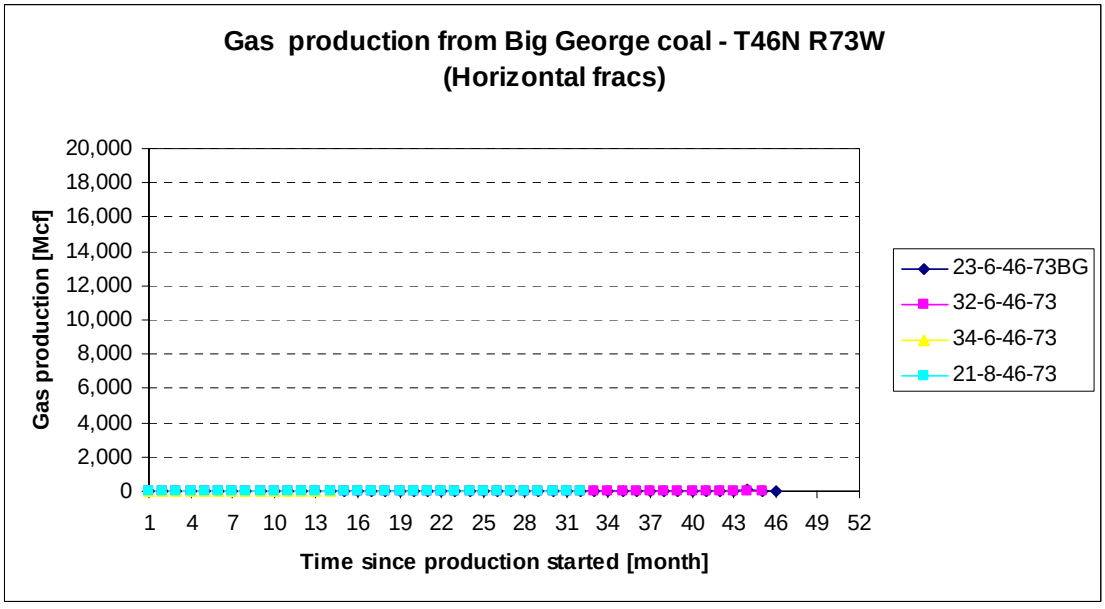
Gas production from Big George coal - T46N R73W
(Horizontal fracs)
Gas production [Mcf]
20,000
18,000
16,000
14,000
12,000
10,000
8,000
6,000
4,000
2,000
0
1 4 7 10 13 16 19 22 25 28 31 34 37 40 43 46 49 52
Time since production started [month]
23-6-46-73BG
32-6-46-73
34-6-46-73
21-8-46-73

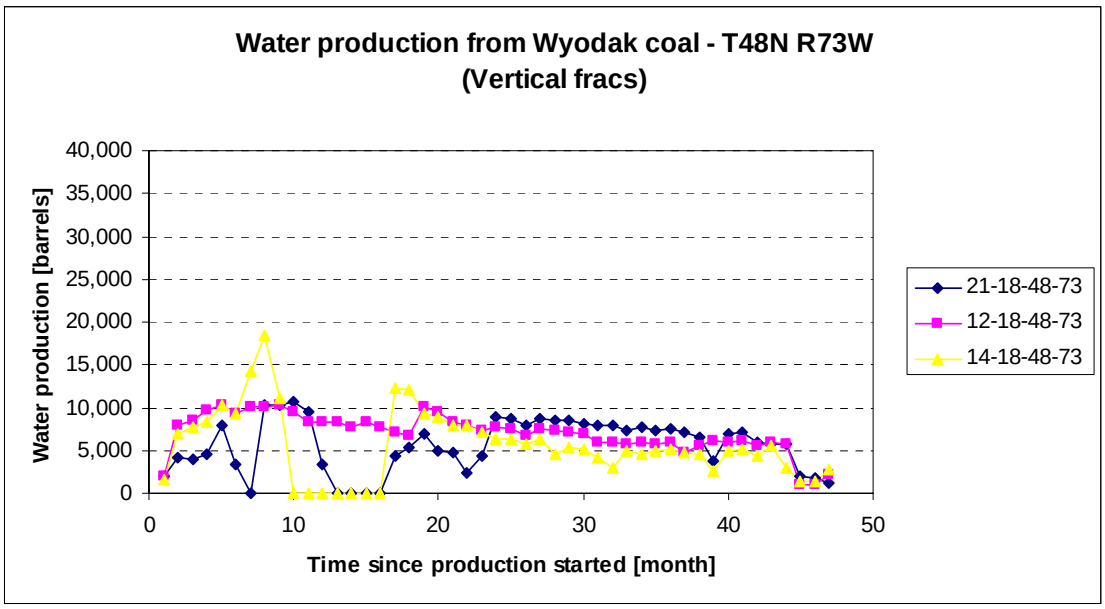
Water production from Wyodak coal - T48N R73W
(Vertical fracs)
Water production [barrels]
40,000
35,000
30,000
25,000
20,000
15,000
10,000
5,000
0
0
10
20
30
40
50
Time since production started [month]
21-18-48-73
12-18-48-73
14-18-48-73

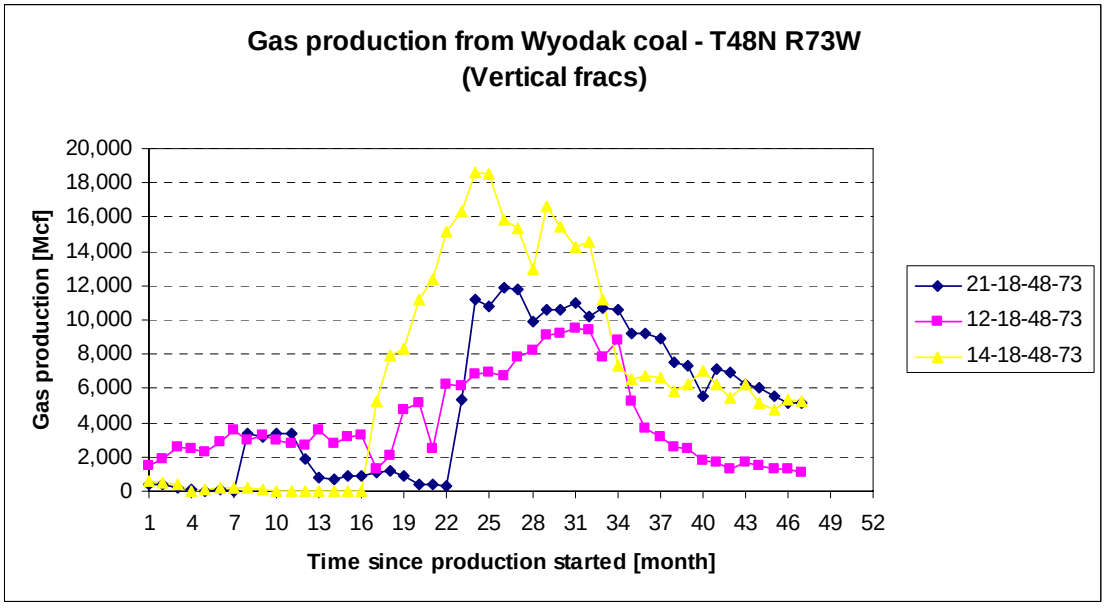
Gas production from Wyodak coal - T48N R73W
(Vertical fracs)
Gas production [Mcf]
20,000
18,000
16,000
14,000
12,000
10,000
8,000
6,000
4,000
2,000
0
1
4
7
10
13
16
19
22
25
28
31
34
37
40
43
46
49
52
Time since production started [month]
21-18-48-73
12-18-48-73
14-18-48-73

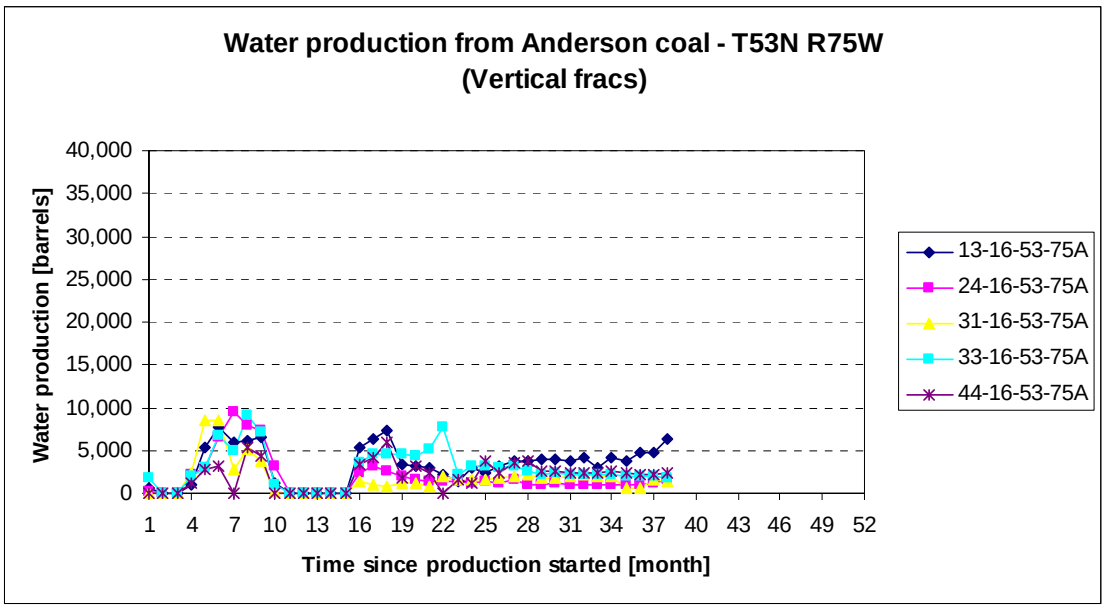
Water production from Anderson coal - T53N R75W
(Vertical fracs)
Water production [barrels]
40,000
35,000
30,000
25,000
20,000
15,000
10,000
5,000
0
1 4 7 10 13 16 19 22 25 28 31 34 37 40 43 46 49 52
Time since production started [month]
13-16-53-75A
24-16-53-75A
31-16-53-75A
33-16-53-75A
44-16-53-75A

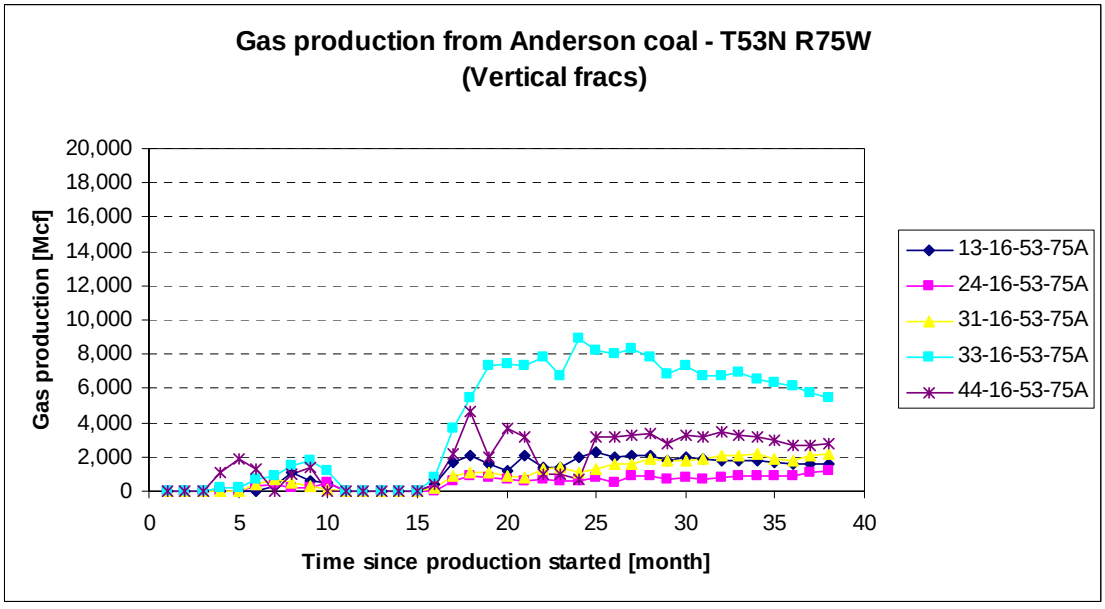
Gas production from Anderson coal - T53N R75W
(Vertical fracs)
Gas production [Mcf]
20,000
18,000
16,000
14,000
12,000
10,000
8,000
6,000
4,000
2,000
0
0 5 10 15 20 25 30 35 40
Time since production started [month]
13-16-53-75A
24-16-53-75A
31-16-53-75A
33-16-53-75A
44-16-53-75A

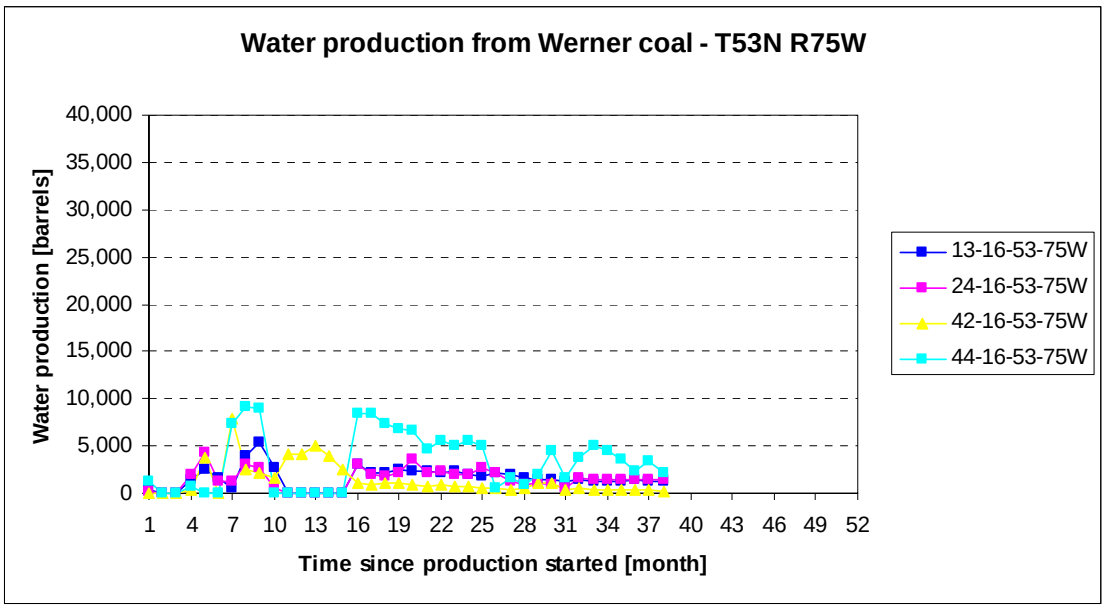
Water production from Werner coal - T53N R75W
Water production [barrels]
40,000
35,000
30,000
25,000
20,000
15,000
10,000
5,000
0
1 4 7 10 13 16 19 22 25 28 31 34 37 40 43 46 49 52
Time since production started [month]
13-16-53-75W
24-16-53-75W
42-16-53-75W
44-16-53-75W

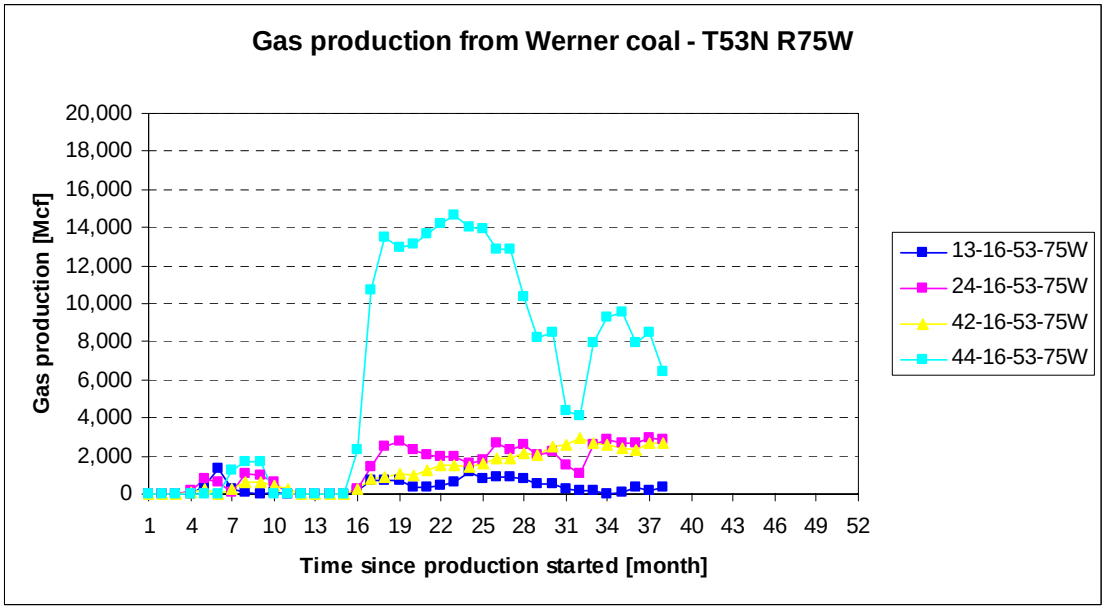
Gas production from Werner coal - T53N R75W
Gas production [Mcf]
20,000
18,000
16,000
14,000
12,000
10,000
8,000
6,000
4,000
2,000
0
1 4 7 10 13 16 19 22 25 28 31 34 37 40 43 46 49 52
Time since production started [month]
13-16-53-75W
24-16-53-75W
42-16-53-75W
44-16-53-75W

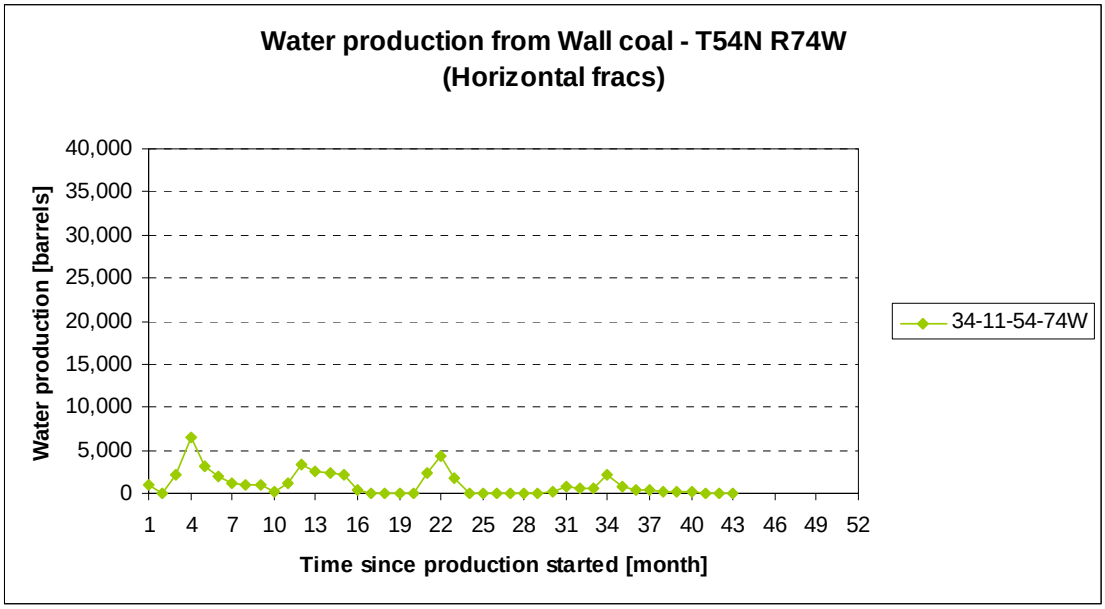
Water production from Wall coal - T54N R74W
(Horizontal fracs)
Water production [barrels]
40,000
35,000
30,000
25,000
20,000
15,000
10,000
5,000
0
1 4 7 10 13 16 19 22 25 28 31 34 37 40 43 46 49 52
Time since production started [month]
34-11-54-74W

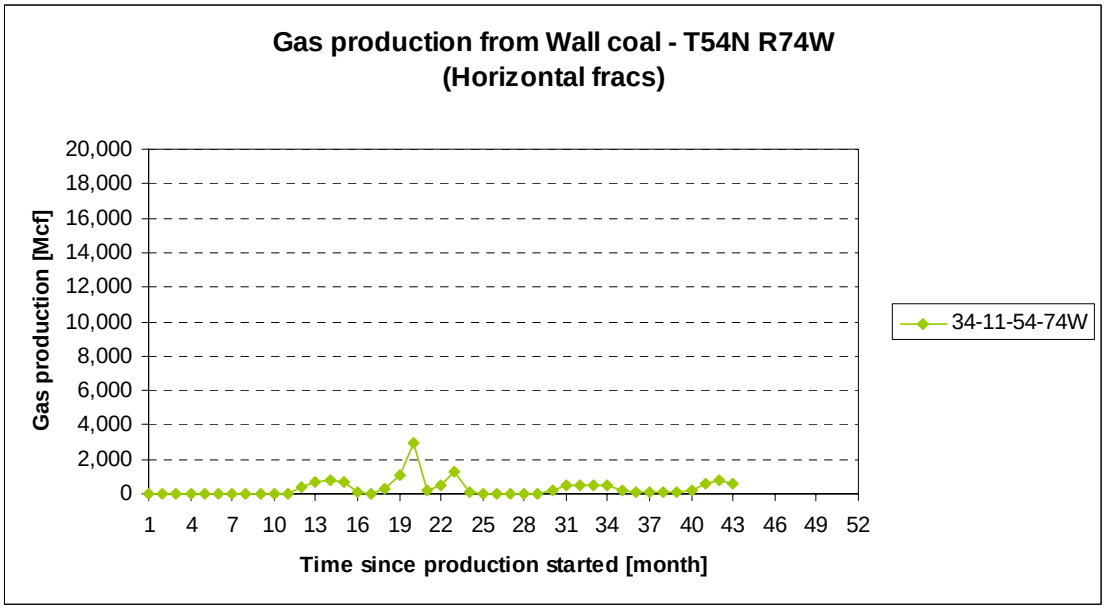
Gas production from Wall coal - T54N R74W
(Horizontal fracs)
Gas production [Mcf]
20,000
18,000
16,000
14,000
12,000
10,000
8,000
6,000
4,000
2,000
0
1 4 7 10 13 16 19 22 25 28 31 34 37 40 43 46 49 52
Time since production started [month]
34-11-54-74W

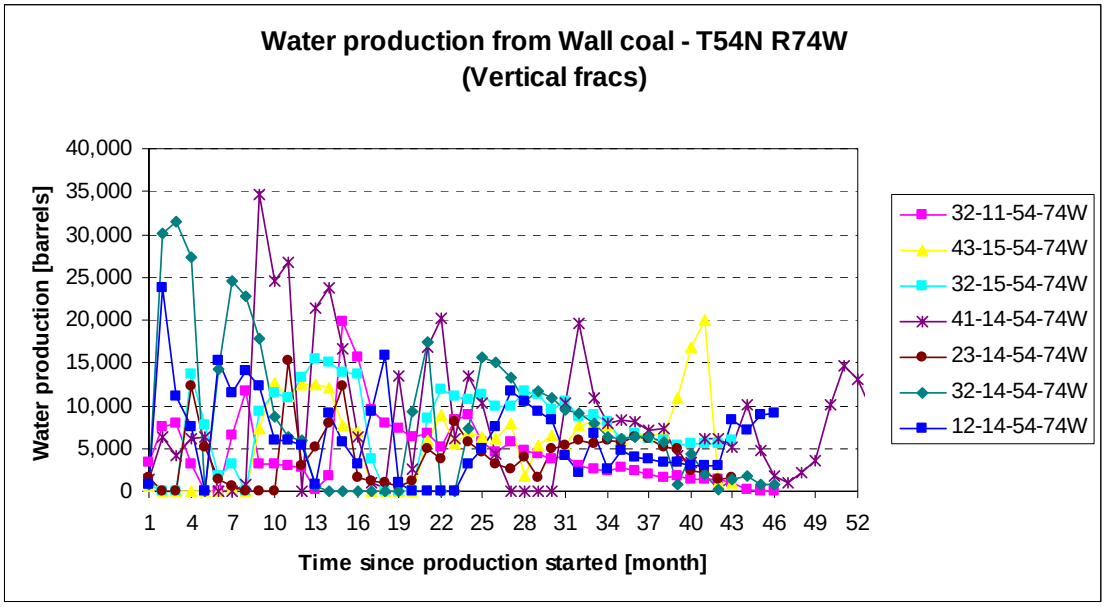
Water production from Wall coal - T54N R74W
(Vertical fracs)
Water production [barrels]
40,000
35,000
30,000
25,000
20,000
15,000
10,000
5,000
0
1 4 7 10 13 16 19 22 25 28 31 34 37 40 43 46 49 52
Time since production started [month]
32-11-54-74W
43-15-54-74W
32-15-54-74W
41-14-54-74W
23-14-54-74W
32-14-54-74W
12-14-54-74W

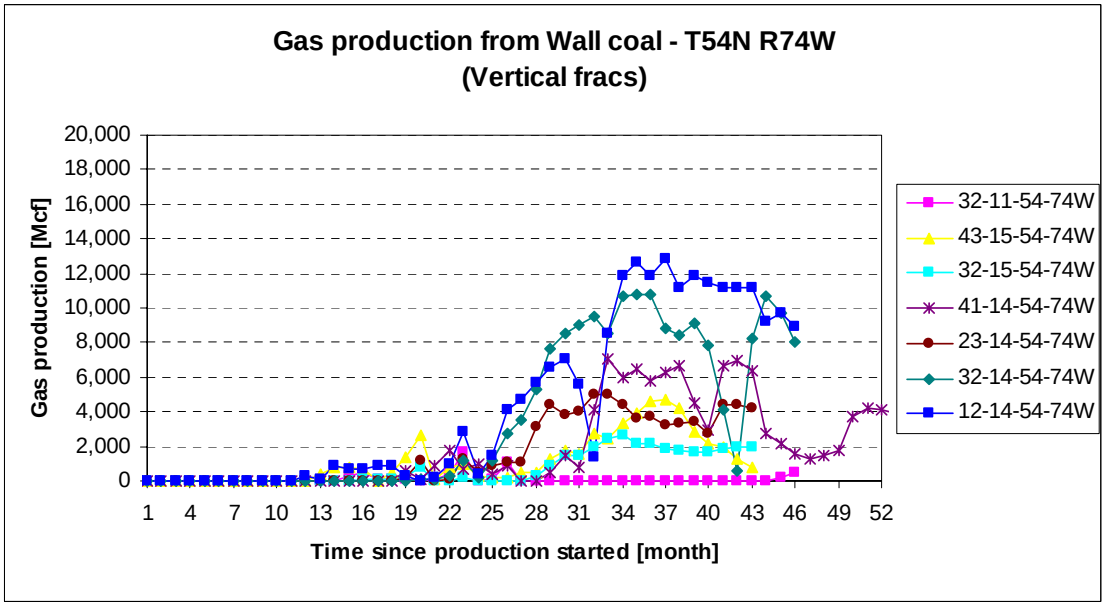
Gas production from Wall coal - T54N R74W
(Vertical fracs)
Gas production [Mcf]
20,000
18,000
16,000
14,000
12,000
10,000
8,000
6,000
4,000
2,000
0
1 4 7 10 13 16 19 22 25 28 31 34 37 40 43 46 49 52
Time since production started [month]
32-11-54-74W
43-15-54-74W
32-15-54-74W
41-14-54-74W
23-14-54-74W
32-14-54-74W
12-14-54-74W

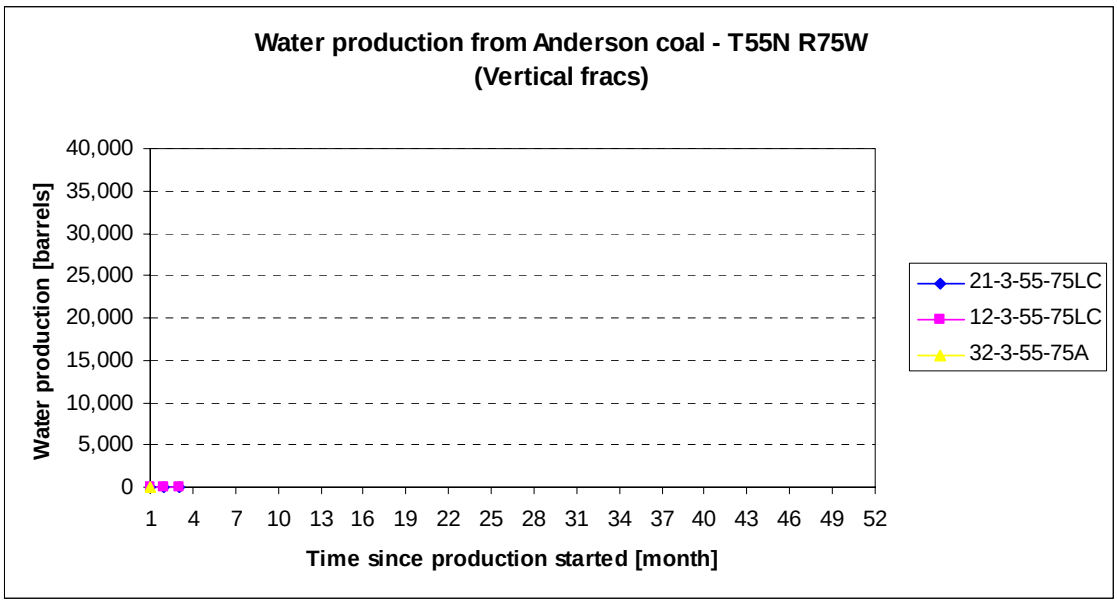
Water production from Anderson coal - T55N R75W
(Vertical fracs)
Water production [barrels]
40,000
35,000
30,000
25,000
20,000
15,000
10,000
5,000
0
1 4 7 10 13 16 19 22 25 28 31 34 37 40 43 46 49 52
Time since production started [month]
21-3-55-75LC
12-3-55-75LC
32-3-55-75A

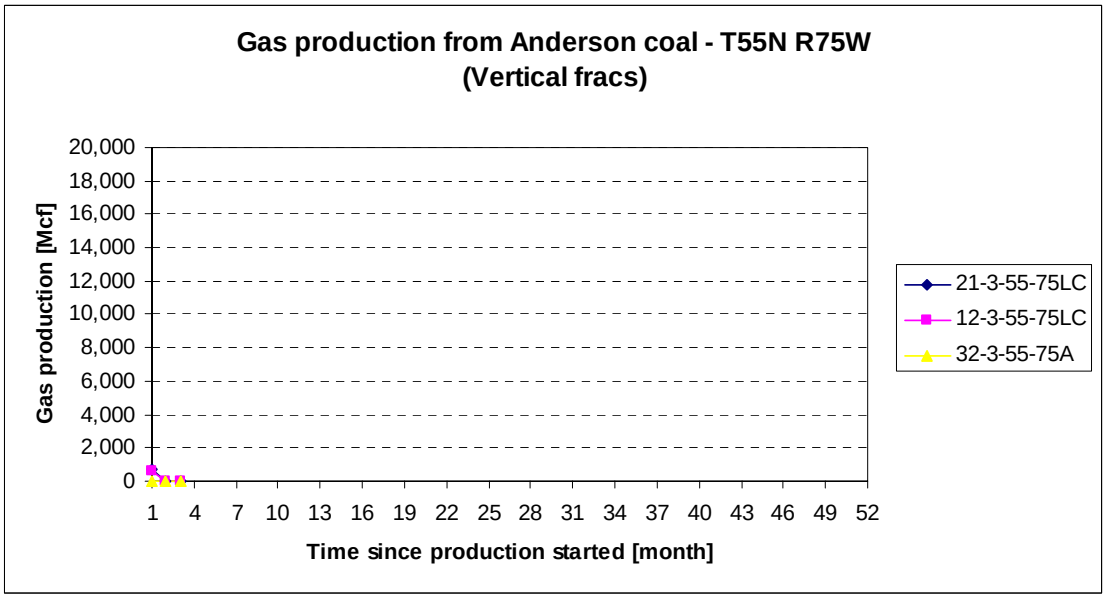
Gas production from Anderson coal - T55N R75W
(Vertical fracs)
Gas production [Mcf]
20,000
18,000
16,000
14,000
12,000
10,000
8,000
6,000
4,000
2,000
0
1 4 7 10 13 16 19 22 25 28 31 34 37 40 43 46 49 52
Time since production started [month]
21-3-55-75LC
12-3-55-75LC
32-3-55-75A

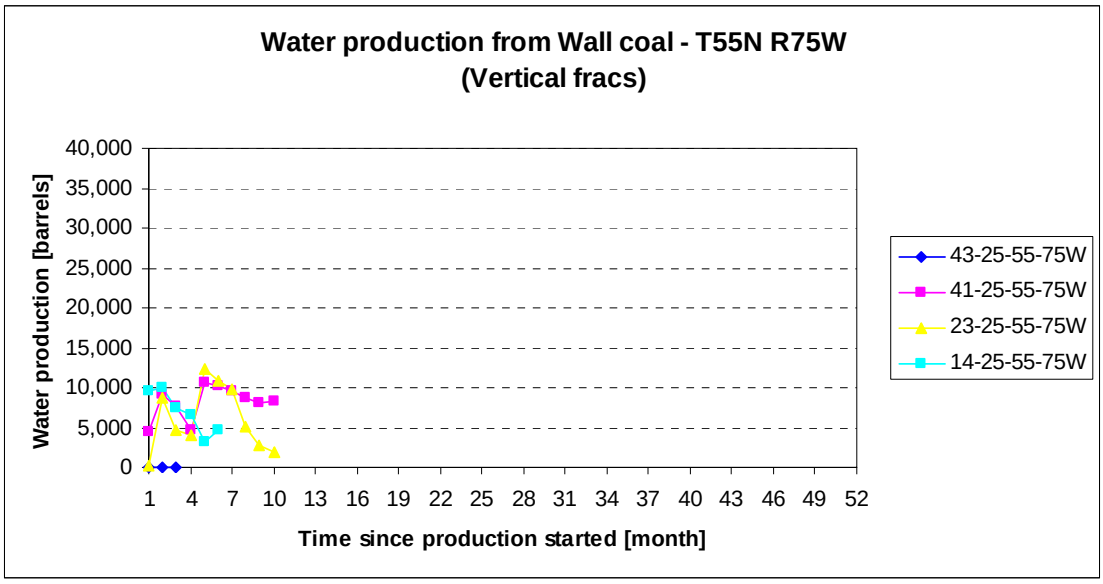
Water production from Wall coal - T55N R75W
(Vertical fracs)
Water production [barrels]
40,000
35,000
30,000
25,000
20,000
15,000
10,000
5,000
0
1 4 7 10 13 16 19 22 25 28 31 34 37 40 43 46 49 52
Time since production started [month]
43-25-55-75W
41-25-55-75W
23-25-55-75W
14-25-55-75W

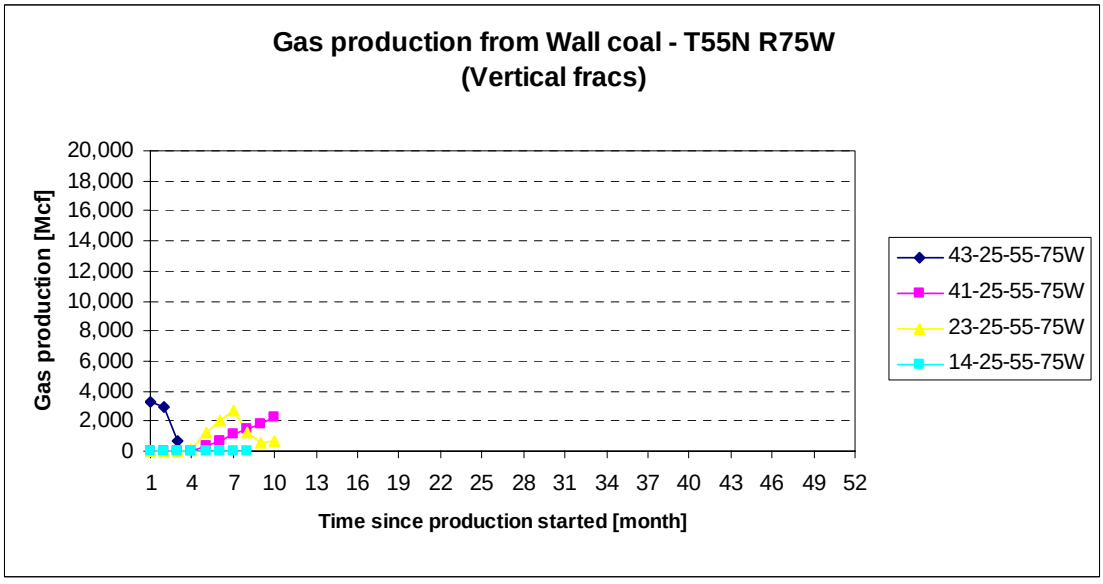
Gas production from Wall coal - T55N R75W
(Vertical fracs)
Gas production [Mcf]
20,000
18,000
16,000
14,000
12,000
10,000
8,000
6,000
4,000
2,000
0
1 4 7 10 13 16 19 22 25 28 31 34 37 40 43 46 49 52
Time since production started [month]
43-25-55-75W
41-25-55-75W
23-25-55-75W
14-25-55-75W

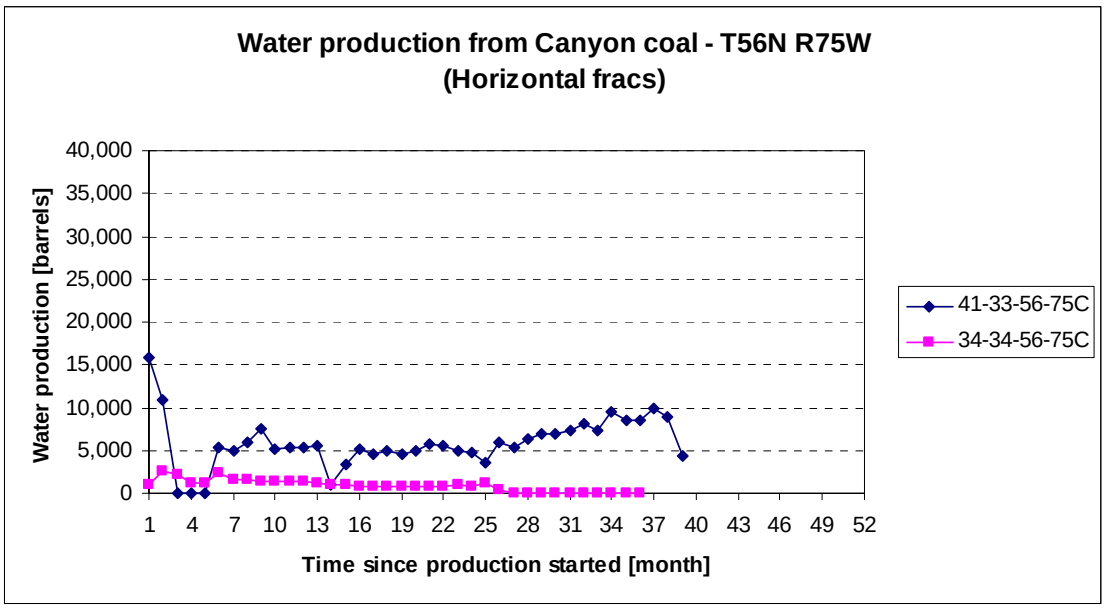
Water production from Canyon coal - T56N R75W
(Horizontal fracs)
Water production [barrels]
40,000
35,000
30,000
25,000
20,000
15,000
10,000
5,000
0
1 4 7 10 13 16 19 22 25 28 31 34 37 40 43 46 49 52
Time since production started [month]
41-33-56-75C
34-34-56-75C

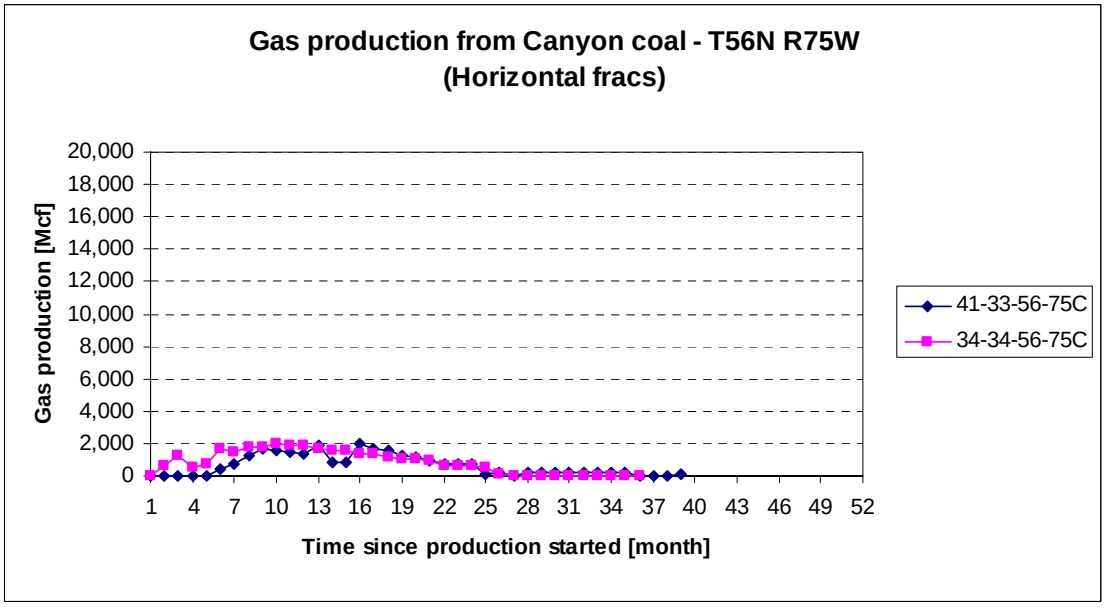
Gas production from Canyon coal - T56N R75W
(Horizontal fracs)
Gas production [Mcf]
20,000
18,000
16,000
14,000
12,000
10,000
8,000
6,000
4,000
2,000
0
1 4 7 10 13 16 19 22 25 28 31 34 37 40 43 46 49 52
Time since production started [month]
41-33-56-75C
34-34-56-75C

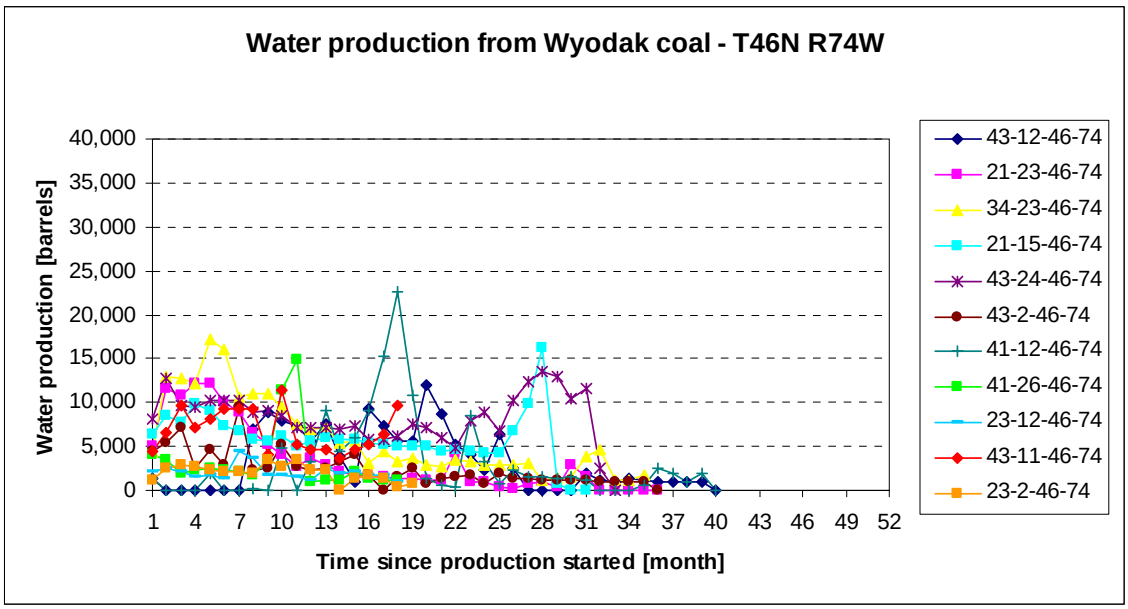
Water production from Wyodak coal - T46N R74W
Water production [barrels]
40,000
35,000
30,000
25,000
20,000
15,000
10,000
5,000
0
1 4 7 10 13 16 19 22 25 28 31 34 37 40 43 46 49 52
Time since production started [month]
43-12-46-74
21-23-46-74
34-23-46-74
21-15-46-74
43-24-46-74
43-2-46-74
41-12-46-74
41-26-46-74
23-12-46-74
43-11-46-74
23-2-46-74

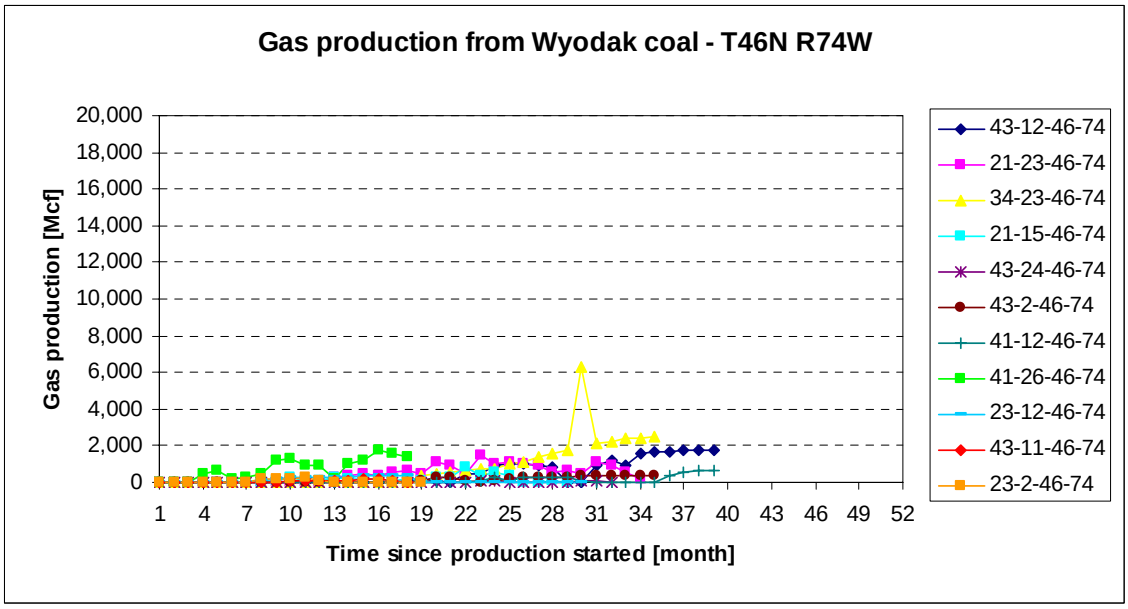
Gas production from Wyodak coal - T46N R74W
Gas production [Mcf]
20,000
18,000
16,000
14,000
12,000
10,000
8,000
6,000
4,000
2,000
0
1 4 7 10 13 16 19 22 25 28 31 34 37 40 43 46 49 52
Time since production started [month]
43-12-46-74
21-23-46-74
34-23-46-74
21-15-46-74
43-24-46-74
43-2-46-74
41-12-46-74
41-26-46-74
23-12-46-74
43-11-46-74
23-2-46-74

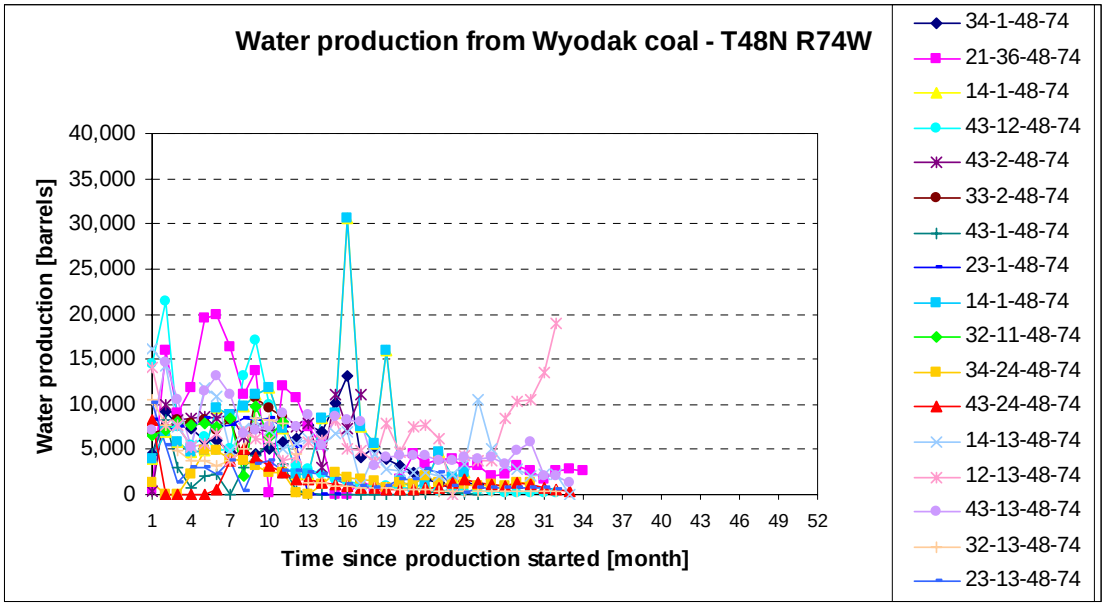
Water production from Wyodak coal - T48N R74W
Water production [barrels]
40,000
35,000
30,000
25,000
20,000
15,000
10,000
5,000
0
1 4 7 10 13 16 19 22 25 28 31 34 37 40 43 46 49 52
Time since production started [month]
34-1-48-74
21-36-48-74
14-1-48-74
43-12-48-74
43-2-48-74
33-2-48-74
43-1-48-74
23-1-48-74
14-1-48-74
32-11-48-74
34-24-48-74
43-24-48-74
14-13-48-74
12-13-48-74
43-13-48-74
32-13-48-74
23-13-48-74

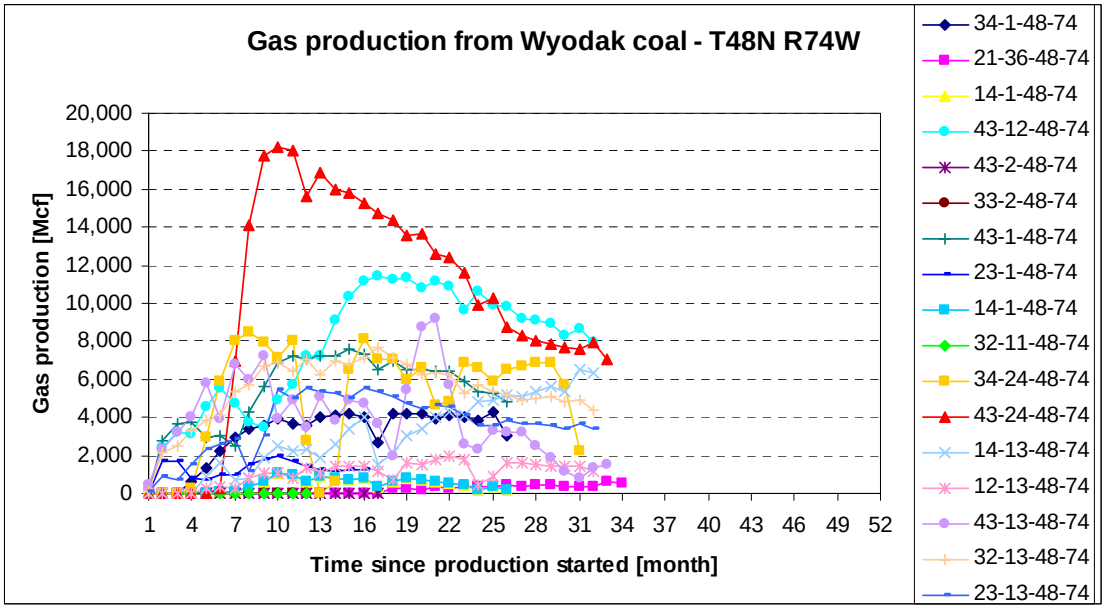
Gas production from Wyodak coal - T48N R74W
Gas production [Mcf]
20,000
18,000
16,000
14,000
12,000
10,000
8,000
6,000
4,000
2,000
0
1 4 7 10 13 16 19 22 25 28 31 34 37 40 43 46 49 52
Time since production started [month]
34-1-48-74
21-36-48-74
14-1-48-74
43-12-48-74
43-2-48-74
33-2-48-74
43-1-48-74
23-1-48-74
14-1-48-74
32-11-48-74
34-24-48-74
43-24-48-74
14-13-48-74
12-13-48-74
43-13-48-74
32-13-48-74
23-13-48-74

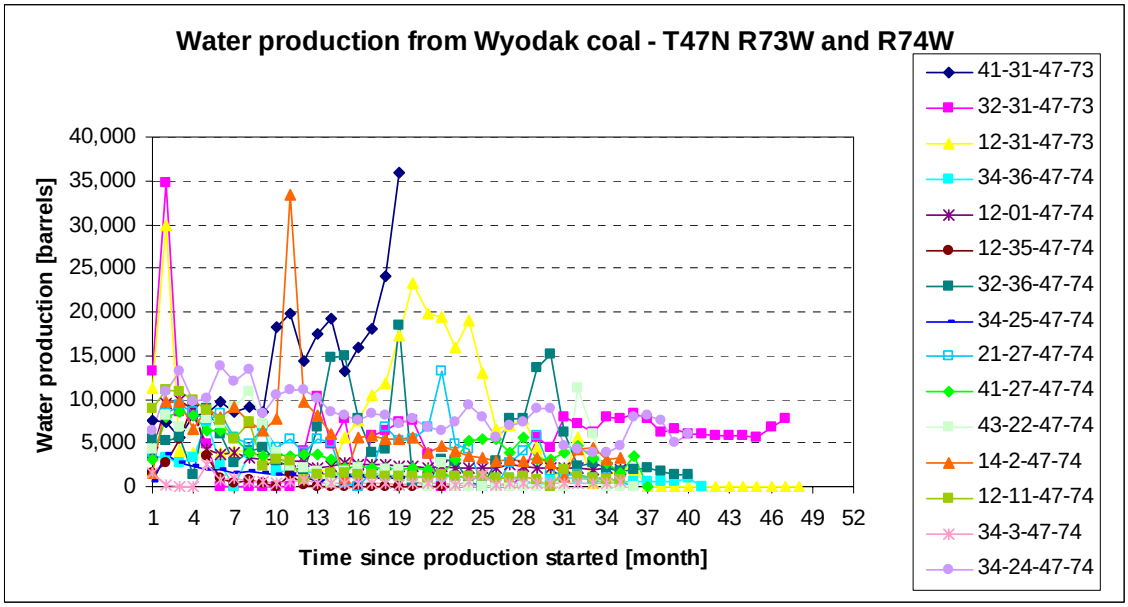
Water production from Wyodak coal - T47N R73W and R74W
Water production [barrels]
40,000
35,000
30,000
25,000
20,000
15,000
10,000
5,000
0
1 4 7 10 13 16 19 22 25 28 31 34 37 40 43 46 49 52
Time since production started [month]
41-31-47-73
32-31-47-73
12-31-47-73
34-36-47-74
12-01-47-74
12-35-47-74
32-36-47-74
34-25-47-74
21-27-47-74
41-27-47-74
43-22-47-74
14-2-47-74
12-11-47-74
34-3-47-74
34-24-47-74

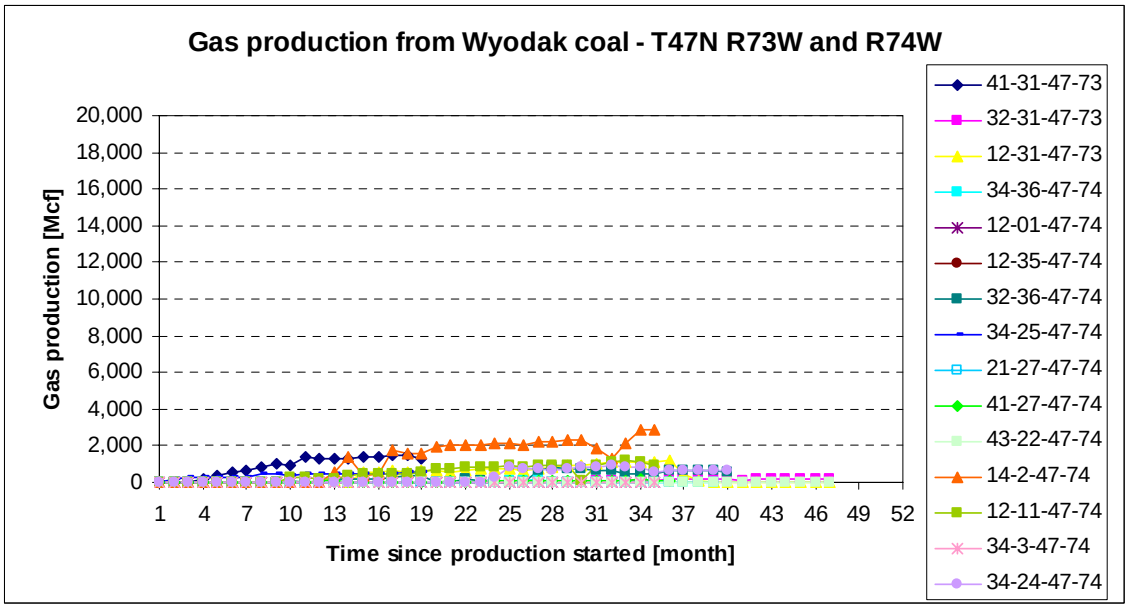
Gas production from Wyodak coal - T47N R73W and R74W
Gas production [Mcf]
20,000
18,000
16,000
14,000
12,000
10,000
8,000
6,000
4,000
2,000
0
1 4 7 10 13 16 19 22 25 28 31 34 37 40 43 46 49 52
Time since production started [month]
41-31-47-73
32-31-47-73
12-31-47-73
34-36-47-74
12-01-47-74
12-35-47-74
32-36-47-74
34-25-47-74
21-27-47-74
41-27-47-74
43-22-47-74
14-2-47-74
12-11-47-74
34-3-47-74
34-24-47-74

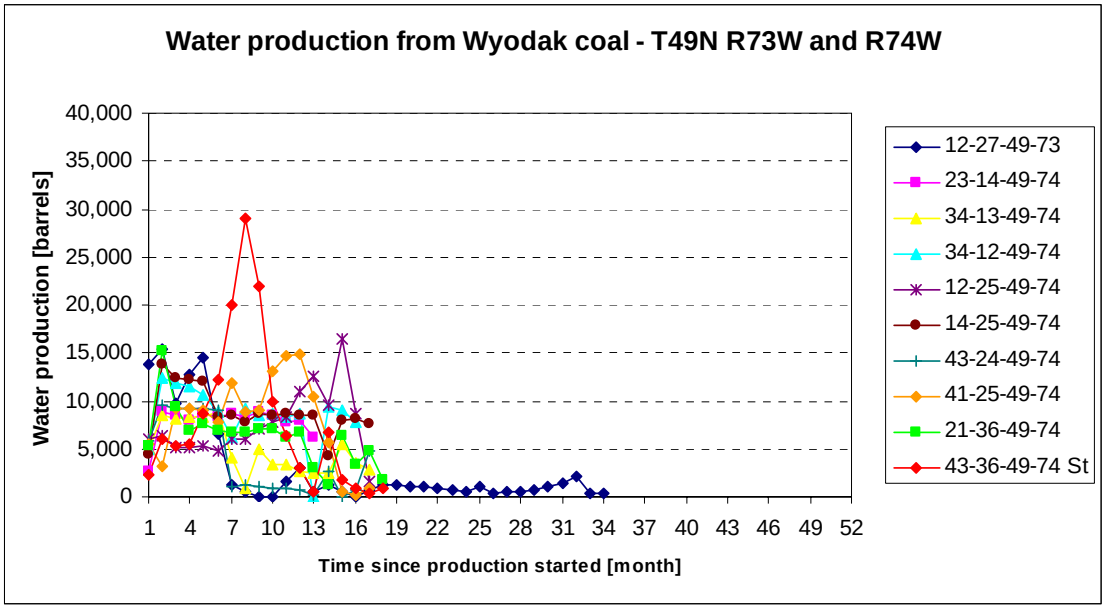
Water production from Wyodak coal - T49N R73W and R74W
Water production [barrels]
40,000
35,000
30,000
25,000
20,000
15,000
10,000
5,000
0
1 4 7 10 13 16 19 22 25 28 31 34 37 40 43 46 49 52
Time since production started [month]
12-27-49-73
23-14-49-74
34-13-49-74
34-12-49-74
12-25-49-74
14-25-49-74
43-24-49-74
41-25-49-74
21-36-49-74
43-36-49-74 St

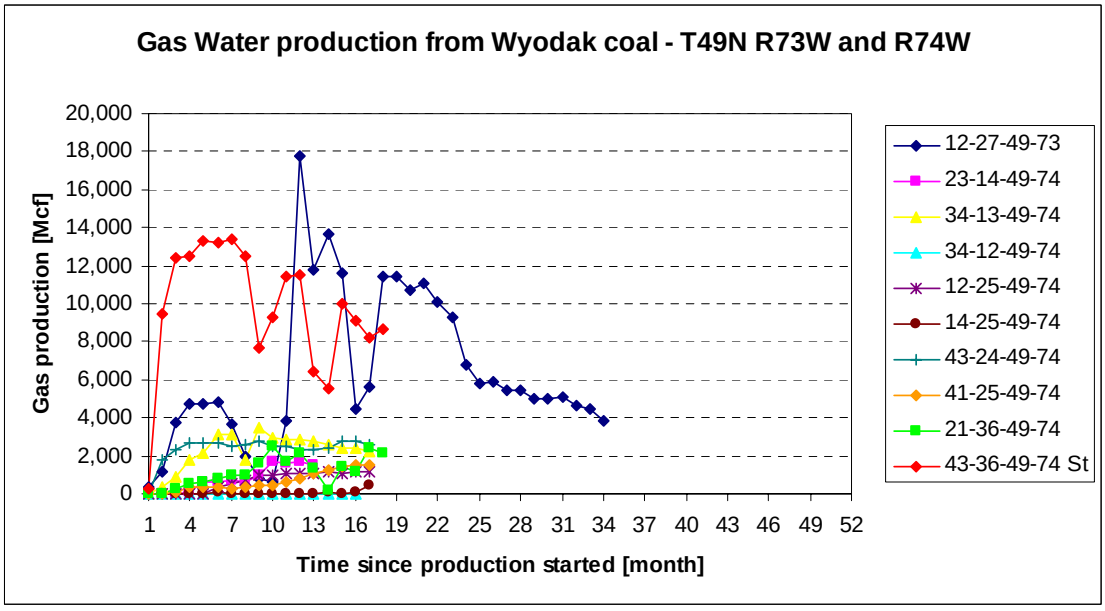
Gas Water production from Wyodak coal - T49N R73W and R74W
Gas production [Mcf]
20,000
18,000
16,000
14,000
12,000
10,000
8,000
6,000
4,000
2,000
0
1 4 7 10 13 16 19 22 25 28 31 34 37 40 43 46 49 52
Time since production started [month]
12-27-49-73
23-14-49-74
34-13-49-74
34-12-49-74
12-25-49-74
14-25-49-74
43-24-49-74
41-25-49-74
21-36-49-74
43-36-49-74 St

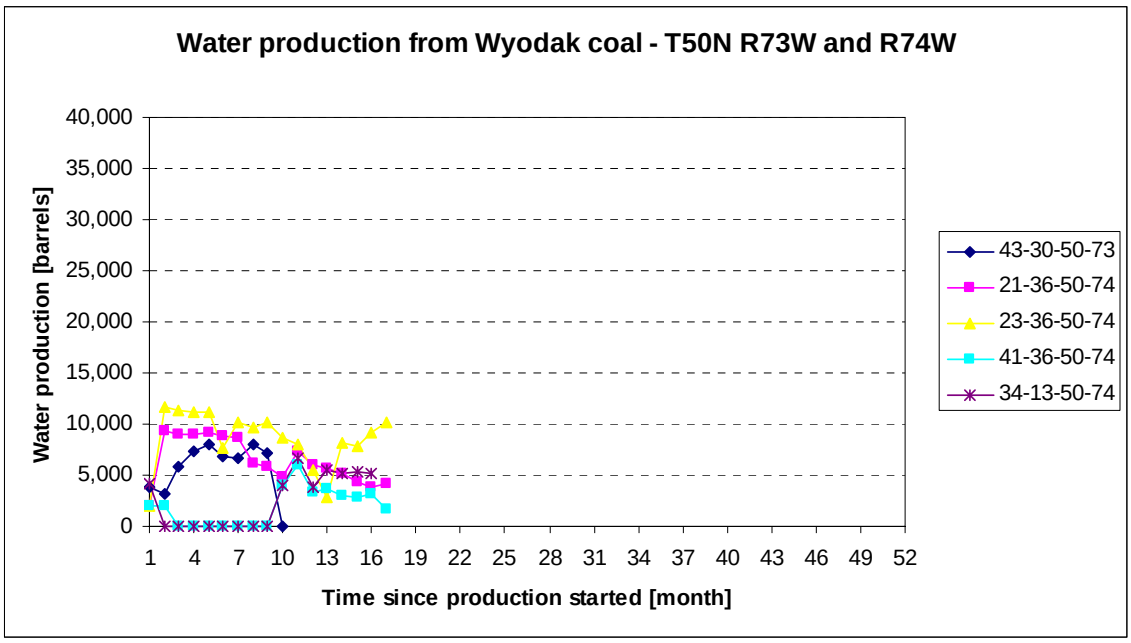
Water production from Wyodak coal - T50N R73W and R74W
Water production [barrels]
40,000
35,000
30,000
25,000
20,000
15,000
10,000
5,000
0
1 4 7 10 13 16 19 22 25 28 31 34 37 40 43 46 49 52
Time since production started [month]
43-30-50-73
21-36-50-74
23-36-50-74
41-36-50-74
34-13-50-74

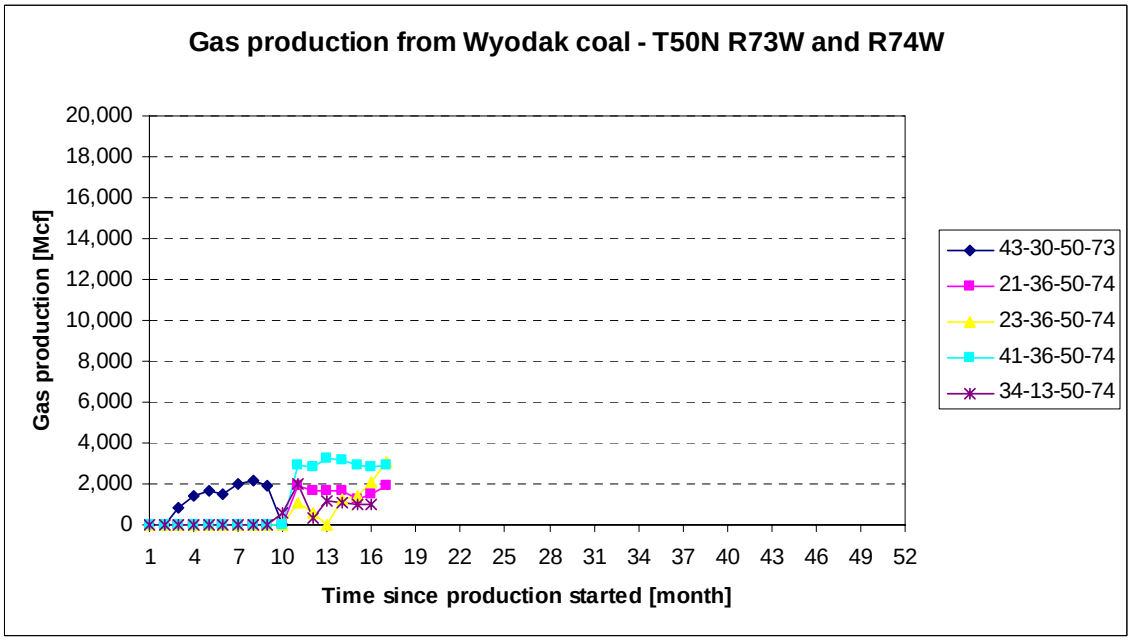
Gas production from Wyodak coal - T50N R73W and R74W
Gas production [Mcf]
20,000
18,000
16,000
14,000
12,000
10,000
8,000
6,000
4,000
2,000
0
1 4 7 10 13 16 19 22 25 28 31 34 37 40 43 46 49 52
Time since production started [month]
43-30-50-73
21-36-50-74
23-36-50-74
41-36-50-74
34-13-50-74

APPENDIX 4.D. THICKNESS MAPS WITH S_3/S_V DATA POINTS

Additional contributions from this study include maps of coal thickness (color scale and contours) for the Anderson (Figure 4.D.1) and Wyodak (Figure 4.D.2) coals. S_3/S_V data are also plotted in these maps (data points), however the relationship between thickness and S_3/S_V is better described in Figures 4.30 and 4.31 from section 4.6.3.

Figure 4.D.3 combines thickness, water production and S_3/S_V data for Big George coal. As can be seen in Figure 4.D.3, water production, which is denoted by the contour lines, generally increases with thickness (color scale). However, for the same thickness, there are areas of anomalous water production. The anomalies may suggest hydraulic connection of the coal with adjacent formations in those specific areas.

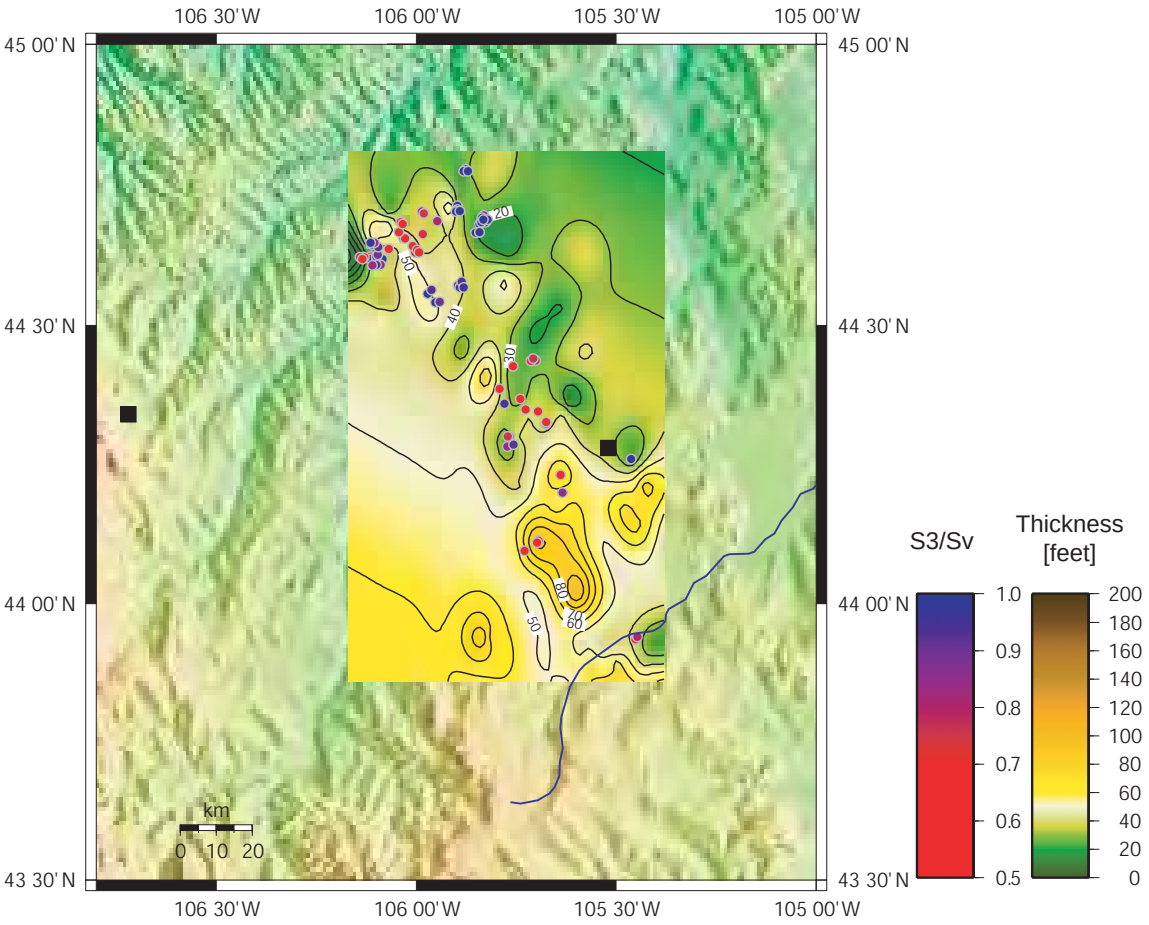

Figure 4.D.1: Map of interpolated thickness and S_3/S_V data points for Anderson coal.

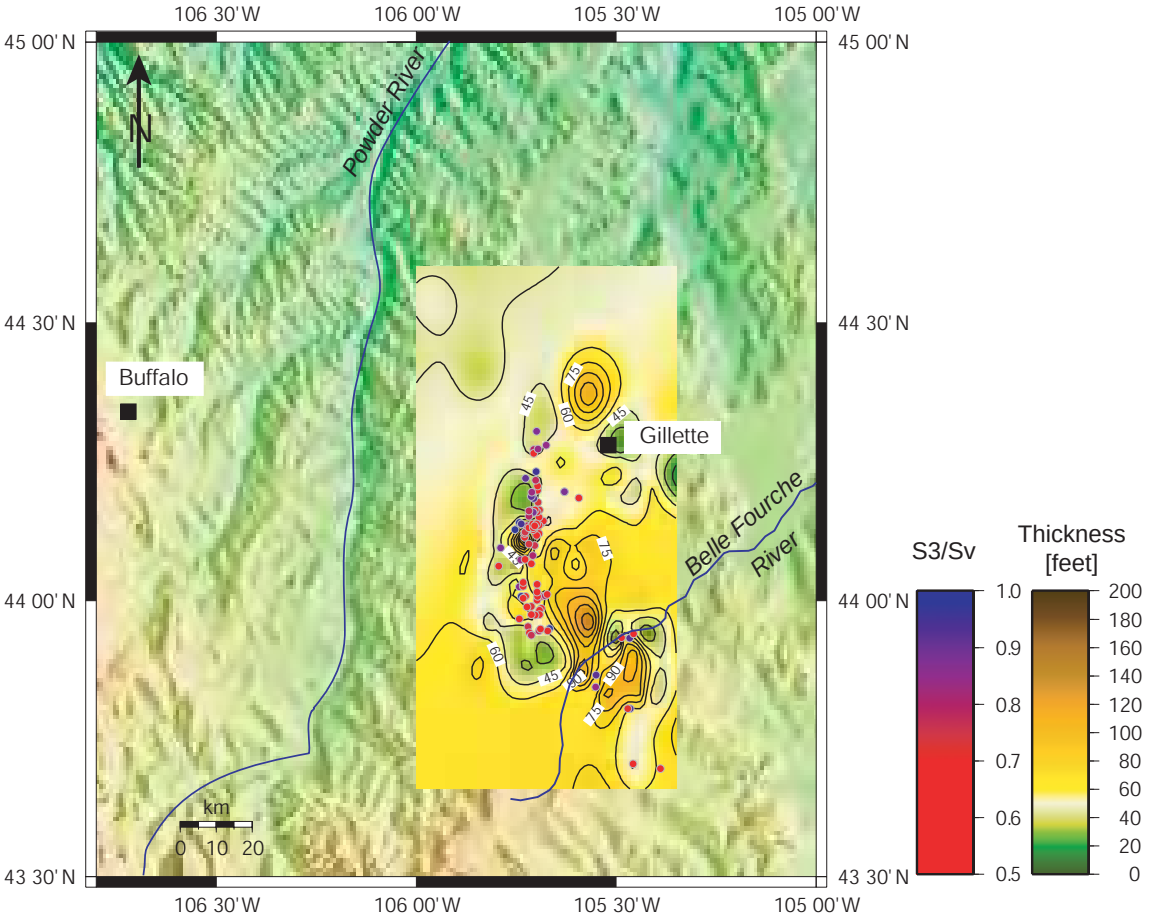

Figure 4.D.2: Map of interpolated thickness and S_3/S_V data points for Wyodak coal.

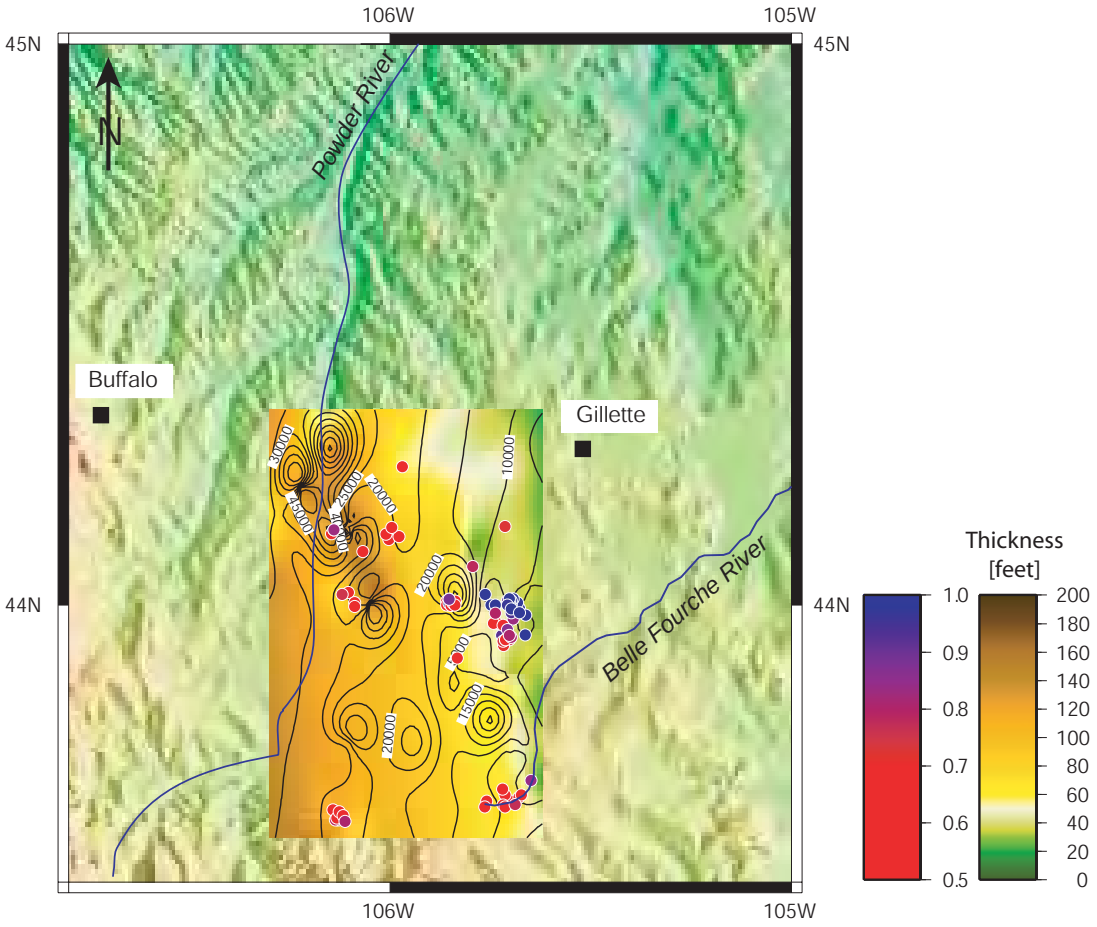

Figure 4.D.3: Map of interpolated thickness and S_3/S_V data points for Big George coal. The contours correspond to the average water production in barrels/month.